Measurement of Muon Neutrino Disappearance with the T2K Experiment

by

Taritree Michael Wongjirad

Department of Physics
Duke University

Date: _____

Approved:

_____
Kate Scholberg, Supervisor

_____
Ayana Arce

_____
Joshua Socolar

_____
Roxanne Springer

_____
Chris Walter

Dissertation submitted in partial fulfillment of the requirements for the degree of
Doctor of Philosophy in the Department of Physics
in the Graduate School of Duke University
2014

Abstract

Measurement of Muon Neutrino Disappearance with the T2K Experiment

by

Taritree Michael Wongjirad

Department of Physics
Duke University

Date: _____

Approved:

_____
Kate Scholberg, Supervisor

_____
Ayana Arce

_____
Joshua Socolar

_____
Roxanne Springer

_____
Chris Walter

An abstract of a dissertation submitted in partial fulfillment of the requirements for the degree of Doctor of Philosophy in the Department of Physics in the Graduate School of Duke University
2014

Abstract

We have made a preciese measurement of neutrino oscillations using the Tokai-2-Kamiokande (T2K) experiment's Run 1-4 (6.57×10^{20} POT) data set. Specifically, we have measured the disappearance of an off-axis muon neutrino beam after it has traveled a total of 295 km. We analyze the data using the conventional Pontecorvo-Maki-Nakagawa-Sakata (PMNS) mixing matrix for the three Standard Model neutrinos. The output of the analysis is a measurement of the parameters $\sin^2\theta_{23}, \Delta m^2_{32}$ when assuming the normal mass hierarchy and $\sin^2\theta_{23}, \Delta m^2_{13}$ when assuming the inverted mass hierarchy. The best-fit oscillation parameters for the normal hierarchy is

$$(\sin^2\theta_{23}, \Delta m^2_{32}) = (0.514, 2.51 \times 10^{-3}\ \mathrm{eV}^2/\mathrm{c}^4).$$

The 90% 1D confidence interval for the normal hierarchy was determined for both parameters using the Feldman-Cousins procedure and is

$$0.428 < \sin^2\theta_{23} < 0.598$$

$$2.34 \times 10^{-3}\ \mathrm{eV}^2/\mathrm{c}^4 < \Delta m^2_{32} < 2.68 \times 10^{-3}\ \mathrm{eV}^2/\mathrm{c}^4.$$

For the inverted hierarchy, the best-fit oscillation parameters are

$$(\sin^2\theta_{23}, \Delta m^2_{13}) = (0.511, 2.48 \times 10^{-3}\ \mathrm{eV}^2/\mathrm{c}^4).$$

The 90% 1D Feldman-Cousins confidence intervals for the inverted hierarchy are

$$0.427 < \sin^2\theta_{23} < 0.596$$

$$2.31 \times 10^{-3}\ \mathrm{eV}^2/\mathrm{c}^4 < \Delta m^2_{13} < 2.64 \times 10^{-3}\ \mathrm{eV}^2/\mathrm{c}^4.$$

To my family.

Contents

List of Tables

List of Figures

Acknowledgements

This dissertation would not have been completed without the support of many whom I can only begin to properly thank here.

In particular, I want to thank my dissertation committee, especially my thesis advisors, Professors Kate Scholberg and Chris Walter. While choosing schools, those whose advice I trusted most said you were excellent physicists who would make great advisors. This certainly turned out to be true, and I thank you for your mentoring. I know I am in the lucky minority of students who have advisors that are available at all times to help. I am sorry that those times were often at the last possible moment.

I also want to thank you, Kate and Chris, for surrounding me with great postdocs and fellow students: Dr. Josh Albert, Dr. Tarek Akiri, Dr. Alex Himmel, and Dr. Roger Wendell. I am better at physics because of all of you, and I am very thankful for your scientific guidance. But I am also thankful that, because of each of you, I am now better at recognizing sumo wrestlers, enjoying the onsen, knowing where thermometers go in Japan, choosing the right sushi, Python, and definitely not Fortran.

Of course, the work in this thesis would not begin to be possible without the hard work of all the collaborators on the T2K and Super-Kamiokande experiments. I really appreciated the opportunity to do interesting science by learning from many excellent scientists. I especially want to thank those with whom I worked closely: Professor Ed Kearns, Professor Masato Shiozawa-san, Professor Tsuyoshi Nakaya-

san, Professor Akihiro Minamino-san, Professor Hiro Tanaka, Dr. Jun Kameda-san, Dr. Kendall Mahn, and Dr. Mike Wilking.

I would also like to thank those who got me started towards the path of pursuing a PhD in physics and those who got me through it. Thanks to Professor Dan McKinsey at Yale who gave me my first lab job and who provided me with, which in retrospect, might have been too much freedom to play in the lab. Building detectors in the pursuit of such interesting questions is what got me hooked. Also thank you to Professors Moshe Gai and Bonnie Fleming for giving me additional opportunities to learn and break things. I also would like to thank my fellow graduate students who got me through classes and who were always there to commiserate with: Ben Cerio, Chris Coleman-Smith, and Georgios Laskaris. Also, special thanks to my friend, Dr. Joshua Spitz, along side whom I worked as an undergraduate. You have been a great friend and colleague whom I hope to be able to ski with every year at various conferences.

Finally, a very big thank you to my family. To my parents, Chatree and Thanida Wongjirad, thank you for your constant love and support both of which has made this dissertation possible. You have always been supportive of whatever I chose to do, and I greatly appreciate all the hard work you put into raising a kid who would end up always too busy to call (Sorry!). I also really appreciate the hard work you did to give me the means to play in labs after college instead of finding a real job. To my sister, Chelsey, I am truly lucky to have someone who I know will always love and support me and who will put up with my many annoying opinions, such as disdain for chain restaurants. Turns out you were right: at least one is good.[1] I really appreciate how you express pride in whatever accomplishments I stumble into, and I want you to know that I am just as proud, if not more so, of you: the real next-Dr. Wongjirad. Last, I also want to thank my fiancée, Anne Pessala, for her

[1] Chipotle

love. I cannot believe how lucky I am to have found someone who has your depth of kindness – and patience.

The point when the dissertation has been written and defended is suppose to mark the moment when its author transitions from a student to a scientist. Now that I am here, I feel it remains to be seen if I will earn that title. But with all the support I have received by those named and unnamed, I know that I have had the tremendous fortune to be given the opportunity. I will do my best to make all of you proud.

1

Introduction

If you can find a way to listen to neutrinos, they can tell you about the quantum world from which they were born. However, they will be quite guarded. The neutrino, to the best of our knowledge, is one of the fundamental particles that make up our universe. We also know that they interact with other matter extremely rarely. So rare that even if a neutrino were to pass through a block of lead four light years long – about the distance from Earth to the nearest star – the particle would have a better than 50% chance of passing through unimpeded. But it is this ability to travel undisturbed over vast distances that makes the behavior of neutrinos so interesting. Their reluctance to interact allow them to display quantum physics effects over human scales. The precise measurement of such an effect, neutrino oscillations, is the topic of this dissertation.

Neutrino oscillation is the name for the observed phenomenon where a neutrino created as one type can change into another and back again as it travels through space. This is a purely quantum process. Oscillations occur because the neutrino exists, in some sense, as a simultaneous combination of different neutrinos with different masses. There is no direct analogue of this in our everyday experience. But

as mentioned, we can observe this process play out over many meters and kilometers.

And there is much we can learn from the study of the neutrino oscillations. Already, this quantum mechanical transformation has told us that the neutrino has mass. Before the discovery of oscillations, there was no universally accepted reason to assign a mass to the neutrino in the Standard Model of particle physics. Therefore, this new fact has led us to the following questions: what is the mass of the neutrino, and does it get its mass like other particles or from some other mechanism? Answers to these questions impact not only what we know about the physics of neutrinos but also might lead to evidence of particles and forces whose energies are much larger than what current particle colliders, such as the Large Hardon Collider, can probe directly (Mohapatra and Smirnov (2005)). And because the neutrino is so abundant in our universe, it turns out that its mass, even though thought to be very small, plays an important role in the evolution of the universe (Bond et al. (1980)).

And through the continued study of oscillations with ever more precise measurements, the community is probing for additional hints to new laws of physics. For example, the current neutrino oscillation model is based on the three neutrino types of the Standard Model. However, confirmed deviations from this model is evidence that there are additional types of neutrinos (Conrad et al. (2013)). Furthermore, if we were to learn that neutrinos and their anti-matter partner, the anti-neutrinos, oscillate differently, then there exist plausible mechanisms that allow us to explain why there is matter in our universe (Covi et al. (1996)).

The work presented in this dissertation adds to the body of experimental data on the nature of neutrino oscillations. We describe here the most precise measurement to date of one type of neutrino, the muon neutrino, changing into either of the two other types, an electron or tau neutrino. This measurement was performed with the T2K experiment, which creates a beam of muon neutrinos that is sampled before and after oscillation effects (Abe et al. (2011b)). Our measurement of this particular

process is a step forward towards the increasingly precise measurement – and test – of the three-neutrino model of neutrino oscillations.

—

While the author is personally responsible for the final physics analysis that extracted the measurement of muon neutrino oscillations from the data, the result is only one part of a collective effort by many members of the T2K collaboration. This is important to note, as this dissertation will show the results of work not performed by the author in order to provide a complete description of the measurement. The author's direction contribution, in addition to service work to the collaboration, is the statistical analysis of the data along with various studies that served to validate the method. The author worked as part of the T2K muon neutrino disappearance working group known as the KDI group (for Kyoto-Duke-ICRR), and implemented changes to the existing analysis framework. As a result, the author performed various studies of the updated analysis, e.g. studying the the consequences of analyzing the data in a different set of parameters (from $\sin^2 2\theta_{23}$ to $\sin^2 \theta_{23}$). The author also implemented a statistical technique known as the Feldman-Cousins method for profiled likelihoods. This work will be the central topic of the dissertation.

Other contributions by the author include service work for one of the detectors in the T2K experiment known as Super-Kamiokande. Much of the work centered around developing the tools and selection for a new class of T2K neutrino events, the OD events. These events get their name from the fact that they involve the veto of the Super-Kamiokande detector known as the Outer Detector, or OD (see Appendix D). This new set of events required studies of the OD response (see Section 4.4.3) that was useful not only for T2K Collaboration but also for the Super-Kamiokande Collaboration. This work was the development of a new calibration technique for the OD using Michel electrons (Section 4.4.8). The OD tools also provided a check of

the backgrounds for the first indication of non-zero value for one of the parameters in the neutrino oscillation model, θ_{13}, by the T2K experiment which is described in Appendix C.

Before beginning the description of our measurement, we first pause to provide a brief summary of the properties of the neutrino and to describe the past and current state of oscillation measurements in Chapters 2 and 3, respectively. We then describe the T2K experiment in Chapter 4 before outlining the strategy of behind the measurement in Chapter 5. The description of the oscillation analysis is given in Chapter 6, followed by the studies into the behavior of the analysis. Finally, in Chapter 8 we present the results.

2

Neutrino History and Theory

The neutrino is a fundamental particle which is currently known to have spin-$\frac{1}{2}$, no electric charge, and interacts with other matter through the weak interaction and gravity. There are three types, or generations, of neutrinos – the electron, muon, and tau – so-named for the leptons they can produce during certain types of weak interactions. At least two of the three Standard Model neutrinos are known to have a non-zero, albeit very small mass. Current limits put the total mass of all neutrino states to be smaller than 1.0 eV/c^2 (Plank Collaboration et al. (2013))(Weinheimer et al. (1999)). Importantly, the three flavor eigenstates of the neutrino are not the same as the three mass eigenstates. This last property is what allows neutrinos to undergo oscillations.

In this chapter, we review the experimental evidence for the neutrino and the Standard Model description of its properties listed above.

2.1 Beta Decay: Pauli's Hypothesis and Fermi's Theory

Wolfgang Pauli is credited with postulating the existence of the neutrino, a particle he proposed in order to explain the kinematics of beta rays. By 1902, through the work of Becquerel, Rutherford, Soddy and Fajans, it was known that beta decay involved the transmutation of one element to another element one place to the right on the periodic table, i.e. an element with one additional proton in its nucleus, with the simultaneous emission of an electron. But when James Chadwick, Lise Meitner, Otto Hahn and others measured the energy spectrum of the beta particles, they found that the energies were distributed in a continuous spectrum (Chadwick (1914)) in contrast to the spectra of other nuclear radiation known at the time, alpha and gamma rays, which both peaked at a single energy. The spectra for the latter made sense, as the nucleus ought to be transitioning from one quantized state to another and, therefore, release a fixed, discrete amount of energy. Therefore, the continuous beta ray spectrum raised the possibility that the law of energy conservation was not valid.

However, out of commitment to the conservation law, Pauli in 1930 postulated that a new, electrically neutral particle was responsible for carrying away the missing energy (Pauli (1930)). He named the particle, the "neutron", and based on evidence at the time postulated that it had a small mass and one-half spin. A neutral particle was soon detected by Chadwick in 1932, but it was clear at the time of the discovery that the new particle was too heavy to be Pauli's "neutron" (Chadwick (1932)). Instead, Chadwick discovered what is now known as the neutron.

Then in 1934, Fermi formulated a theory for beta decay that involved both Chadwick's and Pauli's "neutron" (Fermi (1934a))(Fermi (1934b)). To distinguish the latter, Fermi renamed the particle the neutrino, or "little neutral one". The success of Fermi's theory in eventually explaining much of the data on beta decay gave

increased credibility to the existence of Pauli's proposed particle.

Fermi's theory for beta decay was composed of the following reaction

$$n \rightarrow p + e^{-} + \bar{\nu}_e \tag{2.1}$$

which could be modeled as the interaction between two weak interaction currents, J^{μ}_{nucleon} and J^{μ}_{lepton}, for the nucleons and leptons, respectively. Figure 2.1(a) illustrates Fermi's model for beta decay. The rate of the interaction was then related to the amplitude given by

$$\mathcal{A} = \frac{G_F}{\sqrt{2}} J^{\mu}_{\text{nucleon}} J_{\mu\text{lepton}} \tag{2.2}$$

where G_F was Fermi's constant. In addition to beta decay, the method could describe other types of weak interactions by rearranging the input and output of the same currents. For example, the processes shown in Figure 2.1(a), beta decay, and Figure 2.1(b), inverse beta decay, are related by rearranging the in-coming and out-going particles. Both could be described using Fermi's theory.

Later in 1936, Fermi's theory was extended by Gamow and Teller to be able to explain some types of beta decay that involved a change in 1 unit of nuclear spin. They generalized Fermi's theory so that the weak interaction currents could also include a current composed of an axial vector (Gamow and Teller (1936)). This opened the way to the possibility of many different types of couplings involving scalars, pseudoscalars, and tensors. It would be many decades later until the present form of the weak current was established.

Finally, in 1956, the neutrino was observed by Reines and Cowen. With 1400 L of liquid scintillator positioned near the Savannah river nuclear reactor, they observed the direct evidence of neutrinos (Reines and Cowan (1953)). The observation was through the detection of inverse beta decay interactions where an anti-neutrino interacts with a proton and produces a positron and neutron.

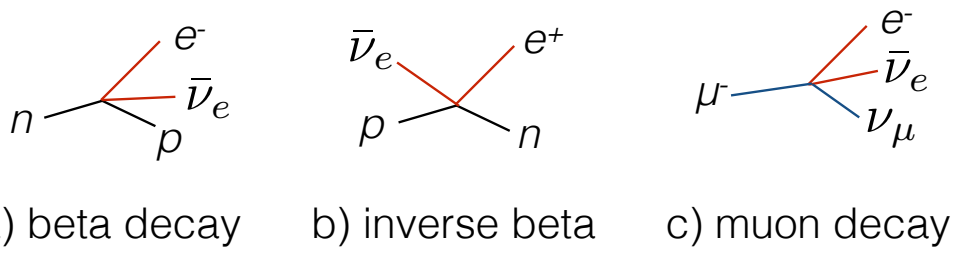

FIGURE 2.1: Diagrams of various weak interactions according to the Fermi's theory. In the theory, two currents interact. One possible current connected the neutron and proton and was known as the nucleon current (shown in black). Another, the leptonic current, connected the electron and neutrino (shown in red). Later, different leptonic currents were postulated that connected different leptons with a neutrino distinguished by the its partner lepton. In the diagram for muon decay (c), two distinct leptonic currents interact. One is for the electron and electron neutrino current (in red). Another is for the muon and muon neutrino current (in blue).

2.2 Charged Leptons and Neutrinos Come in Three Flavors

In 1937 the muon was discovered (Street and Stevenson (1937))(Neddermeyer and Anderson (1937)). Its decay modes were studied, and, eventually, the data led Bruno Pontecorvo to extend Fermi's theory of beta decay to muons (Pontecorvo (1947)). This was done by defining a distinct weak leptonic current between the muon and the neutrino in addition to the current between the electron and neutrino in Fermi's original theory. This interaction is diagrammed in Figure 2.1(c). Such currents could then undergo the same type of interaction as in beta decay. This pointed to the universality of the weak interaction for different currents. Furthermore, it laid the foundation for the eventual idea of generations, or families, of leptons with each generation consisting of a lepton and neutrino pair of a certain type of flavor.

As far as we know, there are three generations of leptons and their neutrino partners. The electron and its neutrino partner, the electron neutrino, make up the first generation, (e, ν_e). The muon and its partner neutrino, the muon neutrino, make up the second generation, (μ, ν_μ). The muon neutrino was established to be distinct from the electron neutrino in 1962 in an experiment that involved the

world's first neutrino beam produced by charged pions decaying into a beam of muon neutrinos (Danby et al. (1962)). The experiment saw that neutrino interactions produced muons but no electrons, establishing that the muon neutrino is distinct and confirmed the lepton generation picture. The third generation includes the tau lepton, which was first observed in 1975 (Perl et al. (1975)). Its partner, tau neutrino was directly observed in 2001 (DONUT Collaboration (2001)). Together they make the third and final generation, (τ, ν_τ).

These generations are associated to conversation laws that have yet to be contradicted by experimental evidence. The concept of lepton number was introduced in 1953 by Konopinski and Mahmoud to explain missing decay modes (Konopinski and Mahmoud (1953)). The particles $e^-, \mu^-, \tau^-, \nu_e, \nu_\mu, \nu_\tau$ are assigned a number $L = 1$, while their anti-partners are assigned a number $L = -1$. All other particles are assigned $L = 0$. Further decays were also found to be missing, for example $\mu \rightarrow e + \gamma$, which led to the stronger conservation law for lepton flavor number. Here (e^-, ν_e), (μ^-, ν_μ), and (τ^-, ν_τ) are all assigned a lepton flavor number of $L_e = 1$, $L_\mu = 1$, and $L_\tau = 1$, respectively, while $L_e = -1$, $L_\mu = -1$, and $L_\tau = -1$ for assigned to the anti-particles. Decays like $\mu \rightarrow e + \gamma$ are thought to be forbidden because they violate strong lepton flavor conservation.

2.3 V-A Nature of the Weak Current

In 1956 Lee and Yang noted that parity conservation had not been tested experimentally for the weak interactions and suggested a number of tests (Lee and Yang (1956)). Wu then measured the beta decays of polarized ^{60}Co nuclei and observed a large asymmetry in the rate as a function of direction. The asymmetry was consistent with maximal parity violation (Wu et al. (1957)). As a result of this experiment, the neutrino was postulated to exist in only one helicity state. It was thought that the neutrino helicity, the scalar product of the neutrino's momentum and spin, is

left-handed, i.e. the momentum and spin are anti-correlated, while the anti-neutrino is right-handed, i.e. correlated momentum and spin. A year later, 1958, Goldhaber et al. demonstrated that the neutrino is created only in the left-handed helicity state (Goldhaber et al. (1958)).

This was important in establishing the form of the weak current. Initially, Fermi defined the leptonic and nucleon currents as a Lorentz invariant vector. Gamow and Teller, as mentioned earlier, added an axial vector component. The experiments above, along with further studies of nuclear recoils, established that the weak current should have the form of the difference between a vector minus an axial vector, V-A. This form of the current maximizes parity violation and only couples to left-handed helicity states (Halzen and Martin (1984)).

2.4 Standard Model Electroweak Interactions

By the 1960s, the modern model of the weak interaction by Glashow-Weinberg-Salam (GWS) was taking form. It merged together the electromagnetic force with the weak interactions. The combined electroweak force is modeled as a gauge field with $SU(2)_L \otimes U(1)$ symmetry (Halzen and Martin (1984)). The $SU(2)_L$ symmetry defines the weak isospin group. The representation of the fermion fields is guided by experiments above, namely that the neutrino is left-handed and the weak interaction ought to have a V-A structure. The left-handed fermion fields are grouped into an isospin doublet composed of a lepton and neutrino pair (and a pair of quarks). Also defined is a right-handed lepton that is a weak isospin singlet. The symmetry is spontaneously broken through the Higgs mechanism and leads to masses for the leptons and quarks. The symmetry breaking of the electroweak interaction also leads to a set of massive vector bosons, the $W^{\pm}$ and Z^0, that mediate the weak interaction.

The Standard Model specifies that, neglecting gravity, the neutrino is only able to interact with other matter through the exchange of these bosons via charged-

current and neutral-current interactions. In the charged-current interaction, a neutrino changes into a lepton (or vice versa) while exchanging a $W^{\pm}$ vector boson with another particle such as different lepton-neutrino pair or a quark. In the neutral-current interaction, a neutrino exchanges a Z^0 vector boson with another particle such as another lepton-neutrino pair or a quark. For the neutral-current interaction, the flavor of the neutrino is irrelevant. Feynman diagrams showing the weak interaction vertices involving neutrinos are shown in Figure 2.2.

It turns out that Fermi's theory of weak interactions was just a low energy description of the charged-current interactions mediated by the $W^{\pm}$. At the time the GWS model was proposed, the other predicted interaction, the neutral-current interaction, was not yet observed. In 1973, neutrinos played a role in affirming the GWS model as correct, when neutral-current neutrino interactions were detected in the Gargamelle experiment at CERN (Hasert and et. al. (1973)) and at Fermilab (Benvenuti and al (1974)).

Later, the coupling between neutrinos and the neutral boson, Z^0, would tell us something about the leptons as the measurement of Z^0 boson decays showed that the Z^0 couples to exactly three generations of leptons (LEP Collaborations and the LEP Electroweak Working Group (2001)).

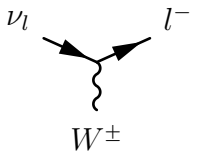

(a) charged-current interactions

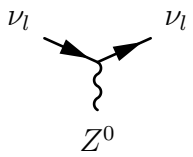

(b) neutral-current interactions

FIGURE 2.2: Neutrino interaction channels in the Standard Model. (a) Feynman diagram vertex for charged-current interactions where a neutrino changes into a lepton (or vice versa) through the exchange of the $W^{\pm}$ vector boson with another particle. (b) Feynman diagram vertex for neutral-current interactions where a neutrino interacts through the exchange of the Z^0 vector boson. The $W^{\pm}$ and Z^0 are the intermediaries of the weak force in the Standard Model.

2.5 The Solar Neutrino Anomaly

Around the same time that the electroweak model was being developed with the help of the neutrino, experiments were proposed and built with the purpose of using neutrinos to study the nuclear reactions in the Sun, which were known to produce many neutrinos. These experiments measured the neutrino flux from the Sun by counting the number of nuclei that changed through the inverse beta decay interaction between a neutrino and a nucleus. One such experiment, known as the Homestake chlorine experiment , consisted of a large vat of C_2Cl_4 that recorded the interactions of neutrinos through the conversion of chlorine atoms into ^{37}Ar atoms by inverse beta decay. The Ar atoms were then extracted by bubbling helium through the tank and then counted in order to provide a measurement of the interaction rate (Davis (1994)). With over 30 years of data, the experiment measured an average rate of 2.56 inverse beta decay captures per 10^{36} atoms per second, which was a unit known as the SNU for "solar neutrino unit". This was much less than the 7.6 SNU that was predicted by models of the sun. Other experiments, such as SAGE and GALLEX, which used ^{71}Ga-based detectors, confirmed the deficit (Abazov et al. (1991))(Anselmann et al. (1992)). The observation of missing neutrinos was known at the time as the "solar neutrino problem" which went on for some time.

Eventually, the measurement of neutrinos coming from the atmosphere would also turn up a deficit, this time in muon neutrinos. Further study would show that both anomalies could be explained by the phenomenon known as neutrino oscillations, which we describe in the next chapter.

3

Neutrino Oscillations

Before continuing with the resolution of the solar neutrino anomaly and the experimental evidence that established neutrino oscillations as the solution, we briefly review the formalism and phenomenology of neutrino oscillations.

3.1 Neutrino Mixing

Neutrino oscillations occur because the flavor eigenstates of the weak interaction are not simultaneous eigenstates of the mass. Therefore, flavor states, ν_α, must be expressible as the mixture of N mass states, ν_i, by

$$\nu_\alpha = \sum_i^N U_{\alpha i} \nu_i, \tag{3.1}$$

where the unitary matrix, U, is a mixing matrix that captures the overlap between the two bases. For this thesis, we analyze neutrino oscillations assuming the three Standard Model neutrinos. Therefore, we continue by defining α as an index over the three generations of neutrino flavors $\{e, \mu, \tau\}$ and i as an index over three mass states. However, we note that the number of mass states could be greater than three.

Any additional mass states are referred to as sterile neutrinos and are considered a possibility in explaining some anomalies in the measurement of neutrino oscillations. For a review of these anomolies please see (Conrad et al. (2013)).

3.2 Vacuum Oscillations

The observation of neutrino flavor oscillations requires that a neutrino is created in a known flavor, ν_α, then later detected by a charged-current weak interaction such that

$$\nu_\beta + n \rightarrow l_\beta^- + p. \tag{3.2}$$

The amplitude of detecting a diferent flavor, ν_β, for neutrinos traveling through the vacuum is

$$\mathcal{A}_{\alpha\beta} = \sum_i e^{iq_i x} U^*_{\alpha i} U_{\beta i}, \tag{3.3}$$

where q_i is the 4-momentum of mass state i, and x is the 4-vector, (t,L), of the measurement which occurs at time t after a distance, L. Furthermore, we have removed some irrelevant overall phase factors.

Oscillations occur as long as the distance between the creation and observation of the neutrino is short enough that the wave packets of the neutrino mass states still overlap (Cohen et al. (2008)). The probability of observing the oscillation is then

$$P_{\alpha\rightarrow\beta} = |\mathcal{A}_{\alpha\beta}|^2 \tag{3.4}$$

$$\begin{aligned} &= \delta_{\alpha\beta} \\ &\quad -4\sum_{i>j} \mathrm{Re}\{U^*_{\alpha i} U_{\beta i} U_{\alpha j} U^*_{\beta j}\} \sin^2\left(\tfrac{\Delta m^2_{ij} L}{4E}\right) \\ &\quad +2\sum_{i>j} \mathrm{Im}\{U^*_{\alpha i} U_{\beta i} U_{\alpha j} U^*_{\beta j}\} \sin\left(\tfrac{\Delta m^2_{ij} L}{2E}\right) \end{aligned} \tag{3.5}$$

where $\Delta m^2_{ij} = m^2_i - m^2_j$, and we have used the fact that the phase between two mass

states, $\phi = (q_i - q_j)x$, can be expressed as $t\frac{m_i^2 - m_j^2}{E_i + E_j}$. We also use $E_i + E_j \approx 2E$, since the mass of the neutrino (< 1 eV) is thought to be much smaller than the energies of current experiments (>1 MeV) (Cohen et al. (2008)). Note that we have used natural units ($c = \hbar = 1$).

3.2.1 Two-flavor Oscillation Probability

In order to briefly demonstrate the phenomenology of oscillations, we can simplify above expression by looking the case of a two-neutrino model. In this scenario, the mixing matrix is a 2x2 unitary matrix with one degree of freedom. We then express the flavor states as a mixture of mass states by

$$U_{\alpha i}^{2\nu} = \begin{pmatrix} \cos\theta & \sin\theta \\ -\sin\theta & \cos\theta \end{pmatrix} \tag{3.6}$$

where θ, the mixing angle, parameterizes the mixing matrix. Calculating the oscillation probability in vacuum through the same manner as above, the probability of observing an initial neutrino of flavor α being detected later as β is

$$P_{\alpha\to\beta} = \sin^2 2\theta \sin^2 \frac{\Delta m^2 L}{4E} \tag{3.7}$$

and the probability of a neutrino of flavor, α, staying the same is

$$P_{\alpha\to\alpha} = 1 - \sin^2 2\theta \sin^2 \frac{\Delta m^2 L}{4E} \tag{3.8}$$

where Δm^2 is the splitting between the squared masses, $m_2^2 - m_1^2$. Note that here and above, we have used natural units.

From Equations (3.7) and (3.8), it is clear that the probability of being in one flavor state or the other is sinusoidal in L/E. This dependence on L/E will turn out to be a key signature of oscillations. The maximum extent to which the flavor amplitudes increase and decrease is modulated by the mixing parameter, θ, or in

other words by how much the mass states are mixed with the different flavor states. For a neutrino to oscillate back and forth between two flavors completely, the mixing between the mass and flavor states must be maximal, i.e. $\theta = \frac{\pi}{4}$ or, equivalently, $\cos\theta = \frac{1}{\sqrt{2}}$. The frequency at which oscillations occur is set by the difference between the square of the masses, Δm^2. We note that it is customary for neutrino oscillation experiments to report the results of their measurement as a value for the mixing angle and mass squared difference.

3.3 Oscillations in Matter

The relatively simple formalism of oscillations in vacuum must be modified when neutrinos pass through matter. As they do, the neutrinos may undergo interactions with the matter via the weak interaction. One channel is through the neutral-current interaction. However, the neutral-current interaction occurs for all flavors of the neutrino. As a result, the neutral-current interaction will produce a common phase for all components of the neutrino and, in the end, does not impact oscillations as this overall phase is inconsequential. However, only the electron neutrino feels an additional scattering potential with the electrons in matter through the charged-current interaction. The resulting effective potential the electron neutrinos feel is expressible as

$$V_e = \pm G_F n_e \tag{3.9}$$

where G_F is Fermi's constant and n_e is the electron number density of the matter. The potential produces an asymmetry in the interactions between the different flavor components of a neutrino as it moves though matter. The result are transitions between flavors similar to oscillations (Wolfenstein (1978)). This phenomenon is known as the MSW effect for Mikheyev, Smirnov, and Wolfenstein.

We demonstrate the phenomonenlogy of the MSW effect by examining two-

neutrino mixing and oscillations where one component is the electron neutrino. The neutrino is then assumed to be passing through a medium with constant density. In this model, the Hamiltonian in vacuum is, in the mass basis,

$$H_{vac} = \begin{pmatrix} E_1 & 0 \\ 0 & E_2 \end{pmatrix} \approx pI + \begin{pmatrix} \frac{m_1^2}{2E} & 0 \\ 0 & \frac{m_2^2}{2E} \end{pmatrix}. \tag{3.10}$$

We define the neutrino mixing by

$$\begin{pmatrix} \nu_e \\ \nu_\beta \end{pmatrix} = \begin{pmatrix} \cos\theta & \sin\theta \\ -\sin\theta & \cos\theta \end{pmatrix} \begin{pmatrix} \nu_1 \\ \nu_2 \end{pmatrix} \tag{3.11}$$

in order to establish the ν_e component. We add to the vacuum H an effective potential that only appears in the e-e component of the weak basis

$$H_m = \begin{pmatrix} V_e & 0 \\ 0 & 0 \end{pmatrix}. \tag{3.12}$$

The total effective Hamiltonian in the weak basis is

$$H = UH_{vac}U^\dagger + H_m = \frac{\Delta m^2}{2E} \begin{pmatrix} \sin^2\theta + \frac{2E}{\Delta m^2}V_e & -\sin\theta\cos\theta \\ -\sin\theta\cos\theta & \cos^2\theta \end{pmatrix}. \tag{3.13}$$

Not that we have subtracted off terms proportional to the identity that will produce an overall phase in the amplitude. Such phases become irrelevant in the expression of the oscillation probability. The Schrodinger equation that governs the time evolution of the flavor states is

$$i\frac{d}{dt}\begin{pmatrix} \nu_e \\ \nu_\beta \end{pmatrix} = H\begin{pmatrix} \nu_e \\ \nu_\beta \end{pmatrix}, \tag{3.14}$$

which, when changing to a diagonal basis of H, becomes

$$i\frac{d}{dt}\begin{pmatrix} \nu_1^M \\ \nu_2^M \end{pmatrix} = \tilde{H}\begin{pmatrix} \nu_1^M \\ \nu_2^M \end{pmatrix}, \tag{3.15}$$

where ν_1^M and ν_M^2 define a new basis of 'matter neutrinos' for $\tilde{H} = \frac{1}{4E}\text{diag}(-\Delta m_M^2, \Delta m_M^2)$ and $\nu_\alpha = U_M^T \nu_1^M$. The eigenvalues are $\pm\Delta m_M^2 = \pm\frac{\Delta m^2}{4E} f_m$ where

$$f_m = \sqrt{\sin^2 2\theta + (\cos 2\theta - \frac{2E}{\Delta m^2} V_m^e)^2}. \tag{3.16}$$

The 'matter' mixing matrix, U_M, is

$$U_M = \begin{pmatrix} \cos \upsilon_M & \sin \upsilon_M \\ -\sin \upsilon_M & \cos \upsilon_M \end{pmatrix}. \tag{3.17}$$

The end result is that the two-neutrino oscillation probability in terms of the 'matter variables' υ_M and Δm_M^2 looks like the vacuum oscillation formula with

$$P_{e\to\alpha} = \sin^2 2\upsilon_M \sin^2 \frac{\Delta m_M^2 L}{E}, \tag{3.18}$$

where it turns out that

$$\begin{aligned} \cos 2\upsilon_M &= \frac{1}{f_m}(\cos 2\theta - \frac{\Delta m^2}{2E} V_e) \\ \sin 2\upsilon_M &= \frac{1}{f_m}(\sin 2\theta). \end{aligned} \tag{3.19}$$

From Equation (3.18), we can see that the passage of neutrino through matter changes the oscillation probability compared to the vacuum case.

There are two things to point out. First, there exists a resonance effect described by Mikheyev and Smirnov (Mikheev and Smirnov (1985)). From Equation (3.18), we note that the extent of mixing between the states is a combination of the neutrino mixing angle, θ, and the flavor transition due to the MSW effect. A resonance occurs when $\sin^2 2\upsilon_M = 1$ or when

$$n_e = \frac{\Delta m^2 \cos 2\theta}{2\sqrt{(}2) G_F E} \tag{3.20}$$

For a neutrino passing through a medium for long enough at this density, maximal oscillations occur between one flavor state and the other. Note that this simple example was for a constant density. The phenomenon of matter flavor transitions is fairly rich when one considers different varying density profiles (Parke (1986a))(Parke (1986b)).

The second thing to note from Equation (3.18) is that the matter effects can determine the sign of the mass splitting. This is in contrast to the vacuum oscillation case. To see this, note that in the mass splitting parameter, Δm^2_M, there is a term $(\Delta m^2 - 2EV_e/\cos\theta)^2$. Here, the matter potential, V_e, is part of a term that adds to or subtracts from the vacuum mass splitting depending on the latter's sign. Therefore, experiments where matter effects are a significant factor, i.e. experiments where neutrinos must travel long distances through matter, can distinguish the sign of the vacuum mass splitting term. This is not possible from the leading terms of the vacuum oscillation probabilities (see Equation 3.5) where the mass splitting is inside a sinusoidal-squared factor. In such a case, only the absolute value of the mass-squared splitting produces observable effects to the probability.

For three-flavor matter oscillation, it is not possible to solve the probability formula so elegantly. For the analysis described here, we use expressions from (Barger et al. (1980)) which are for oscillations through matter of constant density. Then for arbitrary density profiles, we numerically solve for the probabilities by iterating the oscillation probability calculation through a series of constant density slabs (Wendell (2008)).

3.4 Resolution of the Solar Neutrino Anomaly

As mentioned in the previous chapter, experiments to study the nuclear reactions in the sun through the rate of emitted neutrinos seen on Earth turned up an anomaly where only one third of the expected number of neutrinos were observed. For many

decades, the anomaly went unresolved as many believed either the model of the sun or the experiments were in error. But then in the late 1980s, several experiments which were built to look for proton decay would measure hints of missing neutrinos. This would eventually lead to evidence establishing that neutrino oscillations were the explanation for both.

3.4.1 More Missing Neutrinos

It was clear to those who were building experiments to look for proton decay that the process they were attempting to observe was at best rare (and indeed the decay has not been seen to this day). Therefore, large detectors were built in order reach the necessary abundance of protons to observe. The detectors were also housed underground in order to shield them from cosmic ray muons. However, one of the backgrounds intrinsic to this setup would be the presence of charged particles, mostly muons and electrons, produced from neutrino interactions occurring in the detectors. Most of the neutrinos that seen in the detectors derive from cosmic ray particles colliding with the Earth's atmosphere. The collisions produce various particles that eventually decayed into neutrinos that could travel into the detectors from all directions, even from below, as neutrinos can easily pass through the Earth.

Therefore, as an important background, the experiments measured the flux of neutrino events seen versus expected. One of these experiments, IMB, reported in a paper published in 1986 that a significant disagreement in the fraction of events that were tagged as coming from a muon neutrino interaction (Haines et al. (1986)). Later in 1988, another proton decay experiment, Kamiokande, would also publish that they too observed a deficit in the number of muon neutrinos measured when compared to expectation (Hirata et al. (1988)).

However, the existence of an anomaly was not immediately clear. Both IMB and Kamiokande employed a type of detector known as a water Cherenkov detector. (This

type of detector is also used by T2K and will be discussed in more detail in Chapter 4. When two other experiments, Frejus (Berger et al. (1989)) and (Berger et al. (1990)) and NUSEX (Aglietta et al. (1989)), which employed a different detector based on iron, measured the muon neutrino rate in their detectors, they did not observe the deficit seen by IMB and Kamiokande. But the anomaly continued to persist.

In 1991, IMB would again report a discrepancy in the fraction of neutrino interactions coming from muon neutrinos, this time seen by two algorithms to distinguish between muon and electron neutrino events (Casper et al. (1991)). The possibility of oscillations was mentioned, but no other corroborating observation could be significantly detected. As discussed early this chapter, oscillations depend on both the distance the neutrino travels and the energy it has. Therefore, the IMB group looked for signs of the deficit in both the energy of the particles seen in the detector along with the zenith angle of the particles with respect to the axis of the detector. The latter variable ought to correlate with the direction the neutrino was passing through the tank and ultimately the distance the neutrino travel from which ever point in the atmosphere it was created. with the direction of the neutrinos was seen. IMB claimed that though the ratio of muon neutrino to electron neutrino events was low, it was not yet significant enough to require the explanation of neutrino oscillations.

But in 1992 Kamiokande, like IMB, again reported the observation of a deficit in the number of muon neutrino seen (Hirata and others (1992)). Furthermore, they reported to observe that the deficit could also be seen in the distribution of muons observed in the detector. The momentum dependence seen was shown to be consistent with the possibility of neutrino oscillations, specifically the disappearance of muon neutrinos.

3.4.2 Atmospheric Neutrino Oscillations

Finally in 1998, the next generation of the Kamioka experiment, Super-Kamiokande, provided clear evidence that the atmospheric neutrino anomaly was consistent with neutrino oscillation (Fukuda et al. (1998)). Their data showed that when the number of muon neutrino interactions as a function of the zenith angle of the observed muon the deficit in the number of observed than expected was larger the longer the distance the neutrino traveled through the Earth. Figure 3.1 shows the zenith angle plot from (Fukuda et al. (1998)). This disappearance as a function of zenith angle was then confirmed by other experiments a few years later by experiments like MACRO (MACRO Collaboration (2001)) and SOUDAN 2 (Mann (2001))(Sanchez (2001)).

However, even through the correct correlation of the disappearance of muon neutrinos with distance and energy was seen by these experiments, it was still possible that other phenomenon such as neutrino decay or neutrino decoherence was responsible for what was observed. Both of these processes would lead to the disappearance of neutrinos after some distance. The true signature for oscillations, as mentioned above, would be an L/E dependence. This was reported in 2004, when Super-K had enough collected enough atmospheric neutrino data to observe this L/E signature of oscillations and thereby rule out the competing alternatives (Ashie et al. (2004)). Figure 3.2 shows the ratio of observed number of events to the prediction with oscllations as a function L/E.

In addition to the observation of the correct L/E dependence, another experiment, K2K (for KEK-to-Kamioka), set out to measure muon neutrino disappaearance in a controlled experiment. The result from Super-K uses neutrinos from the atmosphere which both require a model of the flux of incoming neutrinos that, in principle, could contain uncertainties that were not accounted for. Therefore, the idea behind

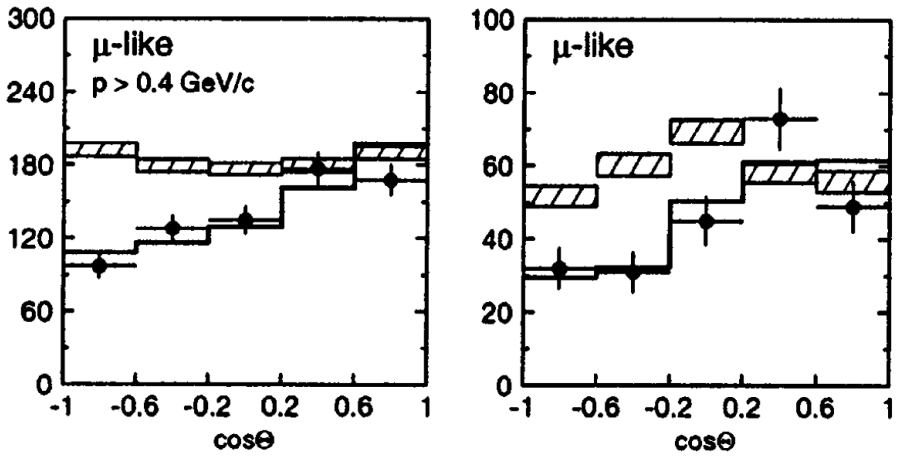

FIGURE 3.1: Angle of in-coming neutrinos from the atmosphere as observed by the Super-Kamiokande detector. The direction is given as the zenith angle with respect to the upward direction of the detector, i.e. $\cos\theta = 1$ corresponds to neutrino-induced leptons moving downward from top to bottom and $\cos\theta = -1$ corresponds to neutrino-induced leptons moving upware from bottom to top. The neutrinos in the left plot have a measured momentum of 0.4 to 1.0 GeV. The neutrinos in the right plot have energies greater than 1.0 GeV. The hashed boxes show the expected number of neutrinos assuming no oscillations. The markers with error bars indicate the observed number of events. The deficit in the number of muon neutrinos coming up from below the detector was the first clear evidence for neutrino oscillations. Figure from Fukuda et al. (1998).

the K2K experiment was to use an accelerator at the KEK facility in Japan to direct a beam of mostly muon neutrinos at the Super-K detector. In principle, the beam of neutrinos was a source experimenters had control over and understood well. In 2003, they reported an indication of muon neutrino oscillations and successfully confirmed what had been seen in the atmospheric neutrino measurement by Super-K (Ahn et al. (2003)).

3.4.3 Resolution of the Solar Neutrino Anomaly

Shortly after the atmospheric neutrino was explained to evidence of neutrino oscillations, the solar neutrino, too, was proven to be the result of the disappearance of electron neutrinos from the sun. The Sudbury Neutrino Observatory (or SNO), would make the measurement establishing this fact.

The SNO experiment was able to measure both charged-current and neutral-

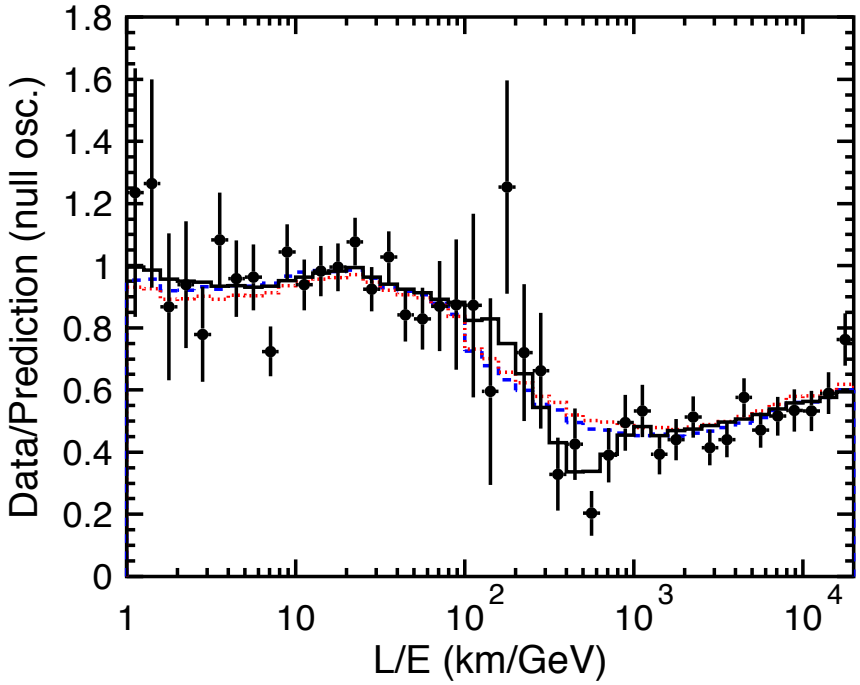

FIGURE 3.2: Ratio of observed events to expectation for no oscillations from the Super-K experiment. Events are plotted as a function of L/E. This was the first measurement of oscillations in the number of events as a function of L/E. Competing models for the neutrino disappearance seen in earlier measurements are shown. Neutrino decay is in red; neutrino decoherence in blue. Figure from (Ashie et al. (2004)).

current interactions in their detector, which was composed of a large tank of heavy water. The only charged-current interactions that could be seen in the detector would be from the electron neutrino component. The low energy of solar neutrinos from the sun (tens of Mev) meant that the muon neutrino componnt did not have enough energy to produce muon neutrinos. Neutral-current interactions, in contrast to the charged-current channel, are insensitive to the flavor of the neutrino and therefore can occur regardless of what mixture of flavor states the neutrino happens to be in as they passed through the SNO detector. SNO, therefore, was able to measure the

solar neutrino flux, ϕ, here given in units of $10^6 \mathrm{cm}^{-2}\mathrm{s}^{-1}$, to be

$$\phi_{CC} = \phi(\nu_e) = 1.76 \pm 0.01 \tag{3.21}$$

$$\phi_{NC} = \phi(\nu_e) + \phi(\nu_\mu) + \phi(\nu_\tau) = 5.09 \pm 0.63, \tag{3.22}$$

The standard solar model predicted a flux of $\phi_{SSM} = 5.05 \pm 1.01$. This flux matched the solar model. It also was composed not only of ν_e but also the two other flavors. Therefore, neutrinos produced by the Sun, which are only made as ν_e, were shown to oscillate into the other flavors which were still present (Ahmad et al. (2002)).

The measurement design for the type of flavor oscillation observed is dictated strongly by the energy at which the experiments are performed. It is conventional to divide measurements into two types: appearance and disappearance. In appearance measurements, the aim is to observe the transition between one flavor and another, $P_{\alpha\to\beta}$. In disappearance experiments, one measures the probability that the same flavor is observed. Often in disappearance measurements, the energy of the neutrinos will be too low to produce interactions that can produce the other flavors. For example, consider oscillation measurements at reactors where anti-neutrinos are produced typically at energies around tens of MeV. At these energies, charged-current interactions that would production muons and tau leptons are energetically forbidden. As a result, at a distance where neutrinos are in a state composed of mostly muon and tau components, most neutrinos will simply pass through a detector positioned there. Such an experiment will observe that most of the neutrinos have disappeared.

For the T2K experiment, the distance over which the neutrinos travel and the energies at which they are produced have been optimized for the measurement of muon neutrino disappearance and muon to electron neutrino appearance. The former, the measurement of muon neutrino disappearance, is the topic of this dissertation.

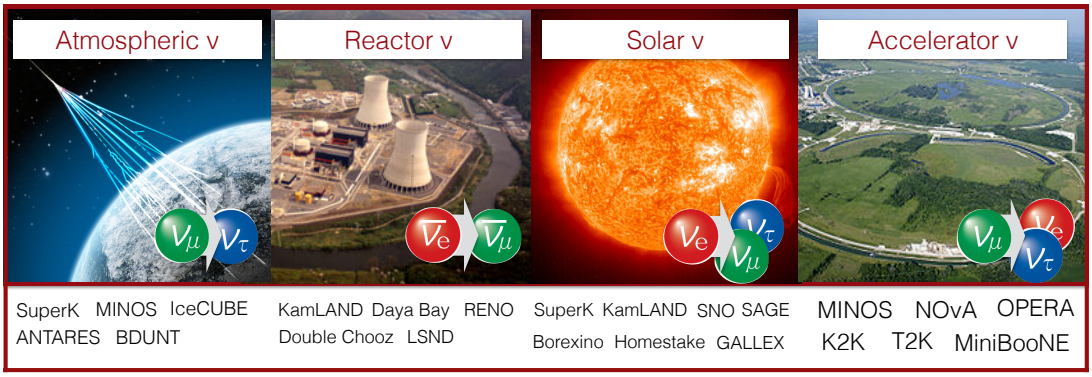

FIGURE 3.3: Infographic displaying some of the neutrino sources used in the measurement of neutrino oscillations. The type of oscillation measured is illustrated by the neutrino cartoons in the corner of each source. Below the pictures of the source, past and present experiments that have measured neutrino oscillations are listed. The list of experiments shown is certainly not complete.

3.5 Current State of the Oscillation Measurements

Over the last couple of decades there has been a lot of experimental effort in measuring different flavor oscillations using diverse sources of neutrinos. These sources of neutrinos include the Sun, nuclear reactors, cosmic ray impacts in the upper atmosphere, the core of the Earth and accelerators. The experiments range over many decades of neutrino energy and distances between source and detection. The collective aim of the experiments has been to measure the elements in the PMNS mixing matrix $U_{\alpha i}$, in Equation (3.1). The experiments report back the value of parameters in this matrix that follow a convention we describe below.

3.5.1 PMNS Neutrino Mixing Matrix

The PMNS mixing matrix is conventionally parameterized as a product matrices. This structure derives from the fact that it is possible to construct a $N \times N$ unitary matrix through the product of $N(N-1)/2+1$ NxN unitary matrices (Murnaghan (1962)). $N(N-1)/2$ of these matrices are constructed to mix only 2 components at

a time and are parameterized by a mixing angle and phase such that

$$U_{ij}(\theta,\phi) = \begin{pmatrix} \ddots & & & & & & & & \\ & 1 & & & & & & & \\ & & \ddots & & & & & & \\ & & & \cos\theta_{ij} & & ... & & \sin\theta_{ij}e^{i\phi_{ij}} & \\ & & & & \ddots & & & & \\ & & & \vdots & & 1 & & \vdots & \\ & & & & & & \ddots & & \\ & & & -\sin\theta_{ij}e^{-i\phi_{ij}} & & ... & & \cos\theta_{ij} & \\ & & & & & & & & \ddots \\ & & & & & & & & & 1 \\ & & & & & & & & & & \ddots \end{pmatrix}, \tag{3.23}$$

where i and j are the indices for the mixed components. The other $N \times N$ matrix is composed of N phases along the diagonal, $U_D(\phi_1, ..., \phi_N) = \text{Diag}(e^{i\phi_1}, e^{i\phi_2}, ..., e^{i\phi_N})$. The end result is a unitary matrix

$$U = \prod_{i>j} U_{ij}(\theta_{ij}, \delta_{ij}) \times U_D(\phi_1, ..., \phi_N) \tag{3.24}$$

that is parameterized by $N(N-1)/2$ mixing angles and $N(N+1)/2$ phases.

However, not all of the phases are used. This is because in the context of observable interactions, the definition of the fermion fields can be given arbitrary phases which can be chosen to cancel some of the phases in the PMNS matrix. To see this, take for example the leptonic charged-current where the neutrinos are in the mass basis,

$$J^{\alpha}_{CC} = \bar{l}^a \gamma^{\alpha}_{ab} U^b_i \nu^i \tag{3.25}$$

where l^a are the N lepton fields; ν^i are N neutrino mass states; and U_{bi} is the unitary neutrino mixing matrix. For Dirac neutrinos, we can redefine both the lepton and

neutrino fields by adding an arbitrary field such that

$$l'^a \rightarrow e^{i\alpha_a} l^a \tag{3.26}$$

$$\nu'^i \rightarrow e^{i\beta_i} \nu^i. \tag{3.27}$$

The current then becomes

$$J'^{\alpha}_{CC} = \sum_a^N \sum_b^N \sum_i^N \bar{l}^a e^{-i\alpha_a} \gamma^{\alpha}_{ab} U^b_i e^{i\beta_i} \nu^i. \tag{3.28}$$

Therefore, one can redefine the matrix, U, to be

$$U' = A^{\dagger}(\alpha) U B(\beta) \tag{3.29}$$

where

$$A^{\dagger} = e^{-i\alpha_N} \mathrm{Diag}(e^{-i(\alpha_1+\alpha_N)}, e^{-i(\alpha_2+\alpha_N)}, .., e^{-i(\alpha_{N-1}+\alpha_N)}, 1), \text{ and} \tag{3.30}$$

$$B = e^{i\alpha_N} \mathrm{Diag}(e^{i(\beta_1-\alpha_N)}, e^{i(\beta_2-\alpha_N)}, ..., e^{i(\beta_3-\alpha_N)}) \tag{3.31}$$

both contain the lepton and neutrino phases. Note that an overall phase has been extracted from both A and B in order to emphasize that the phases can be defined up to an overall phase. The end result is that there are now $2N-1$ phases that can be used to remove some of the $N(N+1)/2$ phases in the original unitary matrix, U. The final mixing matrix can then be parameterized by $N(N+1)/2-(2N-1)$ phases for the case of Dirac neutrinos. For Majorana neutrinos, the neutrino phases are not free but are fixed by the Majorana condition, leaving only the phases of the N leptons. Also, because only the lepton phases are free, there is no longer the overall phase degree of freedom, so the final number of phases in the PMNS matrix for Majorana neutrinos are $N(N+1)/2-N$ phases. For three neutrinos, there is only 1 phase left in the mixing matrix in the Dirac case and 3 phases left in the Majorana case.

The PMNS mixing matrix is conventionally defined as

$$\begin{aligned} U_{\alpha i} &= U_{\alpha l}^{atm/beam} \times U_{lm}^{reactor} \times U_{mn}^{solar} \times U_{ni}^{maj.} \\ &= \begin{pmatrix} 1 & 0 & 0 \\ 0 & c_{23} & s_{23} \\ 0 & -s_{23} & c_{23} \end{pmatrix} \begin{pmatrix} c_{13} & 0 & s_{13}e^{i\delta_{CP}} \\ 0 & 1 & 0 \\ -s_{13}e^{-i\delta_{CP}} & 0 & c_{13} \end{pmatrix} \begin{pmatrix} c_{12} & s_{12} & 0 \\ -s_{12} & c_{12} & 0 \\ 0 & 0 & 1 \end{pmatrix} U^{maj.}, \end{aligned} \tag{3.32}$$

where $c_{ij} = \cos(\theta_{ij})$, $s_{ij} = \sin(\theta_{ij})$, and

$$U_{ni}^{maj.} = \begin{pmatrix} e^{i\phi_1}/2 & 0 & 0 \\ 0 & e^{i\phi_2}/2 & 0 \\ 0 & 0 & 1 \end{pmatrix}. \tag{3.33}$$

The phases in the U^{maj} are non-zero only if the neutrino is Majorana. This leaves the correct number of phases for both Dirac and Majorana cases. Note that the Majorana phases do not affect neutrino oscillations.

The measurement of the parameters in this matrix along with the mass squared differences has been the aim of numerous experiments. The measurement design for the type of flavor oscillation observed and, therefore, the sensitivity to specific parameters is dictated strongly by the energy and baseline at which the experiments are performed. It turns out that oscillations occur at two quite different scales of L/E, due to one mass splitting being much larger than the other, where the larger splitting is $\Delta m^2 \approx 2.4 \times 10^{-3}$ eV^2/c^4 and the smaller one is $\Delta m^2 \approx 7.5 \times 10^{-5}$ eV^2/c^4. With the right choice of baseline and energy, it is possible to isolate an oscillation effect that can be described to first order as oscillations between two flavors. This is useful in setting up experiments to measure certain parameters.

It is conventional to divide measurements into two types: appearance and disappearance. In appearance measurements, the aim is to observe the transition between one flavor and another, $P_{\alpha \to \beta}$. In disappearance experiments, one measures the probability that the same flavor is observed. Often in disappearance measurements, the energy of the neutrinos will be too low to produce interactions that can produce

the other flavors. For example, consider oscillation measurements at reactors where anti-neutrinos are produced typically at energies around tens of MeV. At these energies, charged-current interactions that would production muons and tau leptons are energetically forbidden. As a result, at a distance where neutrinos are in a state composed of mostly muon and tau components, most neutrinos will simply pass through a detector positioned there. Such an experiment will observe that most of the neutrinos have disappeared.

For the T2K experiment, the distance over which the neutrinos travel and the energies at which they are produced have been optimized for the measurement of muon neutrino disappearance and muon to electron neutrino appearance. The former, the measurement of muon neutrino disappearance, is the topic of this dissertation.

The labels of the submatrices in Equation (3.33), are defined by convention and roughly correlate with the type of experiment that is associate with either the first or currently the most precise measurement of their values. In the next sections, we briefly describe the experiments responsible for the current best measurements.

3.5.2 Solar Sector: $\sin^2(\theta_{12})$ *and* Δm^2_{21}

The current values parameters $\sin^2(\theta_{12})$ and Δm^2_{21} come from the combination of experiments measuring neutrinos from the Sun and nuclear reactors. The oscillations of solar neutrinos are measured by Super-K (described in detail later in Chapter 4) and SNO (described earlier in this chapter). For the oscillation measurement of neutrinos produced by nuclear reactions, one of the most important for the solar parameters is by the experiment, KamLAND. KamLAND using anti-neutrinos coming from nuclear reactors measured anti-electron neutrino disappearance. The neutrinos KamLAND measured were from sources at most 1000 km away. As a result, they were exposed to sources whose ranges of L/E together allowed the experiment to make a precise measurement of the characteristic sinusoidal L/E dependence of neu-

trino oscillations (Araki et al. (2005)). KamLAND's ability to measure the shape of this dependence precisely provides a strong constraint on the value of the mass splitting, Δm^2, that governs solar oscillations (Abe et al. (2008)). Figure 3.4 shows the number of events observed as a function of L/E.

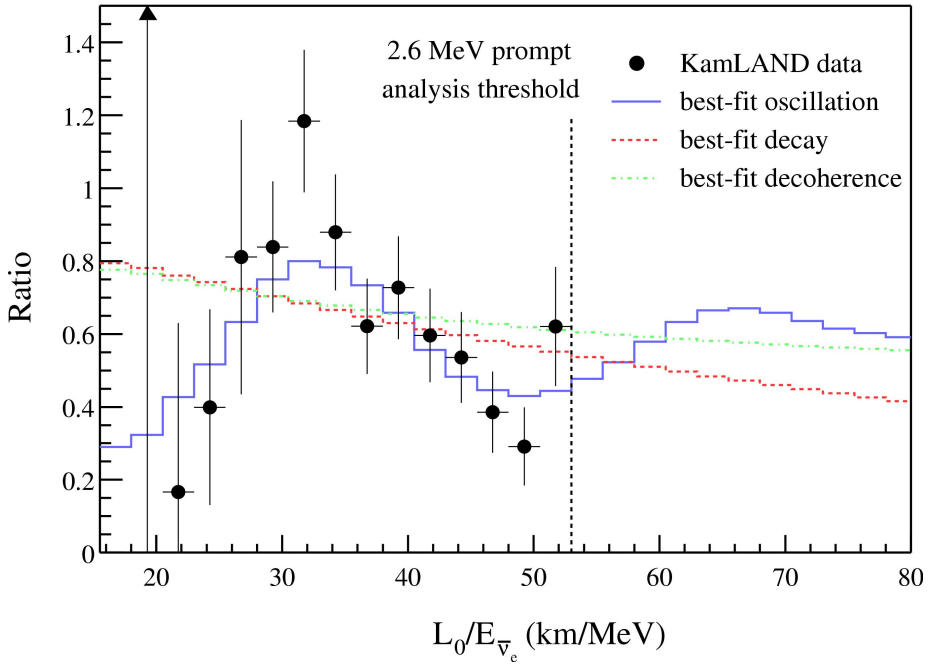

FIGURE 3.4: Ratio of observed events to expectation for no oscillations as a function of L/E. Measurement by the KamLAND experiment (Araki et al. (2005))

Large mixing angle or matter effect

An important effect that must be considered in the current measurements of the solar parameters is the role of matter effects in solar neutrino oscillations. As discussed in Section (3.3), flavor transitions can also be caused by the neutrino's passage through matter. Actually, for some time, the solar neutrino results could be interpreted as either the consequence of a large value for the mixing angle $\sin^2(\theta_{12})$ or as the result of a small mixing angle value enhanced by matter effects due to the the passage of solar neutrinos out of the dense Sun (Parke and Walker (1986)). Eventually in 2003, global analyses combined the results of many different experiments and selected the

large mixing angle solution (Fogli et al. (2003)). However, the matter effect still contributes a large enough effect that the global fits were able to resolve the sign of the neutrino mass splitting $\Delta m^2_{\text{solar}}$. The fits determined that $m_2 > m_1$.

Current values

The oscillations described above are primarily governed by the PMNS parameters, $\sin^2(\theta_{12})$ and Δm^2_{21}. Together, the three experiments, Super-K, SNO, and KamLAND, put the tightest constraints on the solar parameters. Figure 3.5 plots the constraints on these parameters from the three experiments. (The figure shows frequentist confidence-level allowed regions for the values of the parameters. For a brief reminder of what these allowed regions signify, see Appendix A). Note, however, that the figure below is the result of a very recent analysis. In the oscillation described in this thesis, the value for the solar values come from an older global fit which are recorded in the 2012 PDG (Beringer and Particle Data Group (2012)).

3.5.3 Atmospheric/Beam Sector: $\sin^2(\theta_{23})$ *and* Δm^2_{32}

The experiments that currently put the tightest constraints on these parameters are ones measuring neutrinos produce in the atmosphere and by accelerators. Atmospheric neutrinos are produced in the collision of cosmic rays (typically protons) with the upper atmosphere. The collisions produce many types of particles, one type of which, pions, decay to a muon and a muon neutrino. As discussed above, the measurement of atmospheric neutrinos have played an important role in the history of neutrino oscillations, and they continue to do so as the measurement of atmospheric neutrino oscillations by Super-K is one of the best measurements of the atmospheric sector parameters.

Lately, the experiments providing the most precise measurements of these parameters are the ones which utilize neutrinos produced at accelerators. Two of the

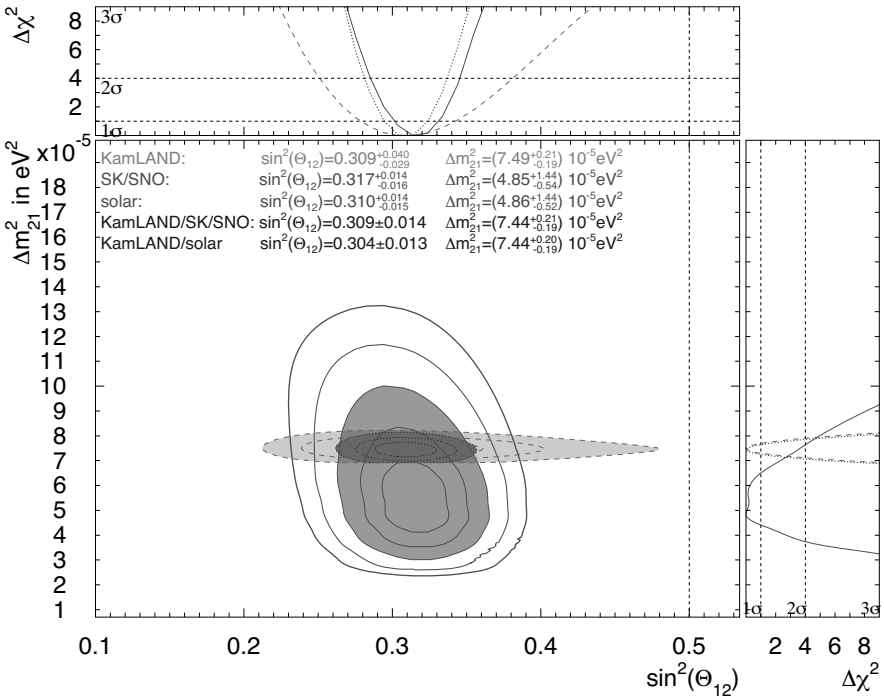

FIGURE 3.5: Recent neutrino oscillation measurements of the parameters in the so-called solar sector. CL allowed regions for 1, 2, 3, 4, and 5 σ for the Super-K experiment (Smy and Collaboration (2013)). The regions for 1, 2, and 3 σ for the KamLAND experiment is overlaid (Abe et al. (2008)). Figure from (Smy and Collaboration (2013)). Super-K and KamLAND combined allowed regions for 1, 2, and 3 σ are also shown. The bet fit values and 1 σ ranges are listed at the top of the plot for different combination of experiments.

strongest constraints come from the accellerator experiment MINOS and the previous numu-disappearance measurement made by T2K, also an accelerator experiment. Figure 3.6 shows the current allowed regions from Super-K (Himmel (2013)), MINOS (MINOS Collaboration et al. (2014)), and the previous T2K analysis (Abe et al. (2013b)).

Making a more precise measurement of these two parameters is the goal of the analysis presented in this thesis.

As an additional note, the Super-K atmospheric neutrino sample measures neutrinos over a very large range of energies and distances. This makes Super-K sensitive to the full complement of oscillation signals, although some produce only a small

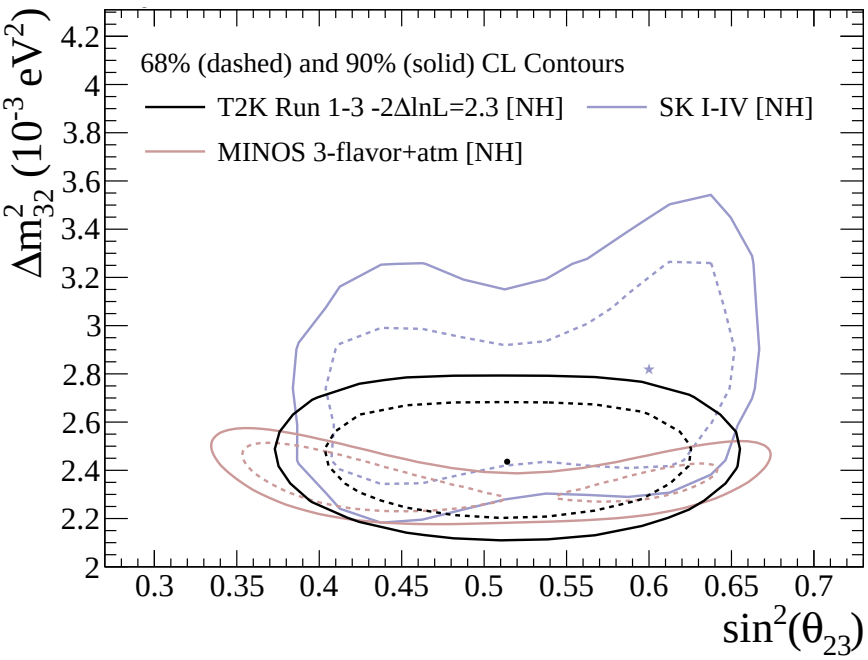

FIGURE 3.6: Allowed regions for $\sin^2(\theta_{23})$ and Δm^2_{32} (assuming the normal hierarchy) from Super-K, MINOS, and a previous analysis from T2K. These regions were the best constraint on these parameters before the work of this dissertation. MINOS contours from (MINOS Collaboration et al. (2014), Super-K atmospheric neutrino contours from (Himmel (2013)), and T2K contours from (Abe et al. (2013b)).

effect. Recently, the statistical evidence of tau neutrino appearance was reported in Super-K (Abe et al. (2013a)).

3.5.4 Reactor Sector: $\sin^2(\theta_{13})$ *and* δ_{CP}

Up until the summer of 2011, experiments aiming to measure the value of $\sin^2(\theta_{13})$ were consistent with zero. The most sensitive experiment, Chooz, put an upper limit of $\sin^2(2\theta_{13}) < 0.1$ at 90% CL (Apollonio et al. (1999)). There was much interest at the time to determine if θ_{13}, was non-zero, and if so, what its value was. Besides interest in the parameter itself, a value of non-zero θ_{13} was necessary to search for possible CP-violation in neutrino oscillations, which will be discussed later in Section 3.6.3.

Then in the summer of 2011, T2K reported the first indication of non-zero

$\sin^2(2\theta_{13})$ (Abe et al. (2011a)). This was followed by another hint from an electron neutrino appearance search by the experiment MINOS (Adamson et al. (2009)). For the T2K appearance measurement, it was observed that most of the electron neutrino events seen were upstream in the detector, Super-K. This motivated a check to rule out unforeseen backgrounds, especially from possible beam neutrino induced backgrounds coming from outside the Super-K detector. A description of this check can be found in Appendix C.

Shortly after the indication from T2K, several reactor experiments measured the value of $\sin^2(2\theta_{13})$ to be fairly large. These experiments measured the disappearance of electron anti-neutrinos. They consist of detectors of liquid scintillators instrumented with PMTs that are placed within several kilometers of nuclear reactors. They typically include putting one (or a set of detectors) near the reactor about a few 100s of meters away and another detector (or set) a couple of kilometers away. The purpose of the near and far detectors is to measure the neutrinos before and after the oscillation occurs. The detectors are filled with a liquid with a high hydrogen content, such as organic solvents, in order to provide free protons to detect neutrinos through inverse beta-decay

$$\bar{\nu}_e + p \rightarrow e^+ + n. \tag{3.34}$$

The liquid is also emits light when energy is deposited into the medium by ionization. For the inverse beta-decay event, there will be a very unique coincidence signature that can be used to select them from any potential backgrounds. The positron from the initial inverse beta-decay interaction will produce a prompt signal of light. Then, by doping the scintillator with some neutron absorber (a common one is gadolinium), the neutron when later captured produces a delayed gamma signal that can be detected.

The reactor experiments extract the value of θ_{13} by looking at the change in the

Table 3.1: Table of oscillation parameter values as listed by the Particle Data Group summary (Beringer and Particle Data Group (2012)). For Δm^2_{32}, the sign is unknown and therefore the uncertainty is on the absolute value.

parameter	value
$\sin^2\theta_{12}$	0.311 ± 0.016
$\sin^2\theta_{13}$	0.0251 ± 0.0034
$\sin^2\theta_{23}$	[0.39,0.61] at 95% CL
Δm^2_{21}	$(7.5 \pm 0.2) \times 10^{-5}$ eV^2/c^4
Δm^2_{32}	$(2.32^{+0.12}_{-0.08}) \times 10^{-3}$ eV^2/c^4

total rate and/or the changes in the position spectrum. Figure 3.7 shows an example of such a spectrum from one of the reactor experiments, Daya Bay (An et al. (2012)). In the figure, a clear distortion in the spectrum can be seen due to electron anti-neutrino disappearance. What was an unmeasured parameter a few years ago is now one of the better measured parameters due to the precise measurements from the reactor experiments. The averaged measured value as listed in the 2012 Particle data group review was $\sin^2\theta_{13} = 0.0251 \pm 0.0034$ (Beringer and Particle Data Group (2012)).

3.5.5 Summary of Current Measured Parameter Values

A table summary of the current best measured values of the oscillation parameters is given in Table 3.1. Current outstanding issues related to the measurement of these parameters are discussed in the next section.

3.6 Outstanding Questions

3.6.1 Mass Hierarchy

Given current experimental precision on the parameters, the oscillation probability in vacuum is insensitive to the sign of the mass splittings. However, in matter, the oscillation probability involving electron neutrinos does provide a means to distinguish the sign as discussed in Section 3.3. For the solar mass splitting, the passage

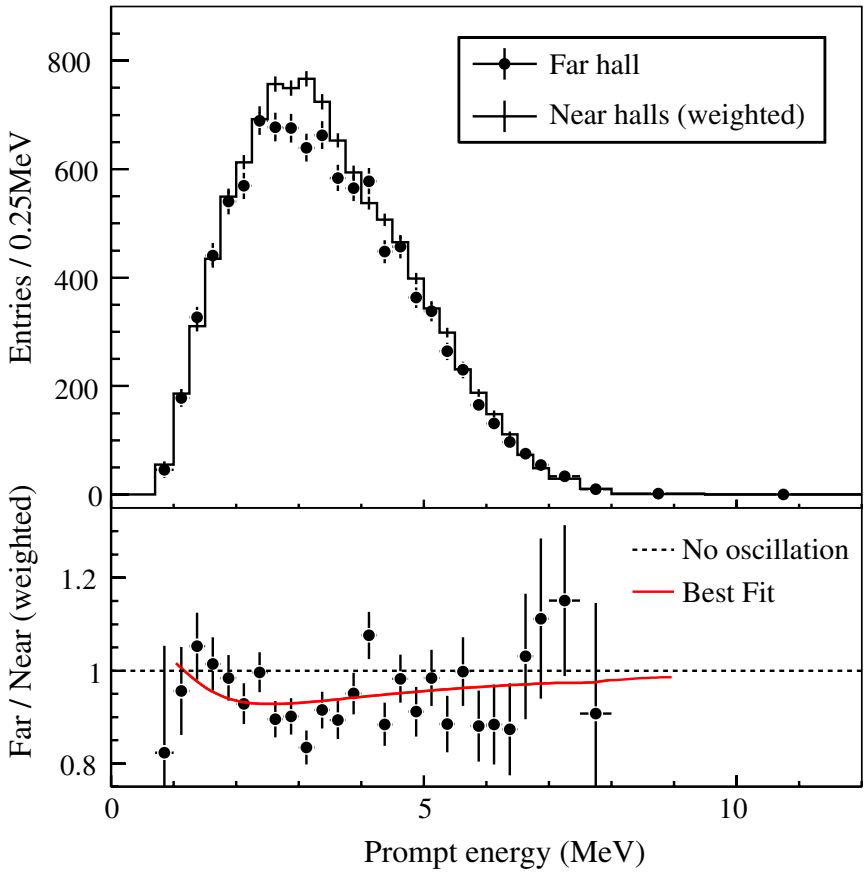

FIGURE 3.7: Top: Measured prompt-energy spectrum of the Daya Bay experiment's set of far detectors (a total of 3) is shown by the points. The predicted spectrum is shown on by the line based on the measurements made at two sets of near detectors. Bottom: The ratio of measured and predicted no-oscillation spectra in the top plot. The solid curve is the Daya Bay best-fit solution when using only the total rate to determine the best value of $\sin^2 2\theta_{13}$. From (An et al. (2012)).

of neutrinos through the Earth has allowed global fits to determine that $m_2 > m_1$. However, for Δm^2 in the atmospheric/beam sector, the sign of the mass splitting has not yet been determined. This ambiguity often causes experiments to analyze results under different assumptions of the mass ordering. In the so called 'normal' hierarchy, $m_3 > m_2 > m_1$, while in the 'inverted', $m_2 > m_1 > m_3$. It is conventional to label the mass splitting terms with the index of the larger mass first. So for the normal hierarchy Δm^2_{32} is used, while for the inverted Δm^2_{13}.

The true hierarchy has an important implication beyond just completing the

measurement of the oscillation parameters. If the mass hierarchy turns out to be inverted, then the next couple of generations of neutrino-less double beta decay experiments have a chance of finding a signal (Beringer and Particle Data Group (2012)). Neutrino-less double beta decay is a process involves the simultaneous emission of two positrons. This process occurs when single beta decay is forbidden because the energy of the daughter nucleus is larger than the parent nucleus. However, in certain instances the energy of the nucleus for a simultaneous decay is possible. In this case, double beta-decay is possible and has been seen (Elliott and Vogel (2002)). However, if the neutrino is its own anti-particle, there is the possibility that two-positrons can be emitted with no neutrinos during a simultaneous beta-decay. This is the neutrino-less double beta decay process, and it has not yet been observed.

3.6.2 Mass Mechanism

The reason that there is much intest in determining if the neutrino is Majorana or alternatively, Dirac, is that this property determines the mechanism by which the neutrino gets its mass. If the neutrino is Dirac, it gets its mass in the same way as the other leptons. This is through Yukawa couplings with the Higgs field. However, the neutrinos of the Standard model are very light compared to the other leptons. Cosmological models put an upper limits below 1 eV (Beringer and Particle Data Group (2012)). This means that the strengths of the couplings are many decades weaker than those of the other matter particles. Alternatively, if the neutrinos are Majorana, the neutrino and anti-neutrino are the same particle. In such a scenario, there are mechanisms, e.g. the see-saw, which suppress the mass of the neutrino by some very high energy scale (Beringer and Particle Data Group (2012)). As a result, there has been much effort to measure neutrino-less double beta decay, which if observed would indicate that the neutrino is Majorana.

3.6.3 Is there CP Violation in the Lepton Sector?

With the value of $\sin^2\theta_{13}$, measured, this leaves only one parameter remaining (observable through oscillations) that has been unmeasured, δ_{CP}. The value of δ_{CP} potentially has much significance. This parameter must be non-zero in order for CP violation in neutrino oscillations to occur. This can be seen by comparing the probability of the CP-conjugate oscillations, $P_{\nu_\mu\to\nu_e}$ and $P_{\bar{\nu}_\mu\to\bar{\nu}_e}$. Their difference to leading order for vacuum oscillations is $\Delta P_{\mu e} \equiv P_{\nu_\mu\to\nu_e} - P_{\bar{\nu}_\mu\to\bar{\nu}_e}$ is

$$\Delta P_{\mu e} = -4\sin(2\theta_{12})\sin^2(2\theta_{23})\cos^2(\theta_{13})\sin\delta_{CP}\sin\theta_{13}\times\Phi_{32}\Phi_{31}\Phi_{21}, \tag{3.35}$$

where $\Phi_{ij} = \sin(\frac{\Delta m^2_{ij}}{4E})$. It is evident from this equation that all the parameters in the PMNS matrix must be non-zero in order for CP violation to occur. Currently, measuring CP violation is considered to be one of the top priorities in particle physics (Particle Physics Project Prioritization Panel (2008)). The motivation behind measuring CP violation comes in part because of potential connections to leptogenesis (Branco et al. (2001))(Kayser (2011)). Leptogenesis serves as a plausible explanation for the matter and anti-matter asymmetry we see in our universe.

3.6.4 Maximal Mixing

Currently, one the parameters with the most uncertainty is the value of the mixing angle, $\sin^2\theta_{23}$, which all data have shown to still be consistent with 0.5. If it has this value, then the mixing between mass states is maximal. It is thought that such a maximal value could be a hint to some underlying symmetry. More broadly, the values of the mixing matrix entries themselves, which are fairly large in contrast to the quark mixing matrix, could be important inputs in trying to develop theories that explain the flavors and generations (Ishimori et al. (2010))(King and Luhn (2013))(Albright et al. (2010)).

3.7 Muon Neutrino Disappearance at T2K

3.7.1 Importance of $\sin^2(\theta_{23})$ *and* Δm^2_{32}

In this dissertation, we present the measurement of muon neutrino disappearance that will aim to improve the precision on the field's knowledge of $\sin^2(\theta_{23})$ and Δm^2_{32}. Besides interest in the parameters themselves, strong constraints on these parameters are required in the search for CP violation. The determination of $\sin^2\theta_{23} = 0.5$, i.e. if the mixing is maximal, also has impact on attempts to explain the structure of mixing matrix and neutrino flavor as mentioned above.

For CP violation, it is clear that precise measurements of all parameters of the PMNS matrix will be important for observing a non-zero value for the expression in Equation 3.35. However, if one looks at the first two leading terms in the vacuum probability of measuring muon to electron neutrino appearance,

$$\begin{aligned} P_{\nu_\mu\to\nu_e} &= \Big[\sin^2(\theta_{23})\sin^2(\theta_{13}) \\ &\quad - \sin\delta_{CP}\sin\theta_{13}\cos\theta_{13}\sin 2\theta_{23}\sin 2\theta_{12}\sin\frac{\Delta m^2_{21}L}{4E}\Big]\sin^2\frac{\Delta m^2_{32}L}{4E} + ..., \end{aligned} \tag{3.36}$$

one can see that the probability depends on $\sin\delta_{CP}$ as well. Precision measurements of this oscillation probability could lead to constraints on $\sin\delta_{CP}$ that indicate it is non-zero.

3.7.2 Disappearance Oscillation Probability

Because the oscillation analysis described in this thesis is of muon neutrino disappearance, we provide the expression to the first two leading terms of the vacuum oscillation probability. It is

$$P_{\mu\to\mu} \approx 1 - (\cos^4\theta_{13}\sin^2(2\theta_{23}) + \sin^2 2\theta_{13}\sin^2\theta_{23}) \times \Phi^2_{32} \tag{3.37}$$

for the normal hierarchy where $\Phi^2_{32} = \sin^2(\frac{\Delta m^2_{32}L}{4E})$. The first thing to note is that the expression is dependent not only on the parameters we are interested in, $\sin^2(\theta_{23})$

and Δm^2_{32}, but also the value of θ_{13}, which plays an important role.

In order to see the role of θ_{13} in muon neutrino disappearance, we rearrange Equation (3.37) into the following form:

$$P_{\mu\to\mu} \approx 1 - \Phi^2_{32} \times (1 - (2\sin^2\theta_{23}\cos^2\theta_{13} - 1)^2). \tag{3.38}$$

In this form, it is clear that the maximum amount of disappearance occurs when

$$\sin^2\theta_{23} = \frac{1}{2\cos^2\theta_{13}}. \tag{3.39}$$

With a non-zero value of θ_{13}, the point where the maximum possible amount of muon neutrino disappearance, i.e. when the factor preceeding the mass splitting factor equals one, is no longer when $\sin^2\theta_{23} = 0.5$. In general, this means that the amount of disappearance is dependent on the value of θ_{13} in addition to θ_{23}. Fortunately, the constraint on θ_{13} is fairly strong in comparison to current uncertainties on the value of θ_{23}. Therefore, in our measurement of θ_{23} we use the averaged value and uncertainty from the reactor experiments (as listed in the PDG2012) to constrain the value of θ_{13}. In our analysis, we assume $\sin^2\theta_{13} \approx 0.0251 \pm .0034$.

Also, note that while we listed an approximation of the muon neutrino disappearance probability in vacuum here for discussion, the analysis uses the full oscillation formula which includes contributions from all terms along with matter effects.

Therefore, with the aim of the measurement in view, we move on to the description of the experiment, T2K, whose several components will allow us to make a measurement of these oscillation parameters.

4

The T2K Experiment

4.1 Overview

The T2K experiment can be partitioned into three primary components (Abe et al. (2011b)), all of which are shown in Figure 4.1. The first is the J-PARC facility located in Tokai, Japan – about 100 km north of Tokyo on the Pacific coast. J-PARC produces a neutrino beam that is directed westward. After 280 meters, the beam passes through the second component of the experiment, a complex of detectors known as ND280 (for Near Detectors at 280 meters). From here, the beam continues west for a total of 295 kilometers where it is measured again by the "far" detector of the T2K experiment, a massive water Cherenkov detector known as Super-Kamiokande, or Super-K. The path of the neutrino beam from Tokai to Super-K is illustrated in Figure 4.2

The approach of the experiment to measuring neutrino oscillations is straightforward. The beam, which consists mostly of muon neutrinos, is measured by the ND280 complex at a short enough distance after its creation before oscillations have occurred. This measurement is then compared to the measurement of the beam once

it arrives at Super-K. Any observed changes in the energy spectrum of the neutrino beam and in the neutrino flavor give us a handle to constrain the values of the parameters in the PMNS mixing matrix.

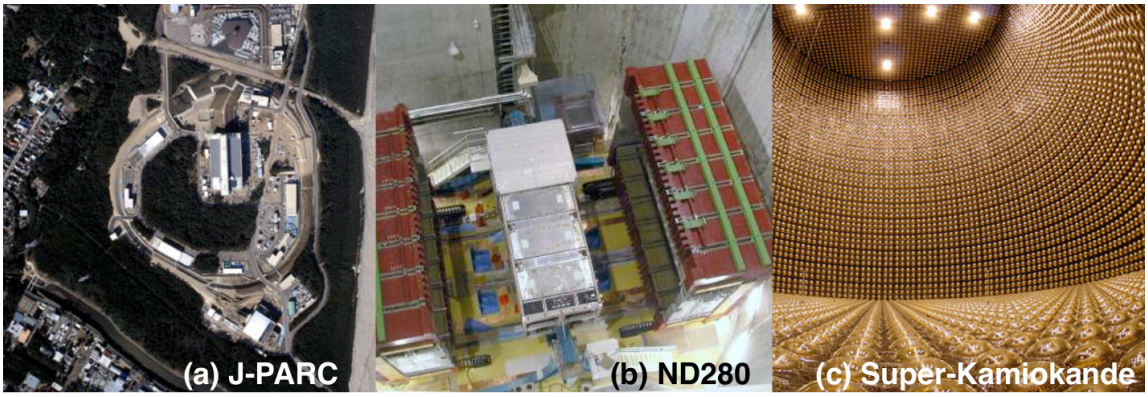

FIGURE 4.1: The three components of the T2K experiment. The beam is created at (a) the Japan Particle Accelerator Research Complex, or J-PARC, travels 280 m to (b) the near detector complex at 280 meters, or ND280, and then finally passes through (c) the Super-Kamokande detector (Super-K).

A primary feature of the T2K experiment is that the Super-Kamiokande detector and some of the ND280 detectors are positioned 2.5 degrees off-axis from the center of the beam. Conducting the oscillation measurement with an off-axis neutrino beam is advantageous because the neutrino energy spectrum will be more sharply peaked at the energy where previous experiments indicate that the maximum amount of muon neutrino oscillations will occur, given a baseline of 295 km.

In this section, we briefly describe the three components of the T2K experiment.

4.2 The J-PARC beam

The neutrino beam produced by J-PARC is made from the decays of mesons created by a proton beam slamming into a target of graphite. The facilities that produce the proton beam are known as the "primary" beam line. The facilities housing the target and the equipment to focus the mesons into a beam that eventually decays into neutrinos is referred to as the "secondary" beam line.

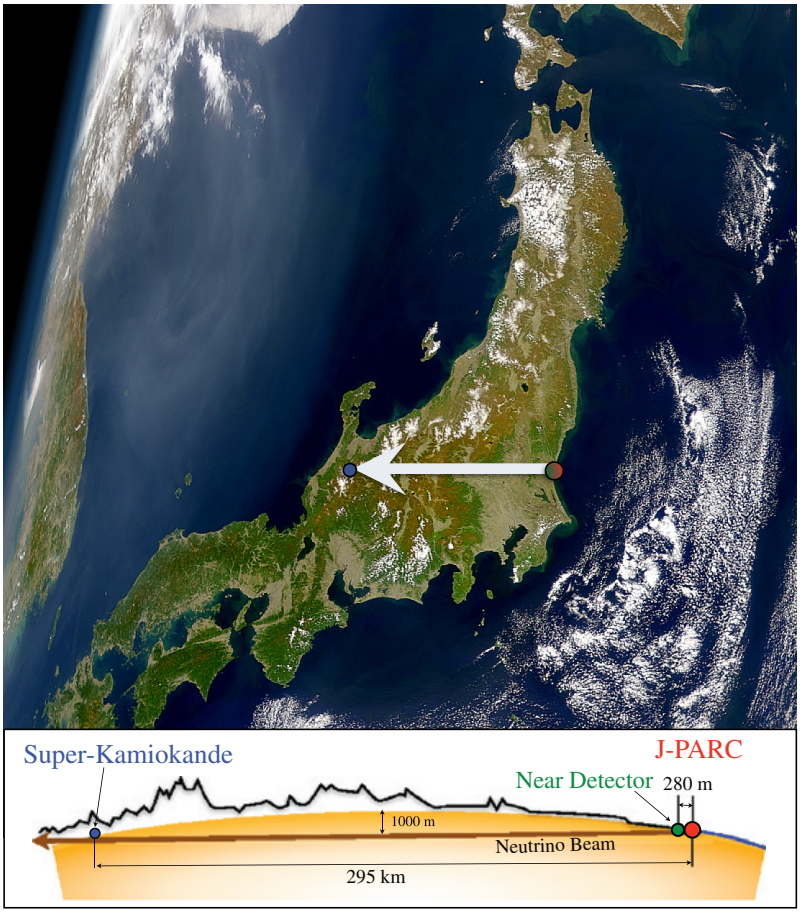

FIGURE 4.2: Schematic of the neutrino beam path from the J-PARC accelerator located in Tokai, Ibaraki Prefecture to the Super-K detector located near Kamioka, Gifu Prefecture. Bottom schematic from (Abe et al. (2011b)).

4.2.1 Primary Beam Line

The proton beam first starts as a bunch of H^- ions accelerated to 181 MeV[1] by a linear accelerator (LINAC). The H^- beam is then converted to H^+, or protons, by passing through charge-stripping foils right before being injected into the rapid-cycling synchrotron (RCS). In the RCS, the protons are accelerated up to 3 GeV. The protons then pass into the main ring synchrotron (MR) where they are accelerated to 30 GeV. At this stage of the beam, the protons are grouped into eight bunches. They are then extracted (in fast extraction mode) into the secondary beam line and

[1] but with capacity for 400 MeV

fired into a graphite target. Figure 4.3 provides an illustration of the proton beam's journey.

FIGURE 4.3: Photo of the J-PARC accelerator with diagrams overlaid. The proton beam starts in the LINAC and then is accelerated first to 3 GeV in the RCS then to 30 GeV in the main ring. The protons are then extracted from the main ring into the secondary beam line where they are directed into a graphite target. Particles produced by the interaction of the protons and target eventually decay into the neutrino beam directed along the path shown. Figure from the J-PARC website.

4.2.2 Secondary Beam Line: Target, Horns, and Decay Hall

The protons extracted from the main ring and into the secondary beam line are used to produce the neutrino beam. Figure 4.4 provides a diagram of the secondary beam line and its components. The process of creating neutrinos starts with the proton beam impacting a graphite target and creating hadrons. The resulting hadrons are then focused into a beam by three magnetic focusing horns and pass into a decay volume filled with helium where charged mesons collected by the horns decay into a beam of neutrinos. Most of the remaining particles that have not decayed are stopped by a beam dump at the end of the decay volume. However, some muons

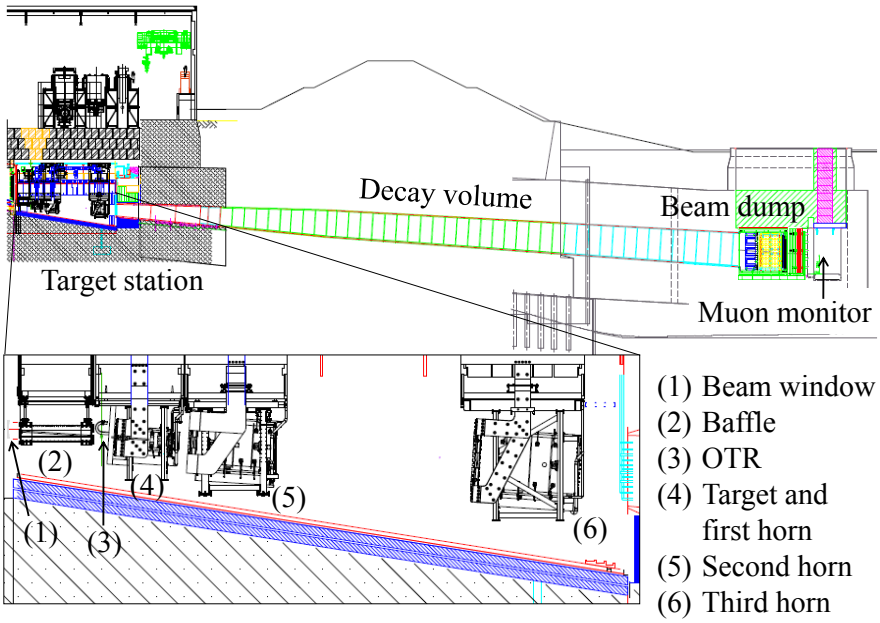

FIGURE 4.4: Diagram of the secondary beam line. Protons from the primary beam line are fired into the target. Hadrons are produced and are focused by three magnetic horns. Out of all the hadrons, the horns are designed to focus π^+ (π^-) into the decay volume where they decay into $\nu_\mu + \mu^+$ ($\bar{\nu}_\mu + \mu^-$) when running in neutrino (anti-neutrino) mode. Any hadrons which have not decayed are stopped at the beam dump, while muons are measured at the muon monitor. Figure taken from (Abe et al. (2013c)).

created in conjunction with the neutrino beam pass through and are then measured by a muon monitor in order to profile the beam.

The target hit by the proton beam is a rod composed of graphite encased in a titanium cylinder for structural support and heat dissipation. The graphite core has a diameter of 2.6 cm, a length of 91.4 cm, and a density of 1.8 g/cm^3 which for the protons amount to 1.9 interaction lengths. The target assembly is cantilevered inside the bore of the first magnetic focusing horn. A photograph of the target assembly while outside the horn is provided in Figure 4.5.

Of all different hadrons created in the target, the decay of π^+ is what produces the bulk of the neutrino beam (when running in 'neutrino mode') via

$$\pi^+ \rightarrow \mu^+ + \nu_\mu \tag{4.1}$$

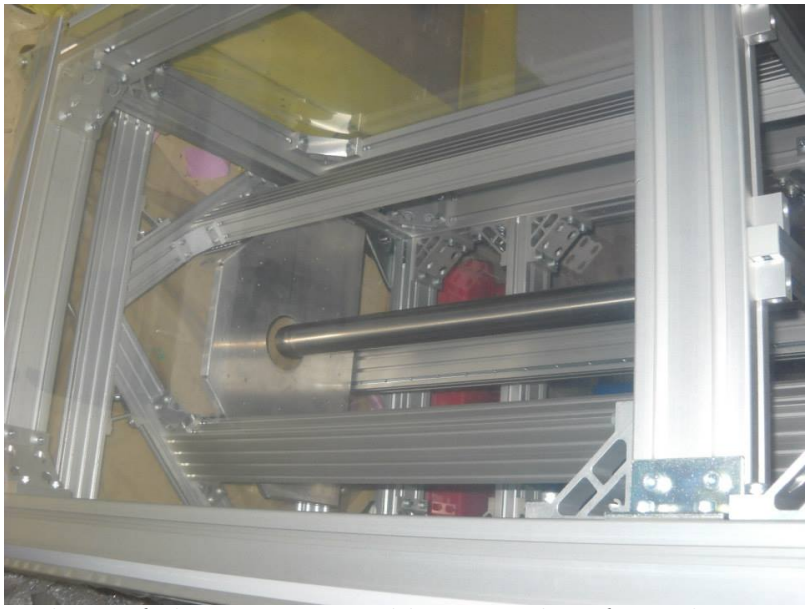

FIGURE 4.5: Photo of the target assembly protruding from the center of the first magnetic focusing horn. Photo by K. Mahn.

with a branching fraction of 99.99% (Beringer and Particle Data Group (2012)). In order to increase the intensity of the eventual neutrino beam, the π^+ are focused using three magnetic focusing horns. If anti-neutrinos are desired the configuration of the horns can be changed to collect π^-.

The magnetic horns consist of two thin coaxial conductors. A cross section of the horns' geometries are shown in Figure 4.6. Opposite polarity currents are run through each of the conductors creating a toroidal magnetic field in the space between the conductors. This toroidal field is created in time with the arrival of the hadrons in order to focus the π^+. The current polarity is flipped in order to focus π^- for a beam of anti-neutrinos. The use of the horns greatly increases the neutrino beam intensity. Figure 4.6 shows the predicted neutrino flux at Super-K with and without the operation of the horns.

As stated before, the bulk of the neutrino beam (in neutrino mode) comes from the decay of π^+ that have been focused into the decay hall. The hall is 96 m long and is filled with about 1500 m^3 of helium gas in order to reduce pion absorption (Abe

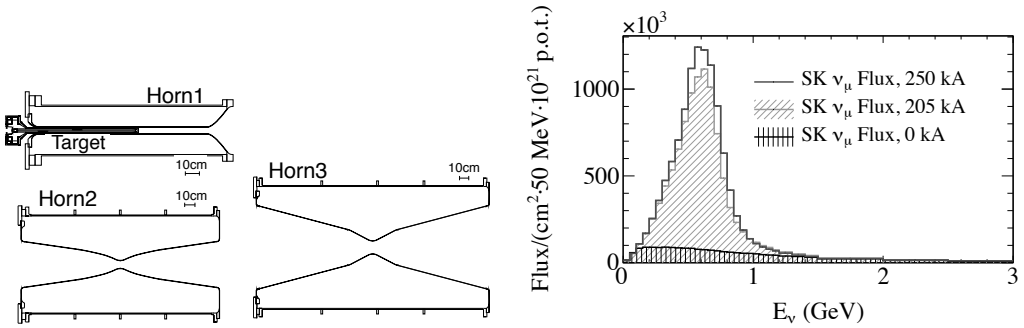

FIGURE 4.6: Left: diagrams presenting the cross section of the magnetic focusing horns. Right: the predicted neutrino flux at Super-K with and without the operation of the magnetic focusing horns. The horns greatly increase the intensity of the neutrino beam. From (Abe et al. (2013c)).

et al. (2011b)).

In addition to the decay of π^+, the decays of other particles produce a non-negligible contribution to the neutrino beam. One of the largest subdominant sources is the decay of kaons

$$K^+ \to \mu^+ + \nu_\mu \qquad 63.55\% \tag{4.2}$$

$$K^+ \to e^+ + \nu_e + \pi^0 \qquad 5.07\% \tag{4.3}$$

$$K^+ \to \mu^+ + \nu_\mu + \pi^0 \qquad 3.35\%, \tag{4.4}$$

where the branching fractions have been listed (Beringer and Particle Data Group (2012)). Another large subdominant source is the decay of muons that were produced in the initial decays. These muons produce both neutrinos and anti-neutrinos by

$$\mu^+ \to e^+ + \bar{\nu}_\mu + \nu_e. \tag{4.5}$$

For the predicted flux of neutrinos by flavor and parent meson, please see Figure 6.6 in Chapter 6. The final predicted flux is discussed later in the context of the simulation of the beam.

Finally, at the end of the decay hall, a water-cooled beam dump composed of 75 tons of graphite absorbs the remaining particles. The beam dump core is 3.174 m

thick, 1.94 m wide, and 4.69 m high. Only muons above approximately 5 GeV are able to pass through the dump. These muons are measured by the muon monitor in order to track the direction of the beam to a precision better than 0.25 mrad. The stability is also measured to a precision of 3% (Abe et al. (2011b)).

4.3 The Near Detector Complex, ND280

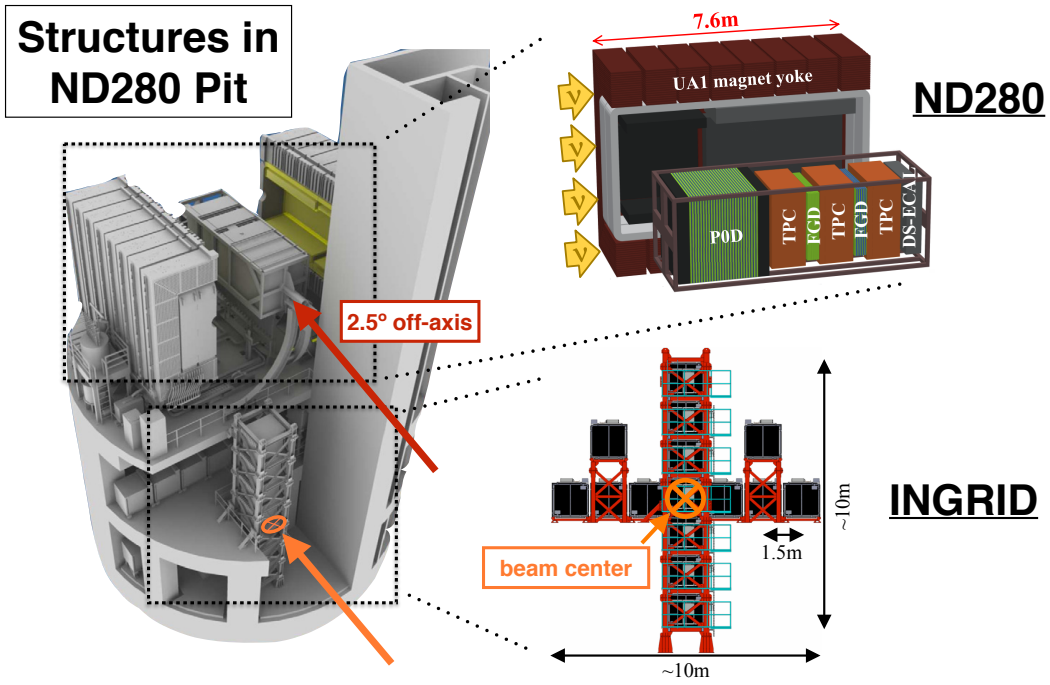

FIGURE 4.7: Diagram illustrating the detector arrangement in the near detector pit (left) along with diagrams of the ND280 complex and the INGRID near detector (top and bottom right). The INGRID detector is placed on the center of the beam, which has been designated in orange. INGRID measures the neutrino beam profile in order to check alignment and stability. The ND280 off-axis detector complex is aligned 2.5° from the center of the beam. The detector complex is composed of different sub-detectors employing different types of particle tracking technology. The sub-detectors are also placed inside the UA1 magnetic in order to allow for determining the sign of charged particles. (Note that the UA1 magnet is shown open in the diagram. When running, the UA1 magnet fully encloses the ND280 off-axis detectors.) The far detector Super-K is also pointed 2.5° off-axis from the center of the beam. The role of the ND280 off-axis detectors is to measure the neutrino beam before oscillation effects. It also measures neutrino interaction cross sections. Diagram produced by modifying figures from (Abe et al. (2011b)).

The second component of the T2K experiment is the ND280 complex which

consists of a collection of detectors situated 280 m downstream from the target. The detectors are housed underground in what is known as the near detector pit. Figure 4.7 provides a diagram showing the arrangement of the detectors in the pit along with illustrations of the two components of the ND280 complex: INGRID and the ND280 off-axis detectors. The latter is itself a complex of sub-detectors that feature different particle tracking technology. In the following, we describe the INGRID detector and then the different sub-detectors in the ND280 off-axis complex.

4.3.1 INGRID

INGRID stands for the Interactive Neutrino GRID. It is a collection of modules with each module made up of alternating slices of plastic scintillator and iron panels. There are a total of 20 panels – 11 scintillating and 9 iron – which are arranged in an alternating pattern. The iron panels serve as a dense target for neutrino interactions with a total of 7.1 tons per module. The scintillator layers are used to record the x-y position of charged particles and are constructed out of two subplanes of plastic scintillator bars. The scintillation light produced by the individual bars are read out using a wavelength-shifting fiber that directs its signal into a MPPC (Multi-Pixel Photon Counter), which is a collection of silicon photomultipliers. The x-y position information is produced through the arrange of the bars: 24 horizontal bars are glued together to form one plane while 24 vertical bars form the other. Each module is surrounded by veto panels made up of 22 scintillator bars segmented along the beam direction. The bars are made of extruded polystyrene doped with 1% PPO (2,5-diphenyloxazole) and 0.03% POPOP (1,4-bis(5-phenyloxazol-2-yl) benzene) and coated with a TiO_2 reflective coating.

As seen in Figure 4.7 the INGRID modules are arranged in a cross pattern with the intersection point lying directly at the center of the neutrino beam. INGRID's primary purpose is to measure the neutrino beam profile and monitor the stability

of the beam flux. INGRID is able to measure the beam to < 1 mrad precision. More details on the INGRID detector and modules can be found in (Abe et al. (2011b)) and (Abe et al. (2013c)).

4.3.2 ND280 off-axis detectors

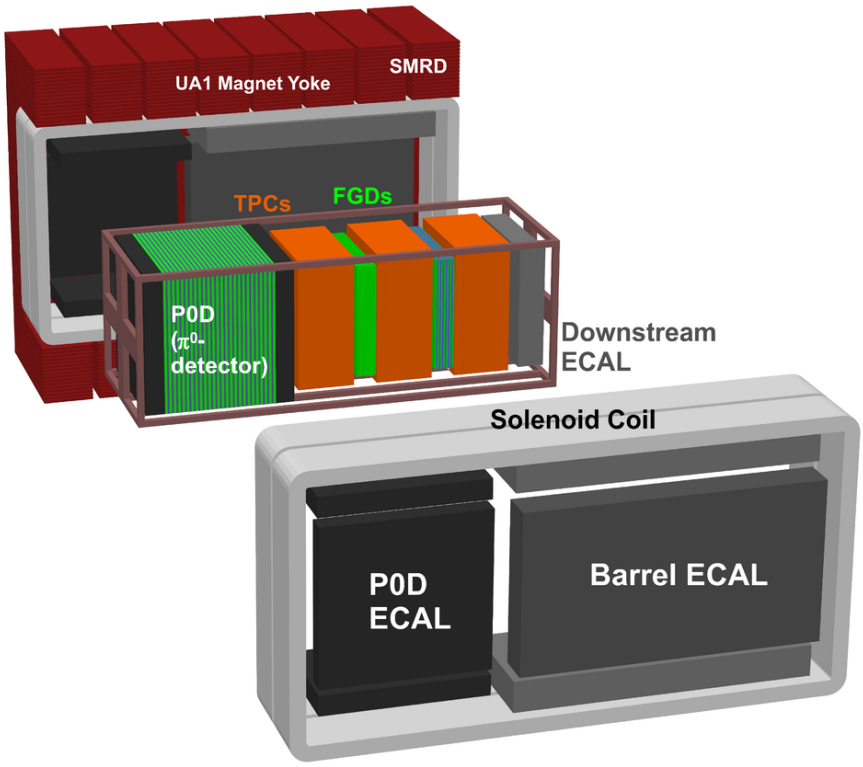

FIGURE 4.8: Exploded diagram of the ND280 off-axis complex.

The arrangement of the sub-detectors that make up the ND280 off-axis complex can be seen in Figure 4.7. The off-axis complex can be divided into two groups. The first is a magnet yoke and a subdetector called the SMRD that together encase a collection of inner detectors. The enclosed detectors are known as the P∅D, TPC, FGD, and ECALs. A description of these all of the detectors and the magnet will follow shortly. The most upstream of these detectors is the P∅D. This is followed by the first of three TPC modules, the first of two FGD modules, the second TPC,

the second FGD, the third TPC, and finally the downstream ECAL. Another set of ECAL modules completely surrounds the sides of the P∅D. A final set of ECAL modules surround the sides of the TPC and FGDs.

An additional key component of the ND280 off-axis detectors, besides the sub-detectors, is an applied dipole magnetic field of 0.2 T which provides the means to measure particle momenta and sign of charged particles. The field is provided by a large aluminum coil and a flux return yoke that encases the inner collection of detectors. The coils run along the beam direction on the top, bottom, front, and back of the sub-detectors. The magnetic yoke and coil is reused from the UA1 and NOMAD experiments, the former responsible for the discovery of the $W^{\pm}$ and Z^0 bosons. Because of this pedigree, it is conventional in the T2K collaboration to refer the coil and yoke as the UA1 magnet.

Finally, as mentioned before, the SMRD encases the entire inner sub-detector collection in conjunction with magnetic assembly thereby completing the ND280 off-axis complex.

A more close-up diagram showing the arrangement of the sub-detectors are shown in Figure 4.8. We now proceed to describe the sub-detector systems listed above.

4.3.3 The P∅D

The P∅D detector stands for the π^0 Detector. Its name derives from its designed purpose which is to measure neutral-current neutrino interactions $\nu + N \rightarrow \nu + \pi^0 + X$ on water. The motivation to focus on this interaction comes from the fact that the production of π^0 is one of the leading backgrounds in measurement of muon to electron neutrino oscillations for T2K (Itow et al. (2001)).

The detector is constructed out of planes of plastic scintillator, water, lead, and brass. The planes of scintillator consist of a sub-plane of vertical bars and another sub-plane of horizontal bars in order to be able to map out the x-y position of the

particles traveling through the detector. The water layers consist of drainable bags of high density polyethylene with each bag instrumented with several photosensors affixed to rods that extend into the bag. The entire structure is encased in a light-tight cover. The photosensors allow neutrino interactions on water occurring inside the bag to be identified in addition to passing charge particles. The fillable/drainable bags allow one to make measurements of the P∅D interaction cross section with and without water present.

The P∅D can be divided into three regions: an upstream electromagnetic calorimeter, the water target, and downstream electromagnetic calorimeter. In the electromagnetic calorimeters, the detector consists of layers of scintillator and lead. In the water target regions, the detector is built of subunits consisting of a water bag, a brass or lead sheet, followed by a scintillator panel. Further details about the P∅D can be found in (Abe et al. (2011b)).

4.3.4 The TPCs

Each of the three TPCs, or Time Projection Chambers, that are found in the inner ND280 off-axis complex are filled with 3000 L of an argon-based drift gas. The drift electrons left by traversing charged particles are read out by micromegas detectors. The TPCs provide the ND280 detectors with excellent images of charged particle tracks in three dimensions. However, it comes at the cost of less target material. Therefore the TPCs are used as an important tool for measuring the momentum and type of particle created neutrino interactions in denser parts of the detector. The momentum can be determined by the curvature of the tracks as the charged particles are bent by the magnetic field provided by the UA1 magnet. The amount of ionization per track length can be combined with the measured momentum to provide a method for particle identification. For further details in the construction and operation of the TPCs please see (Abe et al. (2011b)).

4.3.5 The FGDs

The two fine-grained detectors, or FGDs, embedded in the ND280 off-axis complex balances good particle tracking with good target mass. The most upstream of the FGDs also plays an important role as the target for the ND280 detector. In the ND280 event samples used by this analysis, one of the selection cuts will be that the interaction action vertices start in the upstream FGD. This is done so that muons produced in charged-current interactions with the FGD can be contained within the downstream TPCs and second FGD.

The most upstream FGD is made out of arrays of triangular plastic scintillator bars composed of extruded polystyrene. Each bar has a reflective TiO_2 coating and a wavelength-shifting fiber traveling through a hole drilled down the center of the bar. The wavelength-shifting fiber guides the scintillation light out of one end of the bar to an MPPC and electrons for digitization of the scintillation light. The FGD is constructed by alternating layers of 192 bars that are glued together in the horizontal direction and 192 bars glued together in the vertical direction. This gives the FGD x-y position information. There are a total of 30 layers (half horizontal, half vertical) in the first FGD.

For the second FGD, seven pairs of x-y layers of scintillator bars are alternated with six 2.5 cm thick layers of thin-walled corrugated polycarbonate containers filled with water. These are included in order to provide a target for measuring neutrino interactions on water. Both FGDs are flanked on both sides by the three TPC modules. For further details about the FGDs, please see (Abe et al. (2011b)).

4.3.6 The ECAL Modules

Several ECAL, or electromagnetic calorimeter, modules surround the P∅D, TPC, and FGD modules with the intention of measuring any electromagnetic energy escaping from these detectors. These modules are composed of alternating layers of

plastic scintillator and lead. The lead provides a dense electron material that induces photons and electrons/positrons to shower. Scintillation light produced by showers traveling through the plastic provides a measure of the energy.

4.3.7 The SMRD

The SMRD stands for the Side Muon Range Detector. Panels of plastic scintillator are fitted in the gaps between the sub-detectors encased by the UA1 magnet and in between the different segments of the magnetic yoke. The scintillator is composed of extruded polystyrene and dimethylacetamide with admixtures of POPOP and para-terphenyl. The role of the SMRD is to detect muons escaping the detector and measure their momenta. The SMRD also plays an important role of detecting muons entering the ND280 sub-detectors which originate from both cosmic rays and beam neutrino interactions that occur within the walls of the ND280 pit. The SMRD also identifies beam-produced particles coming from interactions in the magnet.

4.3.8 ND280 Example Event

Figure 4.9 shows an event display from data where a muon enters from the upstream portion of the detector and passes through every sub-detector. The event display provides an example of the type of tracking information provided by the systems along with a sense of the relative resolution. Secondary particles produced by the muon are also stopped by the ECAL. The one detector system not displayed is the SMRD.

4.4 The Far Detector, Super-Kamiokande

The Super-Kamiokande detector, or Super-K, is a large water Cherenkov detector located about 1 km below the peak of Mount Ikenoyama in the Japanese alps (Fukuda et al. (2003)). Figure 4.10 provides a schematic of the detector. The detector consists

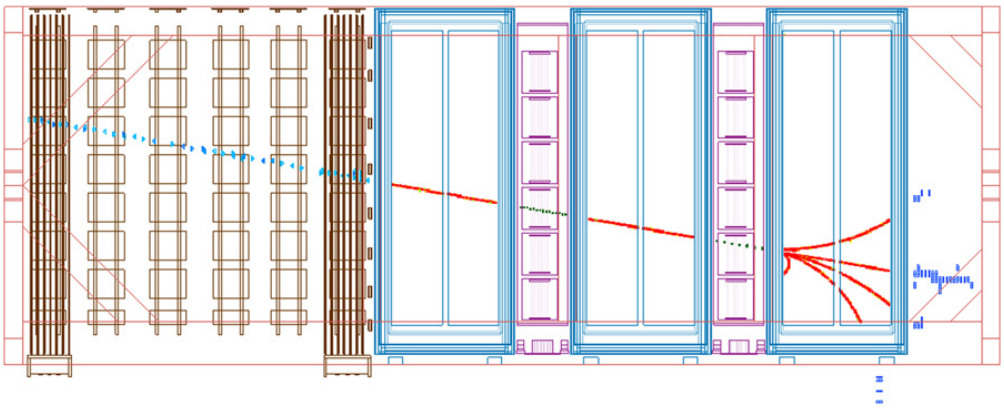

FIGURE 4.9: Example event display from data where a muon has entered into the front of the ND280 off-axis complex via the P∅D ECAL and passed through almost all of the sub-detectors. Secondary particles are seen entering into the downstream ECAL and showering. The only detector subsystem not shown is the SMRD. From (Abe et al. (2011b)).

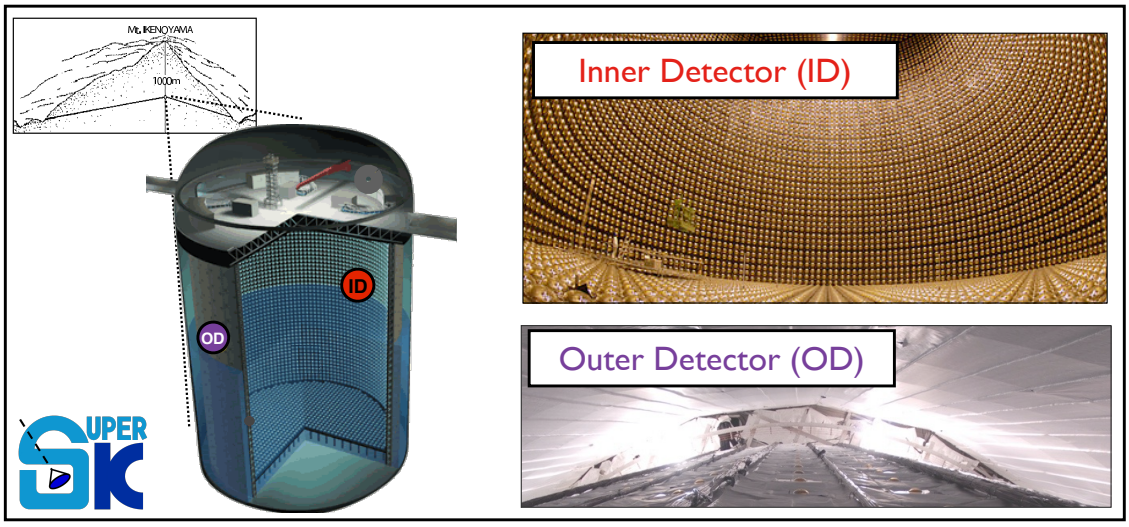

FIGURE 4.10: Schematic of the Super-K detector. The detector is located about 1 km beneath the peak of a mountain in the Japanese Alps known as Mount Ikenoyama. The detector consists of a large cylindrical cavern filled with ultra-pure water. The detector is separated into two optically-separated volumes known as the Inner Detector and Outer Detector. Both volumes are instrumented with photomultiplier tubes. The left illustration is a schematic of the detector. Note that while the drawing shows the detector half-full, the water completely fills both the ID and OD when the detector is operating. The photos on the right provide a view from inside each of the detector segments (before filling).

of a cylindrical cavern 41.4 m high and 39.3 m wide that is filled with 50 ktonnes of ultra-pure water. A stainless-steel, cylindrical scaffold with top and bottom caps is propped up in the center of the tank. The scaffold has an inner height of 36.2 m and inner diameter of 33.8 m and is about 0.55 m thick at all points. The scaffolding provides the structure to which a little over 13,000 photomultiplier tubes (PMTs) are mounted. About 11,000 of these sit on the inside surface and face inward. The remaining phototubes are mounted on the outer surface of the scaffold, facing outward. These outward facing tubes are actually smaller than the inner PMTs. However, this size difference is compensated by using wavelength-shifting plates to help guid light into the smaller outer tubes. The PMTs along the inside surface of the scaffold cover about 40% of the entire area while the PMTs and wavelength-shifting plates along the outer surface together cover about 19%.

The inside and outer surfaces of the scaffold not taken up by the phototubes are covered in sheets of black plastic. The plastic sheets optically separate the inner cylindrical volume from the outer region between the scaffold and the cavern wall. It also optically isolates the volume within the scaffolding itself which has no PMTs observing it. The inner volume is designated as the Inner Detector (ID) while the outer volume is known as the Outer Detector (OD). Views from inside the ID and OD can be found in Figure 4.10.

The roles of the ID and OD differ. The ID is responsible for observing and accurately reconstructing the products of neutrino interactions. The primary role of the outer detector is to serve as a cosmic ray muon veto. To aid in this, additional sheets of Tyvek®[2] are arranged in the OD that optically separate the end caps of the OD from the volume running along the sides, or the "barrel". This optical separation helps in the rejection of cosmic ray muons that enter the top OD end cap and exit through the barrel and in the process, potentially cross the corner of the ID (Dufour

[2] A spun-bound olefin fiber that is a registered trademark of the DuPont Company.

(2009)).

4.4.1 Particle Detection through Cherenkov Radiation

Super-K detects charged particles by the Cherenkov radiation they emit as they pass through the water. If a charged particle travels faster than the phase speed of light in any medium, photons are emitted in a cone along the direction of the particle with an angle given by

$$\cos\theta_c = \frac{n}{\beta}, \tag{4.6}$$

where θ_c is known as the Cherenkov angle, β is the ratio of the velocity of the particle to the speed of light in vacuum, and n is the refractive index of the medium. The phenomenon can be thought of as the electromagnetic analogue of a sonic boom, which occurs when a source of sound waves travels faster than the propagation speed of the wave it emits. The result is that the emitted waves begin to pile atop of one another and produce a wake that trails the source. Figure 4.11(a) provides a diagram that illustrates the Cherenkov radiation as sonic boom analogy.

For a charged particle that is created in the ID and remains inside, the Cherenkov radiation it emits will travel to the walls of the detector and leave a ring-shaped pattern. The PMTs on the detector walls record the charge and time of this light, which is then used to reconstruct the particle momentum and infer the flavor of the particle as well. Figure 4.11(b) provides an illustration of a charged particle leaving a Cherenkov ring on the wall. The figure also provides an event display from the data that contains an example Cherenkov ring recorded by PMTs.

Inferring energy and momentum

The momentum of a particle can be inferred from Cherenkov radiation and the resulting PMT hits in two ways. The first is to use the correlation between the amount of charge in the ring with the energy of the particle. The number of Cherenkov pho-

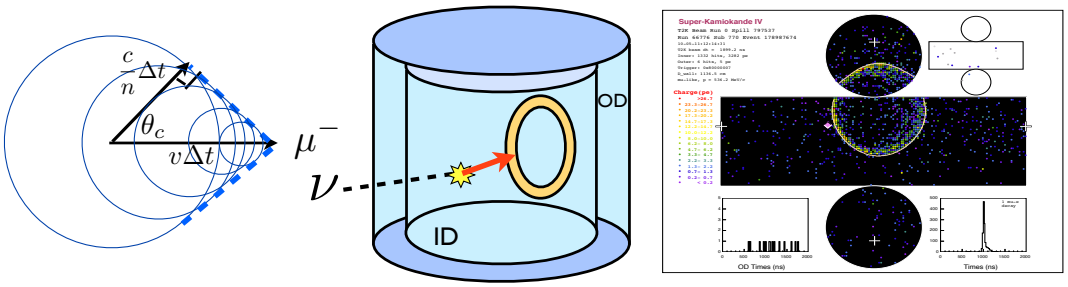

(a) Sonic boom analogy for Cherenkov radiation

(b) charged particle leaving Cherenkov ring on wall

(c) example event display from data of PMT hit pattern

FIGURE 4.11: Illustrations and plots illustrating the use of Cherenkov radiation for detecting charged particles in the Super-K detector. (a) A diagram illustrating the concept of Cherenkov radiation as an electromagnetic analogue to a sonic boom: for a particle traveling faster than the speed of light in the matter, the emitted waves cannot outrun the source. The result is that the wavefronts begin to pile up in a cone with angle, θ_c, trailing the particle. (b) An illustration demonstrating the result of a neutrino interacting in Super-K and producing a charged particle, here a muon: the charged particle is created, and assuming it is traveling faster than the speed of light in water, it produces Cherenkov radiation. Once the particle stops, the radiation travels to the walls of the detector and leaves a ring-shaped pattern. (c) Event display from data: the ring-shaped radiation pattern is recorded by the PMTs lining the walls of the ID. The charge and timing information in these hits are used to reconstruct the particle momentum and to infer the flavor of the type as well.

tons a charged particle, with charge ze, emits per unit length traveled per wavelength is given by

$$\frac{d^2N}{dxd\lambda} = \frac{2\pi\alpha z^2}{\lambda^2}\left(1 - \frac{1}{\beta^2 n^2(\lambda)}\right), \tag{4.7}$$

where α is the fine-structure constant, λ is the wavelength of the emitted Cherenkov photon, and $n(\lambda)$ is the refractive index as a function of wavelength (Beringer and Particle Data Group (2012)). The expression is written in the conventional natural units used in particle physics. Note that the expression must be integrated only over the wavelengths for which the Cherenkov threshold condition is met: $n(\lambda) > \frac{1}{\beta}$.

Though not explicit in Equation 4.7, the Cherenkov photons are emitted in a broad, though bounded range of wavelengths. Assuming the Lorentz oscillator model of dielectric matter interacting with electromagnetic waves, we expect the index of

refraction, $n(\lambda)$ to peak at some resonant wavelength and approach a constant at the far infrared and unity at the far ultraviolet. From the integral, this results in a band of Cherenkov emission.

The number of observed photons per track length observed by the detector must factor in the response of the detector as a function of wavelength in addition to $n(\lambda)$ for water. For Super-K, the PMTs are sensitive between roughly 300-500 nm, which unfortunately, is not very far into the UV. Still, the number of observed photons totals to approximately 20 photons/cm for a 1 GeV muon, when assumes a constant index of refraction and a detector efficiency around 8% between 300-500 nm. The efficiency is approximated from the 40% PMT coverage in the ID times 20% PMT quantum efficiency (QE). (The latter is defined as the probability that a photon hitting the photocathode of a PMT produces a detectable signal. The quantum efficiency and PMTs will be discuss in slightly more detail later.) Using the fact that minimum ionizing particles lose about 2.2 MeV/cm in water, the number of photons per MeV is about 10. For muons, the production of Cherenkov photons per track length is fairly constant making the amount of light seen a useful variable to help reconstruct the particle energy, as will be described later. For electrons or electromagnetic products from gammas, the correlation is less strong, as the electrons shower as they propagate through the detector.

The Cherenkov spectrum observable by the PMTs is unfortunately only a fraction of the light produced. Note that because of the $\frac{1}{\lambda^2}$ dependence in Equation (4.7), the bulk of the Cherenkov photons in water (where $n(\lambda) \approx 1.33$) are emitted in the ultraviolet (UV).

The second method of determining the momentum of particles is to use the Cherenkov ring patterns to determine the distance charged particles travel through the detector. Again, since the muons observed at Super-K detector are mostly minimum ionizing during their path through the detector, the distance traveled correlates

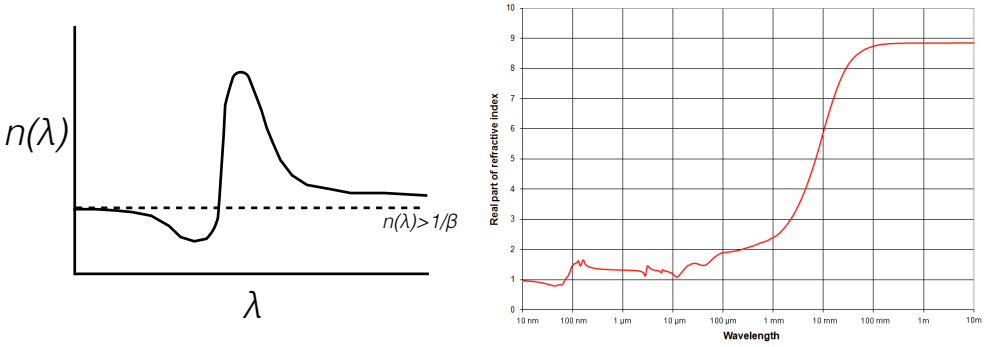

(a) schematic of expected index of refraction for Lorentz oscillator model of dielectric matter

(b) realistic calculation of refractive index for water

FIGURE 4.12: (a) Illustration of the predicted refractive index as a function of wavelength when using the Lorentz oscillator model for matter interacting with a passing electromagnetic wave. (b) Realistic calculation for the refractive index of water by Segelstein et. al. Data based on (Segelstein (1981)) but plot from (Lavin (2012)).

strongly with the particle energy. For other particles like electrons, protons, or pions, the correlation is weaker as these particles tend to lose energy in other ways than ionization. For the reconstruction of electron energies, the energy correlation with distance traveled and photons emitted is weaker than muons. As a result, a realistic detector simulation of the amount of light for a given electron energy is required to assist in reconstruction.

Inferring particle type

Finally, the Cherenkov ring also provides a means to be able to distinguish between minimum ionizing particles and particles which shower. For the former, such as a muon, pion, or proton, the particle travels in a long, straight path. The result is a sharp pattern of hits on the detector wall. For the latter, the showering particle is an electron or photon that converts into an electron/positron pair. Because the electron is light, its path through the water is perturbed due to interactions.

Furthermore, electrons will likely cause an electromagnetic shower in the detector. At the energies above around tens of MeV, the electron loses most of its energy via bremsstrahlung, which is German for braking rays. In this process, an electron changes direction abruptly while emitting a photon. This photon will then convert to electrons/positrons which if above threshold can also bremsstrahlung. The resulting chain reaction is an electromagnetic shower. In a shower, the particles travel in a similar, though more spread-out direction. The Cherenkov light from a shower produces, in the end, a fuzzy ring on the wall. This sharp/fuzzy distinction is used by the Super-K detector to label each track as either muon-like or electron-like.

4.4.2 Inner Detector PMTs

There are a total of 11,129 Hamamatsu PMTs instrumenting the inner detector. The PMTs are bulb-shaped with a 50 cm (20 in) diameter and a depth of 72 cm (28.3 in). A diagram of the PMTs is provided in Figure 4.13a. They are constructed with a bialkali (Sb-K-Cs) photocathode that has a peak quantum efficiency of about 22% at 390 nm. (The quantum efficiency is the probability that a photon interacting with the photocathode will release an electron. A plot showing the quantum efficiency as a function of wavelength for a typical PMT can be found in Figure 4.13b.) The photocathode material is deposited on the inside of the front window of the 4-5 mm thick Pyrex bulbs, all of which were hand-blown. An 11 stage dynode chain is installed at the base of the PMT and is biased between 1.7 and 2.7 kV, depending on the individual PMT. The gains at these bias voltages are about 10^7. The transit times for an electron freed from the photocathode to produce a cascade that reaches the anode is about 90 ± 2.2 nsec (Ishihara (2010)).

The PMTs are enclosed in a case composed of fiber-reinforced plastic (FRP) at the base and a transparent acrylic window in front of the PMT photocathode. The FRP and acrylic are bolted together near the widest point of the PMT bulb. The

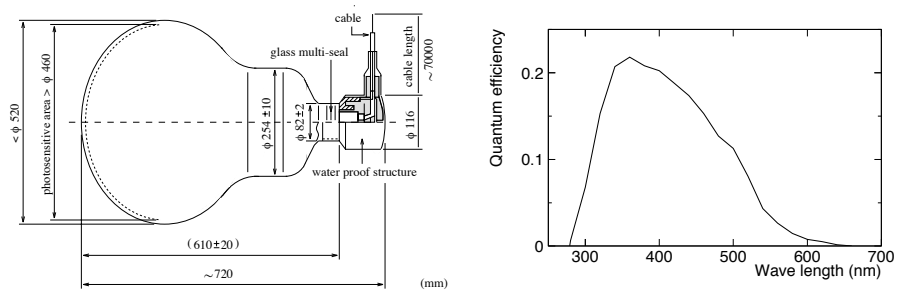

(a) Diagram of the 20" PMTs (b) PMT Quantum Efficiency Curve

FIGURE 4.13: Schematic of the 20" PMTs instrumenting the Super-K Inner Detector. The quantum efficiency as a function of wavelength is also shown for a typical PMT. The quantum efficiency is the probability that a photon hitting with the photocathode of the PMT will liberate an electron. Taken from (Fukuda et al. (2003)).

enclosure is meant to protect against possible shock waves traveling through the water. This measure was motivated by an accident that occurred in July 2001 while the detector was shut down for a scheduled upgrade. While the tank was half empty, a submerged tube imploded under the weight of the water. At the time, the PMTs in Super-K were not enclosed by the FRP+acrylic cases. Therefore, the imploding PMT caused a pressure wave to tear through the water and a chain reaction of collapsing PMTs destroyed 6779 ID and 885 OD tubes.

Because the PMTs used in Super-K are fairly large, the electrons coming off the photocathode have some distance to travel before entering the dynode chain and creating the electron cascade. While all PMTs require that care be taken to keep them away from magnetic fields lest their operation becomes affected, this is particularly important for the 50 cm PMTs. In order to prevent variations in the PMT responses due to the Earth's magnetic field, magnetic compensation coils are installed around the detector to cancel the field for both the ID and OD PMTs.

4.4.3 Outer Detector PMTs/Top-Bottom Asymmetry

For the 1885 PMTs in the outer detector (OD), their setup differs from the ID PMTs and reflects their different environment and role. The OD PMTs, also 20 cm (8 in) in diameter, are surrounded by 60 square cm of acrylic wavelength shifting plates. Examples of this assembly can be spotted in the photo of the OD in Figure 4.10. The acrylic plates are added to increase the light collection of the OD PMTs. When blue Cherenkov photons enter the plate, fluors doped into the plastic absorb the blue light and emit green instead. The green light is trapped by total internal reflection and guided to the photocathode of the OD tubes. The light produced by this method is delayed by 5 ns, but the total light collection is increased by 60% (Wendell (2008)).

The PMT+waveguide construction is motivated by the OD's compact space and primary use as a veto. Because the OD is only 2.5 m wide, only rudimentary track reconstruction is possible. Light will scatter multiple times off of the inner and outer OD walls before reaching the OD tubes. In fact, Tyvek®, which is a highly reflective material for UV light is installed on the outer walls in order to increase the amount of light that reflects back into the PMTs. The emphasis on light collection is motivated by the OD's use as a veto for rejecting events where particles enter the detector from outside the ID. An increased light yield is important to lower the threshold and increase the detection efficiency for spotting entering particles.

The PMTs that are used for the OD come in two types, designated "old" and "new". The old tubes actually come from a previous water Cherenkov detector, IMB, built for searching for proton decay but also used to observe neutrinos (Becker-Szendy et al. (1993)). The old and new tubes have a slightly different responses. They are also not distributed equally over the tank. The old tubes are mostly installed at the top of the OD, while the new tubes are at the bottom.

The difference in response between old and new OD tubes, coupled with their

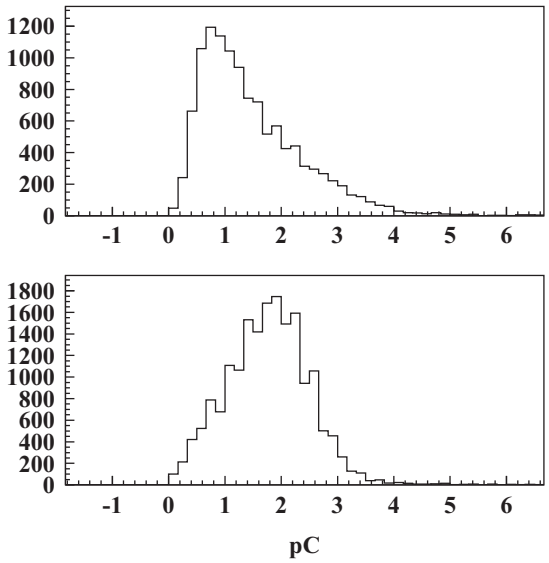

FIGURE 4.14: The single photoelectron distributions for an example"old" OD PMT (top) and "new" OD PMT (bottom). The distributions show quite different shapes. From (Abe et al. (2014)).

clustered distribution, was determined to be at least one of the causes for an asymmetry seen in the OD as a function of the z-position of the tubes. Figure 4.14 compares the single photoelectron (spe) response for a typical old and new tube. There is a difference in the shape, where new tubes have a more well-defined peak while old tubes have an exponential-looking spe distribution. It was observed in both data and MC that the number of hits seen at the top of the detector was less than the number of hits at the bottom given an equal amount of Cherenkov photons produced. Figure 4.15 shows the total amount of OD charge measured for mostly single muons leaving the ID and passing through the OD. The data come from the atmospheric neutrino sample, specifically a type of events known as partially-contained events (PC). These events are classified by a neutrino interaction vertex inside the ID that is at least 200 cm from the wall and a cluster of hits seen in the OD that totals more than 16.

For the most part, the light seen in the OD is made by muons traveling through

the 2.5 m thick OD space. Such events are responsible for the bright band of events in the color plot on the left side of Figure 4.15. In the plot, the expected number of events in the atmospheric sample is shown as a heat map. The events observed in the data are the magenta dots. The plot is a 2D histogram of the observed OD charge as a function of the z-position of the OD cluster from the exiting muon. It can been seen in this distribution a top-bottom asymmetry in the response of the OD in the MC. This was confirmed to also occur in the data. In the right hand plot of Figure 4.15, a profiled histogram displays the mean of the charge bins for each position bin. The asymmetry in both the data and MC is easier to see in this plot.

This asymmetry, a result of the new/old tube differences, was not noticed until recently; therefore, it was not accounted for in one of the selection cuts used in the atmospheric neutrino oscillation analysis. As a consequence, a cut responsible for separating the atmospheric ν PC event sample into high and low energy resolution bins was incorrectly calibrated. The studies of this OD asymmetry led to the proper calibration of this cut (for separating PC Stopping/Through-going events).

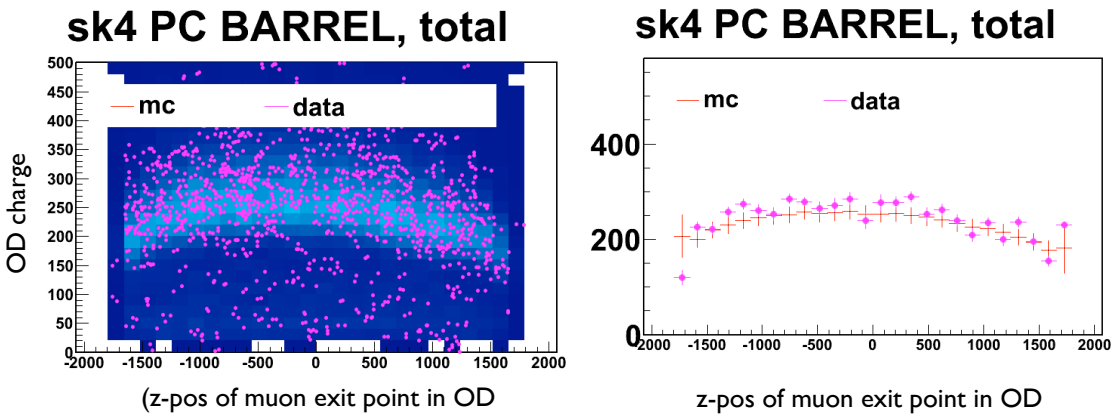

FIGURE 4.15: The plots compares MC (color map) to data (magenta dots) for a sub-sample of the Super-K atmospheric neutrino data, the partially-contained (PC) events. They are both two-dimensional histograms of the total amount of charge observed by the OD as a function of the position where a muon has exited out of the ID and has passed into or through the OD. Note that both plots show the same MC and data. The right hand plot is a profiled plot in x of the left hand plot. What is seen in both data and MC is an asymmetry in the top versus bottom OD response.

4.4.4 Digitization

The PMT pulses are digitized using an ASIC [3] called the QTC for Charge(Q)-to-Time converter. The outputs from the PMTs are fed simultaneously into three inputs that each handle a different range of pulse sizes – low, middle, high – in order to provide a large dynamic range. There are three independent input channels per QTC chip. Once a PMT produces a pulse that rises above a discriminator threshold, the QTC is triggered and begins (1) emitting a digital output signal and (2) integrating the PMT signal over a 400 ns window. After the 400 ns integration time, the circuit begins to discharge. The circuit is built such that the length of time it takes for the discharging signal to fall below some internal threshold is proportional to the total integrated charge. From the time the QTC is triggered to the time the discharging circuit finally falls below threshold, the QTC is outputting a digital signal. The result is a digital output which encodes both the start time of the PMT pulse and its integrated charge.

While the circuit is integrating and discharging, the QTC input is blocked and a VETO signal is started that lasts for a total of 900 ns after the QTC is triggered. After the discharge, a minimum of 150 ns is required to allow the circuit to reset and return to baseline. During this 150 ns reset window, input pulses are blocked. This block will go past the default 900 ns VETO if necessary. Figure 4.16 provides a diagram of the QTC operation. For more details on the QTC design and performance along with the signal conditioning performed on the PMT signal before the QTC refer to (Nishino et al. (2009)).

The calibration of the QTC circuits are performed at frequent intervals. Inputs are available to input known calibration pulses (CAL) into the QTC circuit. Data of forced triggers with zero input charge (PEDESTAL) can also be taken. As an ex-

[3] Application Specific Integrated Circuit

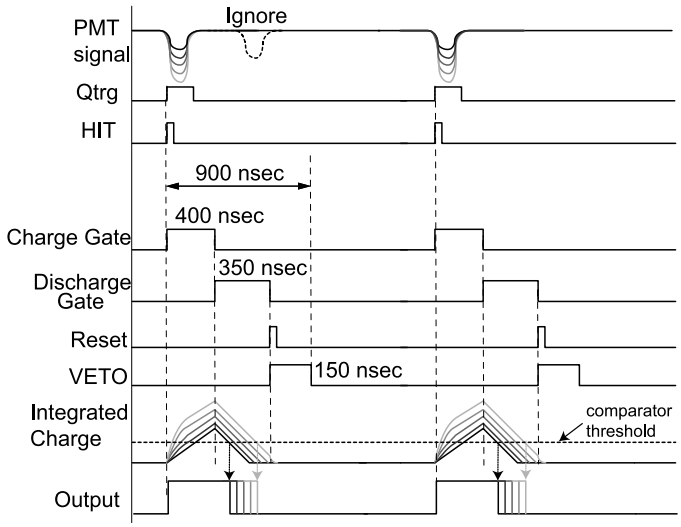

FIGURE 4.16: Diagram illustrating the operation of the QTC circuits which digitize the PMT pulses. Taken from (Nishino et al. (2009)).

ample calibration, the PEDESTAL data is taken periodically to provide information for correcting the QTC response for changes in the ambient temperature, which is known to have an effect on the circuit.

The QTC charge and time resolution are 10% and 0.3 ns, respectively. Both are are better than the intrinsic resolution of the PMTs (Nishino et al. (2009)).

Data Acquisition System (DAQ)

The Super-K front end electronics features a flexible DAQ capable of executing several programmable event triggers simultaneously. Compared to the previous system, the DAQ is capable of a larger dynamic range and higher data processing rate. The motivation for having multiple triggers stems from the different event trigger requirements for present and future neutrino studies. For example, to search for supernova relic neutrinos one needs to look for a neutron produced by the inverse beta decay reaction between a low energy relic neutrino and oxygen nucleus in Super-K. To tag these events one looks for the coincidence of the initial interaction with a low energy event produced by a 2.2 MeV gamma made by the capture of the neutron. The life-

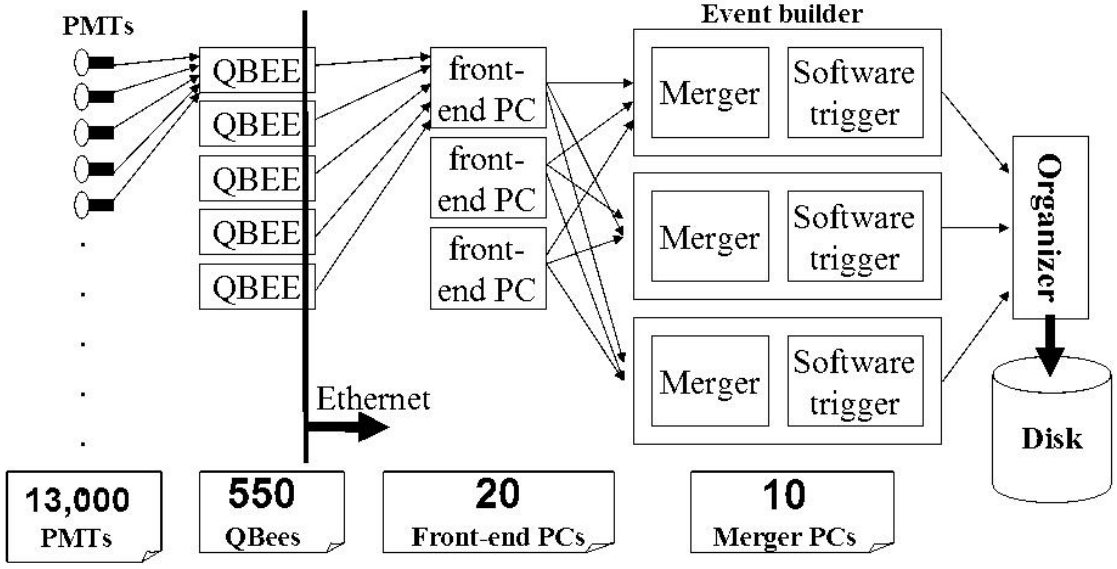

FIGURE 4.17: Diagram showing the organization of the online PCs which are responsible for turning a stream of digitized PMT hits into a single data stream of events. The events are defined by programmable software triggers that scan the data near the end of the data flow. Taken from (Yamada et al. (2009)).

time of this capture reaction is about 200 microseconds. Such a complex coincidence trigger is possible with the new DAQ.

The DAQ system begins with the front-end boards named the "QBEE" boards for QTC-based Electronic with Ethernet (Yamada et al. (2009)). Each QBEE houses 8 QTC chips and therefore provides a total of 24 input channels per board to monitor PMTs. The charge and time of output pulses from the QTCs are measured by a Time-to-Digital convertor (TDC) known as the ATM-3, originally developed for the ATLAS experiment (Arai (2005)). The QBEE collects the records of these hits and sends it via Ethernet to dedicated "online PCs" whose job is to merge the hit and charge information into one data stream.

The online PCs are organized into "Frontend" PCs, "Mergers", and a single "Organizer" (Yamada et al. (2009)). Figure 4.17 provides a schematic that traces the flow of data from the PMTs to the Organizer PC, which is the final stop for the

data before being saved to disk. The role of the Frontend PCs are to collect the hit information from a collection of QBEEs, sort them in time order, and then pass the hits to the Merger PCs. Each Merger PC collects data from all the Frontend PCs in order to merge and sort all the hits in the detector in a given time window. With the data on the full detector, the Merger PCs then apply the triggers programmed in the software to look for events. This data-intensive process is distributed over the cluster of Merger PCs.

There are several algorithms that scan the data for events. The most basic trigger sums up the number of hits within a 200 ns time window, and if the total exceeds a defined threshold, then a window around the hits are organized into an event (Yamada et al. (2009)).

The events observed by the Merger PCs are sent to the one Organizer PC. The Organizer collects the events from the Merger PCs in 22 ms long blocks with a 1 ms overlapping region between adjacent blocks to prevent losing events at the boundary. The Organizer scans the set of events and removes any double-counted events. The final set of events is then written to disk (Yamada et al. (2009)).

4.4.5 Detector Calibration

In this section, we briefly describe the different calibrations performed for the Super-K detector. This work is performed by the Super-K Calibration Group (of which the author is not a member). The calibration includes measurements of instrument performance and of physical constants used to validate and tune the detector simulation. For a more detailed description please see (Abe et al. (2014)).

PMT gain

Because of the large number of PMTS in the Super-K detector, over 13,000, it is simply not practical to calibrate each one individually. Also, it is important to have

methods that allow calibrations to be done while the PMTs are operating in the tank in order to have continuous monitoring and minimize downtime. Therefore, *in situ* techniques have been developed to measure the gain and quantum efficiency of the PMTs (Abe et al. (2014)).

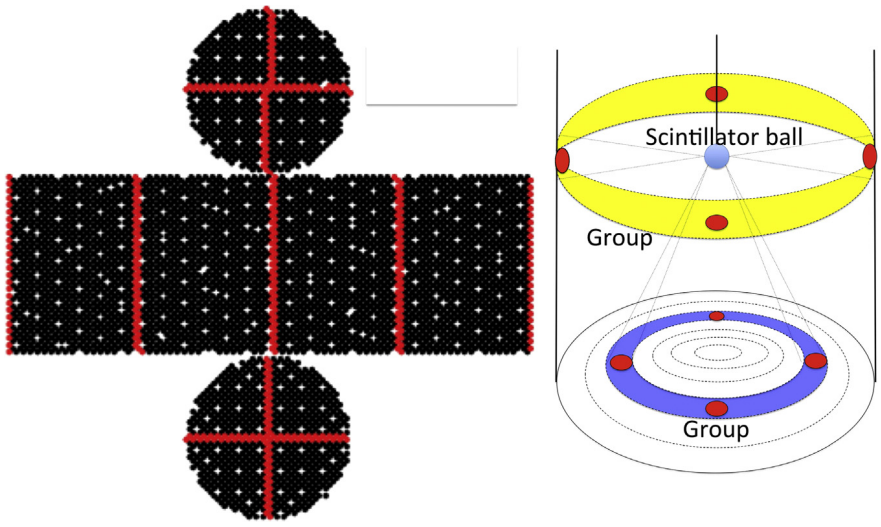

FIGURE 4.18: Left shows the position of "standard" PMTs in the Super-K detector. These are the 420 PMTs whose gains as a function of bias voltage have been measured externally. They act as the reference gains to which the other approximately 11,000 PMTs are calibrated. They are spread out in the detector in order to sample from the detector's different distances and PMT acceptances from a source placed at the center of the tank. The right plot shows how a set of standard and non-standard PMTs are grouped by the geometry relative to the source. The PMTs in each group are adjusted to have similar responses to the calibration source. Figure from (Abe et al. (2014)).

The PMT calibration starts with 420 "standard" PMTs whose gain were calibrated in an external, well-controlled setup before installation in the tank. During this "pre-calibration", the PMT gains as a function of bias voltage were measured. The standard PMTs then were placed in the detector in the arrangement shown in Figure 4.18. To set the initial biases for the PMTs, a scintillator ball capable of emitting light isotropically is lowered into the center of the tank. A relatively large signal is flashed at the PMTs, enough to ensure that about at least tens of photoelectrons are being measured by each PMT. The standard PMTs with their known

gain curves were set to give a uniform charge response after corrections were applied for attenuation, acceptance, and shape of the scintillation ball.

In order to measure the "gain", which in this particular context refers to the amount of charge produced per photoelectron, a method was employed that compared the amount of high and low-intensity light. For the high-intensity measurement, an expression for the charge observed by the PMT will be

$$Q_{obs} \propto N_{photons} \times QE \times g, \tag{4.8}$$

where $N_{photons}$ is the number of photons that strike the PMT, QE is the quantum efficiency, and g is the PMT gain. For the low-intensity measurement, the intensity of flashes from the scintillator ball is set low enough to ensure that for the relatively few PMTs (about 10%) that do see a hit, they see one photon. Such low-intensity measurements then are repeated and summed enough times that the total number of photons seen by each PMT is high. For the measurement of repeated low intensity flashes, the total number of hits observed can be expressed as

$$N_{obs} \propto N_{photons} \times QE. \tag{4.9}$$

Taking the ratio of the high to low-intensity measurement then gives us a measurement of the gain via

$$\frac{Q_{obs}}{N_{obs}} \propto g. \tag{4.10}$$

With these individual gain measurements, we then calculate the relative gain for each PMT defined as the ratio of the individual gain to the average gain of the all the PMTs. These ratios, which are a correction relative to an overall gain, are useful for applying tube-by-tube corrections to data and MC.

To use this relative gain, one needs to measure some sort of global, mean gain for the PMTs. To this end, a Ni+Cf source is lowered into the tank which emits

gamma of about 9 MeV into the detector. This is a low amount of light, so any PMT triggers seen will likely be from a single photoelectron. The amount of charge recorded by the PMTs, after repeated measurements, is averaged and a global gain of 2.658 pC/p.e. is defined. With the relative gain ratios, the gain for each PMT can be calculated.

In order to monitor the stability of the gain as a function of time, the PMT dark rates are used. These come from the spontaneous emission of an electron by the cathode. The peak charge produced by dark noise events is associated with the gain and, therefore, provides a way to regularly check the relative gain of each PMT without stopping the data taking in order to insert the scintillator ball or other source into the detector.

PMT quantum efficiency

The Ni+Cf source is used to make a measurement of the QE of each PMT. Recall that the expression for the number of events observed by a PMT at low-intensity light conditions, Equation 4.9, was only proportional to the number of photons arriving at the PMT times the QE. The primary difficulty of turning this into an exact expression is that the number of photons reaching the detector is a quantity dependent on water attenuation, reflection, and PMT acceptance. Therefore, MC simulations were used to predict the number of photons that reach the PMTs. With such a prediction, the QE can be extracted from the data. Because of the nature of this calculation the absolute QE has large uncertainties. Therefore, the QE for each PMT is normalized by the mean QE from all the PMTs in order to provide relative QE corrections.

One might have noticed that the definition of QE used in the previous section differs from the exact definition which pertains to the photocathode performance. Above, the QE is simply the probability that a photon hitting the PMT produces a photoelectron. This in principle is a mixture of the QE along with quantities like the

transmission through the glass or the collection efficiency, which is the probability that an electron freed from the cathode arrives at the beginning of the dynode chain.

PMT timing

The time response of the various PMTs is expected to vary. This is due to several factors such as different cable lengths, differing performance in readout electronics and characteristics to individual PMTs. Furthermore, the rise times of pulses are expected to vary depending on the intensity of the light. Therefore, each PMT's timing response is measured and is recorded as a function of the pulse size in units of charge. The measurement is made using a "diffuser" ball that is lowered into the middle of the tank. Laser light is injected into the ball which then diffuses it in all directions in the tank. The timing between the laser pulse and the PMT signals are measured for varied amounts of light injected into the ball. This produces a measurement of the relative time versus charge for each PMT, a function known as the 'TQ Map'. Figure 4.19 shows an example map. For more details, please refer to (Abe et al. (2014)).

Photon propagation in water

Many components of the analysis and simulation at Super-K rely on having an accurate description of the propagation of photons through the Super-K water. For example, corrections in the PMT charge are needed to account for light attenuation when calculating an expected hit pattern for particle reconstruction. Therefore, measurements are made to check these models and extract important constants. These constants also serve as a monitor for changes in the water quality as a function of position and time.

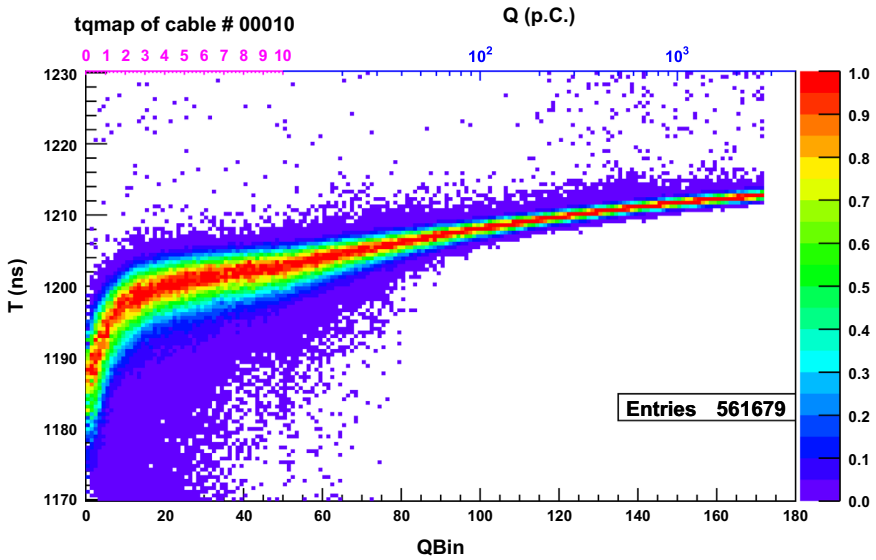

FIGURE 4.19: An example of a 'TQ Map' function for an ID PMT. The timing response of the PMT as a function of pulse size in units of charge is a part of the Super-K calibration measurements. Figure taken from (Abe et al. (2014)).

4.4.6 Simulation of the Super-K Detector Response

A detailed simulation of the particle physics and electronic response of the Super-K detector was build based on CERN's GEANT3 simulation package (Brun et al. (1987)). The simulation includes descriptions of the tank, the different black sheets and Tyvek® lining the walls and scaffolding, and the PMTs with a description of their acrylic/FRP shields. The package also includes several custom models for

- muon decays;
- low-energy pion interactions tuned to external data;
- Cherenkov light generation;
- Raleigh scattering, Mie scattering, and absorbtion of Cherenkov light in the water;
- reflection of Cherenkov light off of the different materials in the detector such as acrylic and Tyvek®;

- PMT electronics response; and
- a full event trigger system.

The calibrations of the PMT response and water scattering parameters provide measurements which are used to tune SKDETSIM. As will be described later in Section 4.4.9, the simulation is used to extract information for the accurate reconstruction of particle tracks. This includes, for example, tables of the expected charge seen by the PMTs for Cherenkov rings due to muons and electrons. For electrons, these tables are central to the reconstruction of the momentum and for particle identification. The simulation also provides the expected distribution of light in the PMTs due to scattering which is a necessary input for recontructing both muons and electrons in the detector.

Because of the importance of the simulation, the ability of skdetsim to describe various calibration samples is quantified and regularly monitored.

4.4.7 ID Energy Scale Calibrations

The energy calibration of the simulation of the Super-K detector is performed through the data and MC comparison of four data samples, which a span a range of energies:

1. Michel electron spectrum: This sample is composed of decay electrons left from cosmic ray muons that stop in Super-K and covers a range of particle momentum below ≈ 60 MeV/c. We used the sample of cosmic rays collected in the month of April 2009. The comparison between the peak of the data and MC distribution gives an error of $-0.7 \pm 0.2\%$.

2. π^0 invariant mass distribution from atmospheric ν neutral current interactions: This sample is composed of 2 electron-like rings from the entire Super-K I-IV atmospheric neutrino sample. The invariant mass distribution is calculated in which a peak is seen between 85 and 185 MeV/c^2. A comparison of the position

of the peak (found by using the mean of fitted a gaussian distribution) between data and MC gives an error $0.5 \pm 0.7\%$.

3. sub-GeV stopping muons: This sample is composed of cosmic ray muons that stop in the Super-K detector and have a momentum of 200 to 440 MeV/c. We use the whole Super-K IV data set for the sample. The comparison between the data and MC energy scale is made comparing the distribution of momentum as calculated by the reconstructed Cherenkov angle of these tracks. At these low energies, the angle will change as a function of the muon momentum and can therefore be used as a check of our simulation's reconstruction which is done by the amount of photoelectrons seen. Events are binned by the angle-derived momentum and the ratio between the momentum calculated by the angle to the momentum calculated by the number of photoelectrons is calculated for each event. The mean of these quanties for each bin is compared between data and MC. The uncertainty derived in this fashion ranges between 0.6 ± 0.3 and 2.4 ± 0.3.

4. multi-GeV stopping muons: This sample is composed of cosmic ray muons that stop in the Super-K detector and have a momentum above 1.0 GeV/c. The muons used for the uncertainty estimate were collected in the month of April 2009. The ratio of the momentum to the track length was compared for data and MC for six subsamples divided by the distance traveled in the detector, a quantity proportional to the momentum of the muon. A difference of $-0.2 \pm 0.3\%$ to $1.3 \pm 0.3\%$ was measured.

A summary of these calibrations are shown in Figure 4.20. The largest observed disagreement between all the measurements is 2.4%. This uncertainty is used as the energy-scale uncertainty in analyses using the Super-K data.

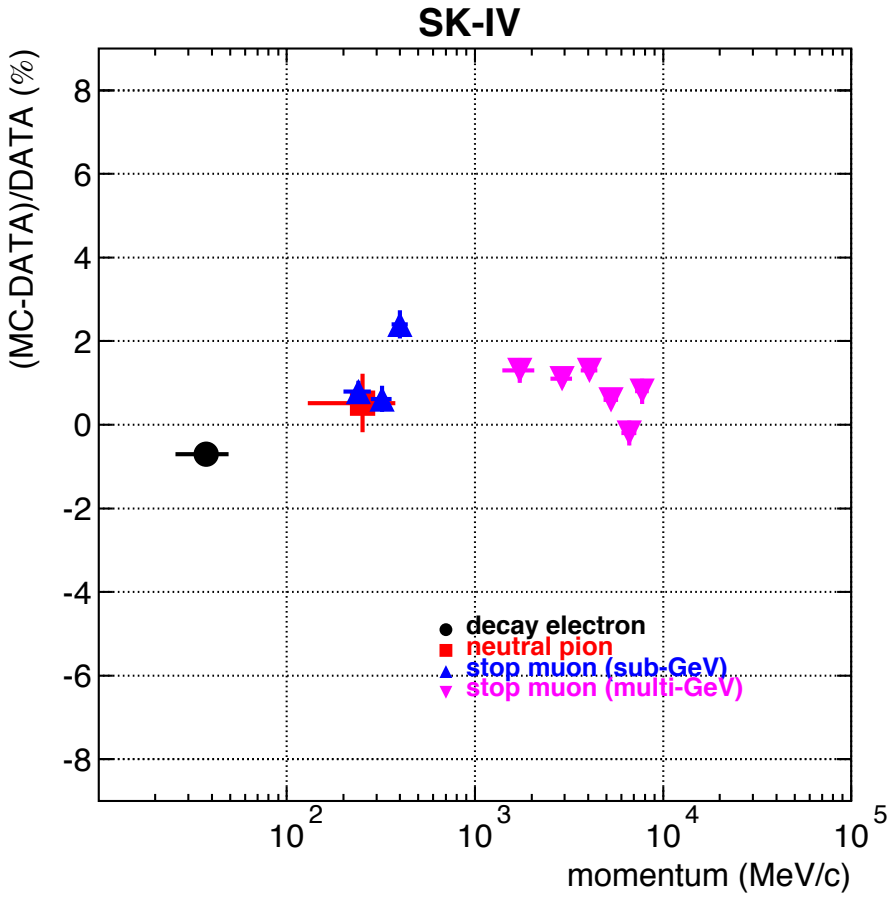

FIGURE 4.20: Comparisons betwen data and MC used to estimate the error in the energy calibration of the simulation of the Super-K detector. From (Abe et al. (2011b)).

4.4.8 OD Energy Scale Calibration

In the same spirit as the ID energy scale calibration, we check the OD response at low energies using the Michel electron spectrum. (Please note that this work was performed by the author.) Decay electrons are selected from the cosmic ray muon events through the following criteria:

1. We select cosmic ray events with light in both the ID and OD. For the OD, we require that there be two clusters of hits. The aim of this criterion is to select cosmic ray muons traveling across the ID and OD.

2. The ID PMT hits are used to reconstruct the direction of the muon, which we then use to determine the point in the OD where the muon exits the ID. For the cluster of OD hits at the exit point, we select events with small OD exit clusters. The aim is to pick muon events which might have stopped in the OD.

3. From this sample, we then check the OD for a cluster of hits greater than 5 that occur in the region of the exit cluster that occur at least 2.5 microseconds after the muon. The veto time is allowed to let the PMTs in the region return to baseline.

4. We also omit events that find a spike of activity between 5 microseconds and 8 microseconds after the initial trigger. This activity is thought to be due to after-pulses in the PMT.

We apply the selection to the current Super-K data-taking period known as SK-IV. The data sample processed ranged between the start of SK-IV (fall of 2008) and the end of September (SK run number 71909). This simple selection produces 12,266 events. Figure 4.21 plots the time of the candidate Michel electron after the initial trigger. A fit to this distribution gives a lifetime of about 2.0 microseconds, close the expected muon lifetime. Note that the stopped muons in this sample will be a mixture of μ^+ and μ^-. In fact, the measured μ^+/μ^- ratio is 1.37 (Yamada et al. (1991)). Also, the expected μ^- lifetime is expected to be lower, 1.7954 ± 0.002, due to the possibility for muon capture on oxygen (Suzuki et al. (1987)). Therefore, we expect a slightly lower muon lifetime to be measured.

In order to check the MC energy scale calibration of the OD, a simulation of Michel electron events in the OD was made. The simulation generated 10,000 μ^+ and 10,000 μ^- at rest and positioned them uniformly in the detector. The 1.37 μ^+/μ^- ratio is then applied by weighting the μ^- events. Therefore, the events in the

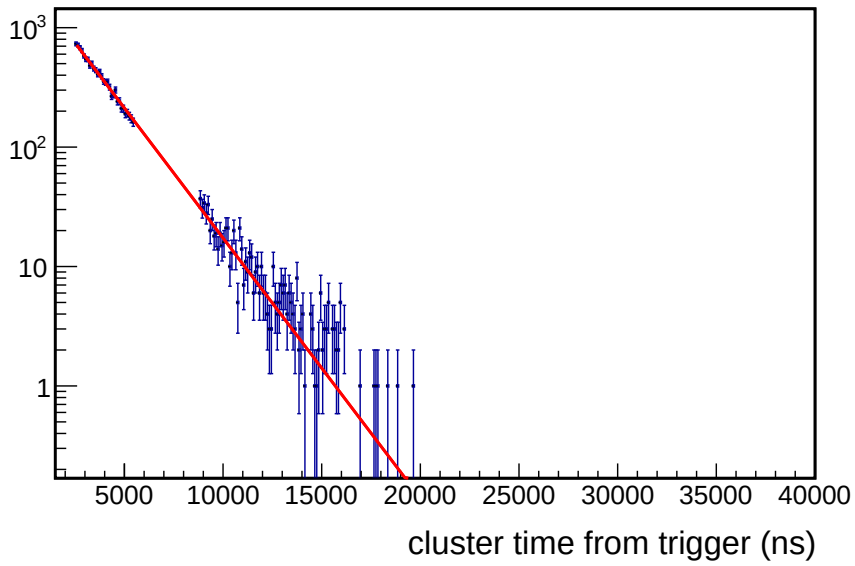

FIGURE 4.21: Time between an initial cosmic ray muon event and the time of a cluster identified in OD near where the muon exited the ID and entered the OD. The events are candidate Michel electrons that deposited energy in the OD. The selection for the events is described in the text. The fitted lifetime of the distribution is 1.99 ± 0.02 μsecs which is close to the expected muon lifetime.

simulation need were further reweighted in order to account for selection biases in the data set.

The first adjustment was for the bias for finding events in the lower half of the detector. This is due to the fact that cosmic ray muons seen at Super-K will be mostly downward going. Therefore, the MC was reweighted to match the distribution of events as a function of position as observed in the data sample. The second adjustment is meant to correct for the fact that the selection chooses muons which are still above Cherenkov threshold when they exit the ID and OD. That means that the position of the Michel electron will not be uniformly distributed in the OD but will have a bias towards the outer wall. For now, a simple cut is made in the MC to remove Michel electrons created closer than 25 cm to the inner OD wall. This approximately accounts for the distance covered by the muon after it

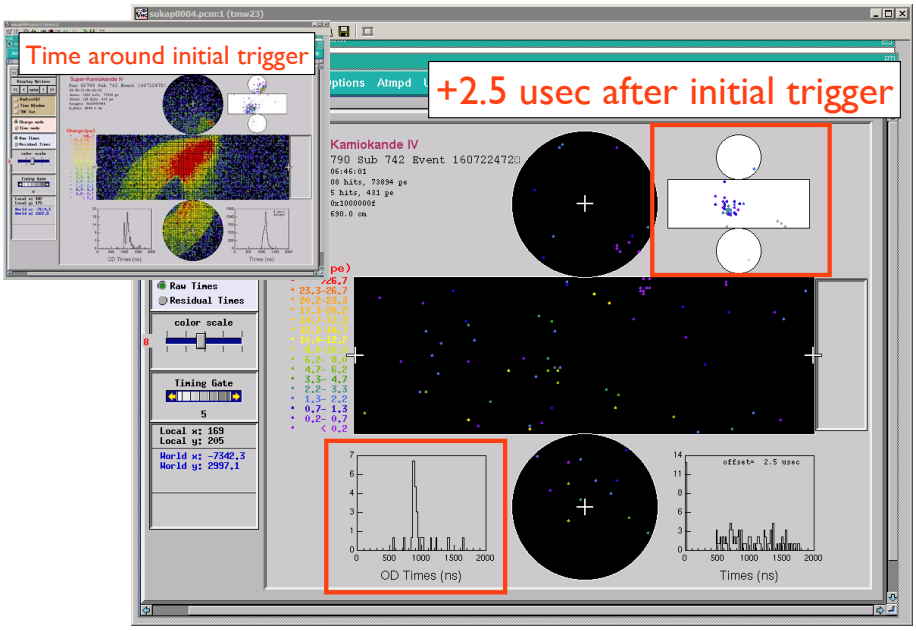

FIGURE 4.22: Super-K data event display for an example candidate Michel electron found in the OD. The initial through-going cosmic ray muon event is shown in the inset in the upper left. The event display shown in the center of the display presents the hits seen 2.5 μs after the initial trigger. In the upper right inset, a cluster of light in the OD can be seen from a candidate a Michel electron. The electron produces a spike of hits some time after the initial trigger which is highlighted in the lower right inset.

has stopped producing Cherenkov photons, assuming it continues to be minimally ionizing. However, this is not correct. Therefore, one place to improve this energy-scale check is to better account for the position bias. One way to do this is to generate muons on the inside surface of the inner wall with a range of momentum and apply the selection in order to mimic this bias.

After the corrections to the MC for the two selection bias, distributions of the charge and number of hits are compared for data and MC. For both distributions the mean of the data is higher than the MC. For the hits, it is about 7% and for the

charge it is 10%. The comparison is shown in Figure 4.23.

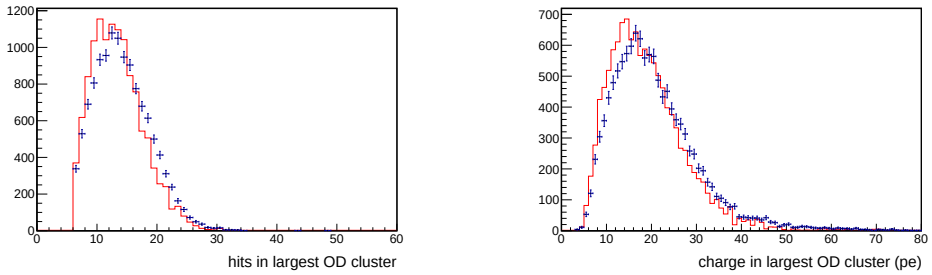

(a) Hits in the OD due to Michel electrons for data (black) and MC (red).

(b) Charge in the OD due to Michel electrons for data (black) and MC (red).

FIGURE 4.23: Result of OD energy scale measurement. The charge and hits distribution due to Michel electrons is higher for the data than MC. The mean of the data is higher by 7% for the hits and for the charge by 10%.

Using the MC truth information, we can get a couple of interesting numbers about the OD threshold. At 30 MeV, the detection efficiency is at 50%. The efficiency reaches 0% around 20 MeV. Note that the selection imposes a five-hit threshold.

4.4.9 Particle Reconstruction

The patterns of hit and charge recorded by the PMTs in the ID provide enough information to reconstruct the momentum of charged particles that travel through the ID of Super-K. What allows this is the characteristic emission pattern and flux of Cherenkov radiation which is highly correlated with both the momentum of the particle. The radiation emission pattern can also be used to distinguish between heavy, minimally ionizing particles, such as muons, and those that shower, such as electrons.

The Super-K reconstruction is performed in stages with the information from one stage informing the next. In the first stage, the interaction vertex is established. Next, the initial vertex anchors the search for one or more rings of hits. Third, for each of the rings found, a determination is made as to whether the rings are

muon-like or electron-like. Finally, the momenta of particles that made the rings are estimated using the pattern of hits. The momentum assigned depends also on the type of particle, muon or electron, is assumed responsible.

Note the description of the algorithm that follows, the names of the Super-K functions are inserted in brackets as documentation.

Vertex fitter

The vertex algorithm [`tfafit`] starts by first assuming that the hits seen by the PMTs all comes from one point. Under that assumption, the estimated time of the interaction can be calculated for each PMT by subtracting the photon time-of-flight from the hit time. A histogram is then made of the estimated interaction time for all hits. The initial vertex is chosen [by `tfpof2`] to be the position that maximizes the goodness function [calculated by `tfgoodne`] composed of a Gaussian function centered at the peak of the estimated interaction time distribution with sigma of 1.5*(2.5 nsec), which accounts for the time resolution of the PMTs. From this initial vertex, an initial direction is estimated by taking the charge-weighted sum of the direction vectors formed by the vertex to each PMT position [`tfpofdir`].

Once the initial vertex is estimated, a two-step algorithm is performed to find the best fit:

Ring Edge Fit: This algorithm [`tfgetdir`] fits for the best particle track direction using expected Cherenkov angles. First, the track direction is varied around the input direction. Next, the charge is binned in a histogram as a function of angle away from the new varied direction. From this, the angle is found that is at the peak of the charge vs. angle distribution [`tfang`] and compared to the expected angle for muons and electrons. The new direction is chosen to be the direction that best matches these angles [`tffixdir`].

Track Fit: Using the optimized direction, this algorithm [`tftdcfit`] finds the best vertex by fitting the PMT hits assuming that the light was produced along a charged particle track. The best vertex is found by maximizing a goodness function [`tfgoodn7`] that compares the distribution of the estimated interaction time to a Gaussian.

These two steps move the vertex to best fit the hits. It is repeated until the distance the vertex is moved falls below a threshold.

Ring counting algorithm

The algorithm [`rirngcnt`] that identifies the pattern of rings in the PMT hits is based around a Hough transform, which in effect transforms the search for rings into a search for peaks. The transform exploits the characteristic Cherenkov angle.

Consider trying to find a circle of known radius in a pattern of hits on a 2D plane. If at each hit, one draws a virtual circle around each hit, the virtual circles will intersect all at a common point. Figure 4.24a demonstrates this principle which guides the ring-finding algorithm.

The Super-K Hough transform implementation [`rimakeqmap2`] bins the location of such virtual circles on a (ϕ, θ) plane where the detector's geometry sets the axes. The virtual rings are drawn around each PMT hit, assuming a 42° Cherenkov cone. Each virtual ring is given a weight based on the charge of the PMT hit. Figure 4.24b shows an example of a transform. The peaks in this (ϕ, θ) are identified.

The algorithm then proceeds iteratively in order to look for numbers of rings. A likelihood is calculated for each set of N rings found. The search then looks for $N + 1$ rings. The likelihoods of the N and $N + 1$ ringed pattern is compared. If the $N + 1$ likelihood is greater, the iteration is continued. The ring counting stops once the $N + 1$ ringed likelihood is less than the likelihood for N rings.

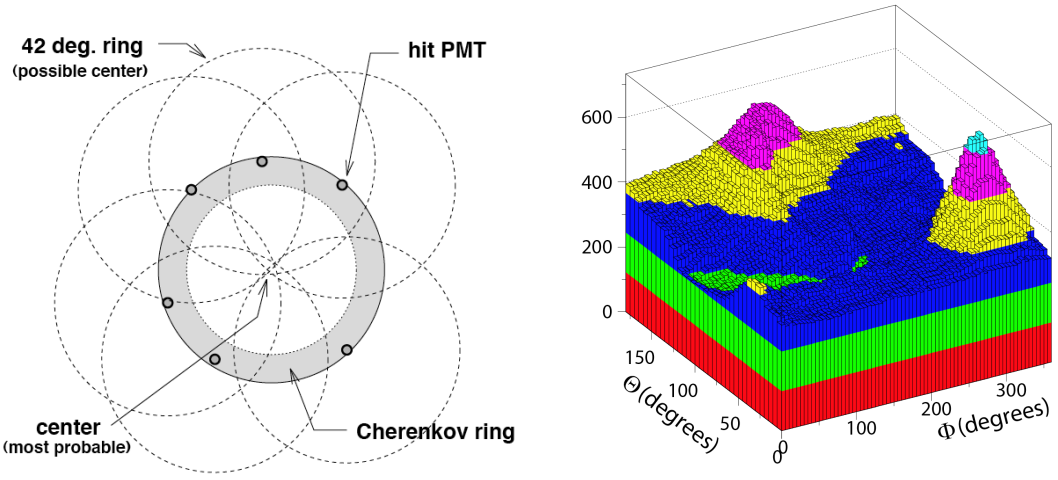

(a) Schematic of Hough transform (b) Example output of transform

FIGURE 4.24: Figures illustrating the implementation of the Hough transform method used in the ring-counting algorithm of Super-K. Figures taken from (Mituska (2009)).

Particle identification

For each ring, the particle identification algorithm [`sppatid`] decides if a ring is more muon-like or more electron-like based on the principles discussed in Section 4.4.1. The basic strategy is to compare the PMT hit charge in the ring to the expected charge distribution for a muon and electron hypothesis which is sharper or fuzzier, respectively. Figure 4.25 provides examples. When multiple rings have been found, the PMT hit charge is divided among the overlapping rings.

The expected muon distribution is based on an analytical expression for the expected charge seen at each PMT. Corrections are made for the PMT acceptance, expected charge due to scattering, and the attenuation length in the water.

The expected electron distribution is based on MC simulations. The expected amount of charge seen at 16.9 m from a test vertex is tabulated from simulations of electrons that were run with a momentum of 100, 300, and 1000 MeV. The charge expected at each PMT is then extrapolated using these tables taking into account

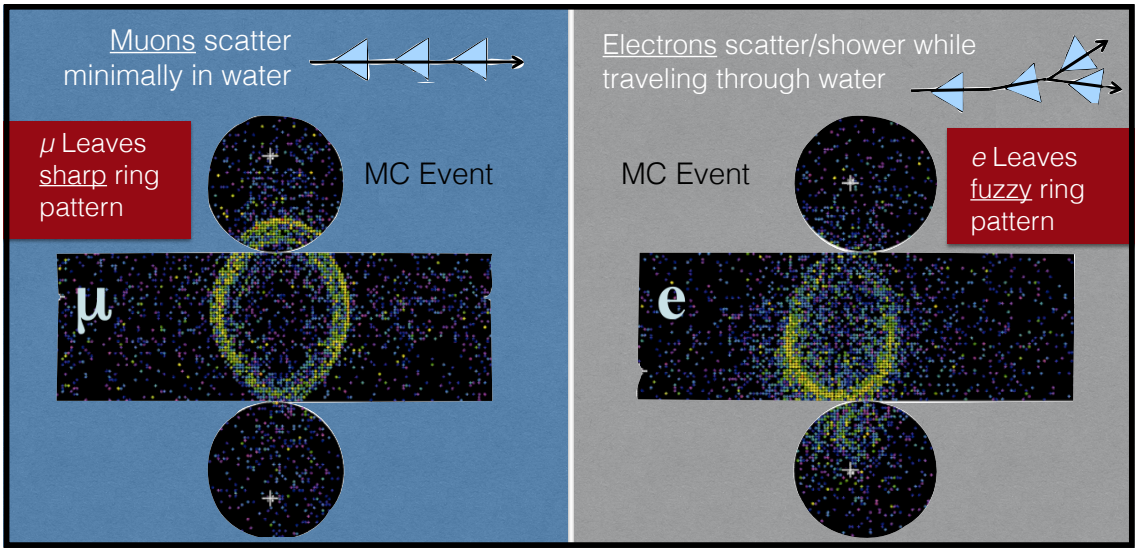

FIGURE 4.25: Event displays from MC which provide an example of the PMT hit pattern from a muon and electron. The color of the PMT hits indicates the charge (with red being the largest, black the lowest). Muons make sharp rings. Electrons leave a fuzzier pattern in comparison.

the attenuation length of the water. The expected charge due to scattering is also added to the expectation.

The particle identification decision comes from a likelihood ratio based on these expected charge patterns. For single rings, a likelihood based on the measured Cherenkov angle of the observed ring is also taken into account. When multiple rings were found, only the pattern comparison is used.

Momentum assignment

Once a set of rings has been identified along with the direction of their track and their assigned particle ID, the momentum associated to the track is determined. The determination [by `spfinalsep`] comes from the amount of PMT hit charge contained in a 70° cone around the track direction. Hits that are situated in overlapping cones are split among the rings as was done for the ring counting algorithm. The timing of the PMT hits is used as well. PMT hits are assigned to each ring only if the expected and measured time of the hit falls within -50 and +250 ns.

The observed charge is corrected by a number of detector parameters. These include the light attenuation in the water, the PMT acceptance of photons as a function of incidence angle, the PMT gain, and water scattering. These parameters are measured periodically through the calibrations described in Section 4.4.5.

Once the corrected observed charge, called RTOT, for each ring is calculated, the momentum of the track is assigned [in `ptamos70`] using a table that relates average RTOT observed to a momentum depending on the particle type. This table is computed using the MC simulation of the detector. The accuracy of this conversion is checked in several ways as described in Section 4.4.7 on the ID energy scale calibrations.

4.4.10 Global Position System (GPS) Timing

The synchronization between the three different components of the experiment is important. Because the T2K experiment uses a self-created source of neutrinos, the timing of the beam can be exploited to help improve the rejection of non-beam neutrino events at the detectors. The experiment uses a common-view GPS system to synchronize the time between the beam and the detectors. J-PARC provides a trigger to the detectors notifying them of a beam spill. The GPS system is used to assign the correct times to these beam triggers.

At Super-K, any hits 500 μs around the beam trigger are tagged as T2K data. Later, tighter cuts are used to pick out T2K neutrino events at Super-K. The tighter cuts takes into account possible delays between the time the neutrino interaction occurs and the time the event trigger is activated. These delays are measured and are due to electronics and signal propagation times through the PMT cables (Iyogi (2011)).

5

Measuring ν_μ Disappearance

In this chapter, we describe the measurement of neutrino events by the T2K experiment, which was designed to measure muon neutrino disappearance by comparing the muon neutrino beam before and after oscillations have occurred. Note that all of the neutrino interactions seen in the near and far detector are not used in our analysis. We choose a subset of neutrino interactions that best suits the method of our analysis and current understanding of the detector systematic uncertainties.

Our analysis measures muon disappearance in the framework of the standard three-flavor neutrino oscillation model. Therefore, we are interested in the values of the PMNS neutrino parameters, $\sin^2(\theta_{23})$ and Δm^2_{32}, which in this framework have the greatest effect on the probability of muon neutrino disappearance. To this aim, we compare the muon neutrino energy spectrum at Super-K with our prediction, which depends on the oscillation parameters. This strategy requires two things: (1) we select the type of neutrino interactions at Super-K with the most reliable energy measurement and (2) we use a measurement of the neutrino interaction rate at ND280, particularly of the interaction types seen at Super-K, to make an accurate

prediction of the spectrum. In what follows, we describe the selection of neutrino events at the near and far detectors which were used in our analysis. The analysis will be described later in Chapter 6.

5.1 Neutrino Events at the ND280

The neutrino events from the near detector measurement of the flux are inclusive ν_μ charged-current events. Such events must contain at only one identified μ^- track but may also contain any number of tracks from other types of particles. The preparation and study of the ND280 data for the T2K collaboration was done by the ND280 working group (Bojechko et al. (2013)).

In order to produce the cleanest sample, the selection started by choosing events where the μ^- originates in the fiducial volume of the most upstream FGD. Cuts were made to ensure that this initial sample did not contain multiple muons or muons that originated from outside the ND280 detectors.

The sample is then split into three sub-samples based on the number and type of tracks seen in addition to muon:

1. Charged-current 0π events
2. Charged-current $1\pi^+$ events
3. Charged-current other events.

Figure 5.1 shows an example event for each of three event types listed. The selection for each type is described below.

5.1.1 Charged-current 0π ($CC0\pi$) Selection

For this sub-sample, various particle identification algorithms for each of the ND280 sub-detectors were utilized to reject events if any particles beyond the single muon

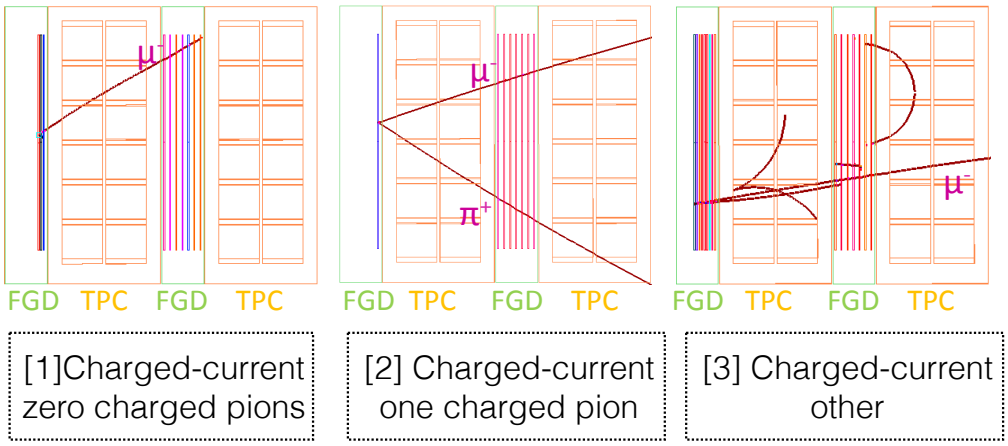

FIGURE 5.1: Examples for the three event types selected at ND280 for the muon disappearance analysis. The first (left) is an example of a charged-current zero pion event. The second (middle) is of a charged-current one pion event. Finally, the remaining events observed are classified as a third type, charged-current other.

was identified. In the TPCs, routines were used to reject events with $\pi^{\pm}$ and $e^{\pm}$ tracks. For the most upstream FGD, a search was conducted for Michel electrons and πs. If none of these tracks and signatures were found, a charged-current event passed into this sample.

5.1.2 Charged-current $1\pi^+$ ($CC1\pi^+$) Selection

The selection for this sub-sample looks for exactly one π^+ created in conjunction with the μ^-. A π^+ track is identified in three different ways. The first is through a track with positive curvature traveling through the FGD+TPC. The charge deposited as a function of track length was used to tag tracks as coming from charged pions. The second method is to look for tracks contained in the FGD (not from the μ^-, of course) that are consistent with energy deposition by a pion. Finally, if no other tracks were seen beside the μ^-, but the signature of a Michel electron was seen in the FGD, the event was considered to be from a stopped π^+ in the FGD that converted into a μ^+ and eventually an electron. π^- were rejected through the curvature of an FGD+TPC track. Events that likely contained a π^0 were rejected by looking for an

electron and/or position track in the TPC separated from the interaction vertex in the FGD.

5.1.3 Charged-current Other (CCother) Selection

The remaining charged-current events not classified as CC0π or CC1π^+ are collected in this sub-sample.

5.1.4 Interaction Types

The charged-current events were subdivided into three samples so that ND280 provided information on not only the muon neutrino flux but also on the types of neutrino-nucleus interactions we expect to measure at the Super-K detector. The CC0π sample isolates charged-current quasi-elastic interactions (CCQE), CC1π^+ aims to isolate charged-current resonant production of pions, and the CC other sample as a result will contain information on higher energy interactions such as deep inelastic scattering. The definition and significance of these interactions will be discussed later in more detail in Chapter 6. This discussion includes in Section 6.7 how the ND280 data sample is used in the measurement of the muon neutrino disappearance parameters.

5.1.5 ND280 Data

The charged-current inclusive events described above are binned by the μ^- momentum and track angle with respect to the beam. These distributions are used in the muon neutrino disappearance analysis to provide a measurement of the rate of neutrion interactions before oscillations. This measurement provides the analysis corrections and constraints on the flux from and neutrino interaction models that depend on external measurements. (The models are desribed later in Chapter 6.) Figure 5.2 shows the data for CC0π events, Figure 5.3 for CC1π^+, and Figure 5.4. In all the figures, the data are shown along with a stacked histogram of the predicted

number of events broken down by neutrino interaction type. These interaction types will be discussed later in Chapter 6.

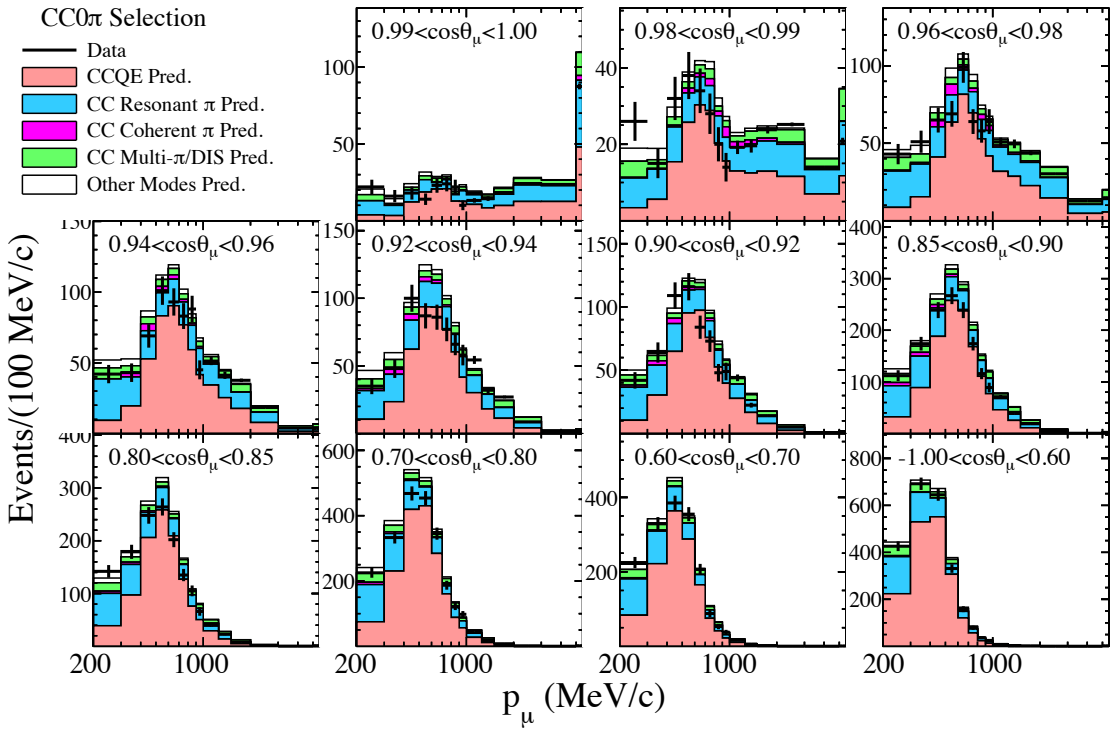

FIGURE 5.2: Data and MC distributions of CC0π events observed at the ND280 complex. Figure by M. Hartz.

5.2 T2K Neutrino Events at Super-K

We use the reconstructed energy spectrum of T2K neutrino events at Super-K for the measurement of neutrino oscillations. The particular events used in the analysis are a subset of all observed T2K neutrino events at Super-K and come from a so-called "golden interaction channel" known as charged-current quasi-elastic (CCQE) events. The interaction channel gets this designation because the selection and reconstruction of these neutrino interactions are well understood and well characterized.

The CCQE channel consists of the following interaction

$$\nu_l + n \rightarrow l^- + p, \tag{5.1}$$

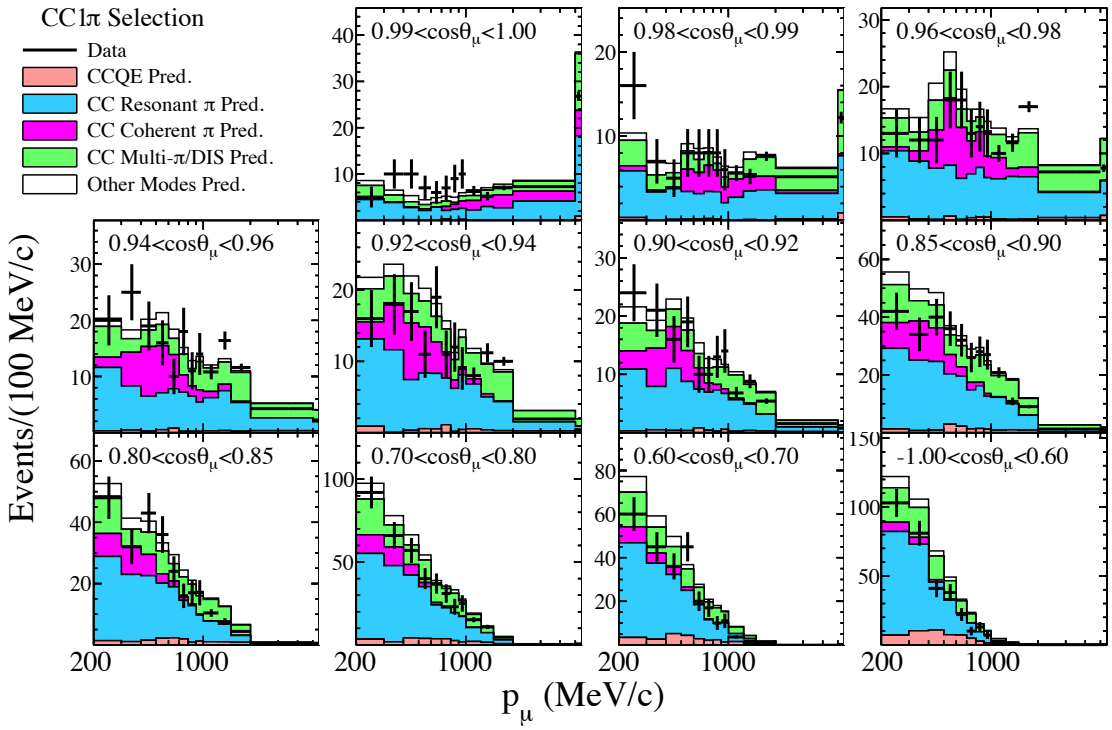

FIGURE 5.3: Data and MC distributions of CC1π^+ events observed at the ND280 complex. Figure by M. Hartz.

where ν_l is a neutrino with flavor, l, n is a neutron, l^- is a lepton of flavor, l, and p is a proton. There are two advantages of using this interaction channel. The first is that the outgoing charged lepton is observable, and, because the interaction is elastic, the incoming neutrino's energy can be calculated using the momentum of the observed lepton and knowledge of the incoming neutrino direction. (The interaction is considered "quasi"-elastic because the incoming and outgoing particle changes from a neutrino to a lepton.) The second advantage is that the flavor of the observed lepton allows us to infer the flavor of the neutrino. Together, these two features allow us to measure the reconstructed energy of muon neutrinos interacting in Super-K.

The formula used to infer the reconstructed neutrino energy, $E_\nu^{\text{recon.}}$, from the

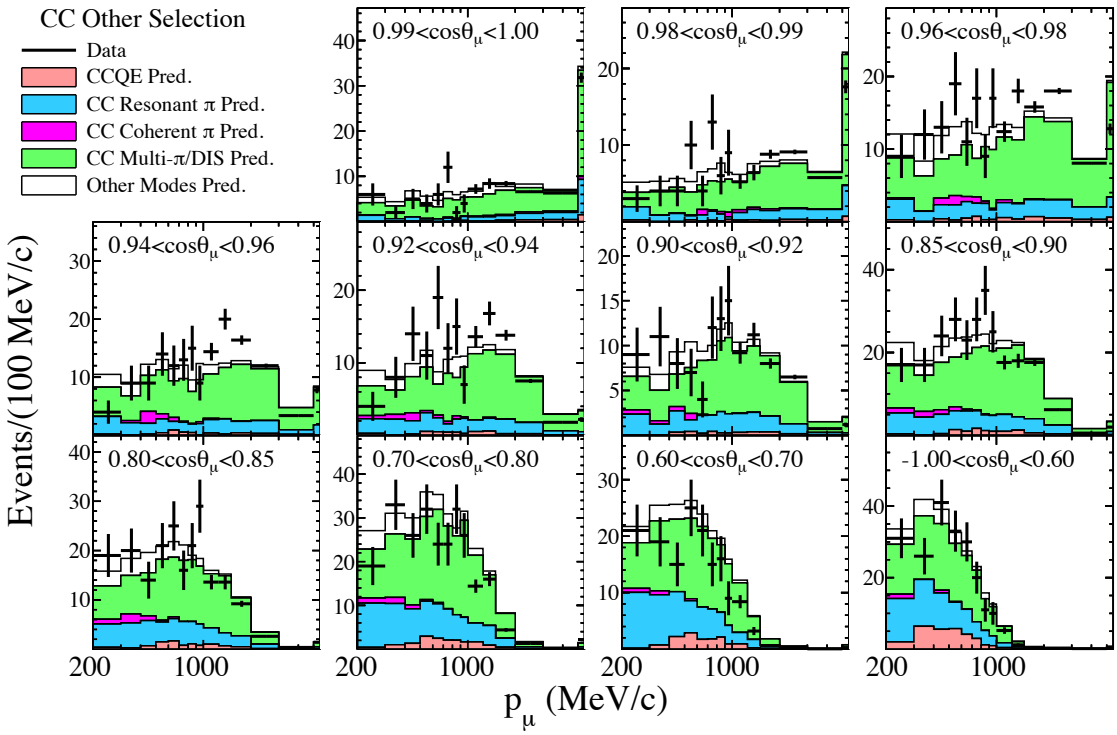

FIGURE 5.4: Data and MC distributions of CCother events observed at the ND280 complex. Figure by M. Hartz.

observed muon is

$$E_{\nu}^{\text{recon.}} = \frac{m_p^2 - (m_n - V_{nuc})^2 - m_\mu^2 + 2(m_n - V_{nuc})E_\mu}{2(m_n - V_{nuc} - E_\mu + p_\mu \cos\theta_{\text{beam}})} \tag{5.2}$$

where m_n is the mass of the neutron, m_p is the mass of proton, m_μ is the mass of muon, V_{nuc} is the nuclear potential (27 MeV for oxygen), E_μ is the energy of the muon, , p_μ is the momentum of the muon, $\cos\theta_{\text{beam}}$ is the direction cosine between the direction of the track and the beam direction.

As one can see from Equation (5.2), all that is needed to infer the energy of the neutrino is the momentum of the single out-going lepton. This means that for our analysis, we will want to select from the neutrino events observed at Super-K ones with only a single muon present.

The CCQE events are selected using the following criteria:

In-time the neutrino interaction occurs in coincidence with the firing of the T2K neutrino beam,

Quality the beam monitors and near and far detector status are normal, data quality is good, the PMT hits at Super-K pass a minimum threshold in observed light

FC observe a total number of outer detector hits below threshold, or are "fully contained (FC)" events in the inner detector,

FV are only in the fiducial volume of the inner detector, or are "fiducial volume (FV)" events,

1-ring the event contains a single-ring,

μ-like the single ring is identified as more μ-like than electron-like,

Momentum have a reconstructed momentum is greater than 0.2 GeV/c, and

Decay-e have no more than one observed decay electron.

The tools needed to calculate the quantities used in the selection of one-ring μ-like events are well-developed and understood. Furthermore, the reconstructed momentum of muons in the detector is accurate and well studied. The selection gives us an energy spectrum whose shape and amplitude we can use to produce a precision measurement of the neutrino oscillation parameters. As mentioned above, the aim of this selection is to isolate CCQE interactions. However, this selection will also select non-CCQE interactions as well.

The backgrounds that enter into our observed CCQE-like sample are those whose interactions can also produce a single track that looks muon-like to our particle identification algorithms. An example includes a NC interaction that produces a

charged pion. Because of their similar mass to a muon, charged pions are mostly indistinguishable from muons. Charged-current interactions which produce both a muon and a charged pion can also enter in our sample when the pion is absorbed in the nucleus or is created below Cherenkov threshold. These interactions are not background in the sense that they too will undergo oscillations. However, we attempt to minimize their presence in the sample because they cause distortions in the energy spectrum that can bias the extraction of the oscillation parameters. Therefore, an accurate model of these interactions and the quantification of our uncertainty in our model is important in making an accurate measurement. One of the primary charged-current modes that will produce a pion in the energy range of the T2K beam is resonant production. This is the type of interaction that the ND280 CC1π^+ sample attempts to isolate.

5.2.1 Events Observed

In Figure 5.5, distributions for the variables used in the selection are shown for the data and MC after the first cut for fully contained events in the fiducial volume (FCFV).

Table 5.1 shows the number of events observed at each step of the data selection. The table also shows the predicted number of events with oscillation assuming a value of $\sin^2(\theta_{23})$ =0.5 and Δm^2_{32} =2.5 $\times$ 10^{-3} eV^2/c^4. The final number of CCQE-like events that pass all the criteria is 120.

As stated, the target interaction channel is CCQE from muon neutrinos. However, there are other interaction channels which also enter as backgrounds. Table 5.2 shows the expected breakdown of modes assuming no oscillations and oscillations with $(\sin^2\theta_{23}, \Delta m^2_{32})$ = (0.5, 2.4 $\times$ 10^{-3} eV^2/c^4).

Table 5.1: Summary of events passing each selection for CCQE-like events. The MC expectation assuming oscillations with the parameters $(\sin^2\theta_{23}, \Delta m^2_{32}) = (0.5,\ 2.4 \times 10^{-3}\ \mathrm{eV}^2/\mathrm{c}^4)$. The parameter values are the measured ones but are chosen to provide a rough estimate of the expected events. They are based on the previous T2K numu disappearance ananlysis.

Selection Step	Data	MC with oscillations
FCFV Events	377	372.35
Single-ring μ-like events	193	198.44
$p_\mu > 0.2$ GeV/c	133	143.99
$N_{\mathrm{decay-e}} \leqslant 1$	120	125.85

Table 5.2: Breakdown of final CCQE-like event sample based on interaction channels.

Selection Step	MC Expectation				
	Total	$\nu_\mu + \bar{\nu}_\mu$ CCQE	$\nu_\mu + \bar{\nu}_\mu$ CCnonQE	$\nu_e + \bar{\nu}_e$ CC	NC All
FCFV Events	372.35	85.55	162.20	41.58	83.02
Single-ring μ-like events	198.44	80.57	61.87	32.54	23.46
$p_\mu > 0.2$ GeV/c	143.99	78.84	57.77	0.35	7.04
$N_{\mathrm{decay-e}} \leqslant 1$	125.85	77.93	40.78	0.35	6.78

5.3 Observed Neutrino Energy Spectrum

The observable used in the analysis is the reconstructed neutrino energy spectrum. Figure 5.7 shows the energy spectrum along with the expected spectrum without oscillations. The presence of muon neutrino oscillations is clear from the large deviation from the expected spectrum without oscillations. It is then the job the analysis described in the remaining chapters to use this data to measure the relevent PMNS neutrino mixing parameters.

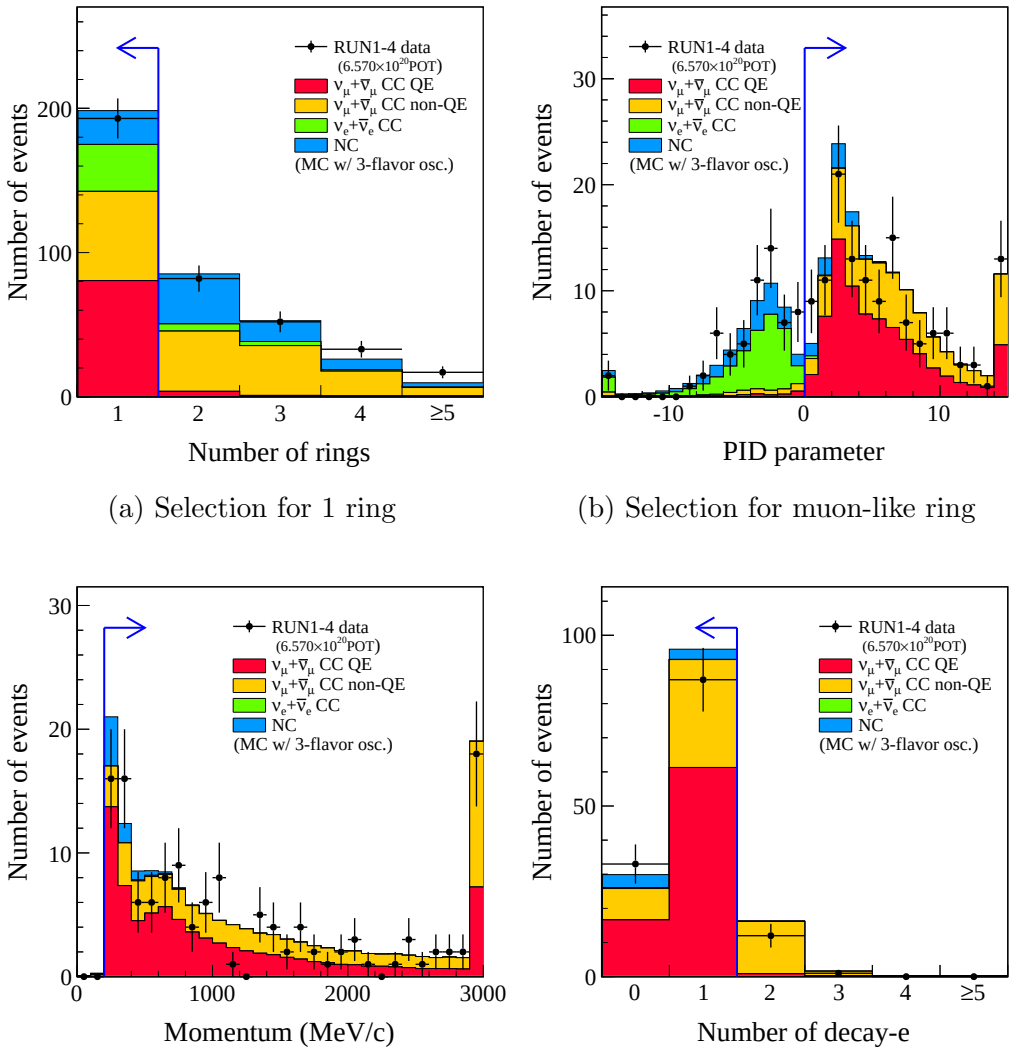

(a) Selection for 1 ring

(b) Selection for muon-like ring

(c) Selection for momentum

(d) Selection for $\leqslant 1$

FIGURE 5.5: Distribution of variables for Super-K event selection. Data and MC expectation shown for event sample after FCFV selection. MC assumes $\sin^2(\theta_{23})$ =0.5 and Δm^2_{32} =2.5 $\times$ 10^{-3} eV^2/c^4 and the normal hierarchy.

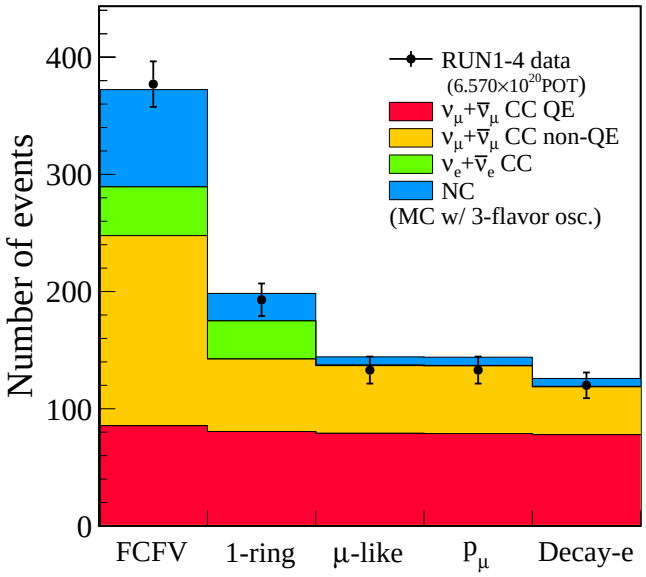

FIGURE 5.6: Number of events remaining after sucessive selection cuts. Data and MC expectation shown for event sample after FCFV selection. MC assumes $\sin^2(\theta_{23})$ =0.5 and Δm^2_{32} =2.5×10^{-3} eV^2/c^4 and the normal hierarchy. These parameter values are not from the analysis but are chosen for a rough comparison. Data and MC agree well.

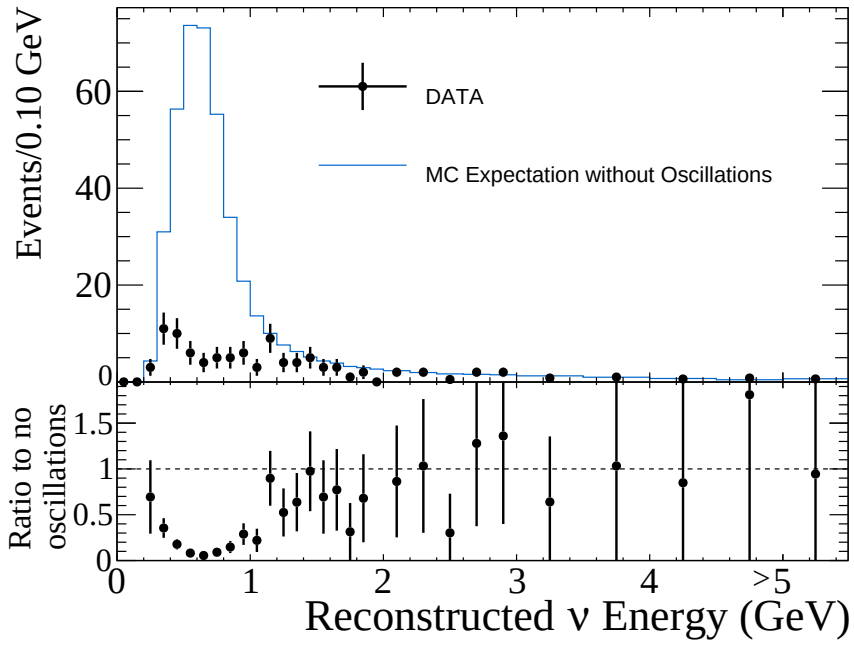

FIGURE 5.7: Observed reconstructed neutrino energy spectrum of T2K events at Super-K. (Top) The black points are the data and the blue line is the expected spectrum for no oscillations. (Bottom) The ratio of the number of events per bin by the expected number of events without oscillations. Note the oscillation dip in the data distribution.

6

Analysis Setup

6.1 Analysis Overview

The primary aim of our analysis is to measure the PMNS neutrino mixing parameters, $\sin^2(\theta_{23})$ and Δm^2_{32}. The analysis' central strategy is to compare the observed neutrino energy spectrum at Super-K with a predicted spectrum that depends on the neutrino mixing parameters. This comparison gives us the most likely values of the parameters through a technique known as the extended unbinned maximum (log) likelihood estimator, or MLE. The observed energy spectrum is composed of events whose selection was described in Section 5.2. The predicted energy spectrum for the same type of neutrino events is built from a simulation that includes the predicted flux at Super-K, a model of neutrino interactions with the water, the detector response, and the neutrino oscillation probability.

In this chapter, we describe the MLE technique and its inputs. We then cover the details of how one of the inputs to the MLE, the predicted neutrino spectrum, is calculated from its different components. We also cover how uncertainties in the model are quantified, and how these uncertainties are incorporated into the

measurement of the oscillation parameters.

6.2 Extended Maximum Likelihood Estimator

The statistical technique we employ to infer the most likely value of the oscillation parameters from the data is known as an extended unbinned maximum log-likelihood estimator (Fisher (1922)). Consider as given a vector, $\mathbf{x}$, that contains a series of N measurements of a observable random variable (or statistic). In our case this vector contains the reconstructed neutrino energies of events observed in Super-K. Furthermore, assume that we know how to compute for every ith component in $\mathbf{x}$ the probability distribution function, $P(x_i|\boldsymbol{\phi})$, which depends on a vector of K parameter values, $\boldsymbol{\phi}$. We can then define a function of the parameter values, $\boldsymbol{\phi}$, called the likelihood, $\mathcal{L}(\boldsymbol{\phi}|\mathbf{x})$, such that

$$\mathcal{L}(\boldsymbol{\phi}|\mathbf{x}) = \prod_{i=0}^{N} P(x_i|\boldsymbol{\phi}) \tag{6.1}$$

for the given vector $\mathbf{x}$. $\mathcal{L}(\boldsymbol{\phi}|\mathbf{x})$ is constructed to be proportional to the probability of the observation, x, as a function of the parameter values.

In order to find the most likely values of the parameters given the vector of measurements, we define the maximum likelihood estimator (MLE), $\hat{\boldsymbol{\phi}}$, to be an instance of the vector $\boldsymbol{\phi}$ such that

$$\left.\frac{\partial \ln \mathcal{L}(\boldsymbol{\phi}|\mathbf{x})}{\partial \boldsymbol{\phi}}\right|_{\boldsymbol{\phi}=\hat{\boldsymbol{\phi}}} = 0. \tag{6.2}$$

In other words, $\hat{\boldsymbol{\phi}}$ is the instance of $\boldsymbol{\phi}$ that maximizes the log of the likelihood. (We use the log of the likelihood for convenience as the product in $\mathcal{L}$ becomes a sum and the values of $\ln \mathcal{L}$ are often more well behaved numerically than the values of $\mathcal{L}$ when implemented in software.)

Now it is common in many types of analyses to want to categorize the parameters in $\boldsymbol{\phi}$ into two types:

- the parameters we are interested in estimating and
- the parameters which represent some uncertainty in our modeling of $P(x_i|\boldsymbol{\phi})$.

In our case, we are interested in splitting $\boldsymbol{\phi}$ into the vector of neutrino oscillation parameters, $\boldsymbol{\theta}$, and the vector of systematic uncertainty parameters, $\mathbf{f}$. The values of $\mathbf{f}$ parameterize the uncertainty in our modeling of the experiment, specifically the uncertainty in the predicted spectrum at Super-K. It is then customary to define the components of $\mathbf{f}$ as observable random variables that we have extracted, in principle, from a previous external measurement. We thus make the further assumption that the probability distribution for each component of $\mathbf{f}$ obeys a Gaussian probability distribution with means, $\boldsymbol{\mu}$, and standard deviations, $\boldsymbol{\sigma}$.

In addition to accounting for systematic errors, we would like the likelihood to take into account the probability of observing the number of events at Super-K, N, from the expected number of events given a set of values for the oscillation and systematic parameters, $N^{exp}(\boldsymbol{\theta}, \mathbf{f})$. We define the probability of observing a certain number of events using the Poisson probability distribution

$$P(N|\boldsymbol{\theta}) = N^{exp}(\boldsymbol{\theta}, \mathbf{f})^N \frac{e^{-N^{exp}(\boldsymbol{\theta}, \mathbf{f})}}{N!} \tag{6.3}$$

where N is the number of measurements in $\mathbf{x}$, $N^{exp}(\boldsymbol{\theta}, \mathbf{f})$ is the expected number of events. As for the probability of observing a neutrino with a given energy, the calculation of the expected number of neutrinos will also have uncertainties which we would like to parameterize with the vector of systematic errors, $\mathbf{f}$.

Under such assumptions we extend the definition of $\mathcal{L}(\boldsymbol{\theta}, \mathbf{f})$ to incorporate the Poisson probability of observing N events along with the likelihood of observing a

given value of $\mathbf{f}$ by

$$\mathcal{L}(\boldsymbol{\theta}, \mathbf{f}|\mathbf{x}) = \left[\prod_{i=0}^{N} P(x_i|\boldsymbol{\theta}, \mathbf{f})\right] \times \frac{N^{exp}(\boldsymbol{\theta}, \mathbf{f})^N e^{-N^{exp}(\boldsymbol{\theta}, \mathbf{f})}}{N!} \times e^{-\frac{1}{2}\Delta\mathbf{f}^T\mathbf{M}^{-1}\Delta\mathbf{f}}, \tag{6.4}$$

where $\Delta\mathbf{f} = \mathbf{f} - \boldsymbol{\mu}$, $\boldsymbol{\mu}$ are the central values the systematic parameters, and $\mathbf{M}$ is the covariance matrix between the components of $\mathbf{f}$. For this likelihood function, we define the extended maximal likelihood estimator, $\hat{\boldsymbol{\theta}}$, such that

$$\left.\frac{\partial^2 \ln \mathcal{L}(\boldsymbol{\theta}, \mathbf{f}|\mathbf{x})}{\partial\boldsymbol{\theta}\partial\mathbf{f}}\right|_{\boldsymbol{\theta}=\hat{\boldsymbol{\theta}}, \mathbf{f}=\hat{\mathbf{f}}} = 0, \tag{6.5}$$

where $\hat{\mathbf{f}}$ is the instance of $\mathbf{f}$ that simultaneously maximizes the likelihood. The components of $\mathbf{f}$ are often known as "nuisance" parameters, as we are effectively uninterested in their values and include them only to parameterize the uncertainty in our model. One can think of the above as the maximum likelihood estimator for a likelihood that is minimized for the nuisance parameters for each value of $\boldsymbol{\theta}$,

$$\ln \mathcal{L}(\boldsymbol{\theta}|\mathbf{x}) = \left.\frac{\partial \ln \mathcal{L}(\boldsymbol{\theta}, \mathbf{f}|\mathbf{x})}{\partial\mathbf{f}}\right|_{\mathbf{f}=\hat{\mathbf{f}}} = 0. \tag{6.6}$$

This expression is known as a profiled-likelihood (Cox (1970)).

In summary, we must produce three inputs in order to perform the analysis via the extended MLE:

1. a set of events with measured reconstructed neutrino energy,
2. the predicted neutrino energy spectrum which will allow us to calculate $P(x_i|\boldsymbol{\theta}, \mathbf{f})$ and $N^{exp}(\boldsymbol{\theta}, \mathbf{f})$, and
3. a parameterization of how the uncertainties in our model affects the predicted spectrum.

In the next few sections of the chapter, we discuss how the above inputs are defined and calculated.

6.3 Measurements of Neutrino Spectrum at Super-K

For the set of observations, we use the reconstructed energy of T2K neutrino events at Super-K. We describe how these events are selected in Section 5.2. The description of the data used for the analysis is in Section 5.2.1.

6.4 Components of Neutrino Spectrum Model

The key component in the calculation of the likelihood is the predicted reconstructed energy spectrum of T2K neutrino events at Super-K. Building up the model for the spectrum requires the effort of many collaborators whose roles span every component of the experiment. Detailed simulations are created starting with the hadronic interactions that create the beam to the photomultiplier responses to neutrino interactions in the Super-K detector. The models are extensively studied and validated in a way where one can define a set of parameters that encode our known uncertainties in the models. In the end, this effort culminates in a model of the reconstructed energy spectrum of the neutrino events at Super-K that pass the CCQE-like selection criteria described in Section 5.2. Figure 6.1 shows a flow chart depicting how the different components interact to make the spectrum prediction at Super-K that is ultimately used in the oscillation fit.

6.4.1 Beam Model and Tuning

The work of modeling the beam and tuning it to external data was performed by the T2K Beam Working Group. The model of the neutrino flux at Super-K starts with the simulation of 30 GeV protons fired into a graphite target. (For a description of the beam line please see Section 4.2 or refer to (Abe et al. (2013c). Also note that the flux model is provided to the analyses by the T2K flux working group.) The simulation of this process is done by the software package, FLUKA2008 (FLUKA

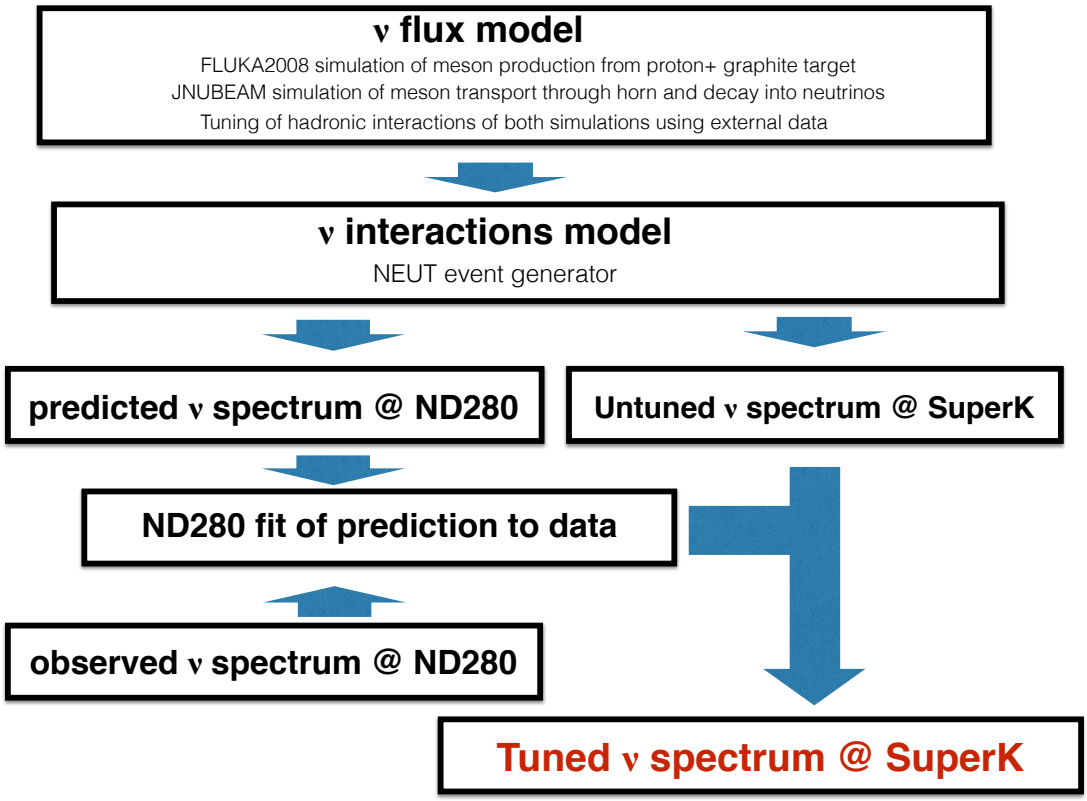

FIGURE 6.1: Flow chart showing the different inputs that go into making the Super-K predicted spectrum that goes into the oscillation fit. In addition to defining the expected spectrum, uncertainties in the model are parameterized as well. The definition of these parameters is also an important input to the fit. For the ND280 detectors, the fit of the predicted to the observed spectrum is used to both tune the spectrum at Super-K and to set the size of the uncertainties for a subset of parameters in the spectrum model.

Collaboration (2005)), which tracks an incident proton and any particle it produces through the model of the target shown in Figure 6.2. The initial kinematics of the proton relative to the center of the target is modeled after measurements taken of the spatial distribution and divergence of the proton beam. Any particles produced by the proton are tracked as they travel through the geometry. For any particle which survives to the boundary of the geometry, i.e. when it reaches the edges of the shaded regions depicted in Figure 6.2, its kinematic information and interaction history are stored and then passed on to the next stage of the simulation.

The list of escaping particles from the FLUKA2008 target simulation is passed onto JNUBEAM, a simulation that is responsible for tracking particles as they travel through a geometry composed of three magnetic focusing horns, a helium decay vessel, concrete shielding, and the beam dump. JNUBEAM is based on the package GEANT3 (Brun et al. (1987)), used to propagate the particles. Hadronic interactions with the geometry materials is handled through a package known as GCALOR (GCALOR Collaboration (????)). The simulation also includes the magnetic field both outside and inside the horns, and therefore, the path of particles through the field is simulated.

For any particle decay that produces a neutrino, the entire chain of hadronic interactions starting from the production particles in the target simulation is stored. This recorded chain of interactions is important, as it is used later to weight the events when the simulation is tuned to agree with external data. When the neutrino is produced in the simulation, it is assumed to point at the Super-K detector or to a region of the near detector. This is done in order to save computation time. The energy of the neutrino in the center of mass frame of the decaying particle is selected based on the decay kinematics. The neutrino is then boosted into the lab frame, again, under the assumption that it points to the detectors. The probability that it points in that direction is then stored as an event weight in order to ensure that the proper flux is derived in the end.

An important part of modeling the flux is tuning the simulation through external data. This is done to correct the modeling of hadronic interactions by FLUKA2008 (in the target) and GCALOR (outside the target/mostly in the horn). The external data is of meson production from a proton hitting a thin target. One of the primary data sets used in the tuning comes from the NA61/SHINE experiment where 31 GeV protons are fired into a 2 cm carbon target. The experiment records the energy and angular distribution of produced pions and kaons. The phase space measured

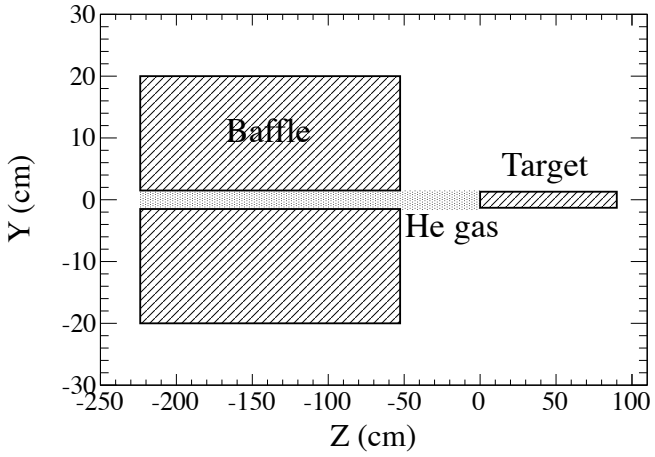

FIGURE 6.2: Cross section of graphite target geometry input into the FLUKA2008 simulation of the beam. The simulation starts with 30 GeV protons which are fired through the graphite baffle and into the target core which is also made of graphite. The simulation then records the position and kinematic information of particles that are produced in the collision and then cross the boundary of the simulation geometry. This particle information is passed on to the next stage of the beam simulation. Figure taken from (Abe et al. (2013c)).

by the NA61/SHINE experiment covers most of the phase space needed for T2K. Figure 6.3 shows the kinematic distribution of pion production for T2K (via the color map). This is compared to the kinematic coverage of the NA61 measurement shown in the boxes. At the time of the current analysis, the one region not covered was the forward region for high energy kaons. In this region, the tuning was done using data from Eichten et al. and Allaby et. al.

The method of tuning the modeling of hadronic interactions was to compare the thin target production data with a simulation of the experimental setup. This simulation was done both with FLUKA2008 and GCALOR in order to tune them separately. For the GCALOR simulation, which is mostly of interactions in the aluminum of the horn, the production data were scaled to apply to the different nuclei. The number of mesons produced at a given angle and momentum were compared between the data and the simulation. The ratio of the differential production between the data to the simulation was then extracted. These ratios were then used

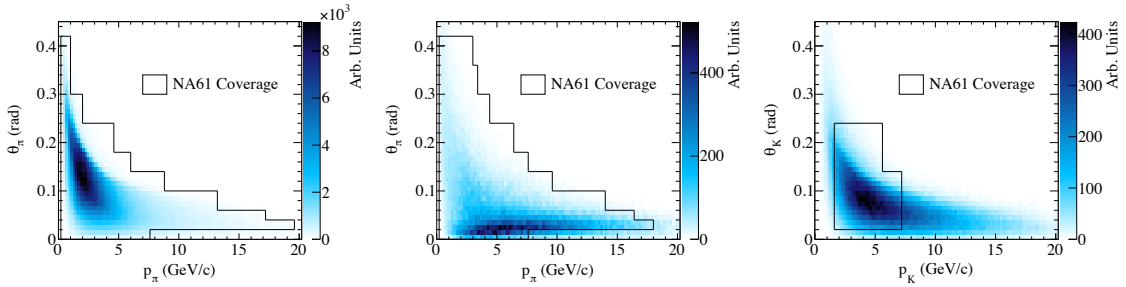

(a) π^+ (b) π^- (c) K^+

FIGURE 6.3: The phase space of pions production from hadronic interactions in the simulation of the neutrino flux at Super-K is shown in the blue heat map. The region outlined in black shows the areas of phase space measured by the NA61 thin target experiment. Figure taken from (Abe et al. (2013c)).

to weight the neutrino spectrum by weighting the chain of hadronic interactions for each neutrino produced in the simulation.

In addition to tuning the differential production rates, external measurements of the total production cross section for pions, kaons and protons on various target materials were used to tune the simulation. Figure 6.4 shows the production cross section from the untuned simulations along with data from several measurements. The ratio between the measured and model cross sections were also used to weight the neutrino flux.

In Figure 6.5, the ratio of the flux at Super-K after to before tuning is shown for different neutrino species. The tuning ratios are given for the different types of tuning: kaon production, pion production and overall interaction cross section. The total tuning is shown as well.

In the end, the tune simulation produces a flux prediction for both the near and far detectors. The final flux is shown in Figure 6.6 for different neutrino species.

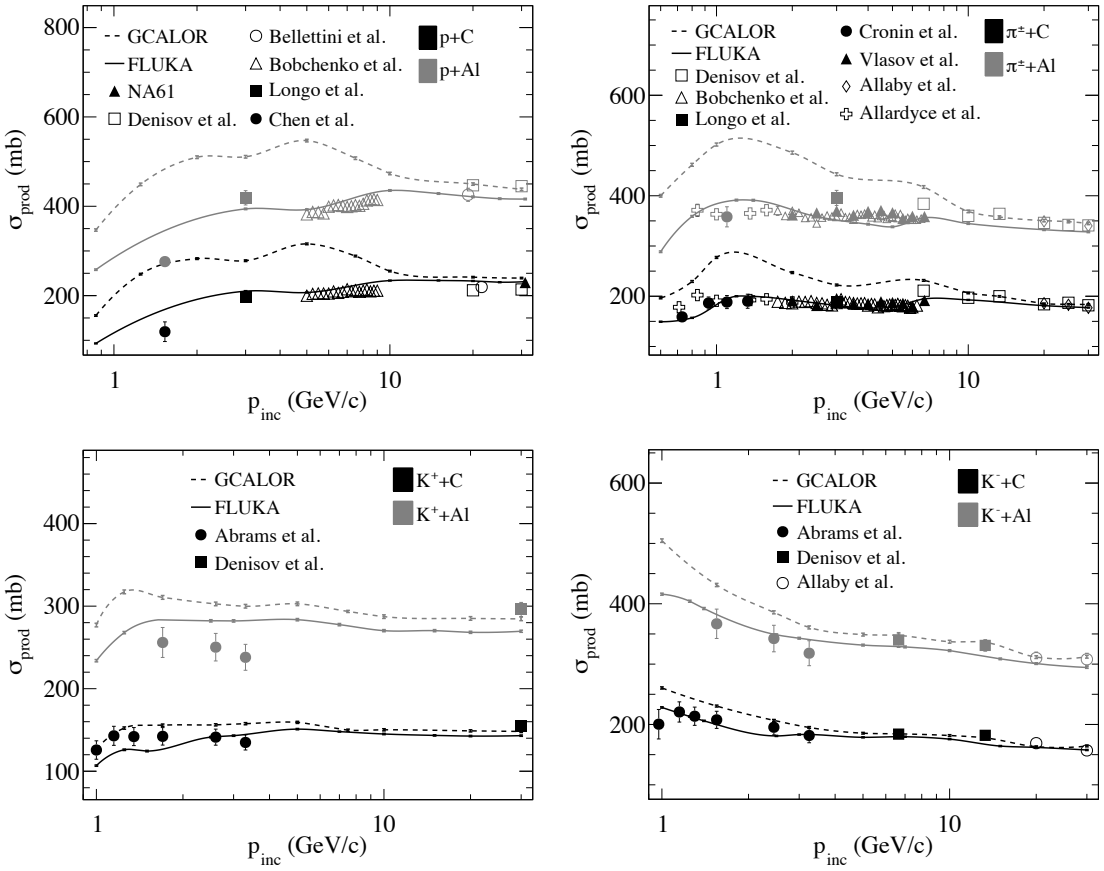

FIGURE 6.4: The production cross section for different types of incident particles: proton (top right), pion (top right), K^+ (bottom left) and K^- (bottom right). Figure taken from (Abe et al. (2013c)).

6.4.2 Model of Neutrino Interactions in ND280 and Super-K

The modeling of neutrino-nucleus interactions is implemented by a neutrino interaction event generator NEUT[1] (Hayato (2002)). For a neutrino with a specified flavor and energy, NEUT selects an interaction from a pre-defined set whose chances of selection are weighted by their relative cross sections. After the selection of the interaction mode, NEUT then defines the appropriate final-state particles (such as an out-going lepton, nucleon, or meson) whose kinematics are chosen by pre-calculated (double) differential cross sections. Tables 6.1 and 6.2 contain the list of modeled

[1] NEUT version 5.1.2.4

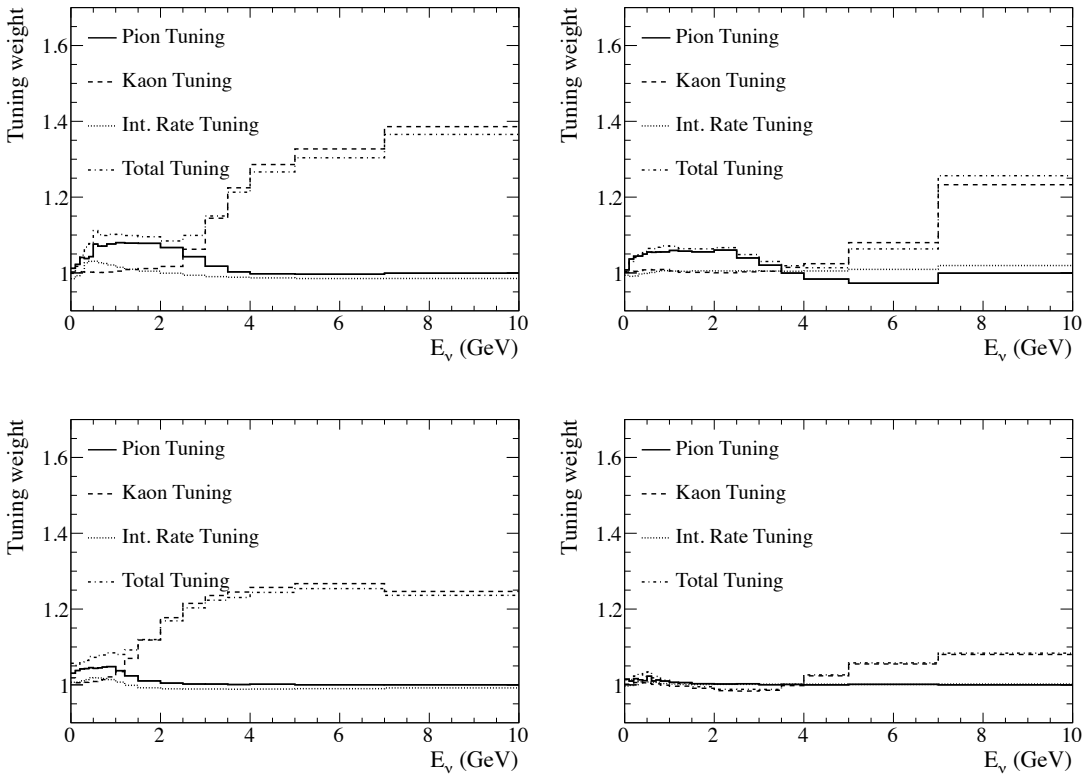

FIGURE 6.5: The ratio of the tuned to untuned flux. The ratio is shown for tuning from pion and kaon multiplicities along with tuning of the interaction cross sections. The total tuned ratio is also shown. Figure taken from (Abe et al. (2013c)).

interactions for charged-current and neutral-current interactions. NEUT models interactions for neutrinos with energies between 0 and 1 TeV. For the T2K experiment, we only simulate neutrino interactions occurring with an energy between 0 and 30 GeV.

At the range of neutrino energies at which T2K operates, the primary interaction channels which will be observed at Super-K are quasi-elastic scattering and pion production from the formation of a Δ resonance. This can be seen from Figure 6.7, which shows the interaction cross section versus energy for both the total cross section and those for three modes: quasi-elastic scattering, resonance production, and deep inelastic scattering. The T2K neutrino energy range at about FWHM

Table 6.1: Table of charged-current neutrino interactions modeled in the event generator NEUT. In the following table, N is used as the symbol for nucleon (neutron or proton) and X is used to mean one or more mesons. The analogous modes exist for charged-current $\bar{\nu}$ interactions.

Interaction Type	Formula	Energy (GeV)
CC Quasi-Elastic	$\nu_l + n \rightarrow l^- + p$	0-1000
CC Single π Production from Δ	$\nu_l + p \rightarrow l^- + p + \pi^+$	0.37-1000
	$\nu_l + n \rightarrow l^- + p + \pi^0$	
	$\nu_l + n \rightarrow l^- + n + \pi^+$	
CC Coherent π Production	$\nu_l + {}^{16}O \rightarrow l^- + {}^{16}O + \pi^+$	0.4-1000
CC Multiple π Production	$\nu_l + N \rightarrow l^- + N + (>1)\pi$	0.5-1000
CC Single γ Production from Δ	$\nu_l + n \rightarrow l^- + p + \gamma$	0.37-1000
CC Single η Production from Δ	$\nu_l + n \rightarrow l^- + p + \eta^0$	0.37-1000
CC Single K Production from Δ	$\nu_l + n \rightarrow l^- + \Lambda + K^+$	0.37-1000
CC Deep Inelastic Scattering	$\nu_l + N \rightarrow l^- + N + X$	0-1000

of the spectrum peak is shown. Other, higher energy interactions do occur, but they are subdominant contributions in the final neutrino spectrum seen in Super-K. Therefore, we limit ourselves to the description of the model used for these two types of interactions. For the rest, please see (Hayato (2002)).

Table 6.2: Table of neutral-current neutrino interactions modeled in the event generator NEUT. In the following table, N is used as the symbol for nucleon (neutron or proton) and X is used to mean one or more mesons. The analogous modes exist for charged-current $\bar{\nu}$ interactions.

Interaction Type	Formula	Energy Range (GeV)
NC Elastic	$\nu + N \rightarrow \nu + N$	0-1000
NC Single π Production from Δ	$\nu + N \rightarrow \nu + N + \pi^0$	0.37-1000
	$\nu + n \rightarrow \nu + p + \pi^-$	
	$\nu + p \rightarrow \nu + n + \pi^+$	
NC Coherent π^0 Production	$\nu + {}^{16}O \rightarrow \nu + {}^{16}O + \pi^0$	0.4-1000
NC Multiple π Production	$\nu + N \rightarrow \nu + N + (>1)\pi$	0.5-1000
NC Single γ Production from Δ	$\nu + N \rightarrow \nu + N + \gamma$	0.37-1000
NC Single η Production from Δ	$\nu + N \rightarrow \nu + N + \eta^0$	0.37-1000
NC Single K Production from Δ	$\nu + n \rightarrow \nu + \Lambda^0 + K^0$	0.37-1000
	$\nu + p \rightarrow \nu + \Lambda^0 + K^+$	0.37-1000
NC Deep Inelastic Scattering	$\nu_l + N \rightarrow \nu + N + X$	0-1000

Quasi-Elastic Scattering

NEUT implements elastic scattering through two models. For elastic scattering off of free protons, NEUT uses a model by C.H. Llewellyn Smith. For neutrino elastic scattering with a nucleon in the nucleus, the Smith and Moniz model is used. The latter is an extension of the former, as the Smith and Moniz model treats the interacting nucleon as free but subject the initial and final kinematics to constraints due to the nuclear environment. These constraints derive from the model of the nucleus which in NEUT is treated as a non-interacting relativistic Fermi gas of nucleons. The distribution of initial nucleon momentum is derived from measurements of electron scattering on a carbon nucleus. The final nucleon momentum is subject to Pauli-blocking, which forbids the out-going nucleon momentum to fall below the nucleus' Fermi momentum, which for oxygen is set at 225 MeV/c. The out-going nucleon is also required to overcome the nucleus' binding energy, which for oxygen is set to 27 MeV/c^2.

The details of this elastic scattering model will become important later as they serve as the basis for parameterizing some of the uncertainties in the expected reconstructed neutrino energy spectrum.

The models listed above are calculated for charged-current elastic scattering. For neutral elastic scattering, several ratios from experiment are used to derive the cross section

$$\sigma_{NC}(\nu p \to \nu p) = 0.153 \times \sigma_{CC}(\nu n \to e^- p) \tag{6.7}$$

$$\sigma_{NC}(\bar{\nu} p \to \bar{\nu} p) = 0.218 \times \sigma_{CC}(\bar{\nu} p \to e^+ n) \tag{6.8}$$

$$\sigma_{NC}(\nu n \to \nu n) = 1.5 \times \sigma_{NC}(\nu p \to \nu p) \tag{6.9}$$

$$\sigma_{NC}(\bar{\nu} n \to \bar{\nu} n) = 1.0 \times \sigma_{NC}(\bar{\nu} p \to \bar{\nu} p) \tag{6.10}$$

Resonance Production

For all the meson production modes coming from a Δ resonance listed in Tables 6.1 and 6.2, NEUT uses cross sections from the Rein and Sehgal model. In this model, the charged-current interaction is separated into two parts

$$\nu + N \rightarrow l + N^* \tag{6.11}$$

$$N^* \rightarrow X + N' \tag{6.12}$$

where N is the nucleon, N^* is the nucleon resonance, X is a single decay product from the resonance, and N' is the final out-going nucleon. The branching fractions and decay kinematics for the different mesons come from the decay of a $\Delta(1232)$. NEUT restricts its use of this model for the decay to single γ, kaons, etas, and pions. This restriction to single decays prevents from overlapping with other interaction modes.

The resonant production of single pions are an important class of interaction because they are expected to be the second largest source of events that eventually pass into the final neutrino event sample. For the events that come from neutral-current interactions, they consist of a single pion being produced by the nucleus-neutrino interaction and then mis-identified as a single muon by the event selection. For charged-current interactions, both a muon and pion are produced. Events that pass have either its pion or muon missed by the reconstruction. This can come about either because of a failure in the reconstruction or because the pion is absorbed through hadronic interactions within the nucleus prior to pion's escape. The pion can also be lost through hadronic interactions with the non-original nuclei in the water. These hadronic interactions both inside the original nucleus are referred to as final state interactions and secondary interactions, respectively.

Final State and Secondary Interactions

Hadrons produced from neutrino interactions can interact with the nucleus before passing out of the nucleus. This is especially true for pions where their cross section with nucleons can be large in the energy region we are interested in. In NEUT, interactions of pions and nucleons that occur in the nucleus after the initial neutrino interaction are known as final state interactions (FSI). NEUT implements a particle cascade model for FSI where pions or nucleons generated in the nucleus are transported step by step until they leave or are absorbed by the nucleus. The initial position of the interaction is generated by the Woods-Saxon nucleon density distribution (Woods and Saxon (1954)).

For pions traveling through the nucleus, they are allowed to undergo quasi-elastic scattering, charge exchange (e.g. $\pi^{\pm} \rightarrow \pi^{0}$), absorption and hadron production. For the hadron production interaction, the model allows a pion interaction to prouce a nucleon and up to six additional pions. At each step, the pion's mean free path is calculated using the four interactions and then is used to determine if an interaction occurs.

The chain of pion interactions as it moves through the nucleus is recorded. Just as was done in the beam flux tuning, recording the chain of interactions allows one to weight the event by adjusting the strength of each interaction type. Such weighting was used to tune the model to agree with $\pi^{\pm}$-^{12}C interaction cross sections (de Perio (2011)). The cross sections before and after the tuning for the different types of interactions are shown in Figure 6.8. The weighting scheme will also play an important role in defining the uncertainty in the FSI model.

For pions that have left the original nuclues and are traveling through the water, their interactions through the Super-K detector are modeled using the same transport method for FSI. These interactions outside the nucleus are referred to as "secondary

interactions", or SI. The only modification to the method is that the pion mean free path is calculated for a pion traveling through Super-K rather than the nucleus. Using the same model allows for a consistent treatment of pion itneractions at low energy and takes advantage of the work that was done to tune the interactions to external data. Furthermore, the same reweighting scheme will be employed for secondary interactions when parameterizing the effect of the uncertainty in this model for the oscillation analysis.

Coherent Pion Production

In addition to pions being made through the interaction of the neutrino with a nucleon, the neutrino may also interact with the entire ^{16}O nucleus. Because the nucleus is much heavier than the neutrino, any out-going products from this reaction will be traveling mostly along the initial direction of the neutrino. For charged-current interactions, this includes pions traveling close to the direction of the muon. For neutral-current interactions, a lone π^0 may be produced close to the initial direction of the neutrino. NEUT implements a model of this interaction by Rein-Sehgal (Rein and Sehgal (1983)).

6.4.3 Simulation of the Super-K Detector Response

The simulation of the Super-K detector, SKDETSIM, is briefly described in 4.4.6. SKDETSIM's role in the analysis is to take the expected interactions in the detector, calculated by combining the flux prediction and the model of neutrino interactions by NEUT, and produce fake MC data similar to what we expect to see at Super-K. The resulting MC data is passed through the same event selection and reconstruction algorithms as the real data in order to produce the expected Super-K spectrum. The MC spectrum also includes the effect of oscillations. Furthermore, the effect of systematic uncertainties in the various flux and interaction models are implemented

as parameterized modifications to the spectrum. The formalism for this calculation is described in the next section, Section 6.5. The definition of the systematic uncertainty parameters are in Section 6.6.

6.5 Formalism of Super-K Spectrum Prediction

In this section, we describe the computation behind the prediction of the Super-K spectrum. This will help define notation that will be useful when describing the action of the systematic error parameters on the model prediction.

For the analysis, the goal is to be able to compute the probability density of observing a neutrino event seen at Super-K with some reconstructed energy. Furthermore, we also require the expected number of events, $N_{\text{exp}}^{SK}(\boldsymbol{\theta}, \mathbf{f})$. For both, the quantities must be computed given values of the systematic uncertainty parameters, $\mathbf{f}$, and oscillation parameters, $\boldsymbol{\theta}$. Unfortunately, it is not possible to calculate either quantity using an analytic function. As an alternative, Monte Carlo (MC) methods generate the spectrum whose values are histogrammed in bins of the reconstructed neutrino energy. The values of each bin, N_i^{rec}, give the number of events in the ith bin number of the predicted reconstructed energy spectrum.

In the analysis, N_i^{rec} is a function of the neutrino oscillation parameters, $\boldsymbol{\theta}$, and systematic uncertainty parameters, $\mathbf{f}$. The neutrino oscillation probability is a function of the true neutrino energy. Therefore, the expression for N_i^{rec} involves a sum over true neutrino energy and takes the form

$$N_i^{rec}(\boldsymbol{\theta}, \mathbf{f}) = \sum_j M_{ij} \cdot P_{osc}(E_j^{true}; \boldsymbol{\theta}) \cdot N_{ij}^{true}(\mathbf{f}^t) \tag{6.13}$$

where

$$
\begin{aligned}
N_i^{rec} \quad &: \quad \text{Number of events in the } i\text{th bin of reconstructed neutrino} \\
&\quad\quad \text{energy distribution} \qquad (6.14) \\
N_{ij}^{true}(\mathbf{f}) \quad &: \quad \text{Number of events in the } i\text{th reconstructed energy bin} \\
&\quad\quad \text{and } j\text{th true energy bin. The value depends on the} \\
&\quad\quad \text{systematic uncertaintity parameters } \mathbf{f} \\
M_{ij} \quad &: \quad \text{Conversion matrix from true neutrino energy distribution} \\
&\quad\quad \text{to reconstructed energy distribution}
\end{aligned}
$$

The values of M_{ij} are calculated in advance from the MC simulation and contain the probability that an event with a true neutrino energy that falls in true neutrino energy bin j will be observed with a reconstructed energy that falls into bin i. The oscillation probabilities, $P_{osc}(E_j^{true};\boldsymbol{\theta})$, in Equation (6.13) are calculated using a library called `Prob3++` (Wendell (2014)) which calculates the oscillation probability using the full three-flavor-neutrino oscillation framework and includes matter effects. The library implements the formalism outlined in (Barger et al. (1980)).

The dependence of N_{ij}^{true} on the systematic parameters $\mathbf{f}^t$ will be different for the various neutrino flavors and the types of interactions. As a result, we split N_{ij}^{true} into a sum over different neutrino flavors, ν, and interaction modes, I. We also factor out the change in the bin due to the systematic errors such that

$$
N_{ij}^{true}(\mathbf{f}^t) = \sum_{\nu}\sum_{I} N_{ij}^{true,\nu I}\mathcal{F}_{ij}^{t,\nu I}(E^{true},\mathbf{f}^t)\mathcal{F}_{i}^{r,\nu I}(E^{rec},\mathbf{f}^r) \qquad (6.15)
$$

where

N_{ij}^{true} : Number of events in jth bin of true neutrino energy distribution from MC

$\mathcal{F}_{ij}^{t,\nu I}(E^{true}, \mathbf{f}^t)$: The weight factor for the ith and jth bin due to the subset of $\mathbf{f}^t$ that are a function of the true energy

$\mathcal{F}_{i}^{r,\nu I}(E^{rec}, \mathbf{f}^r)$: The weight factor for the ith bin due to the subset of $\mathbf{f}^r$ that are a function of the reconstructed energy

ν : Index over different neutrino flavors in the beam whose elements are $\{\nu_\mu$, $\bar{\nu}_\mu$, intrinsic beam ν_e, $\bar{\nu}_e$, signal $\nu_e\}$

I : Index over the different interaction channels or modes, whose elements include:
{charged-current quasi-elastic interactions (CCQE),
charged-current single π resonant production (CC1PI),
charged-current coherent pion production (CCCOH),
other charged-current processes (CCOTH),
neutral-current single π production (NC1PI), and
other neutral-current interactions (NCOTH). }

The functions, $\mathcal{F}_i^r(\mathbf{f}^r)$ and $\mathcal{F}_{ij}^{t,\nu I}(\mathbf{f}^t)$, are the systematic uncertainty weighting functions which parameterize how the expected spectrum changes as a function of the parameter values. These functions are further factorized to separate the individual effect of the systematic uncertainty parameters such that

$$\mathcal{F}_i^{r,\nu I}(E^{rec}, \mathbf{f}^r) = \prod_k F_{ik}^{r,\nu I}(E_i^{rec}, f_k) \tag{6.16}$$

and

$$\mathcal{F}_{ij}^{t,\nu I}(E^{true}, \mathbf{f}^t) = \prod_{k'} F_{ijk'}^{t,\nu I}(E_j^{true}, f_{k'}). \tag{6.17}$$

Note that $\mathbf{f} = \mathbf{f}^r + \mathbf{f}^t$ and that there are no parameters which depend explicitly on both the true and reconstructed energy.

The values of F quantify the effect on the ijth bin due to a single systematic uncertainty parameter and are calculated through the simulation. The way this is done is that the value of the bin as a function of a single systematic uncertainty is recorded and used to define of a function that gives the fractional change in the bin for a given value of the systematic uncertainty parameter. For roughly half of the parameters, this function is linear. For the other half, splines parameterize the function. For almost all the components of $\mathbf{f}$, the parameters are defined so that the value of 1.0 represents the default value of some input parameter to the spectrum prediction.

The bins of the neutrino energy spectrum span the interval of 0.0 GeV to 30.0 GeV. This range is the same for both true and reconstructed neutrino energy. However, the binning for E^{rec} and E^{true} are different and are summarized in Table 6.3 and 6.4, respectively.

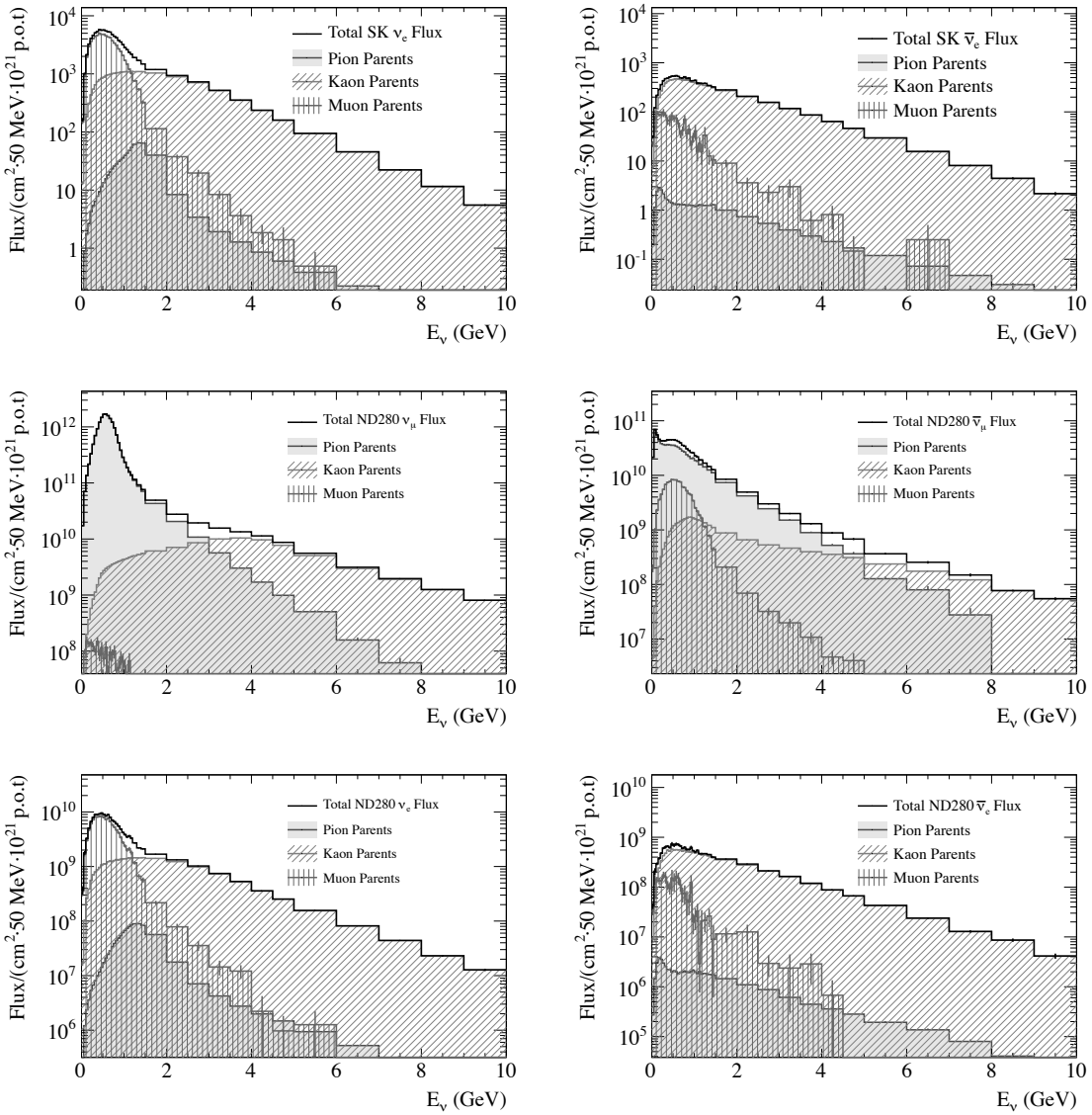

FIGURE 6.6: The tuned neutrino flux prediction for different neutrino species at the near and far detector. Figure taken from (Abe et al. (2013c)).

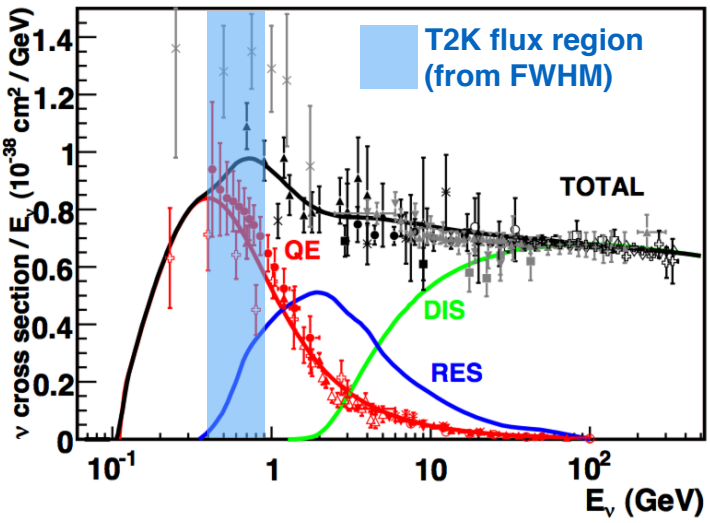

FIGURE 6.7: Neutrino charged current interaction cross section versus energy for model (solid lines) and data (points with error bars). The prediction for three different interaction types are shown as well: quasi-elastic (QE, red), resonant production (RES, blue), and deep inelastic scattering (DIS,green). The full-width half-maximum (FWHM) range of the T2K neutrino spectrum at Super-K is shown in the light blue region. Modified from figure made by G. Zeller.

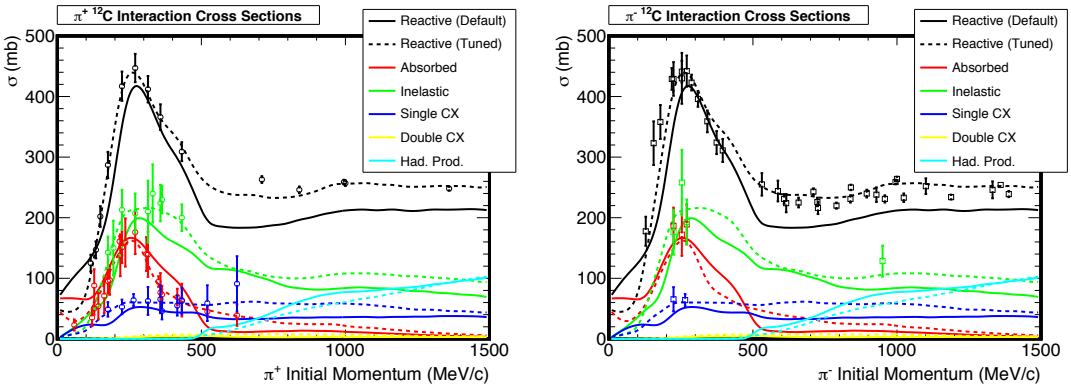

FIGURE 6.8: Figure overlays $\pi^{\pm}$-^{12}C interaction cross sections with the tuned NEUT prediction using its pion hadronic interaction model. Figure from P. de Perio.

Table 6.3: Binning of the true neutrino energy (E^{true}) used in the oscillation analysis. Bins around the oscillation peak (0.3∼1.0 GeV) are set to be fine. The total number of bins is 84.

E^{true} range [GeV]	Bin Width [GeV]	Number of Bins
0.0∼0.3	0.05	6
0.3∼1.0	0.025	28
1.0∼3.0	0.05	40
3.0 ∼ 3.5	0.10	5
3.5 ∼ 4.0	0.50	1
4.0∼5.0	1.0	1
5.0∼7.0	2.0	1
7.0∼10.0	3.0	1
10.0∼30.0	20.0	1

Table 6.4: Binning of the reconstructed neutrino energy (E^{rec}) used in the oscillation analysis. Total number of bins is 73.

E^{rec} range [GeV]	Bin Width [GeV]	Number of Bins
0.0∼3.0	0.05	60
3.0∼4.0	0.25	4
4.0∼6.0	0.5	4
6.0∼10.0	1.0	4
10.0∼30.0	20.0	4

As we have stated above, the goal of the analysis is to measure the values of $\sin^2(\theta_{23})$ and Δm^2_{32} (Δm^2_{13}) when assuming the normal (inverted) hierarchy. The rest of the oscillation parameters are treated as nuisance parameters like the systematic uncertainties. The value of $\sin^2\theta_{13}$,$\sin^2\theta_{12}$, and Δm^2_{12} are assumed to be distributed as a Gaussian random variable whose mean and sigma are taken from best fit values and uncertainties found in the 2012 PDG (Beringer and Particle Data Group (2012)). For the value of δ_{CP}, it is allowed to vary, without a penalty, between $[-\pi, +\pi]$. The means and sigmas used for the oscillation parameters along with other inputs into the Prob3++ calculator are summarized in Table 6.5.

Table 6.5: Summary of "nuisance" oscillation parameter values used in the probability calculation by library Prob3++. These parameters are allowed to vary in the oscillation analysis. All parameters except δ_{CP} are given a Gaussian penalty in the likelihood with mean and sigma defined below. The δ_{CP} is unconstrained and given a starting value of zero.

Parameter	Mean Value	Sigma
Δm^2_{21}	$7.5\times10^{-5}\text{eV}^2/c^4$	$0.20\times10^{-5}\text{eV}^2/c^4$
$\sin^2\theta_{12}$	0.311	0.016
$\sin^2\theta_{13}$	0.0251	0.0034
δ_{CP}	0 (starting value)	unconstrained, bounded in $[-\pi, \pi]$
Mass hierarchy	Normal or Inverted	
Baseline length	295 km	
Earth density	2.6 g/cm^2 (matter effect on)	

The PDF of the reconstructed neutrino spectrum is obtained by linear interpolation of N^{rec}_i:

$$\rho(E^{rec}) = \frac{x \cdot N^{rec}_{i+1} \cdot w_{i+1} + (1-x) \cdot N^{rec}_i \cdot w_i}{N^{SK}_{exp}}, \tag{6.18}$$

where

$$x = \frac{E^{rec} - E^{rec}_i}{E^{rec}_{i+1} - E^{rec}_i}, \quad w_i = \frac{0.05\ GeV}{E^{rec}_{i+1} - E^{rec}_i}, \quad (E^{rec}_{i+1} > E^{rec} > E^{rec}_i). \tag{6.19}$$

Figure 6.9 shows the binned energy spectrum and the PDF according to Equa-

tion (6.18). The black line function in this figure is used as the PDF in the likelihood definition found in Equation (6.4). The integral of the unnormalized spectrum is used as for the value of $N^{exp}(\boldsymbol{\theta}, \mathbf{f})$ also found in the likelihood.

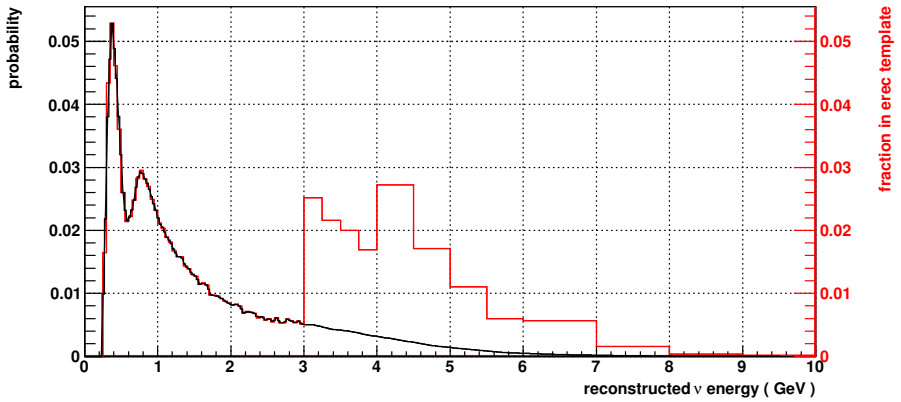

FIGURE 6.9: PDF of the reconstructed neutrino spectrum. Red histogram shows the fraction of the E^{rec} spectrum found in each bin. Black line shows the probability density used in the likelihood, which uses a linear function to interpolate between neighboring bin centers.

6.6 Parameterization of Systematic Uncertainties

For the analysis, it is important to not only produce an accurate prediction of the spectrum at Super-K but also to define a set of parameters that captures the extent of our uncertainty in the model. For example, if there is an input parameter that goes into the calculation of some model, an uncertainty can be set if there is an external measurement that can independently constrain the value of the parameter. Then the uncertainty on the parameter can be passed on to the model and define the model's uncertainty. However, for some uncertainties, the best that can be done is to quantify the disagreement between theories. This method is sometimes used for competing theories that describe an interaction mode.

In total, there are 45 systematic uncertainty parameters in the model of the spectrum at Super-K. The contents of the uncertainty parameter vector, $\mathbf{f}$, are divided

into five groups:

$$\mathbf{f} = \mathbf{f}^{t,flux} + \mathbf{f}^{t,xsec} + \mathbf{f}^{r,SK} + \mathbf{f}^{r,e-scale} + \mathbf{f}^{t,osc} \tag{6.20}$$

where the sub-vectors are

$\mathbf{f}^{t,flux}$ beam flux systematic parameters (total of 16),

$\mathbf{f}^{t,xsec}$**:** neutrino interaction cross section parameters (total of 18),

$\mathbf{f}^{r,SK}$**:** systematic parameters representing combined uncertainties in the SK selection and in the modeling of final state (FSI) and secondary pion interactions (SI) in SK (total of 6),

$\mathbf{f}^{r,e-scale}$**:** the SK energy scale systematic parameter, and

$\mathbf{f}^{t,osc}$**:** the other oscillation parameters (total of 4).

The superscripts, t and r, designate if a parameter applies to bins of true energy or reconstructed energy, respectively.

In this section, we briefly describe the definition of the parameters along with how the size of the uncertainties are derived. Almost all of the components in $\mathbf{f}$ are assumed to be a Gaussian-distributed random variable. Any exceptions will be discussed below. Tables 6.6 and 6.7 list the parameters along with the size of their uncertainties.

6.6.1 Beam flux parameters

The uncertainty in the beam flux is studied for many different sources. The uncertainties come from inputs to the tuning such as the pion and kaon multiplicities discussed above. They also include other inputs to the simulation such as the profile of the proton beam, measured versus input horn current, and the alignment of the

Table 6.6: Table 1 of 2 of systematic parameters used in the oscillation analysis. Parameters number 1 to 16 cover the beam flux systematic uncertainties. The mean value and sigma are listed before and after the ND280 fit.

No.	Parameter	Before ND280 fit		After ND280 fit	
		Value	Error(1σ)[%]	Value	Error(1σ)[%]
Flux Parameters					
1	ν_μ flux Bin 1	1.0	12.1	1.029	8.5
2	ν_μ flux Bin 2	1.0	13.0	1.022	8.8
3	ν_μ flux Bin 3	1.0	12.2	0.995	8.0
4	ν_μ flux Bin 4	1.0	11.5	0.966	7.6
5	ν_μ flux Bin 5	1.0	12.9	0.934	8.5
6	ν_μ flux Bin 6	1.0	11.6	0.992	7.7
7	ν_μ flux Bin 7	1.0	10.0	1.037	6.8
8	ν_μ flux Bin 8	1.0	9.5	1.054	6.5
9	ν_μ flux Bin 9	1.0	11.2	1.035	7.2
10	ν_μ flux Bin 10	1.0	15.2	0.975	7.3
11	ν_μ flux Bin 11	1.0	18.7	0.943	8.2
12	$\bar{\nu}_\mu$ flux Bin 1	1.0	13.3	1.030	10.2
13	$\bar{\nu}_\mu$ flux Bin 2	1.0	11.7	1.011	9.0
14	$\bar{\nu}_\mu$ flux Bin 3	1.0	11.9	1.007	9.4
15	$\bar{\nu}_\mu$ flux Bin 4	1.0	12.3	1.026	10.4
16	$\bar{\nu}_\mu$ flux Bin 5	1.0	12.2	1.008	10.7

horns. Figure 6.10 shows the total uncertainty in the beam flux at Super-K for different neutrino flavors along with the uncertainty due to the different beam inputs analyzed.

However, the output that the T2K beam group provides to the rest of the collaboration condenses the information from the individual inputs into an error matrix that quantifies the uncertainties on the flux normalization for bins of different true neutrino energy and flavor. This matrix is provided for both the Super-K and ND280 detector. The binning used for the flux uncertainty and the error matrix is given in Table 6.8.

For the calculation of the neutrino spectrum at Super-K, the flux uncertainties are defined as normalization factors for each true neutrino energy bin. The contribution from the uncertainties of ν_e and $\bar{\nu}_e$ flux was found to be negligible, ($\sim$0.02 %),

Table 6.7: Table 2 of 2 of the systematic parameters used in the oscillation analysis. The values of most parameters are unit-less. For others, the units are listed alongside the name. Note that the Super-K selection efficiencies and FSI-SI parameters (indicated by *) are combined into common parameters.

No.	Parameter	Before ND280 fit		After ND280 fit	
		Value	1σ Error (% of pre-fit)	Value	1σ Error (% of post-fit)
Cross section parameters constrained by ND280					
17	M_A^{QE} [GeV]	1.21	37.2	1.240	5.8
18	M_A^{RES} [GeV]	1.41	15.7	0.965	7.0
19	CCQE norm (E^{true} <1.5 GeV)	1	11	0.966	7.9
20	CCQE norm ($1.5 \leqslant E^{true} \leqslant 3.5$ GeV)	1	30	0.931	11.1
21	CCQE norm (E^{true} >3.5 GeV)	1	30	0.852	13.3
22	CC1π norm (E^{true} <2.5 GeV)	1.15	31.7	1.265	12.9
23	CC1π norm (E^{true} >2.5 GeV)	1	40	1.122	15.3
24	CC other shape [GeV]	0	40	same as pre-fit	
25	Spectral function	0(Off)	100(On)	same as pre-fit	
26	E_b [MeV]	27	33.3	same as pre-fit	
27	p_F [MeV]	225	13.3	same as pre-fit	
28	CCCoh norm	1	100	same as pre-fit	
29	NC1πC norm	1	30	same as pre-fit	
30	NCOth norm	1	30	same as pre-fit	
31	$\sigma_{\nu_e}/\sigma_{\nu_\mu}$	1	3	same as pre-fit	
32	W-shape [MeV]	87.7	51.7	same as pre-fit	
33	Pi-less delta decay	0	20	same as pre-fit	
34	$\sigma_{\bar{\nu}}/\sigma_{\nu}$	1	40	same as pre-fit	
SK Selection Efficiency and Detector Parameters					
35*	$\nu_\mu, \bar{\nu}_\mu$ CCQE (E^{rec} <0.4 GeV)	1	2.54	same as pre-fit	
36*	$\nu_\mu, \bar{\nu}_\mu$ CCQE (E^{rec}=0.4$\sim$1.1 GeV)	1	2.82	same as pre-fit	
37*	$\nu_\mu, \bar{\nu}_\mu$ CCQE (E^{rec} >1.1 GeV)	1	3.69	same as pre-fit	
38*	$\nu_\mu, \bar{\nu}_\mu$ CCnonQE	1	8.25	same as pre-fit	
39*	ν_e CC	1	100	same as pre-fit	
40*	All NC	1	59.19	same as pre-fit	
41	SK energy scale	1	2.4	same as pre-fit	
Hadronic interaction in oxygen (FSI) and water (SI)					
35*	$\nu_\mu, \bar{\nu}_\mu$ CCQE (E^{rec} <0.4 GeV)	1	0.0002	same as pre-fit	
36*	$\nu_\mu, \bar{\nu}_\mu$ CCQE (E^{rec}=0.4$\sim$1.1 GeV)	1	0.07	same as pre-fit	
37*	$\nu_\mu, \bar{\nu}_\mu$ CCQE (E^{rec} >1.1 GeV)	1	0.3	same as pre-fit	
38*	$\nu_\mu, \bar{\nu}_\mu$ CCnonQE	1	8.6	same as pre-fit	
39*	ν_e CC	1	1.5	same as pre-fit	
40*	All NC	1	9.6	same as pre-fit	
Oscillation Parameters Constrained by External Data					
42	$\sin^2(\theta_{12})$	0.311	5.1	same as pre-fit	
43	Δm^2_{12} [eV^2/c^4]	7.5×10^{-5}	2.7	same as pre-fit	
44	$\sin^2(\theta_{13})$	0.0251	13.5	same as pre-fit	
45	δ_{CP}	0.0	$[-\pi, \pi]$	same as pre-fit	

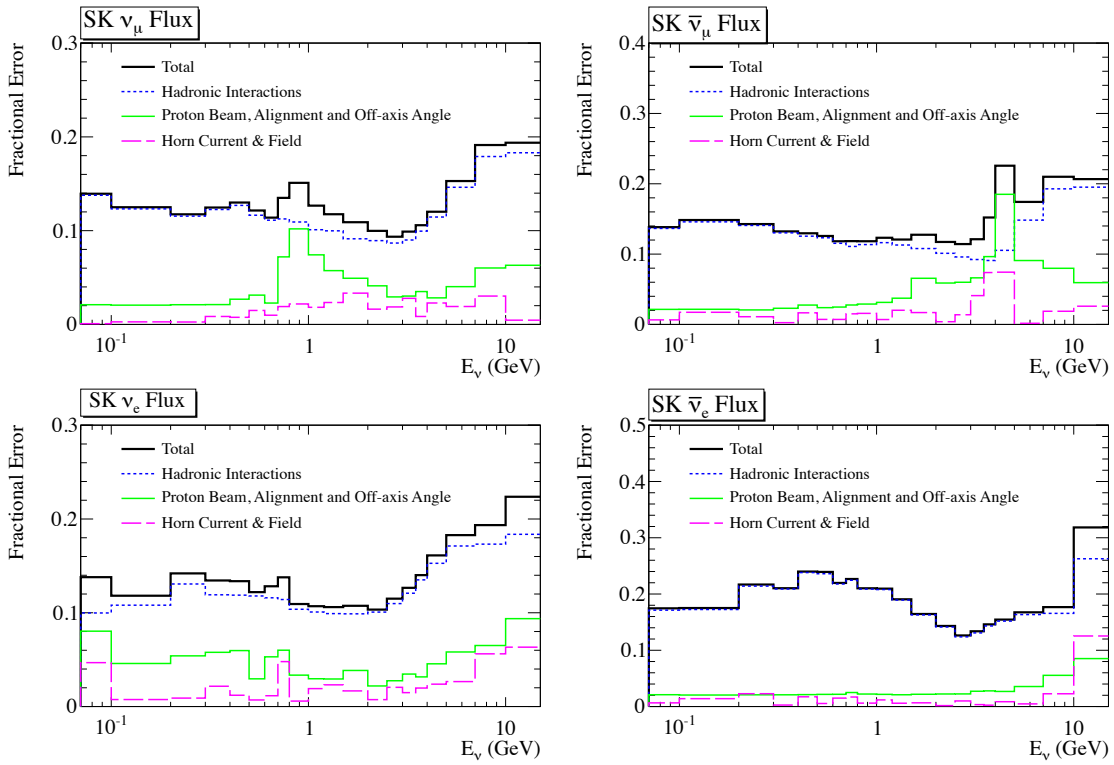

FIGURE 6.10: Total uncertainty in the beam flux (black line) along with the uncertainty due to the different inputs analyzed (color lines). Figure from (Abe et al. (2013c)).

so only uncertainties for ν_μ and $\bar{\nu}_\mu$ are considered. The uncertainty functions in Equation (6.17) for the flux parameters are defined as

$$F_{ijk'}^{t,\nu I}(E_i^{rec}, E_j^{true}, f_{k'}) = f_b^{flux,\nu} \tag{6.21}$$

where b is the appropriate flux parameter that applies for the jth true energy bin and $f_b^{flux,\nu}$ is the value for neutrinos with flavor, ν, and a true energy that falls within the bth flux uncertainty bin. The nominal flux corresponds to a parameter value of 1.0. If ν is for flavors other than ν_μ and $\bar{\nu}_\mu$ the value of $f_b^{flux,\nu}$ is defined to be 1.0.

Table 6.8: Binning of the flux systematic parameters

Flavor	True neutrino energy binning [GeV]	# of bins
ν_μ	0–0.4, 0.4–0.5, 0.5–0.6, 0.6–0.7, 0.7–1.0, 1.0–1.5, 1.5–2.5, 2.5–3.5, 3.5–5.0, 5.0–7.0, 7.0–30	11
$\bar{\nu}_\mu$	0–0.7, 0.7–1.0, 1.0–1.5, 1.5–2.5, 2.5–30	5

6.6.2 Neutrino Interaction Systematic Uncertainty Parameters

Motivation

The motivation behind the choice of parameters for the neutrino-nucleus uncertainties can be generally described as focused on the two most important interaction types: quasi-elastic scattering and resonant production of pions. In Figure 6.11, the expected spectrum after selections is shown broken down by the contribution from different types of interaction modes. As one can see, the most important modes around 0.6 GeV (where most of the oscillation effect is expected to occur) are the charged-current quasi-elastic and pion production modes. This is followed by mostly neutral-current pion production modes (shown in green). As a result, the majority of parameters that are defined relate to these types of interactions. Some of the parameters quantify the uncertainty in the input the models. Others capture the disagreement between our current model and external data. This is particularly true for the parameters related to resonant production interactions. The work to define the parameters and their associated uncertainties was done by the T2K Neutrino Interaction Working Group (NIWG) (de Perio et al. (2013))(de Perio et al. (2012)).

Overview of Neutrino Interaction Parameters

The uncertainty in our neutrino-nucleus interaction model has been parameterized by 20 parameters. A list of these parameters can be found in Table 6.9.[2] In the table,

[2] The default value of M_A^{RES} and CC1π norm.($E_\nu < 2.5$) in NEUT is 1.21 GeV and 1.0, but these values shown Table 6.9 are tuned by the MiniBooNE measurements (Aguilar-Arevalo et al.

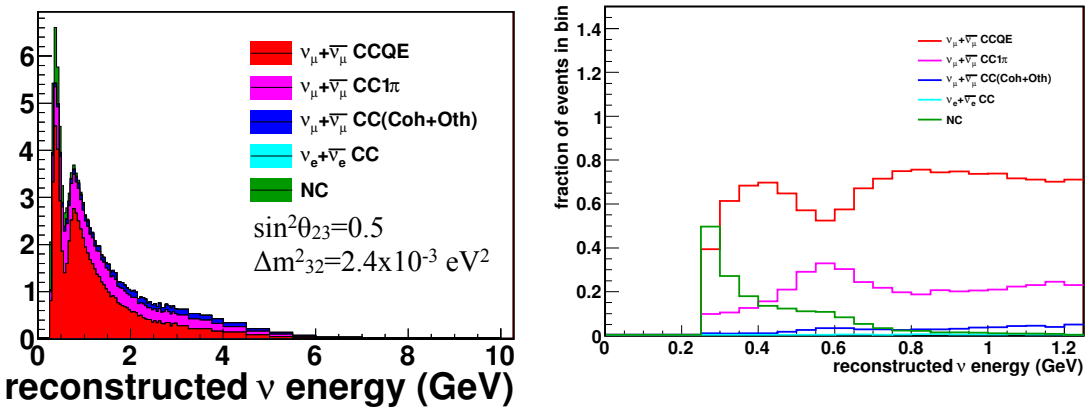

FIGURE 6.11: Left: Predicted reconstructed neutrino energy spectrum at Super-K. Spectrum has been broken down into interaction modes (stacked). Right: the fraction of events in each bin due to types of interaction modes.

the parameters have been sub-divided into two types, A or B, depending on the way they affect the calculation of the Super-K spectrum. The type of each parameter can also be found in the table. Type B parameters are simple factors that adjust the normalization of MC events related to certain interaction types. In other words, Equation (6.17) for type B interaction parameters are defined as

$$F^{t,\nu I}_{ijk'}(E^{rec}_i, E^{true}_j, f_{k'}) = f^{xsec,I}_b, \tag{6.22}$$

where I is for the interaction mode, and $f^{xsec,I}_b$ is both the value of the parameter and the reweighting factors for events. The index, I, indicates to which set of interaction modes the parameter applies. In addition to the mode, the normalization factor that applies sometimes is divided into ranges of true energies. The index b in Equation (6.22) indicates that the parameter applies to events with a true neutrino energy that falls in the bth of the systematic uncertainty binning. These type B parameters operate in the same way as the flux parameters described earlier. The ν index is omitted on the right hand side of Equation (6.22) as each parameter applies for all neutrino flux flavors.

(2011)).

In contrast to type B parameters, the uncertainty factors in Equation (6.17) for type A parameters are a little more complicated. The factors for this type quantify an interaction uncertainty that has a non-linear dependence on the parameter value. For such uncertainties, the factors, $F^{t,\nu I}_{ijk'}(E^{rec}_i, E^{true}_j, f_{k'})$, are not simple normalization factors but instead are parameterized as functions of $f_{k'}$, which are implemented using splines. For example, in Figure 6.12 we show an example of $F^{t,\nu,CCQE}_{ijk'}$ for a type A parameter, $f^{xsec}_{M^{QE}_A}$. This particular parameter is an input into the CCQE cross section calculation. Here one can see that the fractional change in the bin is not a simple linear function of $f^{xsec}_{M^{QE}_A}$. This curve is derived from simulating the spectrum for several values of $f^{xsec}_{M^{QE}_A}$. At each point shown on the curve, the change in the bin from the nominal value is recorded. These points are then used to define the spline.

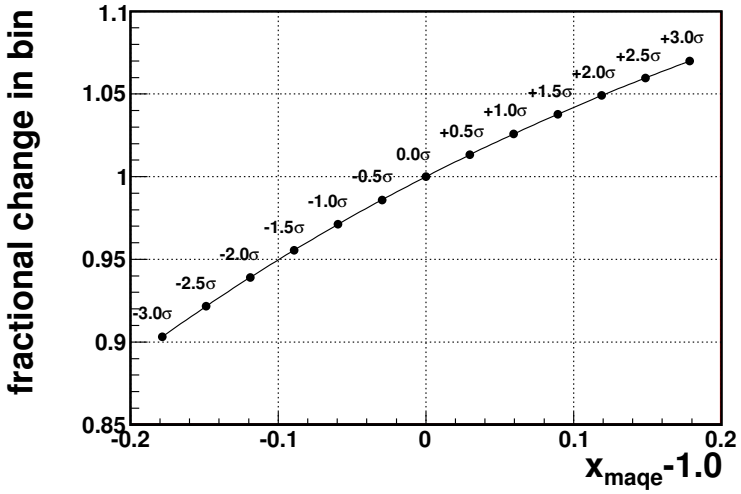

FIGURE 6.12: The M^{QE}_A response function for one energy bin of ν_μ CQQE event. The "σ" represents the error size of M^{QE}_A.

Table 6.9: Table of the neutrino interaction parameters. The nominal values and errors are constrained by external data. Some parameters are binned in E_ν, the true neutrino energy in GeV. The parameters are classified into two types by the way their effect is implemented in the neutrino spectrum calculation discussed in the previous section.

Parameter	Type	Nominal value	Error
M_A^{QE}	A	1.21 GeV/c^2	0.45 GeV/c^2
M_A^{RES}	A	1.41 GeV/c^2	0.22 GeV/c^2
p_F (^{16}O)	A	225 MeV/c	30 MeV/c
E_B (^{16}O)	A	27 MeV/c	9 MeV/c
Spectral function (^{16}O)	A	0 (OFF)	1 (ON)
CC other shape	A	0	0.4
W shape	A	87.7 MeV/c^2	45.3 MeV/c^2
Pion-less delta decay	A	0.0	0.2
CCQE norm. $E_\nu < 1.5$	B	1	0.11
CCQE norm. $1.5 \leqslant E_\nu < 3.5$	B	1	0.3
CCQE norm. $E_\nu \geqslant 3.5$	B	1	0.3
CC1π norm. $E_\nu < 2.5$	B	1.15	0.43
CC1π norm. $E_\nu > 2.5$	B	1	0.40
CCCoh norm.	B	1	1
NC1π Coh norm.	B	1	0.3
NCOth norm.	B	1	0.3
$\sigma_{\nu_e}/\sigma_{\nu_\mu}$	B	1	0.03
$\sigma_{\bar{\nu}_\mu}/\sigma_{\nu_\mu}$	B	1	0.2

Description of Parameters

Quasi-Elastic Parameters: M_A^{QE}, p_F, E_b, 'Spectral function', 'CCQE norm.'

A total of 7 parameters quantify the uncertainty in our model of quasi-elastic interactions. The M_A^{QE} parameter is found in the axial form factor, $F_A(Q^2)$, which is a part of the expression for the hadronic current. This form factor is a function of the momentum transfer, Q^2, and is assumed to have a dipole form where $F_A(Q^2) = F_A(Q^2 = 0)/(1 + Q^2/M_A^{QE^2})^2$. The value of M_A^{QE} is an important input in the calculation of the quasi-elastic scattering cross section. Note that this parameter affects both charged-current and neutral-current quasi-elastic scattering. The

nominal value and error for the parameter are 1.21 ± 0.20 GeV/c^2.

As discussed earlier in Section 6.4.2, the nuclear environment for the interacting nucleon is modeled as a relativistic Fermi gas. One requirement of this model is that the momentum of the out-going nucleon for all CCQE interactions must be above what is known as the Fermi momentum, p_F. The value the interaction generate, NEUT, uses for oxygen is 225 MeV/c. The out-going nucleon is also required to have enough energy to overcome the binding energy, E_b, of the nucleus. In NEUT, this value is set to 27 MeV for oxygen. The values and uncertainties of p_F and E_b, come from electron scattering data (Moniz et al. (1971)).

The spectral function uncertainty parameter attempts to quantify the uncertainty in the choice of model for the assumed momentum distribution, $n(p)$, of the nucleons in the nucleus. To get an estimate of our uncertainty, we compared the CCQE double differential cross section between our generator, NEUT, and another neutrino interaction generator, NuWro, which uses a different model for $n(p)$ (Juszczak et al. (2005)). In fact, the generator defines a model for the more general spectral function, $S(p, \mathcal{E})$, which defines the probability of finding a nucleon with momentum, p, and removal energy, $\mathcal{E}$ ($n(p)$ can be found by integrating over the possible values of $\mathcal{E}$). According to the scheme implemented by NuWro, both the Fermi momentum and nuclear potential are dependent on the of the interaction in the nucleus. Furthermore, this dependence is related directly to the position-dependent nucleon density. Such a scheme used by NuWro is known as the local density approximation (LDA). This is in contrast to NEUT, whose values of $n(p)$, and binding energy, E_b, apply to all regions of the nucleus. The motivation for this more sophisticated model of the spectral function is the improved agreement between electron-nucleus scattering data and models which include a spectral function versus ones that do not (Benhar et al. (2005)).

In our implementation of spectral function uncertainty, the difference between

the NuWro and NEUT differential cross section is calculated for p, θ, and E_ν bins. The value of the parameter in the fit is allowed to vary between 0 and 1. If the value is 0, the cross section from NEUT is used. If the value is 1, then the events in the MC are weighted by the difference between the NuWro and NEUT cross sections relative to the initial NEUT cross section. For intermediate values of the parameter, the weight comes from a linear interpolation between the NEUT and NuWro cross sections. Figure 6.13 shows the cross section in p, θ for $0.55 < E_\nu < 0.6$ GeV for NuWro and NEUT. The difference relative to NEUT, which is used to weight MC events, is also shown.

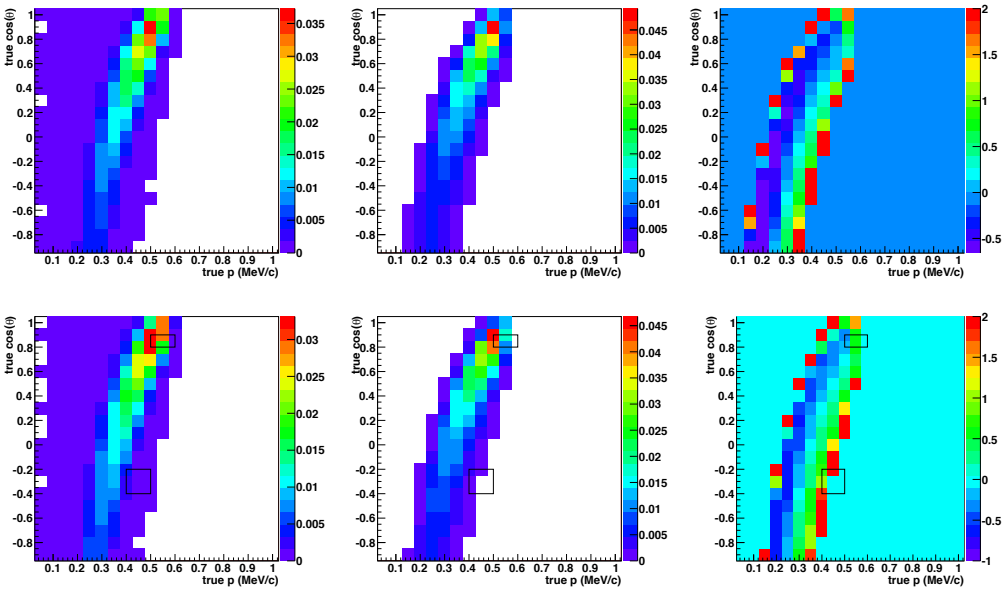

FIGURE 6.13: The cross section in p, θ for $0.55 < E_\nu < 0.6$ GeV for NuWro (left) and NEUT (middle). The difference relative to NEUT (right), which is used to weight MC events, is also shown. Figure by T2K Neutrino Interaction Working Group (de Perio et al. (2013)).

In addition to the parameters discussed, an uncertainty in the overall normalization provided for the CCQE cross section and is parameterized by three CCQE normalization parameters that cover the different energy regions listed in Table 6.9. The uncertainties in these parameters are driven by data. The lowest energy bin is

assigned an error of 11%, which comes from the flux uncertainty in the measurement of the most recent CCQE cross section, which was made by the MiniBooNE experiment (Aguilar-Arevalo et al. (2010)). The high energy normalization parameters are assigned a value of 30%, which comes from the disagreement in the implied CCQE cross section at high energies by the MiniBooNE and NOMAD experiments (Aguilar-Arevalo et al. (2010)) and (Lyubushkin et al. (2009)). This difference is considered implied because the MiniBooNE experiment only measured below 2.0 GeV while the NOMAD experiment measured at higher energies. However, if one fits the MiniBooNE cross section data by moving the value of M_A^{QE} to 1.35 GeV/c^2, the predicted cross section at the energies measured by NOMAD is high by about 30%. Figure 6.14 shows the MiniBooNE and NOMAD measurements of the CCQE cross section and illustrates this difference.

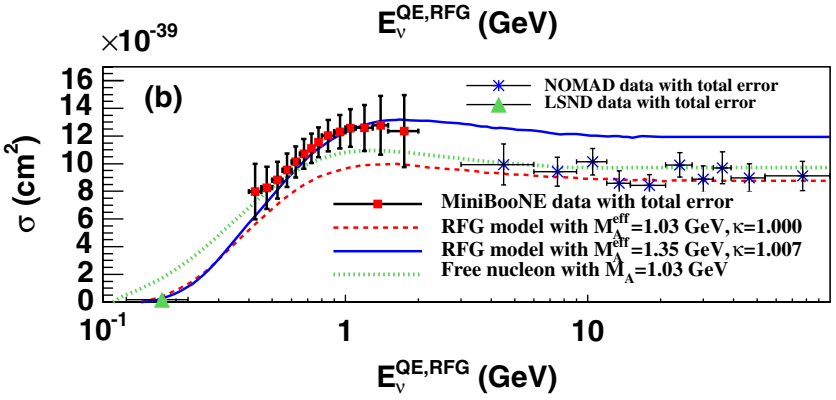

FIGURE 6.14: Differential cross section measurement of CCQE neutrino nucleus scattering. Taken from (Aguilar-Arevalo et al. (2010)).

Single Pion Resonant Production: M_A^{RES}, 'CC1π norm.', 'W shape','NC1π norm'

The parameters M_A^{RES}, 'CC1π norm.', 'W shape', and 'NC1π norm' quantify the uncertainty in our model for different neutrino-nucleus interactions that produce mesons via the creation of a nuclear resonance. Due to the energy range and the type of event selection of the analysis, the mesons we are primarily concerned with

are pions. The motivation for these parameters centers around parameterizing a fit of the NEUT generator to external resonant production measurements made by an experiment, MiniBooNE (Aguilar-Arevalo et al. (2008)).

As described in Section 6.4.2, NEUT uses the Rein-Sehgal model to describe the production of single pions from CC and NC interactions. Like the quasi-elastic model, the formula for the cross section includes form factors in the hadronic currents. For the resonant production modes, there is an axial mass parameter, M_A^{RES}, whose role is analogous to the M_A^{QE} parameter for the quasi-elastic cross sections discussed above. Changing the M_A^{RES} parameter causes the expected spectrum to distort along with changing the number of events expected. In order to provide an additional degree of freedom to just the overall number of events, two normalization parameters, labeled as 'CC1π norm', are introduced to cover energies below and above 2.5 GeV. The lowest energy bin covers the range where MiniBooNE has made measurements of the resonant production cross sections.

Similar to the 'CC1π norm' parameter, the 'W shape' and 'NC1π norm' parameters are data-motivated to provide degrees of freedom to help fit the shape and normalization, respectively, of the MiniBooNE NCπ^0 cross section measurement. The 'NC1π norm' parameter is a simple normalization scale factor for all events in the spectrum produced by such modes. The W-shape is more complicated and was introduced in order to provide a way to distort the pion momentum distribution for resonance interactions. It applies to interactions where a nucleon and either a pion or photon is produced by the decay of the resonance. Events are weighted by a function, r, dependent on the invariant mass, W, and the given value of the W-shape parameter, f_{Wshape}^{Xsec}, such that

$$r(W; f_{Wshape}^{xsec}) = \alpha \frac{f_{Wshape}^{xsec}}{(W - W_0)^2 + {f_{Wshape}^{xsec}}^2/4} P(W; m_\pi, m_N), \tag{6.23}$$

where $P(W; m_\pi, m_N)$ is the phase space probability for a two-body decay of a particle with mass W into particles with mass m_π and m_N; and α is a normalization factor calculated to leave the total nucleon-level cross section unchanged. W_0 is set to 1218 MeV/c^2. The nominal value of f^{Xsec}_{Wshape} is set to 87.7 MeV/c^2 which comes from a fit to the nominal W distribution produced by NEUT. (Note that this parameter also effects resonant production of photons as well. In that case m_π changes to E_γ in the above equation.) Figure 6.15 shows the effect of the parameter on NEUT prediction of the neutral current π^0 differential cross section. The nominal value is shown in red. The black points show the MiniBooNE data. The figure demonstrates that this parameter allows a way to smoothly vary from the nominal prediction to a prediction that better agrees with the data.

In order to set the nominal value and uncertainties on these parameters, a fit was made to MiniBooNE external data. The fit was to differential cross section measurements of CCπ^+, CCπ^0, and NCπ^0. This external fit is performed with M_A^{RES}, 'CC1π norm', 'W shape', and 'NC1π norm' along with other parameters mostly pertaining to other high energy interaction channels. Figure 6.16 shows the different bins used along with the nominal and best-fit distributions. The result of the fit is used to set the nominal value and uncertainties for M_A^{RES} and the lowest energy 'CC1π norm' parameter (below 2.5 GeV). The fit also sets the uncertainty for the NC1π norm. The difference in the nominal and best-fit values for the W-shape is used to set the uncertainty on this parameter.

Remaining Parameters:

Pion-less Delta Decay

In NEUT, 20% of all Δ particles may decay without producing any pions. This "Pion-less Delta Decay" (PDD) mode is potentially important as the resulting final state particle will be a single muon. This makes PDD interactions look the same

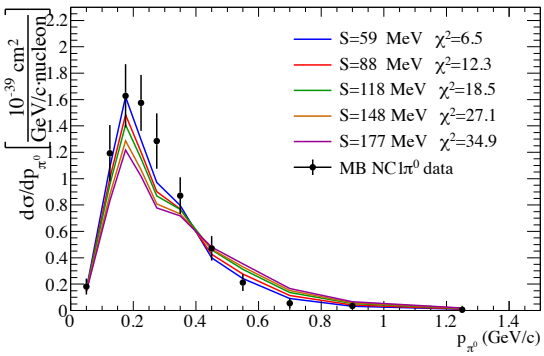

FIGURE 6.15: Example of NEUT prediction (color lines) versus MiniBooNE data (black crosses) for several values of the W-shape parameter, labeled in the plot as S. The line with the closest value to the nominal is in red. Data from (Aguilar-Arevalo et al. (2008)). Figure from (de Perio et al. (2012)).

as CCQE interactions in the Super-K detector. We therefore allow the fraction of Δ resonances that decay without a pion to be a parameter in our analysis. We require that the variation of this parameter does not change the total amount of Δ production but only changes the relative fraction of decays to a pion to decays that do not. We use 20% as the nominal value and define the 1 σ uncertainty as 20% as well.

CC coherent pion production

In this interaction mode, instead of interacting with a single nucleon, a neutrino may interact coherently with the entire nucleus. Because the nucleus is much heavier than the neutrino, any out-going particles will be traveling mostly along the direction of the incoming neutrino. For charged-current reactions, this includes the muon and a pion traveling the forward direction.

Measurements looking for this type of interaction have not found it (Hiraide et al. (2008)). Therefore, we define a simple normalization factor as a parameter for this mode with an assigned 100% uncertainty on its value.

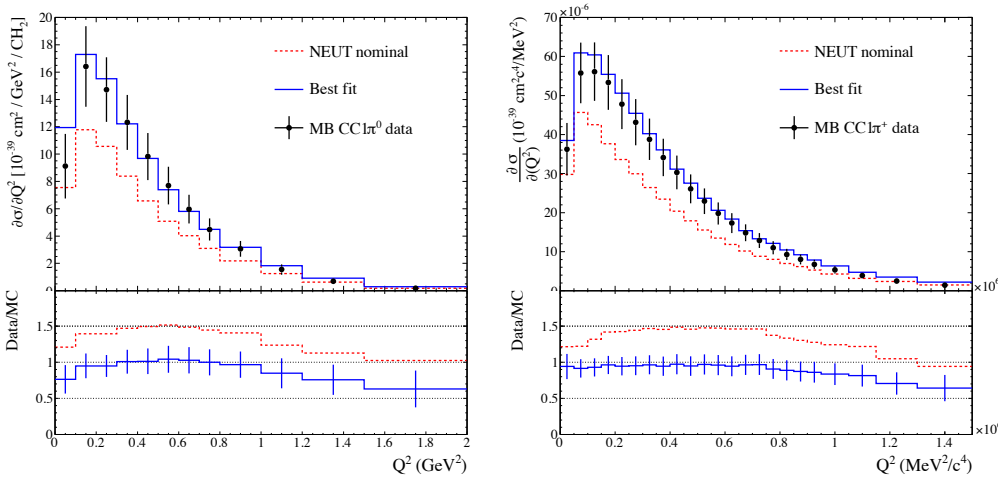

(a) CC1π^0 Q^2

(b) CC1π^+ Q^2

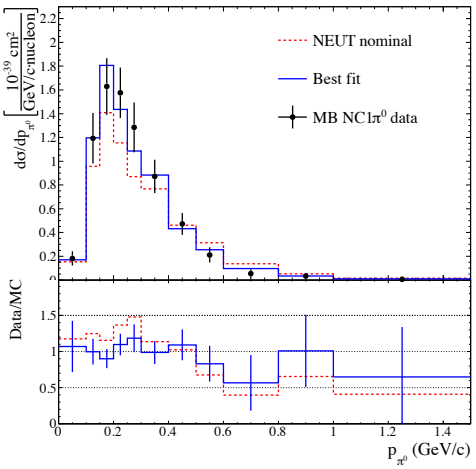

(c) NC1π^0 $|\mathbf{p}_{\pi^0}|$

FIGURE 6.16: Differential cross sections from MiniBooNE used to estimate the uncertainty in our model of single pion production via nuclear resonances. The dashed red line shows the nominal cross sections from our event generator NEUT. The blue line shows a fit to the data using a collection of parameters quantifying the uncertainty in our model. The information from this fit is used to set the values and uncertainties for parameters in the oscillation analysis fit presented in this thesis. Figure from (de Perio et al. (2012)).

CC other Shape

For the remaining charged-current interactions at higher energies, we define a normalization parameter where the weight applied is

$$w = 1 + f^{xsec}_{CCotherShape}/E_\nu. \tag{6.24}$$

The scale factor takes this form because the charged-current inclusive cross section divided by energy has been observed to be flat at high energies. Figure 6.17 demonstrates this finding and also shows a recent measurement from the MINOS experiment (Adamson et al. (2010)). MINOS measured deviations from this trend at low energy. We use the largest deviation of about 10% to set the size of the uncertainty on this parameter.

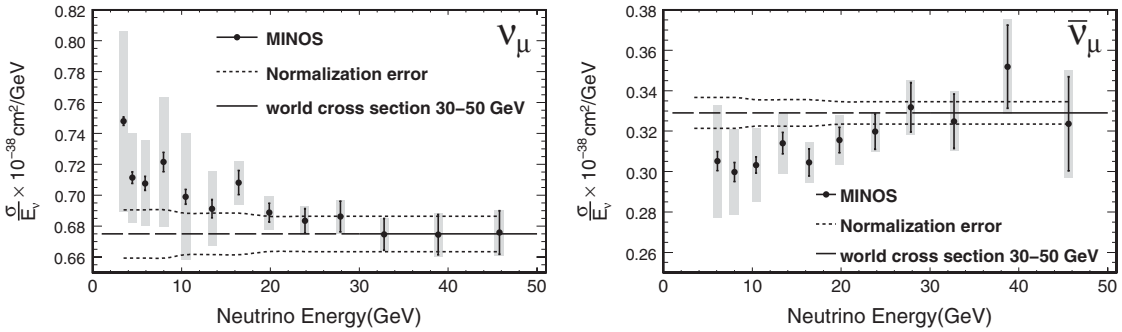

FIGURE 6.17: Neutrino (left) and anti-neutrino (right) charged-current inclusive cross section per nucleon divided by energy measured on iron. The data points are from a measurement by the MINOS experiment (Adamson et al. (2010)). The average of the world data is shown in the solid black line above 30 GeV along with error bars shown by the dashed black line. Extrapolation to lower energies is also shown by the solid dashed line. Deviations from the flat cross section divided by energy line is seen, but still within systematic uncertainties. We use the largest deviation at 4 GeV, 10% to set the uncertainty for high-energy charged-current cross sections. Figure from (Adamson et al. (2010)).

Other NC interactions

A normalization parameter is defined for the remaining neutral-current interactions not considered above. This includes DIS and resonant production of mesons other

than the pion. There is not much data to assign a compelling uncertainty to this parameter, so an uncertainty of 30% is assigned to these interactions based on the data and MC disagreement in the measurement of the NCπ^0 cross section measurement. However, the uncertainties on these modes are not critical for our analysis as the contributions from these interactions play a very small role in the model of the muon neutrino energy spectrum at Super-K.

$\sigma_{\nu_e}/\sigma_{\nu_\mu}$ uncertainty

The difference in cross section for electrons and muons have been studied in (Day and McFarland (2012)). The authors of the study point out two potential differences in the electron and muon neutrino cross sections not accounted for by our generator, NEUT. One difference in the cross section for electrons comes from radiative corrections to the tree-level CCQE calculation which occur at low energies. This could be up to 10% at very low energies, < 0.2 GeV, that are mostly below the relevant energies in our measurement. The other possible correction for electron CCQE interactions has to do with the possible contributions from form factors in the hadronic current that conventionally are assumed to be zero by symmetry and conservation arguments. The authors calculate that experimental evidence still allows as much as a 3% correction at low energies from non-zero values of these form factors. We use this last value as an additional uncertainty on the ν_e-nucleus cross section. This parameter is treated as a simple normalization factor. It is important to note, however, that the expected fraction of electron neutrino interactions in the final analysis sample is small, about 1% or less.

$\sigma_\nu/\sigma_{\bar{\nu}}$ uncertainty

The estimate of this uncertainty comes from a rough comparison of the predicted and observed quasi-elastic cross section measured by MiniBooNE, which shows about

a 20% disagreement. The reasoning behind the estimate of the uncertainty in our model from anti-neutrino cross sections is that this discrepancy for anti-neutrinos might be similar, though the sign of the discrepancy (opposite or the same) is unknown. So an additional 20% normalization uncertainty is given to anti-neutrino events. Most of the effect of anti-neutrinos come at higher energies above the oscillation dip, so the analysis is not affected much by this parameter.

6.6.3 Final State and Secondary Interactions

We use $\pi^{\pm}$-^{12}C cross section data, used to tune the model of pion final state interactions, to estimate the uncertainty in the modeling of pion final state interactions (FSI) in the nucleus and pion secondary interactions (SI) in Super-K (de Perio (2011)). Recall that the modeling of these two distinct types of interactions is done by the same routines. The tuning to the data is done by adjusting the probabilities of the different type of interactions: quasi-elastic scattering, absorption, and charge exchange. The adjustments in the probabilities were incorporated through a re-weighting scheme of the the individual interactions.

This weighting scheme was also used to investigate the uncertainty. This was done by defining 16 sets of probability adjustments that were simultaneously 1 sigma away from the tuned values as determined by the change of χ^2 calculated from the data and prediction. Figure 6.18 compares the $\pi^{\pm}$-^{12}C cross section data with predictions using the NEUT FSI model for the different parameter variations.

The 16 parameter sets were used to weight the expected reconstructed neutrino energy spectrum at Super-K. The variations from these sets were passed onto the simulation and the resulting spectra were calculated. The variations in the spectrum were then used to construct a covariance matrix via

$$V_{ij} = \frac{1}{16}\sum_{k=1}^{16}(N_i^{nom} - N_i^k)(N_i^{nom} - N_j^k), \tag{6.25}$$

where N_i^k are the number of events in the ith bin of the expected reconstructed energy spectrum due to the kth variation, and N_i^{nom} is the number of events due to the nominal parameter values. Note that the variation in the spectrum comes both from changes in the final state interactions but also from secondary interactions. The bins used in the equation are partitioned by reconstructed energy and also by interaction type and neutrino flavor. The definitions of the bins are found in Table 6.10.

Table 6.10: Bins used for the final state and secondary interaction uncertainty parameters.

Bin Number	Interaction	Flux	Energy Range
1	CCQE	ν_μ, $\bar{\nu}_\mu$	$E_\nu^{recon} < 0.4$ GeV
2	CCQE	ν_μ, $\bar{\nu}_\mu$	$0.4 < E_\nu^{recon} < 1.1$ GeV
3	CCQE	ν_μ, $\bar{\nu}_\mu$	$E_\nu^{recon} > 1.1$ GeV
4	CCnonQE	ν_μ, $\bar{\nu}_\mu$	$0 < E_\nu^{recon} < 30$ GeV
5	CC	ν_e, $\bar{\nu}_e$	$0 < E_\nu^{recon} < 30$ GeV
6	NC	all flavors	$0 < E_\nu^{recon} < 30$ GeV

For the parameterization of this uncertainty, we define six parameters with each acting as a normalization factor for the events that fall in the bins defined in Table 6.10.

6.6.4 Super-K Event Selection Efficiencies

For each of the selection criteria we use to build the event sample for the final analysis, we estimate its contribution to the uncertainty in the final predicted spectrum. Table 6.11 lists these selection criteria along with their contributions to the total uncertainty. A description of the selection can be found in Section 5.2.

The Super-K atmospheric neutrino sample is used to estimate these uncertainties. For all but the single-ring and μ-like criteria, the data and MC distributions of the variables used to make the selection are compared and their differences are used to define an uncertainty on the variables. The cut values used are then varied by the

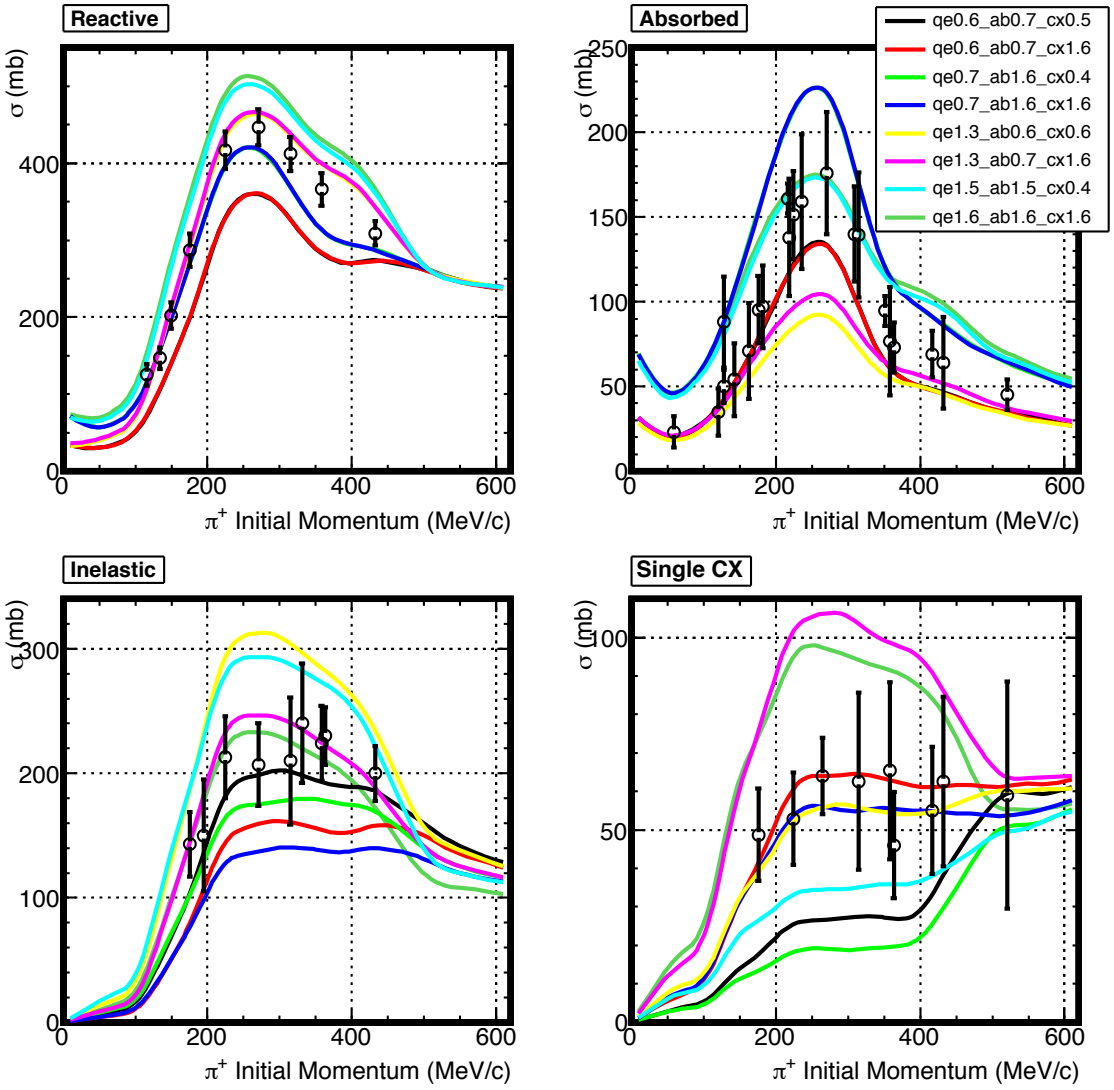

FIGURE 6.18: Comparison of π^+-^{12}C cross section for data (black points) and NEUT predictions (colored lines) for 8 sets of values of the NEUT FSI cascade parameters. The sets are 1σ variation curves from the best fit parameters. These sets are used to study the variation in the neutrino energy spectrum at Super-K due to the uncertainty in the FSI and SI model. Ultimately, the variations help us define the systematic uncertainty parameters for the FSI and SI. Figure from (de Perio et al. (2013))

measured uncertainty and the change in the number of events due to each cut is calculated. The changes in percent are listed in Table 6.11 and are small for most, because the selection variables are modeled well and the cuts are typically made far away from where the neutrino events are expected to be measured. The exception to this is the uncertainty in the selection for one-ring events and the uncertainty in the identification of μ-like tracks.

The method for estimating the remaining uncertainties due to the selections for the number of rings (1) and the flavor of the particle (μ-like) is different and more complicated. Effectively, a comparison is made between the number of events observed and prediction in the Super-K atmospheric neutrino sample. However, the comparison is done using a χ^2 fit to the data in order to separate the uncertainty in the predicted number of events due to the selection criteria and the uncertainty due to the neutrino interactions model and assumed atmospheric neutrino flux (Kameda (2013)). Furthermore, care was taken to estimate the uncertainty as a function of reconstructed neutrino energy and for different neutrino flavors and interaction modes. This fit also provided a means to find correlations between energy, flavor, and interaction bins for the single-ring selection uncertainty. The results of the fit are summarized by the following covariance matrix:

$$\begin{array}{ccc} E_\nu^{rec} < 0.4\ GeV & E_\nu^{rec} = 0.4 \sim 1.1\ GeV & E_\nu^{rec} > 1.1\ GeV \\ \left(\begin{array}{ccc} \sigma_1^2 & 0.76\sigma_1\sigma_2 & 0.46\sigma_1\sigma_3 \\ & \sigma_2^2 & 0.71\sigma_2\sigma_3 \\ & & \sigma_3^2 \end{array} \right), \end{array} \tag{6.26}$$

where $\sigma_1 = 1.1\%, \sigma_2 = 2.9\%, \sigma_3 = 3.5\%$.

The Super-K detector uncertainty parameters are implemented in the calculation of the predicted spectrum through the use of simple normalization factors on bins of

Table 6.11: Breakdown of the systematic errors for the SK detector efficiency. The uncertainty is assumed to affect the spectrum uniformly over the entire range of reconstructed energy,E^{rec}, unless otherwise noted. The uncertainty estimates are made for different flavors and interaction categories as listed in the table. For CC $\nu_e + \bar{\nu}_e$, a 100% efficiency uncertainty is applied at all reconstructed energy. This information is omitted from the table.

Selection Criteria	ν_μ CCQE	ν_μ CCnonQE	NC
Hits in Veto<16	$\ll$1%		
Event not flashing PMT	1%		
Inside Fiducial Volume	1%		
# of decay electron$\leqslant 1$	1%		
$p_\mu \geqslant 250$ MeV/c^2	$\ll$1%		
Single-track Event	1.1% ($E_\nu^{rec} < 0.4$ GeV) 2.9% ($E_\nu^{rec} = 0.4 \sim 1.1$ GeV) 3.5% ($E_\nu^{rec} > 1.1$ GeV)	8.1%	21.8%
Ring is μ-like	0.3%		55.0%

reconstructed neutrino energy, such that

$$F_{ik'}^{r,\nu I}(E_i^{rec}, f_{k'}) = f_b^{SK}, \tag{6.27}$$

where the appropriate f_b^{SK} is chosen based on the neutrino interaction, flux, and reconstructed energy. The components of b follow the definition given in Table 6.10, which is the same binning as the FSI parameters.

6.6.5 Super-K Energy Scale

The energy calibration of the Super-K simulation is checked using four types of data samples. These measurements are briefly discussed in Section 4.4.7. For the analysis, we use the largest observed disagreement, 2.4%, to set the size of the uncertainty in the energy scale.

We incorporate the uncertainty in the energy scale as a shift in the spectrum represented by a parameter, $f^{e-scale}$. We implement this shift by re-calculating the number of events in each bin of the reconstructed spectrum, N_i^{rec}. The modification

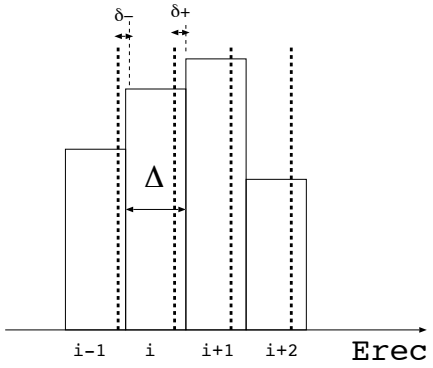

FIGURE 6.19: Schematic view of calculation of the effect of energy scale.

of the bin is found by calculating the number of incoming and outgoing events due to a change in the edge of the bins. Figure 6.19 shows the schematic view of the calculation. For a change in the energy scale by $f^{e-scale} = \alpha\%$, E^{rec} changes to $E^{rec} \cdot (1 + f^{e-scale})$, therefore the edge of the i-th bin, $E_i^{rec} \pm \Delta/2$, effectively changes to $(E_i^{rec} \pm \Delta/2) \cdot (1 + \alpha)$, where Δ is the width of the bin. As a result, the N_i^{rec} is re-calculated by

$$N_i^{rec'} = N_i^{rec} - N_i^{rec} \cdot \frac{\delta+}{\Delta} + N_{i-1}^{rec} \cdot \frac{\delta-}{\Delta}, \tag{6.28}$$

where

$$\delta+ = E_i^{rec} + \Delta/2 - (1 - f^{e-scale}) \cdot (E_i^{rec} + \Delta/2) \tag{6.29}$$

$$\delta- = E_{i-1}^{rec} + \Delta/2 - (1 - f^{e-scale}) \cdot (E_{i-1}^{rec} + \Delta/2). \tag{6.30}$$

6.7 ND280 Constraint on Parameter Uncertainties

The ND280 measurement plays an important role in tuning our model of the Super-K spectrum. The ND280 ν_μ charged-current inclusive data described in Chapter 5 is used to set and constrain the parameter values of the flux and some of the interaction action parameters described above. This is done via a separate χ^2 fit between

the ND280 data and the predicted distribution of events at the near detector (Hartz et al. (2013)). The ND280 prediction is built using the same flux model and neutrino interaction generator, NEUT, and therefore also uses almost all of the same parameters for the flux and cross sections to parameterize the effect of these uncertainties. Furthermore, parameters for the systematic uncertainties related to the ND280 selection are included.

The ND280 fit produces new central values for the flux and interaction parameters along with a covariance matrix that constrains the error. Importantly, this matrix also captures the correlations between the flux and cross section uncertainties. These "post-fit" parameter values and the covariance matrix are passed along to the oscillation fit. In the table summarizing the parameters, Tables 6.6 and 6.7, the post-fit value for the parameters constrained by the ND280 fit are listed along with the prior values for comparison. One result of the ND280 fit is the presence of strong correlations between the flux and interaction parameters. This correlation occurs because the ND280 detectors measure the total neutrino rate which varies directly with the amont of flux and strength of the different interactions. As a result, the fit defines anti-correlations between the two parameter types. These correlations reduce the amount of freedom in the uncertainty parameters and therefore quantify the reduction in the spectrum uncertainty that comes from the ND280 measurement. Note that not all the parameters are affected by the ND280 fit. The data at the near detector are primarily sensitive to CCQE and charged-current resonant production of pions so only the subset of the parameters that pertain to these interactions is constrained.

After the best-fit prediction was found, a goodness of fit test was performed and a p-value 0.64 was calculated indicating that the final tuned flux and interaction model fits the data well.

Figure 6.20 shows the value of the uncertainty assigned to the parameters in the

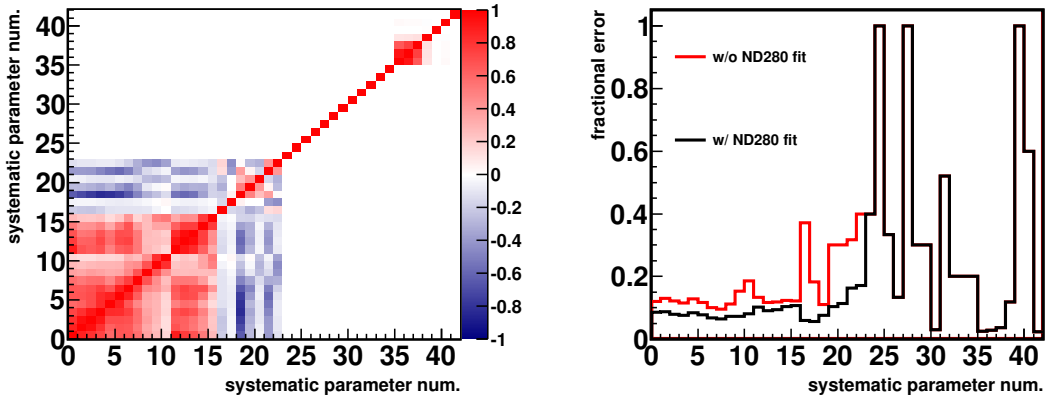

FIGURE 6.20: Left: the covariance error matrix for the uncertainty parameters in our analysis. The first 16 parameters govern the flux, the next 7 parameters are for cross section parameters whose uncertainties are constrained by the ND280 fit. Note the anti-correlation between the flux and cross-section that comes from the ND280 fit. Right: the uncertainty in fraction in each parameter. The red line indicates the uncertainty size before the ND280 fit. The black line is the uncertainty after the ND280, which for some parameters are greatly reduced.

oscillation analysis fit before and after the ND280 fit is performed. The figure demonstrates the constraint the ND280 measurement provides on our uncertainty in the spectrum. Figure 6.21 further demonstrates this by showing the prediction spectrum at Super-K along with 1-sigma uncertainty bands before the ND280 fit in black and after in red. The uncertainty bands come from randomly varying the systematic parameters by their assigned uncertainties while taking correlations into account. The uncertainty is reduced considerably. Also, the ND280 fit pulls the expectation down. As it turns out, the pre-fit ND280 prediction, based on prior parameter values from the flux tuning and external neutrino interaction measurements was higher than the data observed.

6.8 Effect of Systematic Uncertainties

We measure the effect of the systematic uncertainty in two ways, by calculating the variation in the total number of events and the variation in the number of events in the binned spectrum. We generated 20,000 toy experiments drawing a random

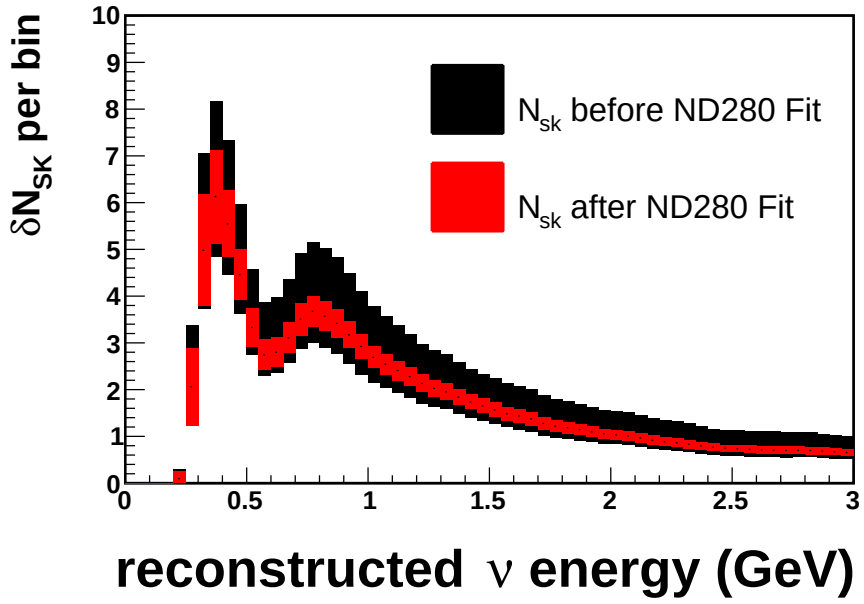

FIGURE 6.21: Uncertainty in the spectrum from all the systematic parameters as measured by the variation in the number of events per bin. Spectrum is zoomed in below 2 GeV in order to focus on the oscillation dip. The figure shows the size of the uncertainty in the number of events in each bin of the spectrum before the ND280 fit in red and after the ND280 fit in black. As one can see, ND280 tunes the normalization of the MC downward while also constraining the uncertainty in the spectrum.

value of the systematic errors based on their uncertainty and taking correlations into account. We then produced a distribution for both the number of events and the binned spectrum. Table 6.12 shows the variations in the total number of events broken down by different systematic error types. The total variation is 8.1% when including the ND280 constraint. The largest type of error when computing in this manner is the combined selection efficiency and hadronic interaction uncertainties which produces a 5.6% variation in the total number of events. However, this measure is only on the normalization. We expect the spectrum shape to provide a lot of the constraint on the parameters.

To get a better sense of which systematic parameters affect the shape, we calculated the variation in the expected number of events in each bin due to different

Table 6.12: Uncertainty in the spectrum from all the systematic parameters as measured by the variation in the total number of events. The variation in the events are shown for the uncertainties before the ND280 fit and after ND280. Note that only a subset of the parameters are directly constrained by the ND280 fit. However, the other parameters are indirectly affected as the mixture of interaction modes after the ND280 fit are adjusted.

Systematic Uncertainty	**Before ND280 Fit RMS/Mean N_{SK} (%)**	**After ND280 Fit RMS/Mean N_{SK} (%)**
ND280 Constrained Flux and Xsecs	21.6	2.7
SK Only Xsecs	5.9	4.9
Combined SK Detector and Hadronic Interactions	6.3	5.6
SK Detector Uncertainties	5.3	4.8
Hadronic Interactions in Oxygen and Water	3.4	3.0
$\sin^2\theta_{12}, \Delta m^2_{12}$, $\sin^2\theta_{13}$, δ_{CP}	0.2	0.2
Total	23.4	8.1

sets of parameters. Figure 6.22a shows the 1-sigma uncertainty in the spectrum after the ND280 fit. The total variation is shown by the total width of the color block. The individual contribution of different types of parameters is illustration by their relative size to the total width. The plot is zoomed in on the spectrum below 2 GeV in order to concentrate on the region of the oscillation dip which has the most shape information. The two types of the parameters that play the largest role is the selection efficiency parameters along with interaction parameters not constrained by the ND280 fit. Figure 6.22b shows the fractional variation in each bin due to the different sets of uncertainties.

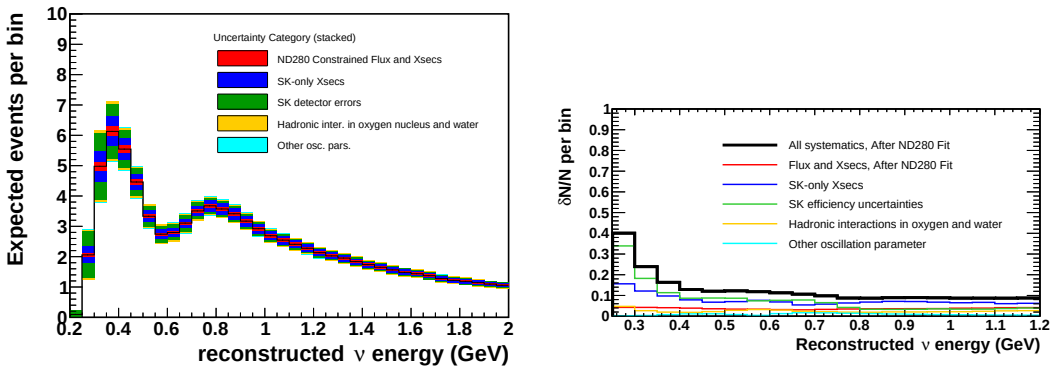

(a) 1-sigma uncertainty band

(b) Fractional change in bin due to each type of systematic

FIGURE 6.22: Left: Uncertainty in spectrum by all systematics as calculated by the variation in the number of events in each bin. The total width of the bars in the total uncertainty due to all systematic error types. The breakdown within the bar tries to reflect the relative contribution of each error type to the total uncertainty. Fraction of bar, f, for each type, x, determined by: $f_x = \frac{\sigma_x^N}{\sum_x \sigma_x^N}$. Note that the normalizing sum is not added in quadrature. Right: Fractional amount of variation in each bin due to all (black) and individual (color lines) systematic uncertainties.

6.9 Fitting Method

Now that we have defined the likelihood in eq. 6.4 and defined the MLE through eq. 6.5, the task of estimating the oscillation parameters from the data transforms into an optimization problem. To solve it, we employ a common optimization algorithm called gradient descent. We use a numerical implementation of this algorithm, called MINUIT, which is a software package often used by the particle physics community (James and Roos (1975)).

Another thing to note is that because of the almost symmetric nature of the muon disappearance oscillation formula (see Section 3.7.2), we expect it is possible for the negative log likelihood surface we are exploring to have two local minima, one for a value above and below the maximal disappearance value of $\sin^2(\theta_{23})$. Therefore, when we fit, we do so twice: once by seeding the fit with the value of $\sin^2(\theta_{23})$ of 0.4 and then another time with 0.6. We then compare the result of the two fits and

choose the result to be the one with the lower negative log-likelihood value.

6.10 Summary

Finally, with the details of the analysis defined, we proceed to validation studies that use simulated fake data to understand the behavior of the analysis. This is the topic of the next chapter. After that we discuss the results of the analysis run on the data.

7

Study of Analysis Method

In this chapter we present the results of toy MC studies where we performed a large number of fits on a set of fake data sets in order to understand the behavior of our analysis. One important finding of this study is that because of the relatively low number of events in our data sample, our analysis will need to take into account the effects of fitting parameters near a physical boundary. We also use these studies to understand the systematic uncertainties that have the largest effect on the analysis.

7.1 Generating Toy Data Sets for Study

Toy MC studies were performed to study the biases, if any, that exist in the oscillation parameter measurement.

We generated 10,000 fake data sets at two oscillation points in $\sin^2(\theta_{23})$ and Δm^2_{32} at 6.57×10^{20} POT. The oscillation parameter values were

1. near maximal mixing, (0.5, 2.4×10^{-3} eV^2/c^4) and

2. away from maximal mixing and maximal disappearance, (0.4125, 2.35×10^{-3} eV^2/c^4).

When the toy MC sets are generated we include variations in both the systematic uncertainty parameters and statistical fluctuations in the expected number of events. Almost all the systematic uncertainty parameters were thrown assuming a multivariate Gaussian distribution with a mean and covariance defined in Chapter 6. We use the Cholesky decomposition method to draw random values from the multivariate Gaussian distribution. The one exception is the spectral function systematic uncertainty parameter, whose value is chosen separately from a one-sided Gaussian with mean 0 and sigma of 1. Only positive values were chosen for this parameter.

7.2 Study of Bias of Analysis from Fits to Toy Data Sets

We performed the analysis exactly as we would on the data on each of the toy data sets. For these studies, we only perform the analysis assuming the normal hierarchy. We expect the analysis to behave similarly if we were to assume the inverted hierarchy.

7.2.1 Distribution of Best-fit Parameter Values

Figure 7.1 shows the distribution of the best-fit oscillation parameter values for $\sin^2(\theta_{23})$ and Δm^2_{32} for toy data sets generated at maximal mixing (Figure 7.1a) and further away from maximal mixing (Figure 7.1b).

There are two features common to both plots. For one, the distribution of the best-fit parameter values is symmetric about $\sin^2(\theta_{23})$ =0.514. This is the value of $\sin^2(\theta_{23})$ that corresponds to maximal disappearance. The reason for this symmetrical distribution is that our analysis is not very sensitive to the octant of $\sin^2(\theta_{23})$. The reconstructed neutrino energy spectrum is expected to look very similar for values of $\sin^2(\theta_{23})$ equidistant from the value of maximal disappearance. To understand why, recall the ν_μ-disappearance probability expression from Equation (3.38)

$$P_{\mu\to\mu} \approx 1 - \sin^2(\Phi)(1 - (2\sin^2\theta_{23}\cos^2\theta_{13} - 1)^2). \tag{7.1}$$

Here we can see that the oscillation probability is symmetric about some value of $\sin^2(\theta_{23})$. Figure 7.2 shows the expected reconstructed energy distribution for two values of $\sin^2(\theta_{23})$ equidistant from the maximal disappearance value. The spectra are almost identical. Which side of maximal disappearance the best-fit oscillation parameters are fitted to depends mostly on random fluctuations of the spectrum causing one side to have a slightly smaller value of $-2\Delta \ln \mathcal{L}$.

The second feature in the distribution of the best-fit parameters in Figure 7.1 is that there is a band of toy data sets with a best-fit value of $\sin^2(\theta_{23})$ near 0.514. This is the value of $\sin^2(\theta_{23})$ that gives maximal muon neutrino disappearance. The characteristic property of the toy data within this band is that their average spectrum is below the spectrum expected for maximal disappearance. This is shown in Figure 7.3 where the average spectrum for toy data sets whose fitted values lie within a band near $\sin^2(\theta_{23})$ =0.514 is plotted (by the solid black line) in comparison to the expected spectrum for maximal disappearance (shown by the blue dashed line). The interpretation of this result is that for the data sets fitted within the band, some part of the spectrum has fluctuated lower than what the oscillation effect can account for near or below the dip. For these fits, the fitted value of $\sin^2(\theta_{23})$ is forced to choose the value of $\sin^2(\theta_{23})$ that gives maximal disappearance in order to best match the low fluctuation. In these cases, the fit is up against the physical boundary imposed by the oscillation probability formula. In such cases, the value of the Δm^2_{32} and the systematic uncertainties are then the only effective degrees of freedom the analysis has to best match the spectrum.

We note here that the possibility of these fluctuations in the data will be a recurring theme later on when we analyze the results. We, therefore, refer to these class of fits as "boundary" fits as the value of $\sin^2(\theta_{23})$ is fitted against the physical boundary at $\sin^2(\theta_{23})$ =0.514 where maximal disappearance occurs.

Because these boundary fits are due to fluctuations in the spectrum, we assume

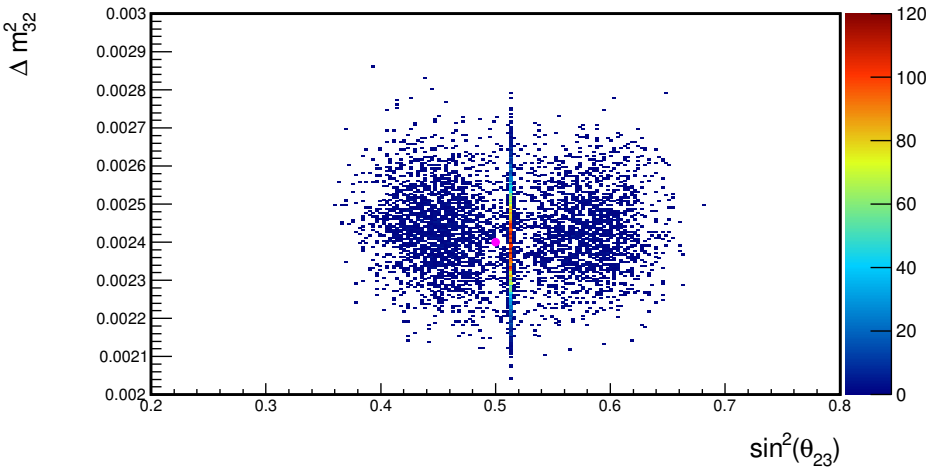

(a) Fits from toys generated near maximal mixing and disappearance.

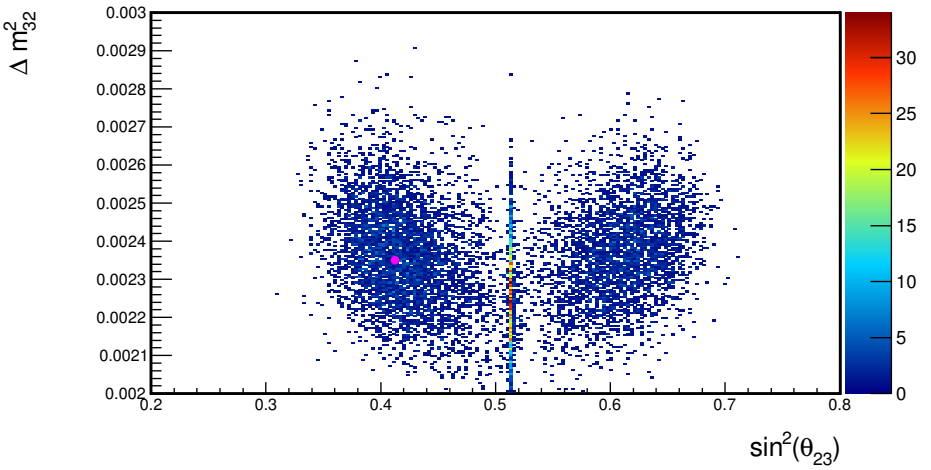

(b) Fits from toys generated away from maximal mixing and disappearance.

FIGURE 7.1: The distribution of best fit oscillation values coming from fits of an essemble of 10,000 toy MC data sets. The data sets in (7.1a) were generated with the true oscillation parameter values for ($\sin^2(\theta_{23})$,Δm^2_{32}) were set to (0.5,2.4 $\times 10^{-3}$ eV^2/c^4) at 6.57$\times 10^{20}$ POT. The data sets in (7.1b) were generated with the oscillation parameters ($\sin^2(\theta_{23})$,Δm^2_{32}) set to (0.4125,2.35 $\times 10^{-3}$ eV^2/c^4) with the same POT. In both figures, the generation point is labeled with the pink dot. The toy MC sets are made by radomly varying the systematic uncertainty parameter values which were drawn from a multivariate normal distribution.

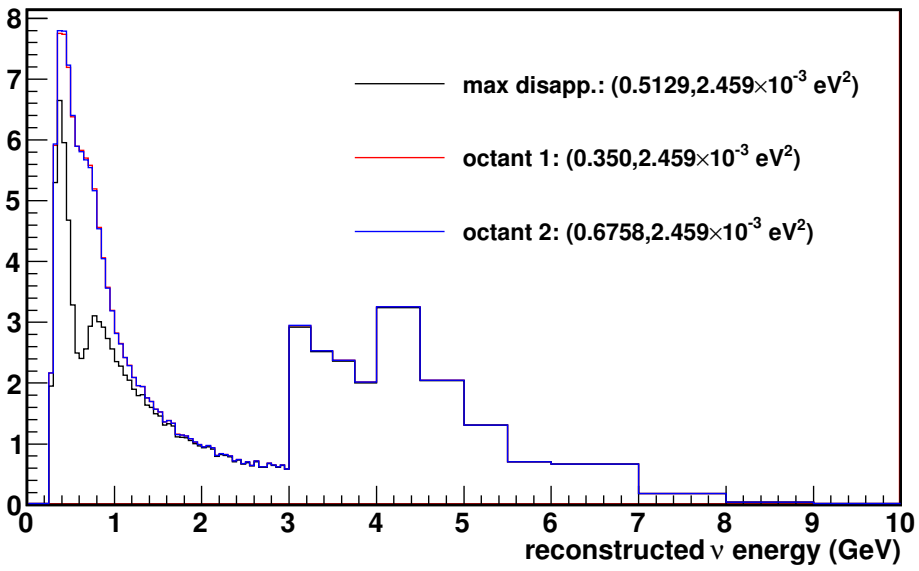

FIGURE 7.2: Predicted reconstructed energy spectra for different values of $\sin^2\theta_{23}$ when $\sin^2\theta_{13} = 0.0251$. The black plot is the spectrum at the value of maximal disappearance according to equation (3.37), $\sin^2\theta_{23} = 0.5129$. The red and blue plots show the spectra for values of $\sin^2\theta_{23}$ equal distance from 0.5129. Non-zero θ_{13} causes a shift of the maximal disappearance point, which is also the point around which the oscillation probability is approximately symmetric.

that when the expected number of events in the data set is large enough, "boundary" fits will no longer occur. Figure 7.4 shows the distribution of $\sin^2(\theta_{23})$ and Δm^2_{32} for ten thousand toy data sets generated for parameters $(\sin^2\theta_{23}, \Delta m^2_{32})$ at $(0.35, 2.33 \times 10^{-3}\ \mathrm{eV}^2/\mathrm{c}^4)$ for 6.39×10^{22} POT. The POT is almost 100 times the amount of data in our current data set. This amount is unrealistic as T2K will likely never run long enough to gather this much data. However, we chose this data set in order to prove our assertion that boundary fits are caused by statistical fluctations and will eventually disappear at high statistics. This is important to rule out the possibility that there is some problem in our analysis implementation that is causing the best-fit values to be biased towards maximal disappearance. In the figure, we see that the

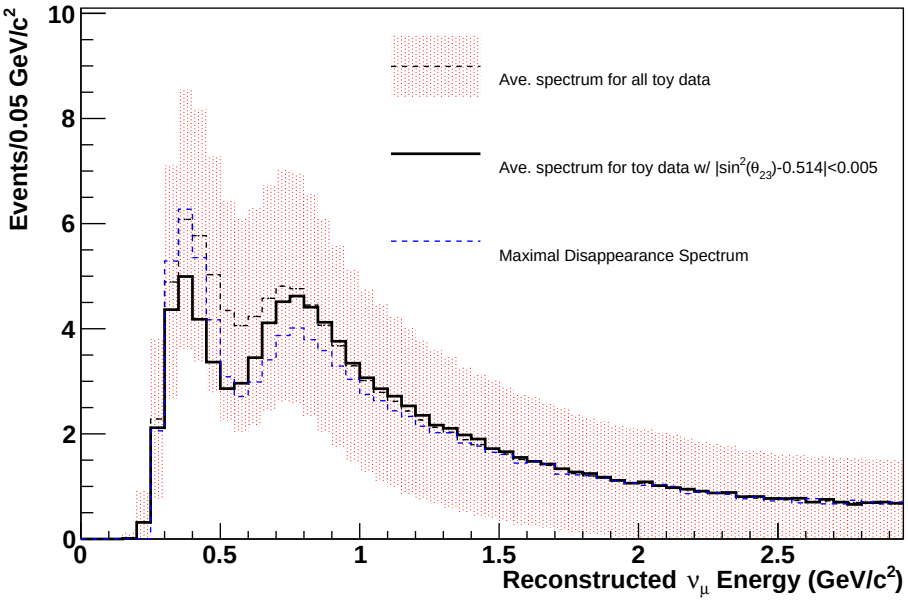

FIGURE 7.3: Average reconstructed energy spectrum for an example set of fake experiments where the experiments are separated by the fitted values of $\sin^2(\theta_{23})$. The dashed black line is the average spectrum for all fake experiments generated at $(\sin^2(\theta_{23}),\Delta m^2_{32})=(0.4125,2.35 \times 10^{-3}$ eV^2/c$^4)$. The shaded red region shows the approximate standard deviation in the spectrum one would expect due to statistical fluctuations. The black solid line is the average of all toy data sets whose fitted value of $\sin^2(\theta_{23})$ falls within a band around 0.514. The blue dashed line shows the expected spectrum for maximal disappearance (i.e. when $\sin^2(\theta_{23})$ =0.514). One can see that for those fits that fall within the band near 0.514 the average spectrum falls below the maximal disappearance expectation in the region at and below the oscillation dip. For these fits, the fitted value of $\sin^2(\theta_{23})$ is forced to choose the value of $\sin^2(\theta_{23})$ that gives maximal disappearance – in other words the fit is up against the physical boundary imposed by the oscillation probability formula. For these fits, the value of Δm^2_{32} and the systematic uncertainties are then the only effective degrees of freedom the analysis has to best match the spectrum.

band of fits near $\sin^2(\theta_{23})$ =0.514 no longer occur.

7.2.2 Estimate of the Bias in the Analysis

Using the toy MC data sets, we study the bias of the analysis by comparing the distribution of fitted parameter values to the true parameter values used to generate the toy data.

Figure 7.5 shows the fitted oscillation parameter value for toy fits generated

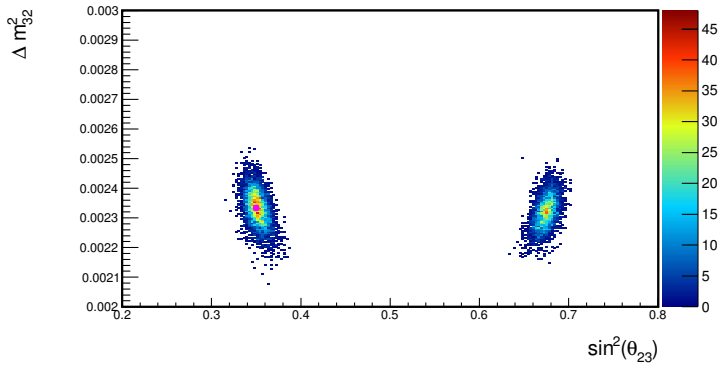

(a) Distribution of best-fit oscillation parameters

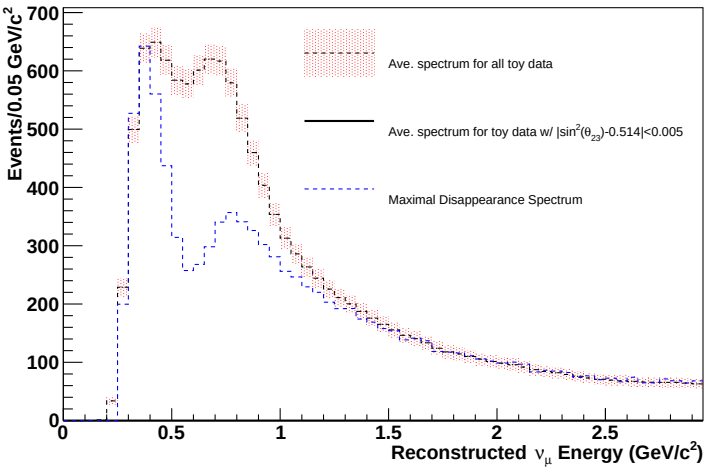

(b) Average spectrum of toy data sets

FIGURE 7.4: (top) The best-fit oscillation values for a set of 10,000 toy MC sets generated for the parameters, $(\sin^2\theta_{23}, \Delta m^2_{32})$, with $(0.35, 2.33 \times 10^{-3}$ eV^2/c^4 at 6.39×10^{22} POT, i.e. 100 times our current data set. The generation point is labeled with the pink dot. The toy MC sets are made by varying the systematic parameter values whose values are drawn from a multivariate normal distribution. At this POT, the number of events are large enough that fluctuations in the reconstructed energy spectrum cannot produce "boundary" fits which fall in a band near $\sin^2(\theta_{23})$ =0.514. (bottom) The average spectrum for the toy data sets (dashed black line). The shaded red region shows the one standard deviation range in the number of events expected for this POT. One can see that the chances of the spectrum fluctuating below the expected spectrum for maximal disappearance (dashed blue line) is remote. None of the ten thousand toy data sets produced a "boundary" fit, which is why the black line histogram is not present.

near (7.5a) and far (7.6b) from maximal mixing. In both figures, one can see in the $\sin^2(\theta_{23})$ distributions the two features observed and discussed above in the 2D distributions: (1) the distribution is symmetric around maximal disappearance reflecting the inability of the analysis to determine the octant of $\sin^2(\theta_{23})$ and (2) the band of fits near $\sin^2(\theta_{23})$ =0.514 for the $\sin^2(\theta_{23})$ distribution which comes from "boundary" fits.

In Figure 7.6 the normalized difference between the fitted and true oscillation parameter values is shown. The difference is normalized by the size of the fitter error on the oscillation parameters. This normalized difference is called the "pull" and is defined as

$$\text{pull} = \frac{\theta_{\text{fit}} - \theta_{\text{true}}}{\sigma_{\text{fit}}}, \tag{7.2}$$

where θ_{fit} and θ_{true} are the true and fitted oscillation parameter values, respectively, and σ_{fit} is the error on the parameter value given by the fitter used in the analysis. The pull gives us a measure of the difference of the true and fitted values. The inclusion of the fit error takes into account the amount of uncertainty for a given fit.

For Δm^2_{32}, the bias is relatively small at about 1% or less than the true value. This estimate comes from subtracting the mean of the fitted Δm^2_{32} distribution from the true value and normalizing by the true value.

For $\sin^2(\theta_{23})$, the bias is not small and derives from two sources. One source of bias comes from the large fraction of "boundary" fits relative to all toy fits. These fits will choose a value of $\sin^2(\theta_{23})$ =0.514. Also, there is an additional bias coming from the fit choosing the wrong octant. Due to the complicated nature of these two sources of bias, simply estimating the bias in $\sin^2(\theta_{23})$ by taking the ratio of the fitted mean value to the true value will be uninformative.

Because the distribution of $\sin^2\theta_{23}$, though understood, is non-Gaussian, we provide an alternative measure of the bias in $\sin^2\theta_{23}$ by slightly modifying the fit pro-

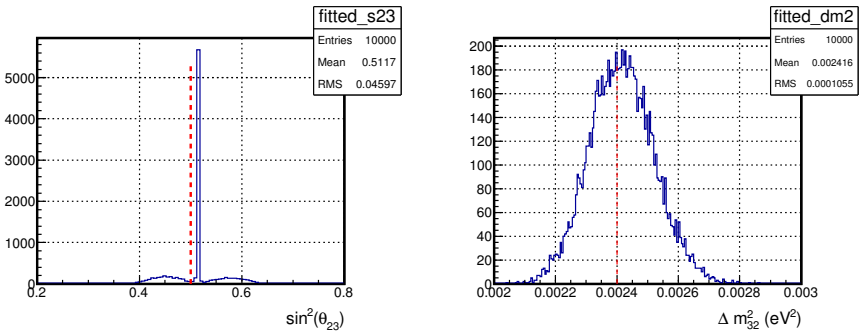

(a) Fitted values for toy data generated at maximal mixing.

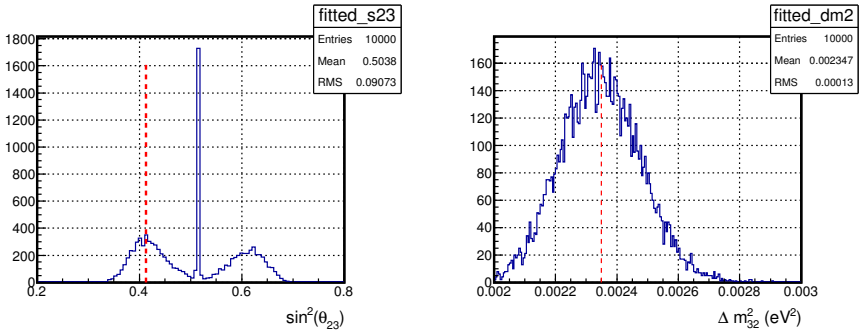

(b) Fitted values for toy data generated away from maximal mixing.

FIGURE 7.5: Fitted oscillation parameter value for toy fits generated near (7.5a) and far (7.5b) from maximal mixing. The location of the true oscillation parameter values used to generate the toy data sets are shown by the red dashed line.

cedure. As mentioned in Section 6.9, when we fit each toy data set, we perform the fit twice. One fit is seeded with the value $\sin^2\theta_{23}$=0.4; the other fit is seeded with the value $\sin^2\theta_{23}$=0.6. The fit with the best-fit parameters from the fit with lowest χ^2 value is chosen as the solution. This is to done in order to let the fitter test both local minima. In the alternative measure, we only fit the fake experiments with one seed. This seed is chosen to be in the same octant as the true oscillation value. Figure 7.7 shows the distribution of $\sin^2\theta_{23}$ for fake experiments generated at $(\sin^2\theta_{23}, \Delta m^2_{32}) = (0.35, 2.33\times10^{-3})$ at the current POT. Here we can see that most of the fits settle on a value of $\sin^2\theta_{23}$ that is in the same octant as the true value.

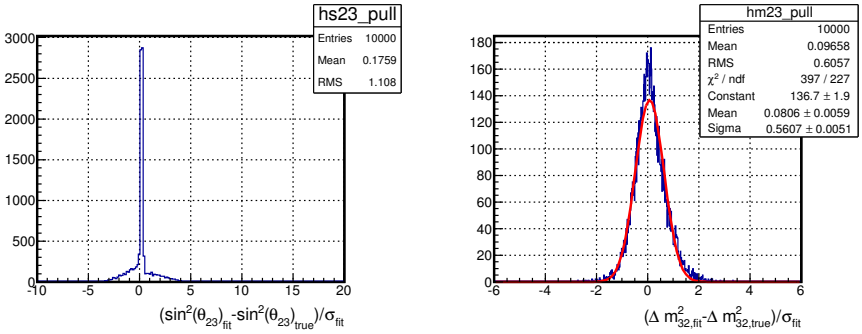

(a) Pull values for toy data generated at maximal mixing

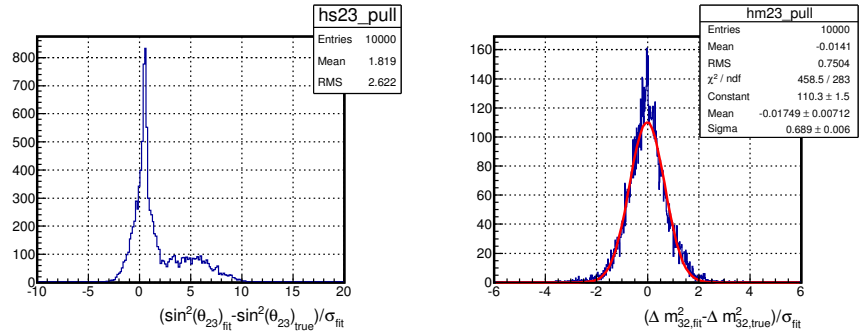

(b) Pull values for toy data generated away from maximal mixing

FIGURE 7.6: Pulls of the oscillation parameters for toy fits generated near (7.6a) and far (7.6b) from maximal mixing. The expression for the pull is given in Equation (7.2). This quantity measures the size of the bias in the fit.

Using the the mean of the pull distribution for the alternative measure of the bias in $\sin^2\theta_{23}$, we find the bias is about 3% percent. This is due in part to the presence of boundary fits, which can be seen as the spike in the bias distribution. Therefore, we expect the bias to fall as the statistics of the sample increases. Unfortunately, this bias is unavoidable, but it is understood. Consequently, we believe the fitter is behaving as expected.

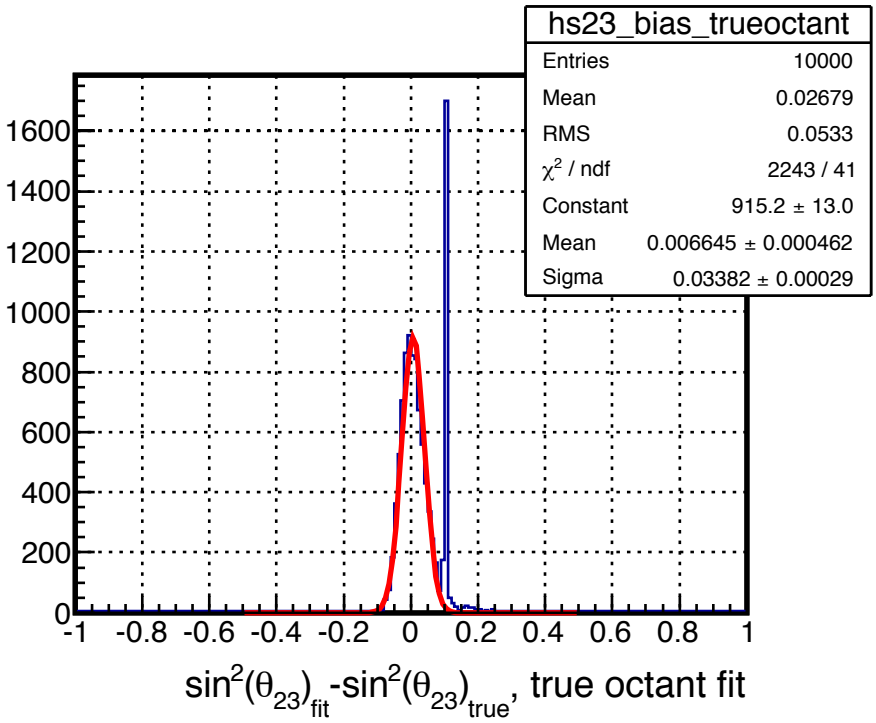

FIGURE 7.7: The best-fit value less the true value for $\sin^2(\theta_{23})$ for a set of 10,000 toy experiments generated with the parameters, $(\sin^2\theta_{23}, \Delta m^2_{32})$, set to a value of $(0.35, 2.33\times10^{-3}\ \mathrm{eV}^2/\mathrm{c}^4)$ at 6.57×10^{20}. When fitting the toy experiments, the fitter was seeded only with a value of the oscillation parameters in the same octant as the generating values. Typically, the fit to a data set is done twice, with one fit seeded with a value of $\sin^2\theta_{23}$ in the first octant and the other with a value in the second octant. For the plots here, we seed the fit only with a value in the same octant as the true value. Using this modified procedure, we quantify any bias in $\sin^2\theta_{23}$ around the peak of the true solution without dealing with the complication caused by occasional statistical fluctuations which result in the fit sometimes preferring the wrong octant.

7.3 Sensitivity Studies

In addition to studies of the bias, we calculate the expected constraints on $\sin^2(\theta_{23})$ and Δm^2_{32} given the current size of the data set (6.57×10^{20} POT). We generated 400 fake data sets and then ran the analysis on them in the same way as the data. The expected constraint was then calculated by averaging the $-2\Delta\ln\mathcal{L}$ surfaces. We present the results as constant $-2\Delta\ln\mathcal{L}$ =2.3 and $-2\Delta\ln\mathcal{L}$ =4.6 contours that approximate the 68% and 90% CL allowed regions, respectively.

The fake data sets are generated by first choosing the random values of the systematic uncertainty parameters, using them to generate a predicted spectrum, and then to generate toy measurements of the reconstructed energy spectrum. This is the same way toy data sets were drawn for the bias studies as described in Section 7.1.

Fake data sets are generated for two oscillation parameters sets:

1. $(\sin^2\theta_{23}, \Delta m^2_{32}) = (0.5,\ 2.4 \times 10^{-3}\ \mathrm{eV}^2/\mathrm{c}^4)$

2. $(\sin^2\theta_{23}, \Delta m^2_{32}) = (0.396,\ 2.39 \times 10^{-3}\ \mathrm{eV}^2/\mathrm{c}^4)$.

The first was chosen as it was the measured best-fit by the previous T2K numu-disappearance measurement. The second value was chosen based on the best-fit values measured by the MINOS experiment[1] (Adamson et al. (2013)). For both sets, we assume the normal hierarchy. Fits assuming the inverted hierarchy are expected to be very similar.

Besides studying the expected sensitivity of the full analysis, additional contours were made by fixing the values of different sets of systematic parameter values both when the fake data sets were generated and when the fit was performed. This was done in order to evaluate the contribution of each systematic parameter type.

The following groups are considered:

- "No syst.": only statistical contribution. All systematic parameters are fixed. All oscillation parameters fixed.

- "All syst.+osc.": All systematic errors are fitted. All oscillation parameters are fitted. This is the configuration used for the data fit.

- "All syst. Fixed osc.": All systematic errors are fitted. All oscillation parameters are fixed.

[1] To be precise, MINOS measured $\sin^2(2\theta_{23}) = 0.957$ which is then converted to a value of $\sin^2(\theta_{23})$. However, there are two solutions to this conversion, so we arbitrarily choosing the one $< \frac{\pi}{4}$, i.e. the first-octant solution.

- "ND280 fit (after)": the systematic parameters associated with ND280 fit. These are varied with the their errors before/after the ND280 fit. Other systematic parameters are fixed.

- "Other ν int.": the other ν interaction parameters not refined by the ND280 fit. Other parameters are fixed.

- "SK&FSI-SI": the combined parameters of the SK detection efficiency and FSI-SI parameters. Other parameters are fixed.

The results of the toy data fits for the first oscillation parameter values are shown in Figure 7.8. Contours for the second oscillation parameter are shown in Figure 7.9. The sensitivity contours show us that the group of systematic uncertainty parameters that have the largest effect on the analysis are the combined Super-K detector and hadronic interaction uncertainties (i.e. FSI-SI) and the neutrino interaction uncertainties not constrained by the ND280 fit. The interaction uncertainties have the biggest effect on both the mass splitting and mixing angle constraint. The combined detector and hadronic interaction uncertainties are just as important as as combined detector and hadronic uncertainties for the mixing angle.

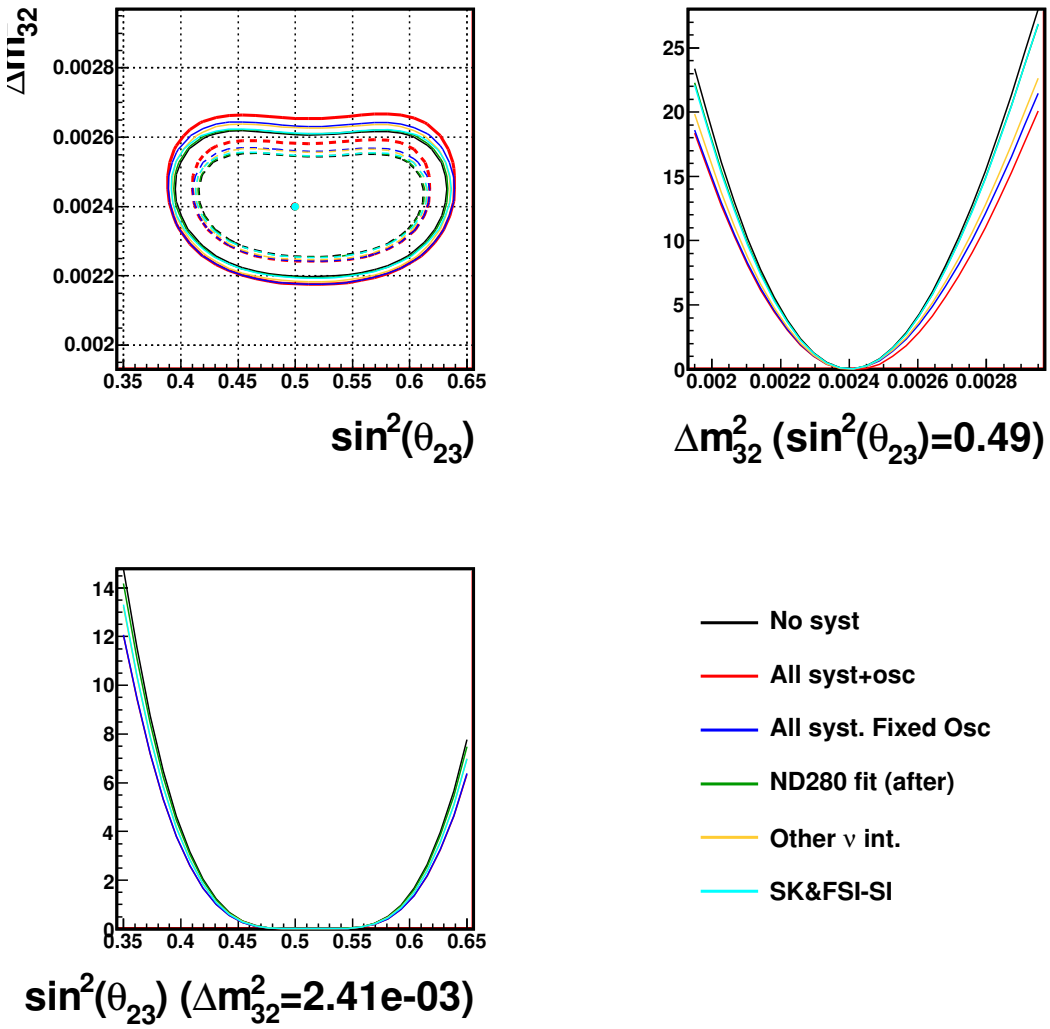

FIGURE 7.8: Expected allowed contour (upper right) and average $-2\Delta \ln \mathcal{L}$ slices for $(\sin^2\theta_{23}, \Delta m^2_{32}) = (0.5, 2.4 \times 10^{-3}\ \mathrm{eV}^2/\mathrm{c}^4)$ at 6.57×10^{20} POT. The contour plot (upper left) shows the 90% (68%) CL contours with a solid (dashed) line based on a constant $-2\Delta \ln \mathcal{L}$ =4.6 (2.3). The $-2\Delta \ln \mathcal{L}$ =4.6 slices are shown across the bin value closest to the best fit value for the full fit.

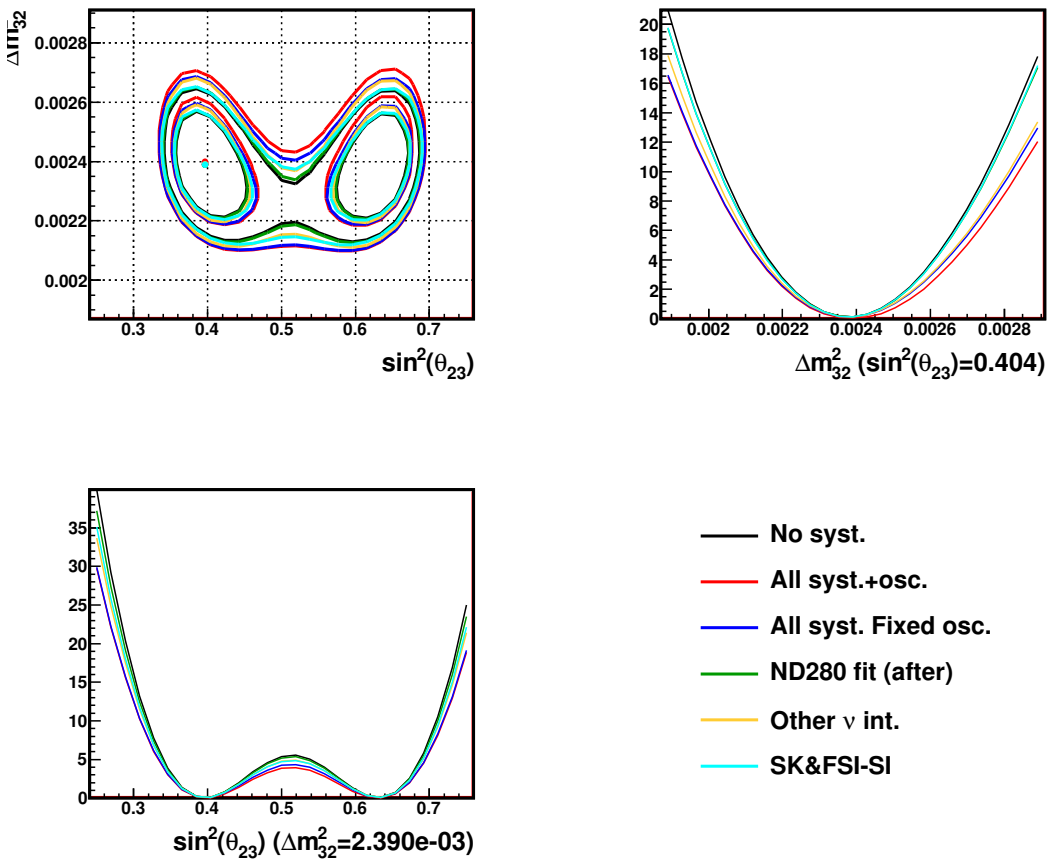

FIGURE 7.9: $\Delta\chi^2$ map (left top), expected allowed contours (right top) and average $\Delta\chi^2$ slices of $\sin^2\theta_{23}$ (bottom left) and Δm^2_{32} (bottom right) for the MINOS 2012 best fit oscillation parameters: $(\sin^2 2\theta_{23}, \Delta m^2_{32}) = (0.957, 2.39 \times 10^{-3}\ \mathrm{eV}^2/\mathrm{c}^4)$ at 6.57×10^{20} POT. The contour plot (upper left) shows the 90% (68%) CL contours with a solid (dashed) line based on a constant $\Delta\chi^2$ limit. The $\Delta\chi^2$ slices are shown across the bin value closest to the best fit value. Several contours are shown for fits with different sets of systematic error parameters.

8

Results of the Analysis

8.1 Fit Result

8.1.1 Best-fit Oscillation Parameters and $-2\ln\mathcal{L}$

We perform the ν_μ-disappearance fit on the data in $\sin^2\theta_{23}$-Δm^2_{32} twice. One fit is performed with the normal hierarchy assumed, and another separate fit is performed with the inverted hierarchy assumed.

Normal Hierarchy Fit

For the normal hierarchy fit, the best-fit oscillation parameters are

$$(\sin^2\theta_{23}, \Delta m^2_{32}) = (0.514, 2.51 \times 10^{-3}\ \mathrm{eV}^2/\mathrm{c}^4).$$

The best-fit value of $\sin^2(\theta_{23})$ corresponds to the value where there is a maximal amount of muon neutrino disappearance which is different from the maximal mixing value of $\sin^2(\theta_{23})$ =0.5. As we will see, however, the analysis of this data set cannot distinguish between these two values of $\sin^2(\theta_{23})$ with any significance.

The best-fit spectrum had a -2ln$\mathcal{L}$ value of 1039.69. The expected number of events at the best-fit point is 121.41. For the other oscillation parameters (the ones

we treated as nuisance parameters) the best-fit values and errors from the fitter, MINUIT, were

$$\begin{array}{rl} \sin^2(\theta_{12}) & 0.311 \pm 0.016 \\ \Delta m^2_{12}\ (\mathrm{eV}^2/\mathrm{c}^4) & (7.5 \pm 0.2) \times 10^{-5} \\ \sin^2(\theta_{13}) & 0.0251 \pm 0.0034 \\ \delta_{CP} & (0.52 \pm 3.0)\pi. \end{array}$$

The fitted values of the other oscillation parameters did not deviate far from their input values. All values are well within their 1-σ uncertainties (for those parameters where σ is defined). The large error on δ_{CP} is due to the fact that the predicted spectrum has a very small dependence on the value of this parameter. This weak constraint on δ_{CP} is expected.

Inverted Hierarchy Fit

For the inverted hierarchy, the best-fit oscillation parameters are

$$(\sin^2\theta_{23}, \Delta m^2_{13}) = (0.511, 2.48 \times 10^{-3}\ \mathrm{eV}^2/\mathrm{c}^4).$$

Similar to the normal hierarchy case, the best-fit value of $\sin^2(\theta_{23})$ corresponds to the value where there is a maximal amount of muon neutrino disappearance. Note that the maximal disappearance value of $\sin^2(\theta_{23})$ is expected to be different for the normal and inverted hierarchy. The best-fit spectrum fit has a final $-2\ln\mathcal{L}$ value of 1039.68. Note that the mixing angle used in the inverted hierarchy fit is Δm^2_{13}.

Because the $-2\ln\mathcal{L}$ value is lower in the inverted hierarchy fit, the data very slightly prefer the inverted hierarchy assumption. However, the difference between the two values is only 0.01 which means that the data and analysis cannot distinguish the two mass hierarchies with any significance. This is a result we expect.

For the other oscillation parameters in the inverted hierarchy fit, the best-fit values and errors from MINUIT are

$$
\begin{array}{rl}
\sin^2(\theta_{12}) & 0.311 \pm 0.016 \\
\Delta m^2_{12}\ (\mathrm{eV}^2/\mathrm{c}^4) & (7.5 \pm 0.2) \times 10^{-5} \\
\sin^2(\theta_{13}) & 0.0251 \pm 0.0034 \\
\delta_{CP} & (0.61 \pm 3.2)\pi
\end{array}
$$

The expected number of events at the best-fit oscillation parameters is 121.39.

8.1.2 Best-fit neutrino energy spectrum

Our model of the predicted best-fit spectrum describes the observed spectrum well. Figure 8.1 shows the expected energy spectrum and the ratio to the predicted spectrum with no oscillations for the best-fit value of $\sin^2\theta_{23}$-Δm^2_{32} (assuming the normal hierarchy). The good agreement can be seen by visual inspection but is also supported by the results of a goodness-of-fit test.

8.1.3 Goodness-of-fit Tests

Unfortunately, the value of the likelihood we get from the MLE does not provide provide a meaningful statistic of how well the model fits the data (Heinrich,J (2003)). Therefore, in order to perform a goodness-of-fit test, we bin the data and our prediction of the spectrum in order to calculate the value of the χ^2 statistic, which can give us a probability that the data we observed comes from our predicted distribution. The binning was chosen so that each bin has about 10 events. Having enough events in each bin is important because with low occupancy in most bins, the significance of deviations between the observed and predicted spectrum will be overestimated (Yates (1934)). Conversely, binning too coarsely washes out the details in the shape of the observed and predicted spectrum and causes the binned χ^2 statistic to be a poor test of our analysis. Ultimately, we binned the data into energy bins of (0.0∼0.4, 0.4∼0.7, 0.7∼1.0, 1.0∼2.0, 2.0∼30.0) GeV.

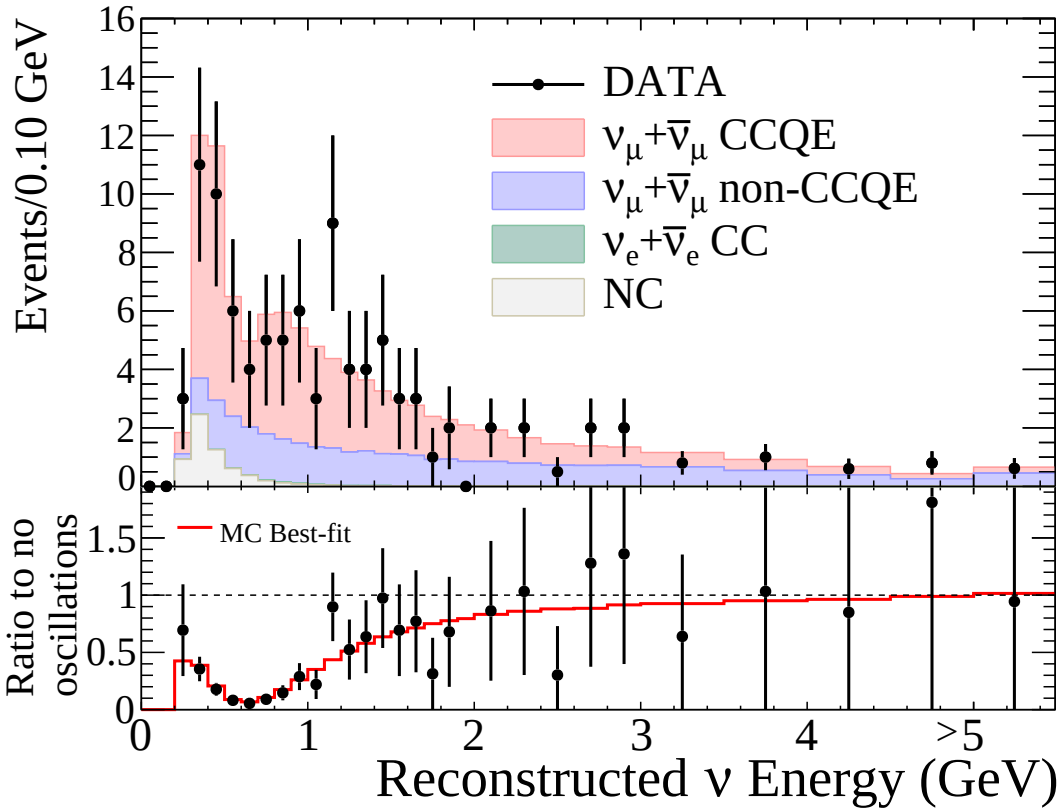

FIGURE 8.1: (Top) E_ν^{rec} distribution for the data (black point) and the best-fit predicted spectrum (stacked histogram). The predicted spectrum shows the component interaction types that make up the total. The signal channel, ν_μ CCQE, is shown in red. Background channels ν_μ CC non quasi-elastic (CCnonQE), ν_e CC, and NC interactions are shown in blue, green, and gray, respectively. The predicted ν_e CC contribution is too small to be visible in the figure. (Bottom) The ratio of the number of events in each bin to the number of expected events assuming no oscillation is shown for the data (black) and best-fit predicted spectrum (red).

The simple binned χ^2 for the goodness-of-fit test is defined as

$$\chi^2_{gof} = 2\sum_{i=1}^{5}\left[n_i^{obs} \times \ln\left(\frac{n_i^{obs}}{n_i^{exp}}\right) + n_i^{exp} - n_i^{obs}\right] + \mathbf{f}^T M^{-1}\mathbf{f}, \tag{8.1}$$

where n_i^{obs} and n_i^{exp} are the number of events observed and expected in each bin i, respectively, $\mathbf{f}$ is a vector of systematic error parameter values, and M is the covariance matrix for the parameters in $\mathbf{f}$. The χ^2_{gof} obtained with the data is 0.799 (0.796) at the best-fit point assuming the normal (inverted) hierarchy. This gives us a p-value of 93.9% for both hierarchies using the χ^2 distribution.

To double-check this goodness-of-fit p-value, we generate the χ^2 distribution from 10,000 repeated fits of fake data drawn from the best-fit spectrum. We include variations in the data that are not only due to statistical variations but also the uncertainty in our systematic parameter values, $\mathbf{f}$. We pass along the uncertainty in the systematic parameters by first drawing an instance of $\mathbf{f}$ from its assumed multivariate normal distribution, next calculating the predicted spectrum, and then finally using the spectrum to draw a set of observed values. The number of observed values was drawn from a Poisson distribution whose mean was determined from the integral of the predicted spectrum.

The distribution of χ^2_{gof} calculated from the 10,000 fake data sets is shown in Fig 8.2. The data χ^2_{gof} is compared with the possible χ^2_{gof} values from the fake data sets. The p-value is evaluated as the fraction of fake data sets whose χ^2_{gof} are larger than data χ^2_{gof} value of 0.799. The obtained p-value is 97.4%, which is close to the p-value estimated from the χ^2 distribution alone.

We conclude from these tests that best-fit prediction of the neutrino energy spectrum is a reasonable description of the data.

8.1.4 Best-fit Values of the Nuisance Parameters

Even though the systematic uncertainty parameters, $\mathbf{f}$, are known as the "nuisance parameters," the values of $\mathbf{f}$ after the fit still provide useful information as a diagnostic of our analysis. Recall that each of the nuisance parameters is treated in our analysis as an observable random variable that obeys a Gaussian probability distribution with a mean and sigma that we, in principle, have determined from some external calibration. If the final value of a given nuisance parameter were several sigmas away from the input mean, this would mean that the constraint imposed by the data on the nuisance parameters is inconsistent with the prior calibration. This would be an indication that either the model is wrong, the calibration is wrong, the

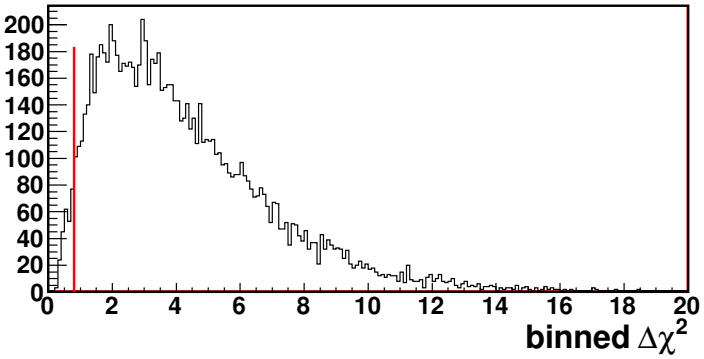

FIGURE 8.2: χ^2_{gof} distribution for 10,000 fake data samples. The fake data are generated by assuming the best-fit oscillation parameters and then drawing variations in the systematic error parameters to produce instances of the predicted neutrino energy spectrum which was then used to create samples of observations. The red line is the χ^2_{gof} value for the fit to the data. According to this distribution, the probability that data fit value of χ^2_{gof} is 0.799 or larger is 97.4%

data has problems, or we were unlucky. Conversely, if the values of the nuisance parameters are within their prior constraints, then this is an indication that the data are consistent with the model and our prior calibrations are reasonable.

Figure 8.3 shows the deviations of the nuisance parameter values from their means in units of their input sigma values, a quantity known as the "pull" of the parameter. The definition for the pull is

$$\text{pull}^i = \frac{f^i_{fitted} - f^i_{prior}}{\sigma^i_{prior}}, \tag{8.2}$$

where f^i_{fitted} is the fitted value of the nuisance parameter, f^i_{prior} is the mean prior to the fit, and σ^i_{prior} is the prior uncertainty. We can see that the pull values for all of the nuisance parameters are well within their 1-sigma prior uncertainties.

8.2 Confidence Intervals

In addition to the best-fit values of the oscillation parameters, we are interested in which values are consistent with the data. We report this information using

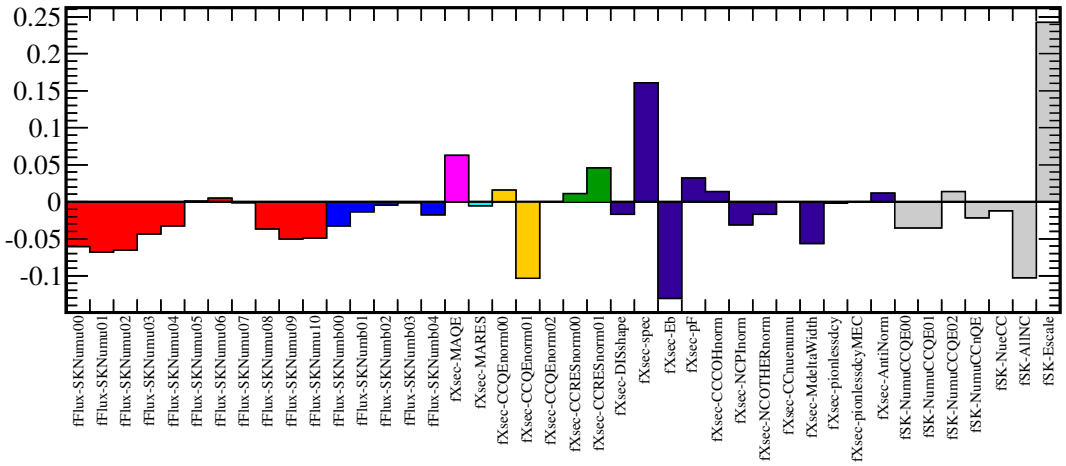

FIGURE 8.3: Pulls of systematic parameters at the best-fit point. In these plots the pull for the ith nuisance parameter is defined as $\text{pull}^i = \frac{f^i_{fitted} - f^i_{prior}}{\sigma^i_{prior}}$. (Top) the horizontal axis represents the labels of systematic parameters. The colors group the parameters by type. Red indicates parameters related to the ν_μ flux uncertainty; blue the parameters related to the $\bar{\nu_\mu}$ uncertainty; magenta the value of M_A; cyan the value of M_{RES}, yellow the parameters controlling the CCQE normalization; green the parameters controlling the resonant production interactions; dark blue the non-ND280 constrained interaction parameters; and gray the uncertainty in the Super-K detector efficiencies and energy scale. The pull values are all within one standard deviation of their prior constraints. This fact gives suggests that the data, prior calibrations of the systematic uncertainties, and the model are all consistent.

frequentist confidence intervals (Neyman (1937)). What these intervals tell us is that if any of the parameter values inside the interval were the true value of the parameter, we would expect to make the measurement we observed at least α percent of the time, where α is some confidence level we are free to choose. For example, suppose we are told that a measurement of the parameter θ is $\hat{\theta}$ and has a 90% confidence interval of $[\theta_1, \theta_2]$. Then we should infer that if we were to repeat the experiment many times, at least 90% of the time the intervals we calcualte will contain the true value of the parameter. Note that what the frequentist confidence interval does **not** tell us is that there is a 90% probability that the true value of θ lies inside $[\theta_1, \theta_2]$.[1] For

[1] Frequentist statistical techniques give information on $P(\mathbf{x}|\theta)$, while Bayesian statistical techniques provide information on $P(\theta|\mathbf{x})$.

a more detailed discussion of the classical confidence interval and common methods to define them, please see Appendix A.

The confidence intervals we report here are made using a technique known as the Feldman-Cousins prescription (Feldman and Cousins (1998)). The prescription defines an ordering parameter that allows us to determine what values of a parameter should be in the interval given some measurement. The procedure properly handles situations where the amount of data is small and when the analysis is trying to fit a parameter near some physical boundary. Both cases apply for this analysis. Please see Appendix B for a description of this technique and for details of our implementation. For the results below, we note that the ordering parameter we use is $-2\Delta \ln \mathcal{L}$ and that the parameter values that fall into the Feldman-Cousins confidence interval at some designated confidence level will be below some threshold value of the order parameter, known as $-2\Delta \ln \mathcal{L}_{\text{crit}}$. This threshold is found using pseudo-experiments (i.e. fits of many toy MC data sets).

8.2.1 1D Confidence Intervals

We calculate the confidence intervals for the oscillation parameters, $\sin^2(\theta_{23})$ and $\Delta m^2_{32}/\Delta m^2_{13}$, twice: once assuming the normal hierarchy and once assuming the inverted hierarchy.

Normal Hierarchy Confidence Intervals

The 68% confidence intervals for the oscillation parameters are

$$\begin{aligned} 0.458 \quad &< \sin^2\theta_{23} < \quad 0.568 \\ 2.41 \times 10^{-3}\ \text{eV}^2/\text{c}^4 \quad &< \Delta m^2_{32} < \quad 2.61 \times 10^{-3}\ \text{eV}^2/\text{c}^4. \end{aligned} \tag{8.3}$$

The 90% confidence intervals are

$$\begin{aligned} 0.428 \quad &< \sin^2\theta_{23} < \quad 0.598 \\ 2.34 \times 10^{-3}\ \mathrm{eV}^2/\mathrm{c}^4 \quad &< \Delta m^2_{32} < \quad 2.68 \times 10^{-3}\ \mathrm{eV}^2/\mathrm{c}^4. \end{aligned} \tag{8.4}$$

Figure 8.4 and Figure 8.5 show the value of $-2\Delta \ln \mathcal{L}$ for the data as a function of $\sin^2(\theta_{23})$ and Δm^2_{32}, respectively, assuming the normal hierarchy. Because we are only interested in the likelihood as a function of one of the oscillation parameters at a time, in both fits, the "other" oscillation parameter has been removed by a technique known as profiling. Profiling in our analysis means that we treat the oscillation parameter we are not currently interested in as a nuisance parameter but do not assign it a constraint term with mean or sigma. In other words, we allow the "other" parameter to chose the value that maximizes the likelihood for each value of the parameter we are interested in. Overlaid in blue in the figures are the profiled $-2\Delta \ln \mathcal{L}_{\mathrm{crit}}$ for the 68% and 90% confidence level. For oscillation parameter values with profiled $-2\Delta \ln \mathcal{L}$ less than the profiled $-2\Delta \ln \mathcal{L}_{\mathrm{crit}}$ value, the parameter value is considered inside the confidence interval. The boundary of the region where this condition is true is demarcated by the dashed red lines and is what defines the reported confidence intervals.

As can be seen in Figure 8.4 and Figure 8.5, the $-2\Delta \ln \mathcal{L}_{\mathrm{crit}}$ values depend on the value of the oscillation parameters. The value of $-2\Delta \ln \mathcal{L}_{\mathrm{crit}}$ becomes smaller as one gets closer to the best-fit value. This is because the best-fit values are near the point of maximal disappearance. At these values, there is a bigger chance of generating a toy MC data set whose number of events have fluctuated lower than what can be fit assuming maximal disappearance. (These are the so-called "pseudo-maximal" fits discussed in Chapter 7.)

For values of $\sin^2(\theta_{23})$ near maximal disappearance, the deviation from the constant-$\Delta\chi^2$ is very large. This is consistent with the results of the toy MC studies discussed

in Chapter 7. What we observe from the studies is that a sizable portion of the toy MC data have spectra where the number of events near the oscillation dip is less than the number of events predicted, even when one assumes the maximum amount of muon neutrino disappearance. For these toy data sets, the value of $\sin^2(\theta_{23})$ will be fit to its physical limit, i.e. where the maximal amount of neutrino disappearance occurs. But because the number of events is still smaller than what the model can predict, the value of $-2\Delta \ln \mathcal{L}$ will be high compared to cases where the model can vary without running up against a physical bound. The effect will cause the value of $-2\Delta \ln \mathcal{L}_{\text{crit}}$ to be less than the value for an ensemble of fits where the physical bound is not important.

Figure 8.6 shows the distribution of $-2\Delta \ln \mathcal{L}$ of toy MC data at values of $\sin^2(\theta_{23})$ near and away from the maximal disappearance value. These distributions are used to calculate $-2\Delta \ln \mathcal{L}_{\text{crit}}$ which are in turn used to construct the 1D confidence intervals for $\sin^2(\theta_{23})$. For the toy fits far from the value of maximal disappearance in Figure 8.6a, the number of events near the oscillation dip is large enough so that statistical fluctuations do not create spectra where the model will run up against its physical boundary. In such a case, the distribution of $-2\Delta \ln \mathcal{L}$ is very similar to the χ^2 distribution for one degree of freedom, which is shown as the overlaid black line in the figure. This is the typical distribution one would expect. For the toy fits near the value of of maximal disappearance 8.6b, the average expected number of events near the dip is small enough that the statistical variation in this part of the spectrum is large enough that the model runs up against its physical boundary. In this case one gets a deviation in the $-2\Delta \ln \mathcal{L}$ from the χ^2 distribution.

One way to interpret what is happening to the $-2\Delta \ln \mathcal{L}_{\text{crit}}$ is to consider the effective degrees of freedom. For the toy MC fits near maximal disappearance, the model would like to follow the data and fit a value of $\sin^2(\theta_{23})$ that is "unphysical", i.e. the probability of muon neutrino disappearance is greater than one. But because

of the physical boundary, the fits to the data are restricted, lowering the effective degrees of freedom. This is why the toy MC distribution of $-2\Delta \ln \mathcal{L}$ in Figure 8.6b is more narrow than the χ^2 distribution distribution indicated by the black line.

Inverted Hierarchy Confidence Intervals

For the inverted hierarchy, the 68% confidence intervals are

$$\begin{aligned} 0.456 &< \sin^2\theta_{23} < 0.566 \\ 2.38 \times 10^{-3}\ \mathrm{eV}^2/\mathrm{c}^4 &< \Delta m^2_{13} < 2.58 \times 10^{-3}\ \mathrm{eV}^2/\mathrm{c}^4. \end{aligned} \tag{8.5}$$

The 90% confidence intervals are

$$\begin{aligned} 0.427 &< \sin^2\theta_{23} < 0.596 \\ 2.31 \times 10^{-3}\ \mathrm{eV}^2/\mathrm{c}^4 &< \Delta m^2_{13} < 2.64 \times 10^{-3}\ \mathrm{eV}^2/\mathrm{c}^4. \end{aligned} \tag{8.6}$$

Figure 8.7 and Figure 8.8 also show the $-2\Delta \ln \mathcal{L}$ surface of profiled fits to the data for $\sin^2(\theta_{23})$ and Δm^2_{32}, respectively, except now the fits assume the inverted hierarchy.

8.2.2 Comparison of 1D Intervals to Sensitivity Estimates

One well-known difficulty of the Feldman-Cousins procedure is that the size of the intervals can sometimes be influenced by large fluctuations in the data that do not necessarily have to do with the value of the parameters we are trying to measure. This can occur for measurements with a small number of expected events. In such cases, a large fluctuation from the expectation can be observed in the background or signal that affect the confidence intervals significantly. A more detailed discussion of this difficulty can be found in Appendix B. However, we will simply mention here that it is useful to compare the intervals from the data fit to the average expected confidence intervals from toy MC studies of the analysis. Doing this allows us to get

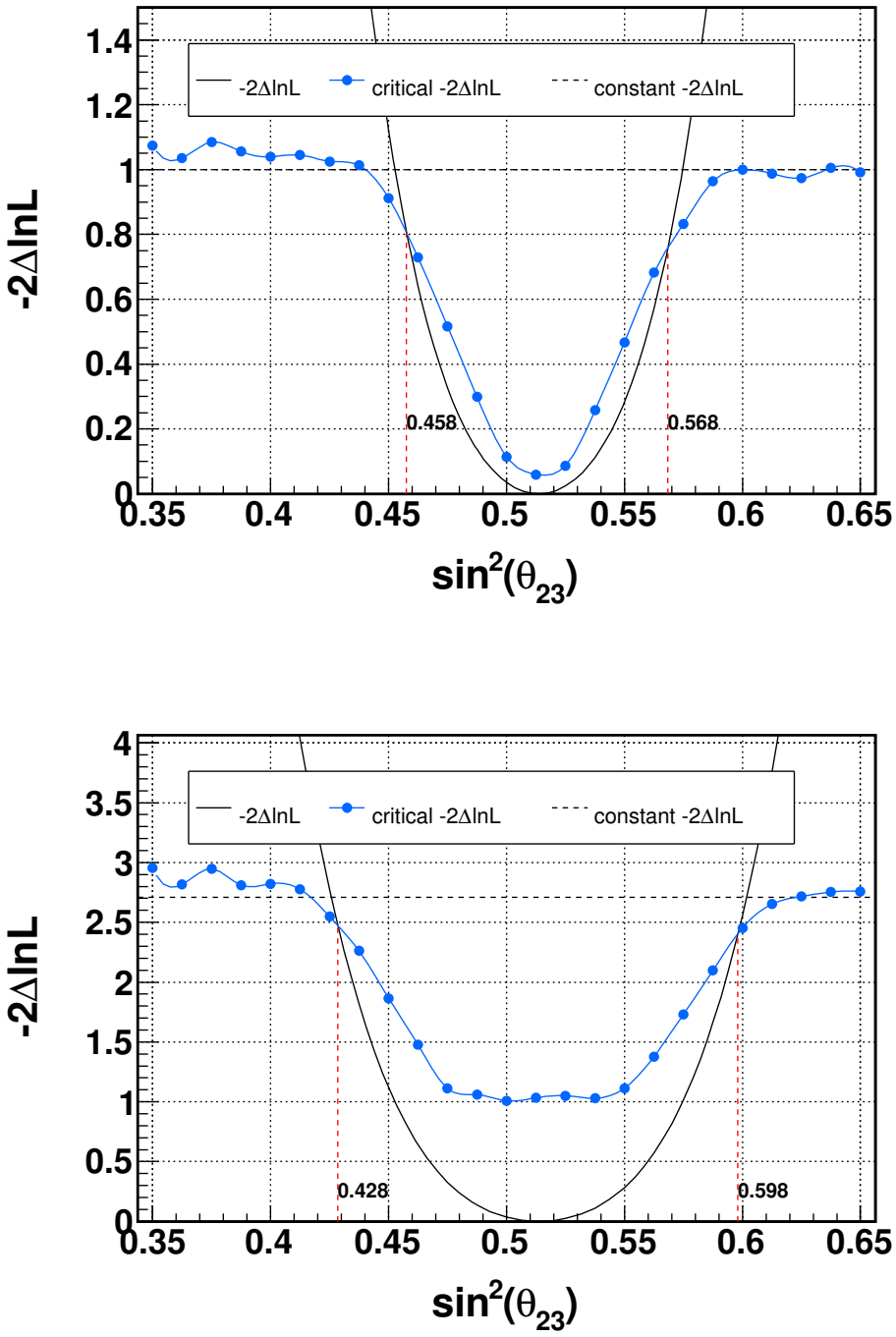

FIGURE 8.4: $-2\Delta \ln \mathcal{L}$ surface as a function of $\sin^2(\theta_{23})$ (black) for the 1D profiled fit to the data. Overlaid in blue with points is the $-2\Delta \ln \mathcal{L}_{\text{crit}}$ value as a function of $\sin^2(\theta_{23})$ for 68% (top) and 90% (bottom). The fit assumes the normal hierarchy.

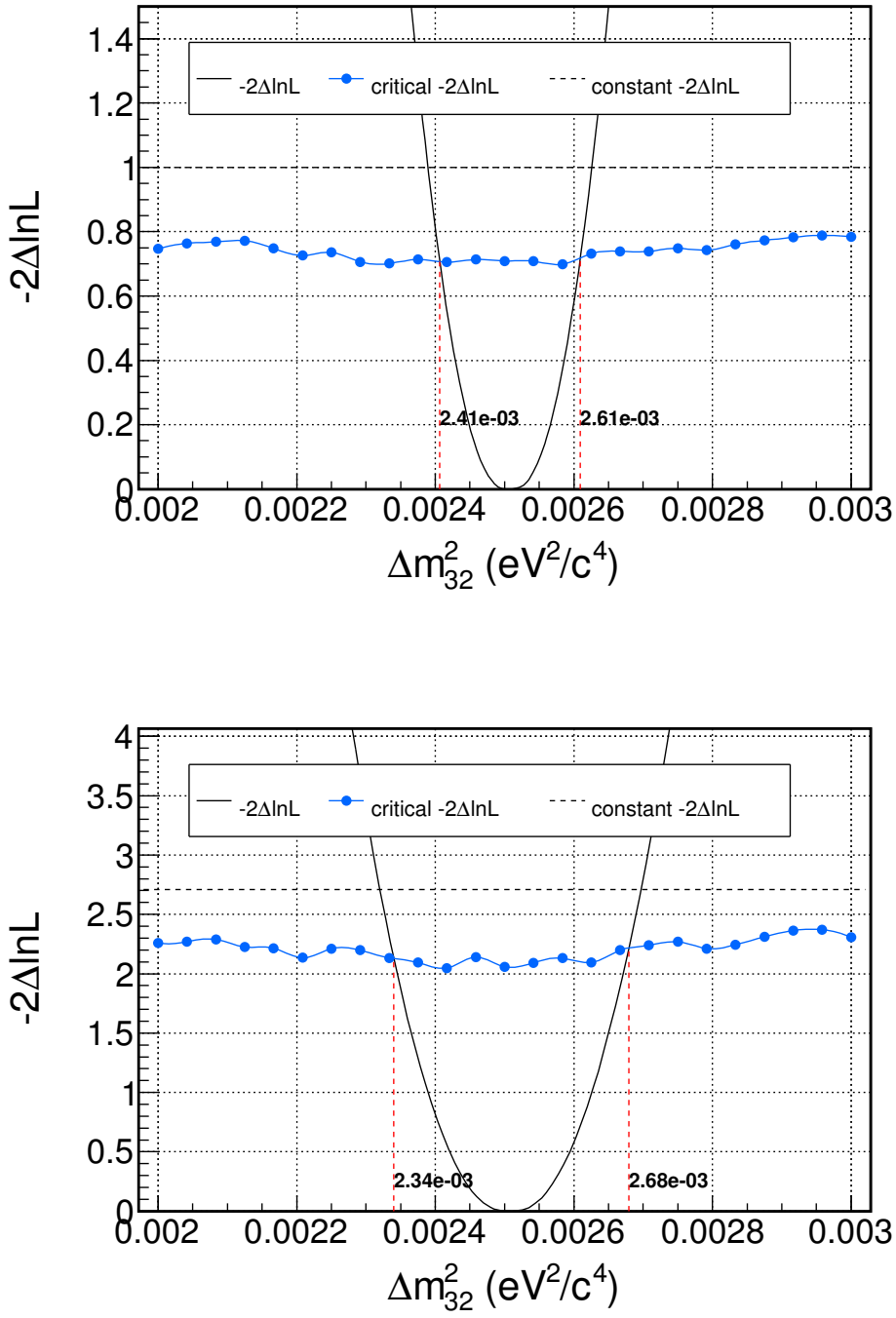

FIGURE 8.5: $-2\Delta \ln \mathcal{L}$ surface as a function of Δm^2_{32} (black) for the $Deltam^2_{32}$ 1D profiled fit to the data. Overlaid in blue with points is the $-2\Delta \ln \mathcal{L}_{\text{crit}}$ value as a function of Δm^2_{32} for 68% (top) and 90% (bottom). The fit assumes the normal hierarchy.

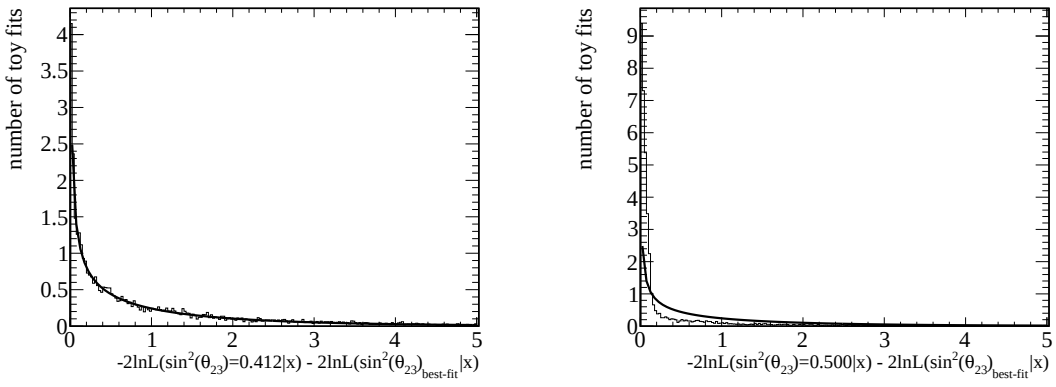

(a) $-2\Delta \ln \mathcal{L}$ for $\sin^2(\theta_{23})$ =0.412 (b) $-2\Delta \ln \mathcal{L}$ for $\sin^2(\theta_{23})$ =0.5

FIGURE 8.6: $-2\Delta \ln \mathcal{L}$ distribution for toy MC fits. These distributions are used to calculate the values of $-2\Delta \ln \mathcal{L}_{\text{crit}}$ which are used to construct the Feldman-Cousins 1D confidence intervals for $\sin^2(\theta_{23})$. The solid line is the χ^2 distribution for one degree of freedom. In Figure 8.6b, the distribution deviates from the χ^2 curve because of boundary fits discussed in Chapter 7. This deviation is why the Feldman-Cousins procedure is used to calculated the allowed regions.

a qualitative sense of how much of the result has been influenced by fluctuations. This is helpful if one wants to use the results to make more Bayesian-like inferences such as, "what is the probability of a certain value of the parameter given the data" (as opposed to the frequentist inference which is only about the probability of observing the same data given the values of the parameters). Large deviations from the sensitivity indicate that the confidence regions could deviate significantly if one analyzed the data using Bayesian statistical methods. Note, however, that even for intervals affected largely by fluctuations the confidence interval from the data fit is still correctly constructed according to the definition of the frequentist confidence interval (which has the advantage over a Bayesian interval of not requiring the analyzer to define prior probabilities when calculating the interval).

Figure 8.9 shows the 1D dimensional profiled $-2\Delta \ln \mathcal{L}$ curves of $\sin^2(\theta_{23})$ for a collection of toy MC data fits. The average of the curves is shown by the thick black line. The $-2\Delta \ln \mathcal{L}$ curve for the T2K data fit is shown in red. The figure

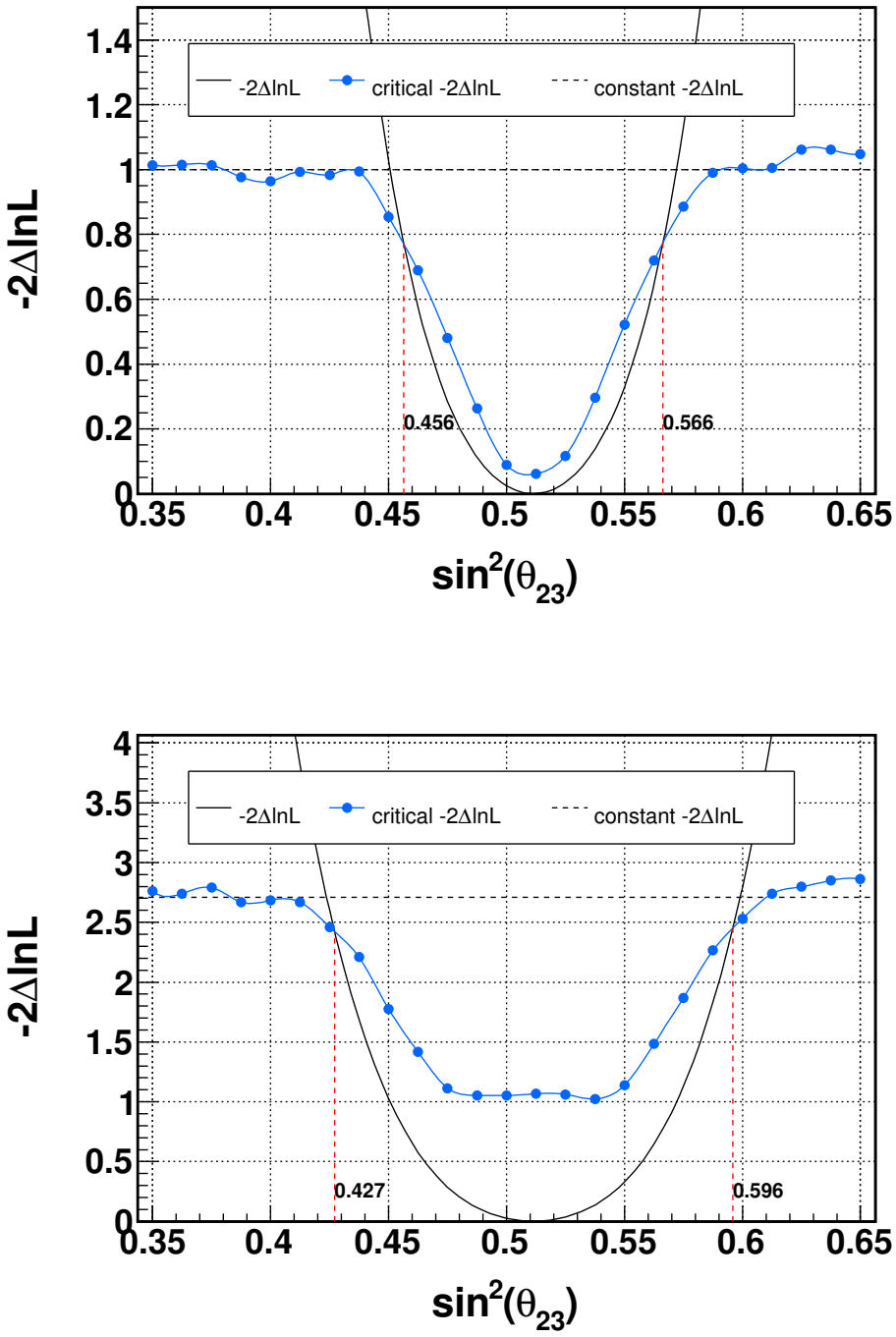

FIGURE 8.7: $-2\Delta \ln \mathcal{L}$ surface as a function of $\sin^2(\theta_{23})$ (black) for the 1D profiled fit to the data. Overlaid in blue with points is the critical $-2\Delta \ln \mathcal{L}$ value as a function of $\sin^2(\theta_{23})$ for 68% (top) and 90% (bottom). The fit assumes the inverted hierarchy.

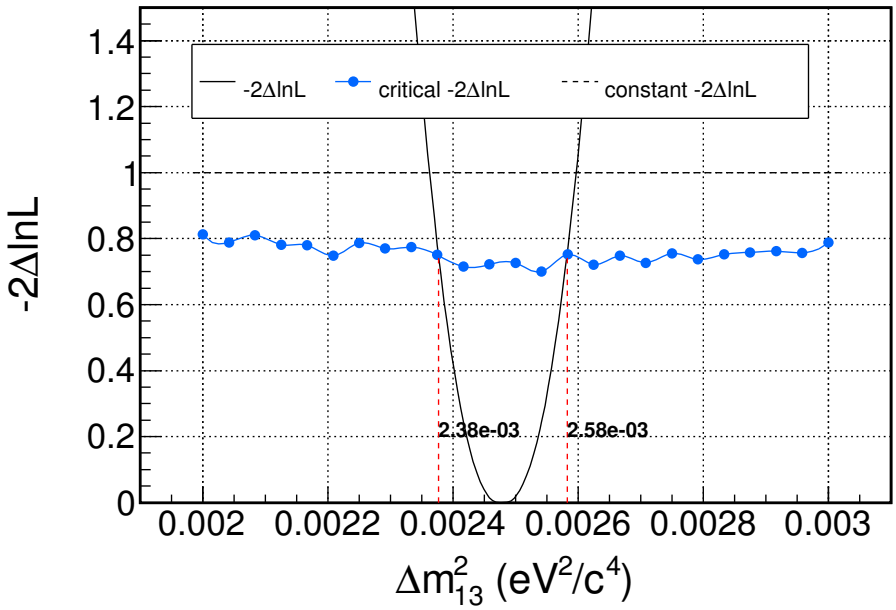

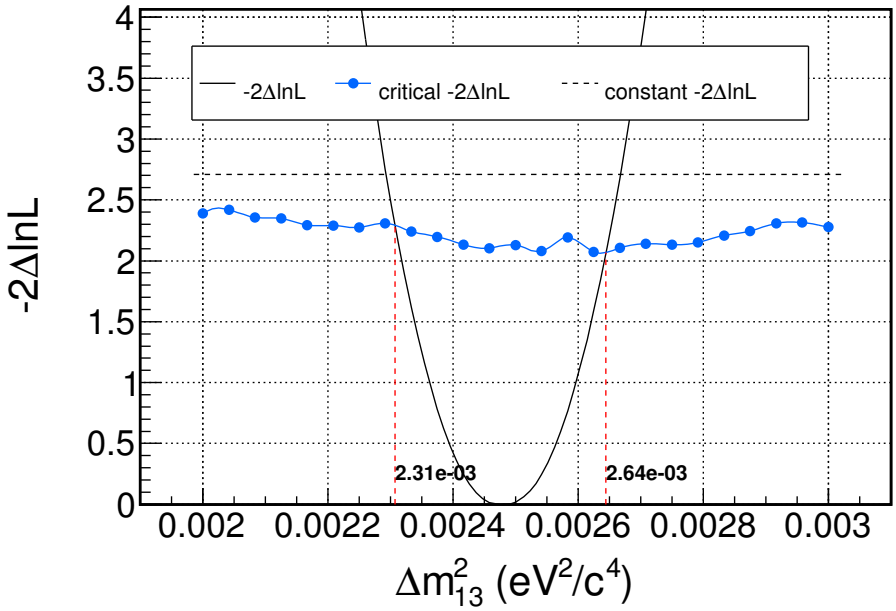

FIGURE 8.8: $-2\Delta \ln \mathcal{L}$ surface as a function of Δm^2_{13} (black) for the 1D profiled fit to the data. Overlaid in blue with points is the $-2\Delta \ln \mathcal{L}_{\text{crit}}$ value as a function of Δm^2_{13} for 68% (left) and 90% (right). The fit assumes the inverted hierarchy.

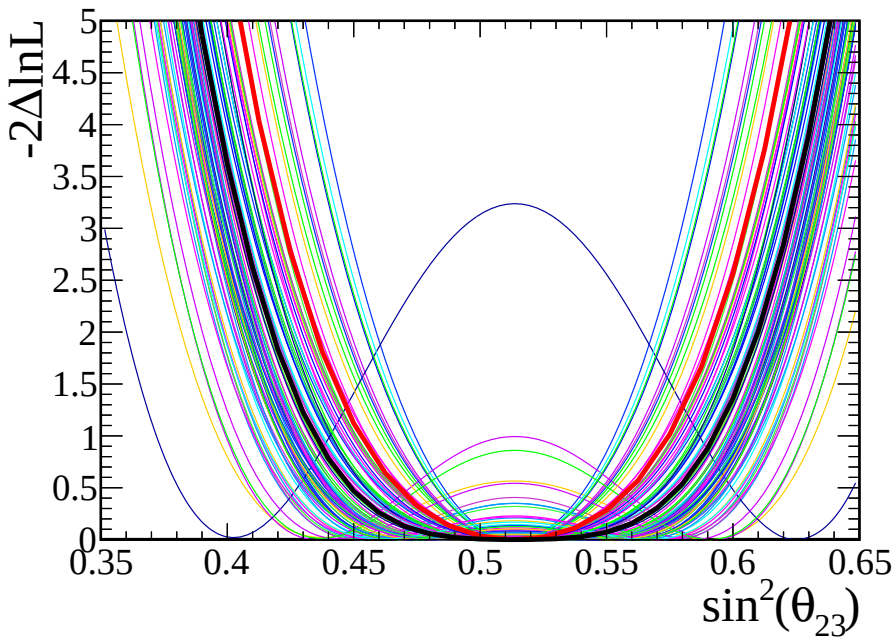

FIGURE 8.9: One dimensional profiled $-2\Delta \ln \mathcal{L}$ curves of $\sin^2(\theta_{23})$ for a collection of toy MC data fits. The average of the curves is shown by the thick black line. The $-2\Delta \ln \mathcal{L}$ curve for the T2K data fit is shown in red.

demonstrates that the $-2\Delta \ln \mathcal{L}$ curve for the data fit is narrower than the expected average from toy MC fits. However, the data fit curve is consistent with the ensemble of curves. We conclude that the constraint on $\sin^2(\theta_{23})$ is "lucky" in the sense that the $-2\Delta \ln \mathcal{L}$ is more narrow than average. However, the data are still consistent with our model of the expected spectrum.

8.2.3 2D Confidence Level Regions

Just as we did for the parameters one at a time, we can also look at the 2D region of parameter space that is consistent with the data. We again use the Feldman-Cousins procedure which can be extended to two dimensions in a straightforward manner. We calculate the 2D confidence level regions twice: once when assuming the normal hierarchy and another when assuming the inverted hierarchy.

Figures 8.10 and 8.11 show the 2D contours for the 68% (dashed line) and 90% (solid line) confidence level regions for a fit assuming the normal and inverted hi-

erarchy, respectively. The location of the best-fit point in ($\sin^2(\theta_{23})$,Δm^2_{32}) and ($\sin^2(\theta_{23})$,Δm^2_{13}) for the normal and inverted hierarchy, respectively, are indicated in the figures by a dot. Both contours are similar in shape indicating that our measurement is mostly insensitive to the mass hierarchy. The location of the best-fit point for $\sin^2(\theta_{23})$ corresponds to the maximal disappearance value for both the normal and inverted hierarchy. As was mentioned earlier in this chapter when discussing the best-fit oscillation parameter values of the fit, the current analysis cannot distinguish with statistical significance between the maximal disappearance value and the maximal mixing value of $\sin^2(\theta_{23})$. This can be seen in these 2D confidence level contours as both maximal disappearance and maximal mixing values are well within the 68% CL region.

Just as for the 1D case, the confidence level regions shown in Figures 8.10 and 8.11 were made by calculating $-2\Delta \ln \mathcal{L}$ for the data as a function of the oscillation parameters and the including only those regions of parameter space where $-2\Delta \ln \mathcal{L}$ $<-2\Delta \ln \mathcal{L}_{\rm crit}$. Figure 8.13 plots the values of $-2\Delta \ln \mathcal{L}$ from the data fit, while Figure 8.14 shows the values of $-2\Delta \ln \mathcal{L}_{\rm crit}$. In Figure 8.14, we can see that the value of $-2\Delta \ln \mathcal{L}_{\rm crit}$ get smaller the closer one gets to the region of maximal disappearance, about $\sin^2(\theta_{23})$ =0.513 (normal) and $\sin^2(\theta_{23})$ =0.511 (inverted). This is the same relationship seen in the 1D $-2\Delta \ln \mathcal{L}_{\rm crit}$ calculations and for the 2D calculations, due to the same reason as discussed above.

8.2.4 Comparison of the 2D Confidence Level Contours from the Data Fit to the Expected Sensitivity Contours

Just as we had done in Section 8.2.2, we compare the confidence regions calculated from the data fit to the average expected regions from toy MC studies. The latter confidence regions give us the expected "sensitivity" of the analysis to the parameter values. The sensitivity is calculated by performing a binned likelihood fit to the

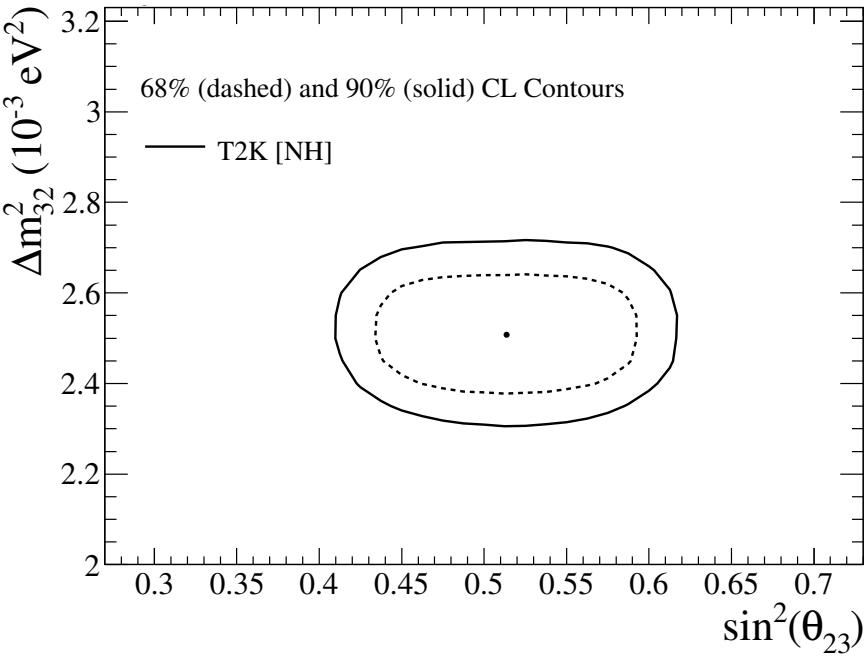

FIGURE 8.10: Allowed region of ($\sin^2\theta_{23}$, Δm^2_{32}) for data assuming the normal hierarchy. The contour is estimated with the F&C method.

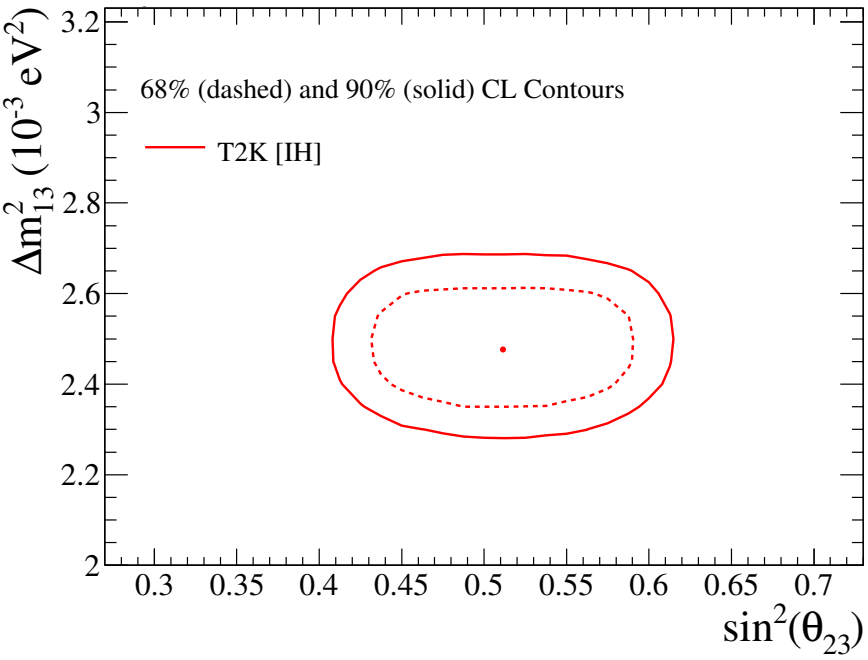

FIGURE 8.11: Allowed region of ($\sin^2\theta_{23}$, Δm^2_{13}) for data assuming the inverted hierarchy. The contour is estimated with the F&C method.

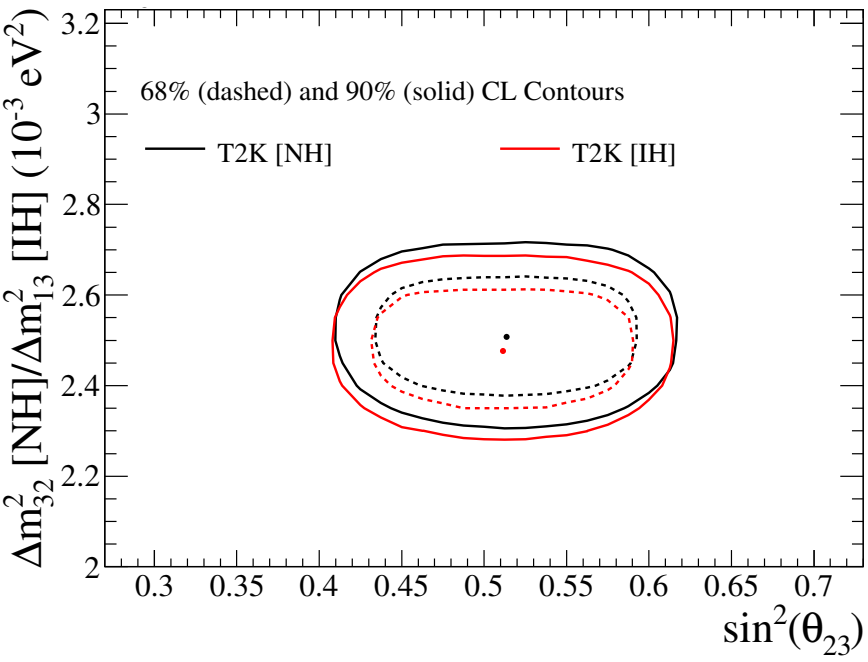

FIGURE 8.12: The 68% (dashed) and 90% (solid) confidence level allowed region for the data assuming the normal (black) and inverted (red) hierarchy. Both contours were calculated using the Feldman-Cousins procedure. The best-fit points are shown by the dot. Both best-fit points are at the value of $\sin^2(\theta_{23})$ that corresponds to the maximal amount of muon neutrino disappearance. This value of $\sin^2(\theta_{23})$ is expected to be different between the normal and inverted hierarchy. Also, please note that the mass splitting for the normal hierarchy is Δm^2_{32} while the inverted hierarchy is Δm^2_{13}. The analysis is sensitive to the size of the largest mass-squared splitting, which is different for when assuming the normal and inverted hierarchy.

average expected spectrum. Fitting with a binned likelihood is expected to give us the approximate average confidence regions in the limit of running an infinite number of toy MC fits.

Figure 8.15 overlays the confidence regions for the data fit (black) and MC sensitivity (purple) for comparison. As for what was seen in the 1D confidence level comparison, there is a fairly large difference in the allowed regions in the data fit and the expected sensitivity. Again, we can attribute this difference to a fluctuation in the number of events near the oscillation dip. As one can see in the reconstructed neutrino energy spectrum in Figure 8.1, the number of events near the dip is systematically lower than the prediction from the model despite the fact that the spectrum

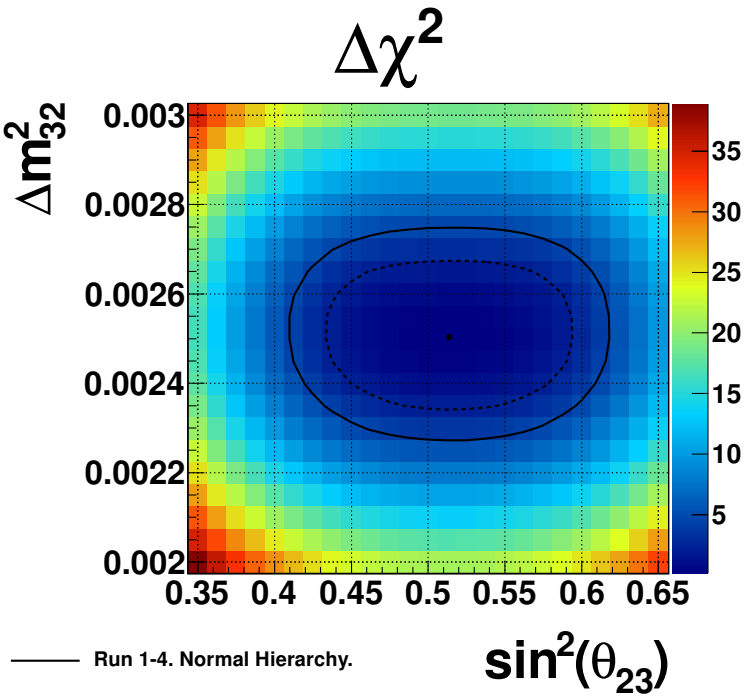

(a) $-2\Delta \ln \mathcal{L}$ surface for the normal hierarchy

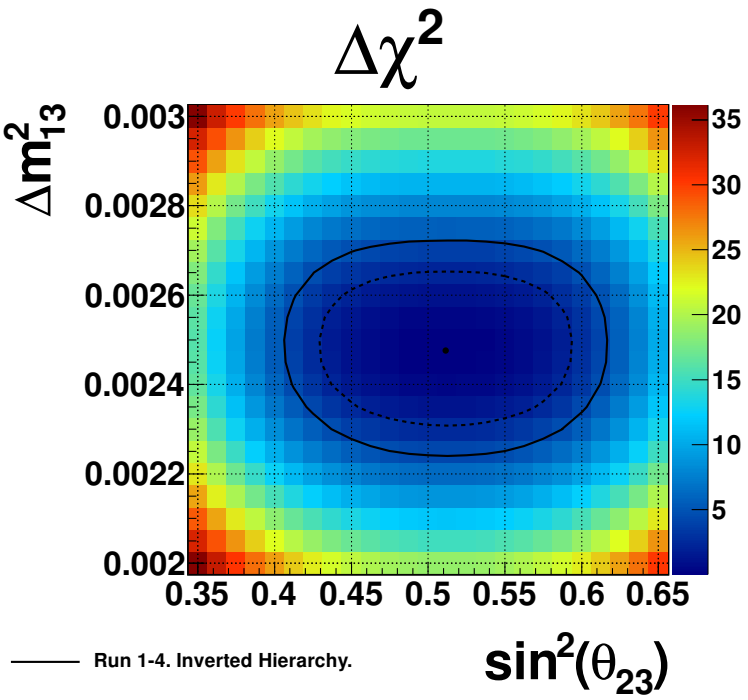

(b) $-2\Delta \ln \mathcal{L}$ surface for the inverted hierarchy

FIGURE 8.13: $-2\Delta \ln \mathcal{L}$ surface as a function of the oscillation parameters, $\sin^2(\theta_{23})$ and Δm^2_{32} (Δm^2_{13}) for the normal and (inverted) hierarchies. Contour lines indicate the $-2\Delta \ln \mathcal{L}$ =2.7 (dashed) and $-2\Delta \ln \mathcal{L}$ =4.6 (solid) contours.

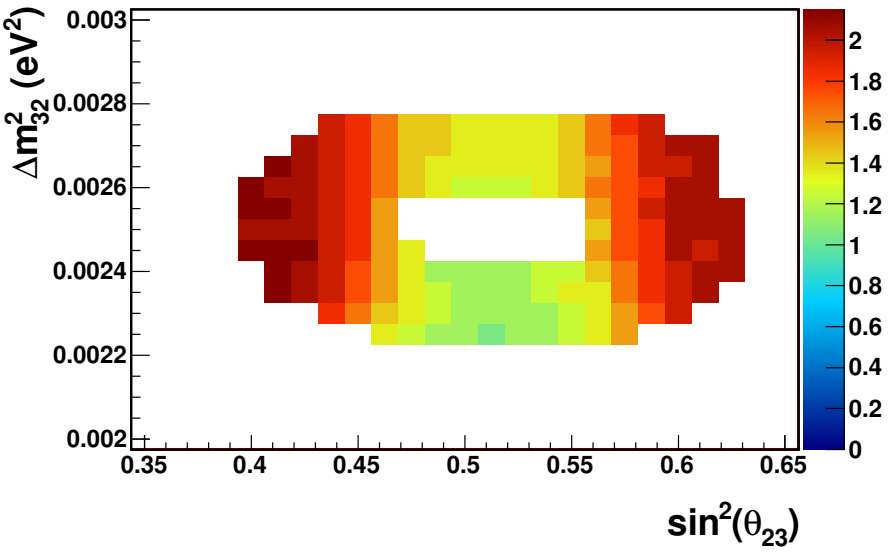

(a) $-2\Delta \ln \mathcal{L}_{\text{crit}}$ distribution for 68% CL

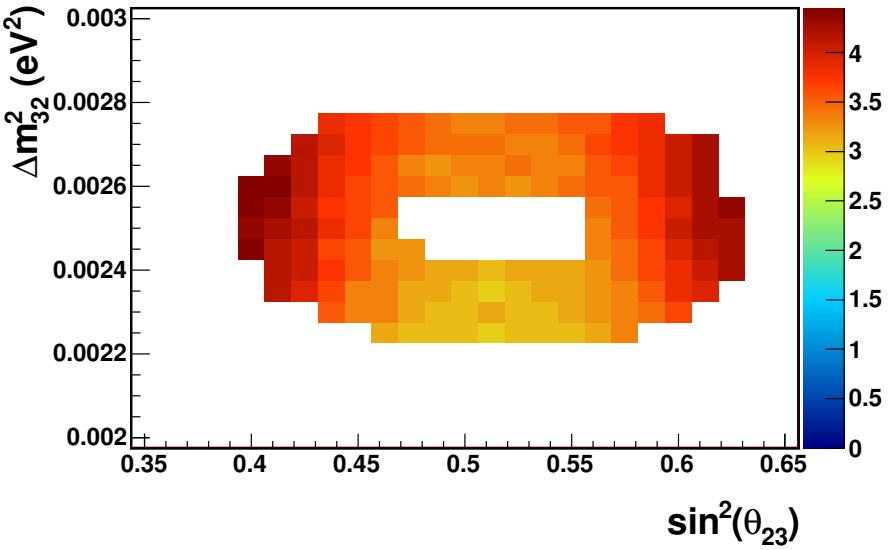

(b) $-2\Delta \ln \mathcal{L}_{\text{crit}}$ distribution for 90% CL

FIGURE 8.14: $-2\Delta \ln \mathcal{L}_{\text{crit}}$ distribution for (a) 68% and (b) 90% confidence levels. The value of $-2\Delta \ln \mathcal{L}_{\text{crit}}$ was not calculated for the bins without color in order to save on computation time. Calculated bins were chosen to be in the region where where $-2\Delta \ln \mathcal{L}$ =2.7 and $-2\Delta \ln \mathcal{L}$ =4.6.

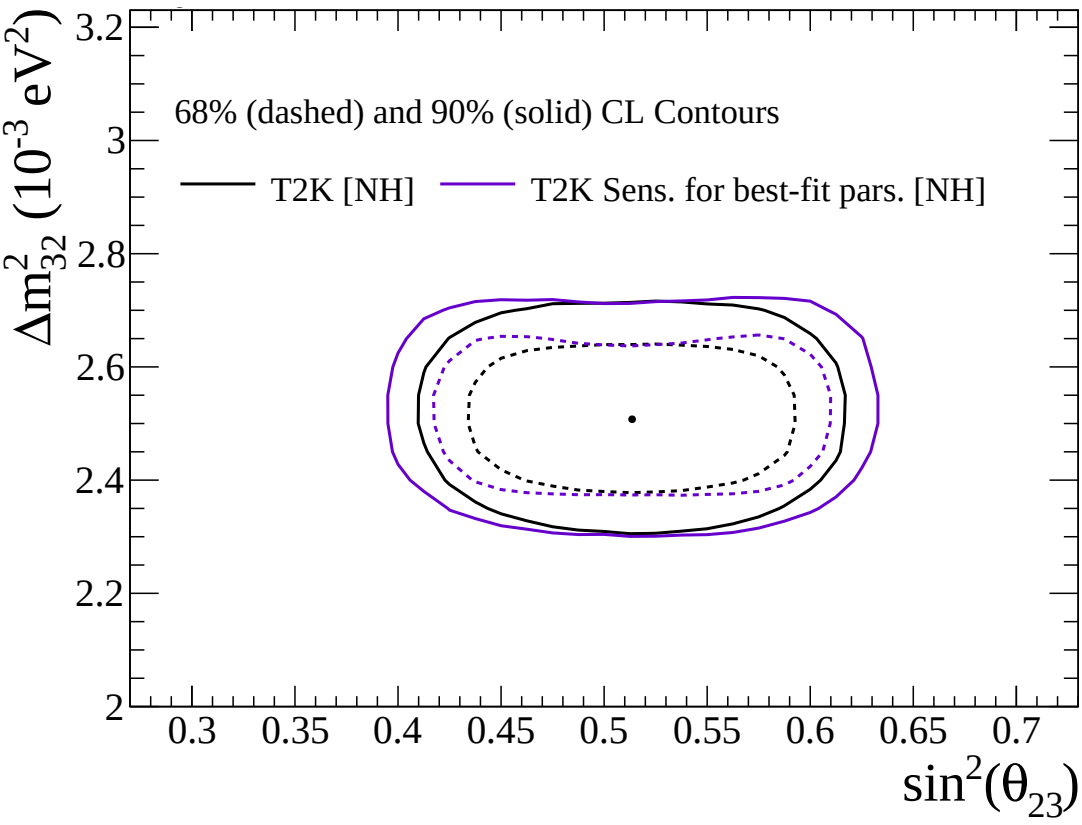

FIGURE 8.15: Comparison of the Feldman-Cousins 68% and 90% confidence level regions for the data fit (black) and the expected average regions from MC (purple). The latter indicates the expected sensitivity of the analysis assuming some true value of the oscillation parameters. For this figure, the sensitivity is made assuming that the true values were equal to the best-fit values from the data fit ($\sin^2(\theta_{23})$ =0.514, Δm^2_{32} =2.51 $\times$ 10^{-3} eV^2/c^4). Both regions are calculated assuming the normal hierarchy.

assumes maximal muon neutrino disappearance. Such a result is not unexpected as toy MC studies presented in Chapter 7 indicate that such low fluctuation in the data should not be rare at the current amount of statistics for this data set.

As a final demonstration that the 2D contour is reasonable, Figure 8.16 compares the contour for the fit (in black) and the expected sensitivity (in magenta) to the contours from 30 toy MC fits. The toy MCs were generated at the data best-fit oscillation parameter values. Though the observed contour from the data is smaller than the sensitivity contour, we can see from the contours shown that the data fit

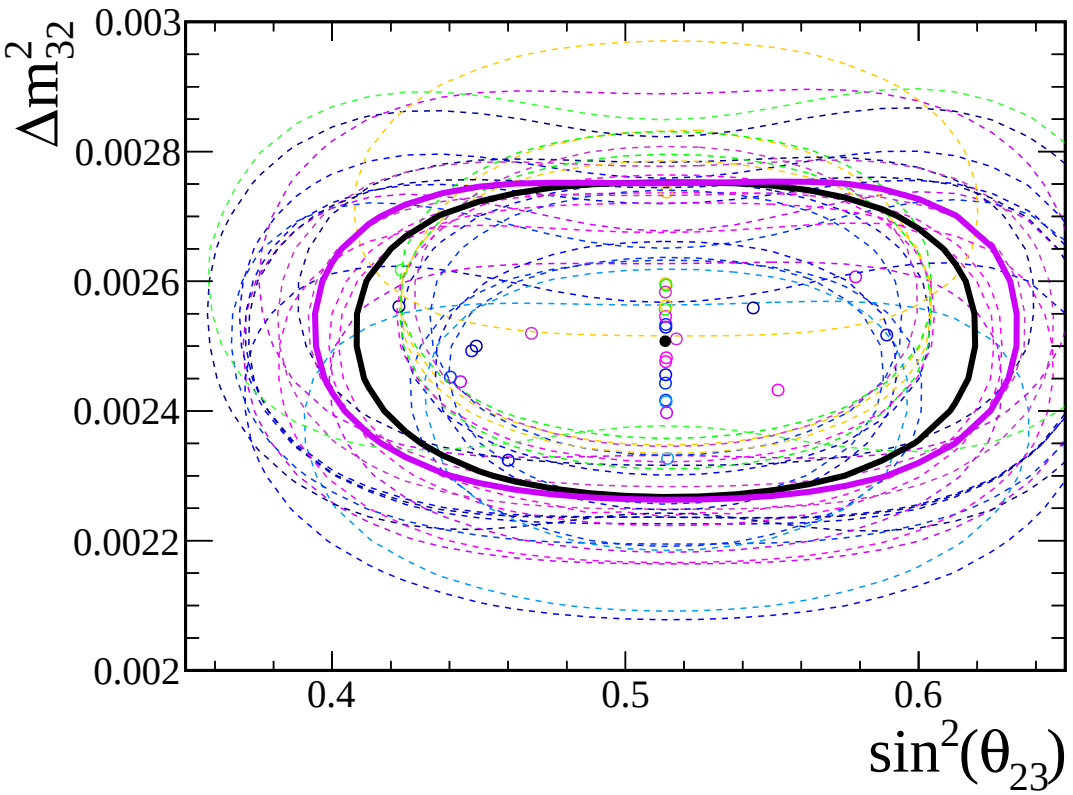

FIGURE 8.16: Contours of $-2\Delta \ln \mathcal{L} = 4.3$ for 30 toy MC fits (dashed color lines), the data fit (solid black), and expected sensitivity (solid magenta line). The observed contour from the data is consistent with the ensemble of toy fit contours.

result is not an unlikely one. Even with such a small sampling to toy MC fits, several toy fits are tighter or comparable to the data fit.

8.3 Investigation of Result Using Different Likelihoods

For further investigation of the data fit, we repeat the analysis using with different likelihoods. From Chapter 6 which described the analysis technique, the likelihood used in the data fit is

$$\mathcal{L}(\boldsymbol{\theta}, \mathbf{f}|\mathbf{x}) = \left[\prod_{i=0}^{N} P(x_i|\boldsymbol{\theta}, \mathbf{f})\right] \times \frac{N^{exp}(\boldsymbol{\theta}, \mathbf{f})^N e^{-N^{exp}(\boldsymbol{\theta}, \mathbf{f})}}{N!} \times e^{-\frac{1}{2}\Delta\mathbf{f}^T\mathbf{M}^{-1}\Delta\mathbf{f}}, \tag{8.7}$$

where $\mathbf{x}$ is the vector of N measurements, $P(x_i|\boldsymbol{\theta}, \mathbf{f})$ is the probability of observing measurement x_i, $\boldsymbol{\theta}$ is the vector model parameters, $\mathbf{f}$ is the vector of systematic error values, N^{exp} is the expected number of events as a function of $\boldsymbol{\theta}$ and $\mathbf{f}$, $\Delta\mathbf{f} = \mathbf{f} - \boldsymbol{\mu}$ and $\mathbf{M}$ is the covariance matrix between the components of $\mathbf{f}$. We split up the likelihood into different factors and define them as

$$\mathcal{L}(\boldsymbol{\theta}, \mathbf{f}|\mathbf{x}) = \mathcal{L}_{shape}\mathcal{L}_{norm}\mathcal{L}_{sys} \tag{8.8}$$

where

$$\mathcal{L}_{shape} = \prod_{i=0}^{N} P(x_i|\boldsymbol{\theta}, \mathbf{f}) \tag{8.9}$$

$$\mathcal{L}_{norm} = \frac{N^{exp}(\boldsymbol{\theta}, \mathbf{f})^N e^{-N^{exp}(\boldsymbol{\theta}, \mathbf{f})}}{N!} \tag{8.10}$$

$$\mathcal{L}_{sys} = e^{-\frac{1}{2}\Delta\mathbf{f}^T\mathbf{M}^{-1}\Delta\mathbf{f}}. \tag{8.11}$$

We combine these different likelihood components into several combinations:

- $\mathcal{L}_{norm} \cdot \mathcal{L}_{shape}$ (with all systematic parameters are fixed to their input values) in order to remove the contribution of systematic parameters and check their effect,
- $\mathcal{L}_{norm} \cdot \mathcal{L}_{syst}$ in order to investigate the constraint on the oscillation parameters from the number of data events only, and
- $\mathcal{L}_{shape} \cdot \mathcal{L}_{syst}$ in order to investigate the constraint from the shape of the reconstructed energy spectrum.

Table 8.1 shows the best-fit values of the oscillation parameters for the different likelihoods. All the fits performed assume the normal hierarchy. For all the different combinations tested, the best-fit value for $\sin^2(\theta_{23})$ is the value for maximal disappearance where $\sin^2(\theta_{23}) \approx 0.514$. For the likelihood that focuses on the number of

events observed, $\mathcal{L}_{norm}\mathcal{L}_{sys}$, the best-fit value for Δm^2_{32} is higher than the value when using the full likelihood. This is because the predicted number of events, 120.88, is minimized when $\Delta m^2_{32} \approx 2.6 \times 10^{-3}$ eV^2/c^4 and is a better match to the number of events observed, 120, than the number of events predicted by the fit using the full likelihood, 121.41.

However, we can see that when the fit is performed with the shape and systematic error likelihoods, $\mathcal{L}_{shape}\mathcal{L}_{sys}$, the fitted value of Δm^2_{32} is closer to the value from the full likelihood. It turns out that the shape provides a stronger constraint on the parameters than the number of events as demonstrated in Figure 8.17. This figure shows the best-fit point and contours of $-2\Delta \ln \mathcal{L}$ =4.6 for several of the likelihood combinations. Here one can see that the constraint on the parameters by $\mathcal{L}_{shape}$ is much stronger than from $\mathcal{L}_{norm}$. This is why the best-fit value of Δm^2_{32} is closer to 2.50×10^{-3} eV^2/c^4 than the value with the smallest number of events.

Table 8.1: Results for several fits using different combinations of likelihoods

Likelihood	Fitted N^{exp}_{SK}	$\sin^2\theta_{23}$	Δm^2_{32} (eV^2)
$\mathcal{L}_{norm}\mathcal{L}_{shape}\mathcal{L}_{syst}$	121.41	0.514	2.51×10^{-3}
$\mathcal{L}_{norm}\mathcal{L}_{shape}$	122.39	0.514	2.50×10^{-3}
$\mathcal{L}_{norm}\mathcal{L}_{syst}$	120.88	0.514	2.60×10^{-3}
$\mathcal{L}_{shape}\mathcal{L}_{syst}$	122.62	0.514	2.50×10^{-3}

8.4 Effect of Assumed $\sin^2(\theta_{13})$ Value

As discussed in Section 3.7.2, the value of $\sin^2(\theta_{13})$ has an important effect on the ν_μ disappearance oscillation probability. According to Equation (3.38), the larger the value of $\sin^2(\theta_{13})$, the further the value of maximal disappearance moves away from $\sin^2(\theta_{23}) = 0.5$. As a result, we expect the best-fit value of $\sin^2(\theta_{23})$ to be affected by the choice of $\sin^2(\theta_{13})$. In our analysis the value of $\sin^2(\theta_{13})$ is constrained by external

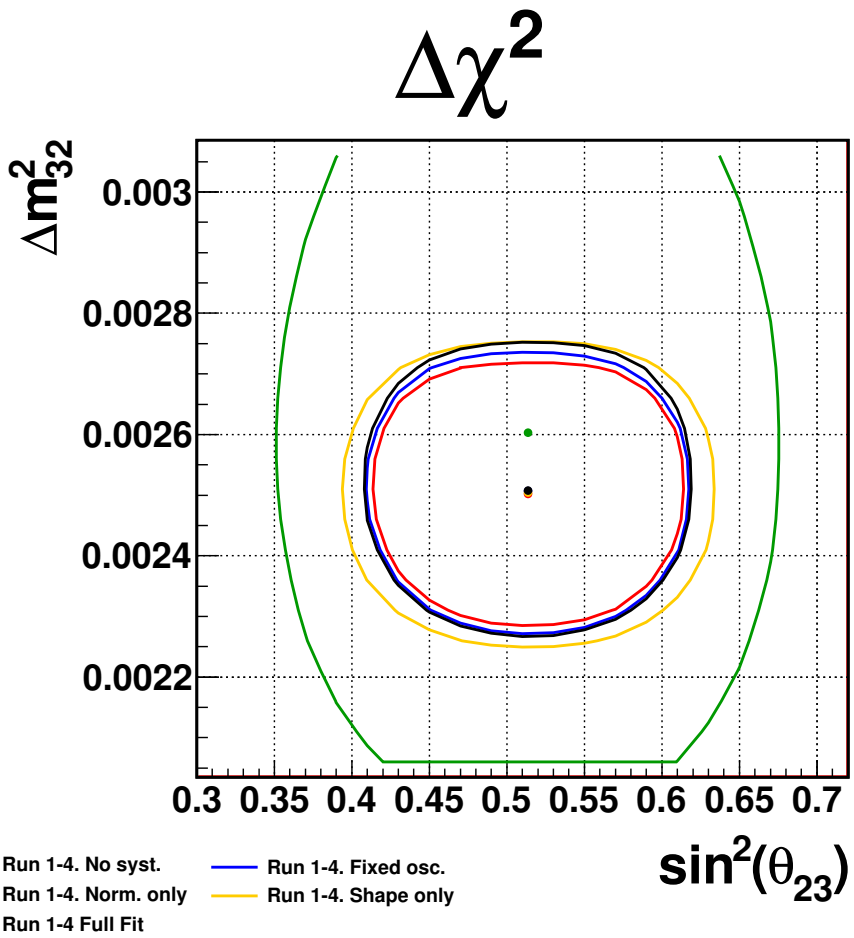

FIGURE 8.17: Contours of $-2\Delta \ln \mathcal{L}$ =4.6 for ($\sin^2\theta_{23}$, Δm^2_{32}) from performing the fit to the data using several different likelihood combinations. The shape information is providing most of the constraint on the oscillation parameters.

experiments. These experiments produce a global best-fit value of $\sin^2(\theta_{13})$=0.0251.

But because the effect of $\sin^2(\theta_{13})$ on the value of maximal disappearance is fairly large, we wish to know how the best-fit value of $\sin^2(\theta_{23})$ relates to the value of $\sin^2(\theta_{13})$. The dashed black line in Figure 8.18 shows the best-fit value of $\sin^2(\theta_{23})$ for several fits with $\sin^2(\theta_{13})$ fixed to different values. Note that the parameter Δm^2_{32} is profiled out, i.e. allowed to chose any value that minimizes the likelihood, much in the same way as the systematic parameters. It is clear from the figure that the best-fit value of $\sin^2(\theta_{23})$ changes when assuming different values of $\sin^2(\theta_{13})$. In other words, the results of the analysis have a dependence on the true value of $\sin^2(\theta_{13})$.

Figure 8.18 also shows the current measured 68% confidence level intervals on the value of $\sin^2(\theta_{13})$ from two sources. One of these, shown in magenta, is a contraint that combines the results from several ν_e-disappearance measurements of $\sin^2(\theta_{13})$ made from neutrinos from nuclear reactors. The other intervals come from T2K and its analysis measuring ν_e-appearance. Note that the T2K ν_e-appearance measurement is made with data taken over the same period as the data used by the analysis presented here. These intervals show our current knowledge about the value of $\sin^2(\theta_{13})$. Within the bounds from the external experiments the range over which $\sin^2(\theta_{23})$ changes is small. The range of $\sin^2(\theta_{23})$ values within the T2K bounds are larger, as one might expect, as the T2K constraint on the value of $\sin^2(\theta_{13})$ is weaker. Because the constraint by the reactor experiments are much stronger and are consistent with the T2K result, we choose to use them as inputs. If in the future, more measurements indicate that the value of $\sin^2(\theta_{13})$ are quite different from the value assumed by this analysis ($\sin^2(\theta_{13}) = 0.0251$), then the best-fit values and the confidence regions produced by this analysis are expected to change, but in a well-understood manner.

8.5 Comparison with Other Experimental Results

8.5.1 Comparison of 2D Allowed Regions

The analysis presented here provides the world's tightest constraint on $\sin^2(\theta_{23})$ to date. Figure 8.19 and compares the confidence region in $\sin^2(\theta_{23})$ and Δm^2_{32} as measured by T2K with the regions measured by two other experiments, Super-K and MINOS. Figure 8.20 makes the same comparison, except here the fits assume the inverted hierarchy and use the parameters $\sin^2(\theta_{23})$ and Δm^2_{13}. The Super-K experiment measures the parameters using their latest data set of neutrinos produced in the atmosphere (Himmel (2013)). The MINOS experiment measures the parameters with data that comes from both atmospheric neutrinos and accelerator-

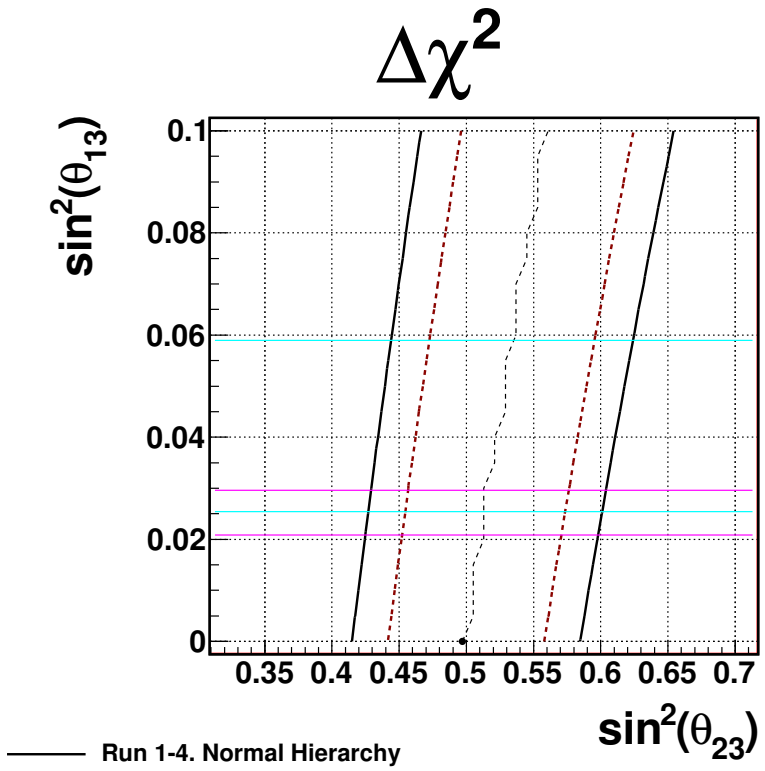

FIGURE 8.18: Best-fit values and 1D confidence intervals on $\sin^2(\theta_{23})$ for given values of $\sin^2(\theta_{13})$. Note that Δm^2_{32} is profiled out in all of the fits. The black, dashed line shows the best-fit values. The red, dashed line and black solid show the 1D 68% and 90% CL intervals, respectively. The magenta lines show the 1-sigma range of $\sin^2(\theta_{13})$ from the reactor experiments. The cyan lines show the 1-sigma range taken from the T2K ν_e-appearance analysis data taken during the same period as the ν_μ-disappearance analysis presented here.

produced neutrinos (MINOS Collaboration et al. (2014)). For all three experiments, the neutrino oscillation probability is calculated using all three flavors of neutrinos.

8.5.2 Effects of Current Measurement on Global Fits

We measured a value of the mixing angle that is consistent with both maximal mixing, i.e. $\sin^2\theta_{23} = 0.5$, and the maximal amount of muon neutrino disappearance. The latter situation is preferred though the analysis cannot distinguish between the two with significance. This result is noteworthy because previous measurements of $\sin^2(\theta_{23})$ favored values away from maximal mixing. Global fits of the oscillation

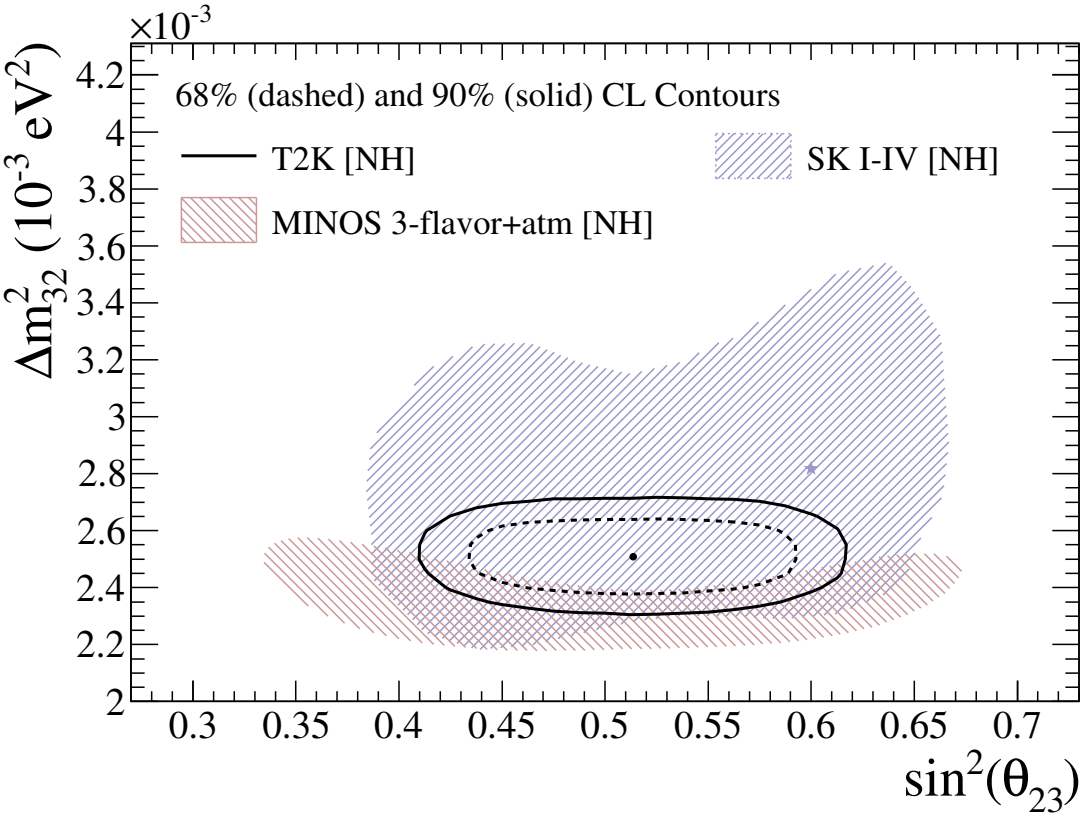

FIGURE 8.19: The 90% confidence regions allowed by T2K, Super-Kamiokande, and MINOS for the normal hierarchy. The T2K 68% confidence region is also shown in the dashed black line.

parameters, which combined previous measurements, excluded maximal mixing near the 2 σ level (Forero et al. (2012)). Our result will reduce this significance as can be seen in Figure 8.21a which compares the 1D $\Delta\chi^2$ of our result and other recent measurements. The figure also shows the combined $\Delta\chi^2$ curve for $\sin^2(\theta_{23})$ which illustrates the likely effect this result will have on global constraints on the $\sin^2(\theta_{23})$.

The constraint on the value of Δm^2 by T2K is comparable to the tightest constraint provided by the MINOS experiment (MINOS Collaboration et al. (2014)). A comparison of the 1D $\Delta\chi^2$ curve for the mass splitting is shown in Figure 8.21b. In combination with MINOS and Super-K, the 1 σ uncertainty in Δm^2 is reduced to a few percent ($\approx 3\%$) and now is similar to the uncertainty ($\approx 2.5\%$) on the solar

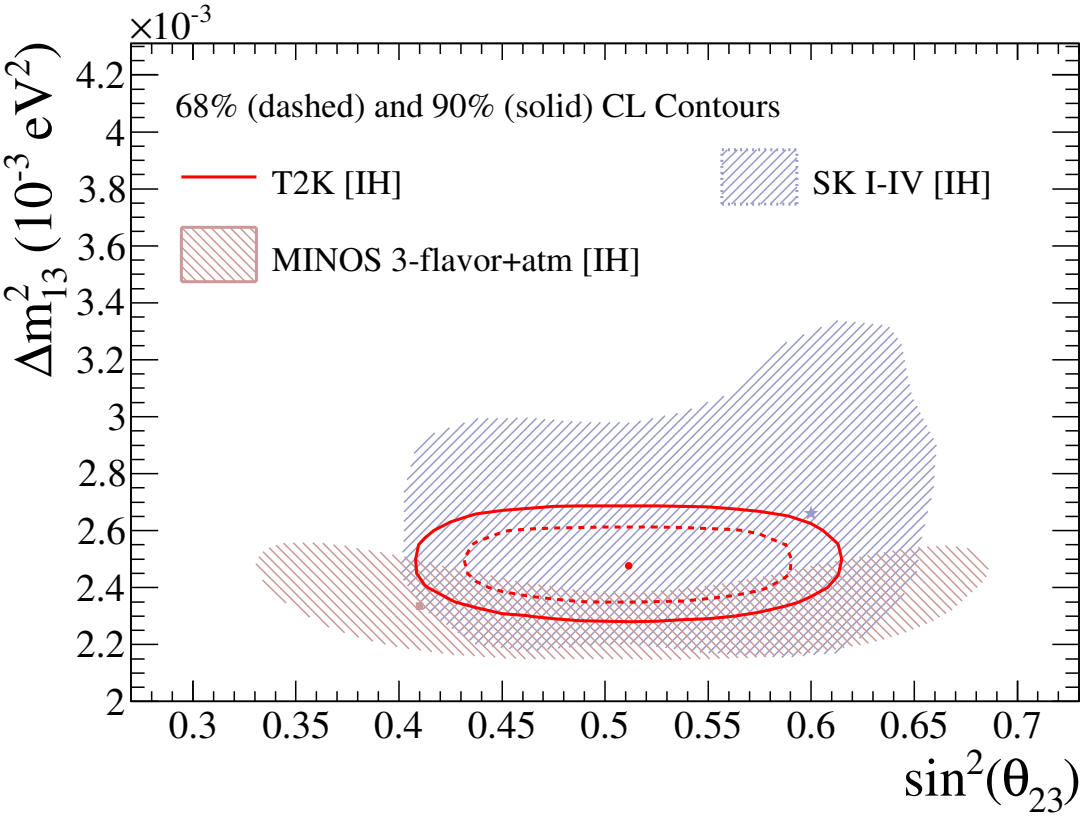

FIGURE 8.20: The 90% confidence regions allowed by T2K, Super-Kamiokande and MINOS for the inverted hierarchy.

mass splitting parameter, Δm^2, from global fits (Forero et al. (2012)).

8.6 Future Directions

For future improvements to this analysis, the largest gain will likely come from simply gathering more statistics. With the current amount of data, the statistical uncertainty is still dominant. This can be seen by inspecting Figure 8.17 which shows that analyzing the results with and without the systematic uncertainties produces similar allowed regions. Therefore, with additional events, the constraint on the parameters will improve.

Still it is useful to note that the dominant systematic uncertainties come from those associated with the event selection at Super-K. In particular, the largest con-

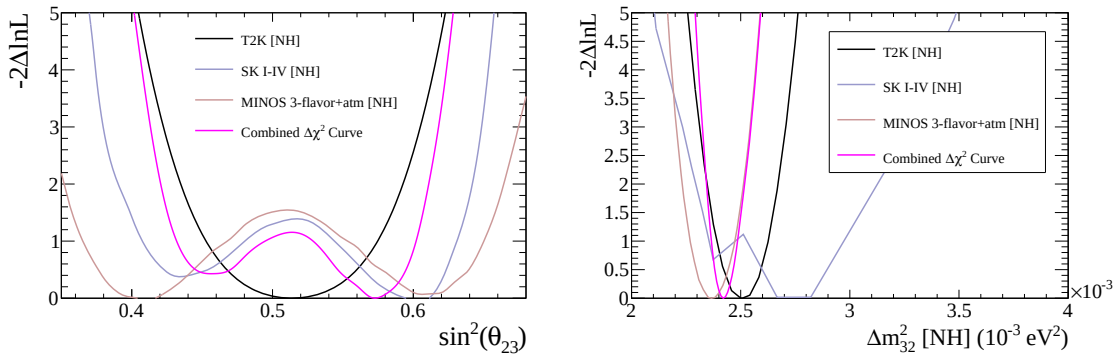

(a) $\sin^2\theta_{23}$ $\Delta\chi^2$ curves (b) Δm^2_{32} $\Delta\chi^2$ curves

FIGURE 8.21: 1D $\Delta\chi^2$ curves for the mixing parameters $\sin^2\theta_{23}$ and Δm^2_{32} for the Super-K (Himmel (2013)), and MINOS (MINOS Collaboration et al. (2014)) results compared with the results from T2K presented in this dissertation. This is a preliminary figure, and the combined $\Delta\chi^2$ is not an official result of T2K.

tributors from this class of uncertainties are from the uncertainty in the energy scale and the uncertainty in the rejection efficiency of neutral current events by both the particle ID selection and the 1-ring selection. The current size of the energy scale uncertainty is 2.3% which is already small. This makes possible improvements difficult. Such improvements would come from better modeling of the detector and improved momentum and direction reconstruction. Efforts towards such goals are on-going at Super-K, but already, the performance of existing methods is quite good.

The effort to reduce the uncertainty in the selection of neutral current events is hampered by the fact that there is no way to estimate this value with a clean data sample. The uncertainty, as described in Chapter 6, is extracted statistically from a fit of the atmospheric neutrino events which are used as a side-band sample for this analysis. However, this method is, in part, limited by the statistics of the atmospheric neutrino sample. Therefore the extracted uncertainty might improve with a larger atmospheric neutrino events sample collected by Super-K.

In addition, improvements in the analysis technique can potentially reduce the fraction of the neutral current events seen at Super-K, and, therefore, reduce the

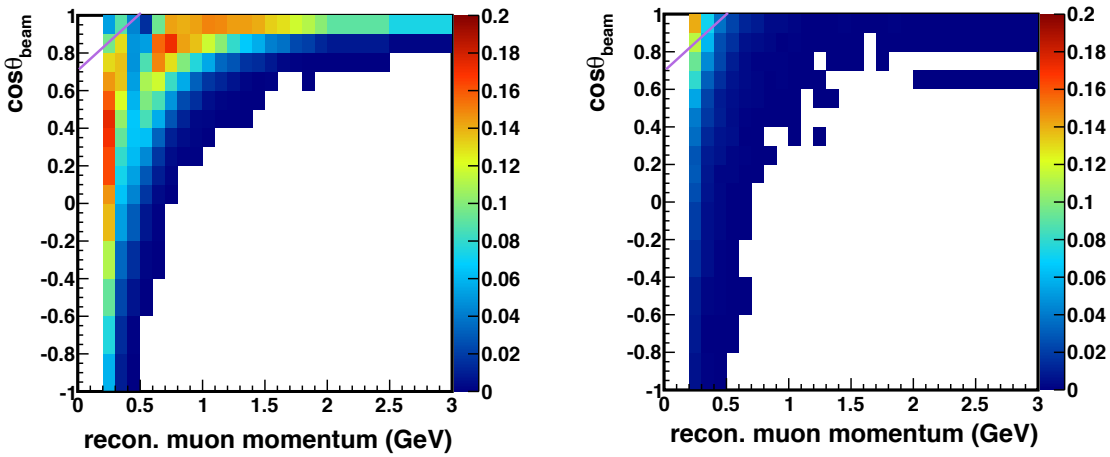

FIGURE 8.22: Predicted kinematic distribution of single muon track for events that pass the event selection. The predicted distribution on the left is for events that interact via the charged-current quasi-elastic (CCQE) channel. The distribution on the right is of neutral current (NC) events that pass the selection. The magenta line is provided as a visual aid to show the boundary between the CCQE and NC distributions. Future muon disappearance analyses at T2K that are more systematics limited could exploit the kinematic separation between the signal interactions (CCQE) and the NC interactions which are associated with one of the largest uncertainties in the current analysis.

effect of the associated uncertainty. Figure 8.22 shows the predicted distribution of events that pass the selection as a function of reconstructed muon direction with respect to the beam direction versus the reconstructed muon momentum for neutrino events from charged-current interactions and neutral current interactions. One can see that a large portion of the neutral current interactions include observed tracks that travel close to the beam direction and have low momentum. One method to improve the measurement is to perform the fit using the 2D distribution of muon momentum and the cosine of the muon direction with respect to the beam. Such an analysis would provide a way to separate the effect of the neutral current selection uncertainty from the oscillation effect. This is one direction of improvement by the T2K oscillation analysis group.

9

Conclusion

T2K has collected 120 single-ring, muon-like events at the Super-K detector which we have used to measure muon neutrino disappearance. Our analysis was performed in the context of the current standard three-neutrino mixing model. Therefore, we have produced constraints on the neutrino mixing parameters, $\sin^2(\theta_{23})$ and $\Delta m^2_{32}/\Delta m^2_{13}$, which are the leading contributors to the oscillation probability of muon neutrino disappearance. The constraints on $\sin^2(\theta_{23})$ are currently the world's best, while the constraints on $\Delta m^2_{32}/\Delta m^2_{13}$ are comparable to previous measurements. We find that the parameter values are $\sin^2\theta_{23} = 0.514^{+0.055}_{-0.056}$ and $\Delta m^2_{32} = (2.51 \pm 0.10) \times 10^{-3}$ $\mathrm{eV}^2/\mathrm{c}^4$ under the the normal hierarchy assumption and $\sin^2\theta_{23} = 0.511 \pm 0.055$ and $\Delta m^2_{13} = (2.48 \pm 0.10) \times 10^{-3}$ $\mathrm{eV}^2/\mathrm{c}^4$ under the inverted hierarchy assumption. This measurement is a step forward in precisely measuring the neutrino mixing matrix.

Ultimately, the physical parameters that this and other measurements are after are the values for the elements of the PMNS mixing matrix. The magnitude of the

elements in the matrix are

$$\begin{pmatrix} |U_{e1}| & |U_{\mu 1}| & |U_{\tau 1}| \\ |U_{e2}| & |U_{\mu 2}| & |U_{\tau 2}| \\ |U_{e3}| & |U_{\mu 3}| & |U_{\tau 3}| \end{pmatrix} = \begin{pmatrix} 0.819 & 0.552 & 0.158 \\ 0.483 & 0.515 & 0.708 \\ 0.309 & 0.656 & 0.688 \end{pmatrix}. \quad (9.1)$$

The magnitudes were calculate using the results of the current measurement of $\sin^2(\theta_{23})$ and the current best values for the other mixing angles. Note that the magnitudes are shown because one of the parameters, δ_{CP}, has yet to be constrained directly by experiment.

Much of the effort in the field, both in the near and far term, is directed at the measurement of δ_{CP}. While it will require next-generation neutrino oscillation experiments to measure a non-zero value of δ_{CP} at high significances, in the near term current experiments such as T2K and another accelerator experiment called NOvA (Patterson (2013)), can begin to constrain the value of δ_{CP}. A precision measurement of the parameters, $\sin^2(\theta_{23})$ and Δm^2_{32}, is important in such efforts.

For example, in addition to the measurement of muon neutrino disappearance, T2K also used the same data set to measure electron neutrino appearance. The primary parameter that this oscillation process is sensitive to is $\sin^2\theta_{13}$. However, the process has some dependence on δ_{CP} as well as discussed in Section 3.7.1. Figure 9.1 shows three 1D 68% confidence level intervals for the parameter $\sin^3\theta_{13}$ as a function of δ_{CP} where each interval assumes a different value of $\sin^2(\theta_{23})$. The figure demonstrates that the measurement of electron neutrino appearance depends on a precise measurement of $\sin^2(\theta_{23})$. Furthermore, Figure 9.1 overlays the constraints on $\sin^3\theta_{13}$ from the nuclear reactor experiments (in the yellow band). One can see in the figure that for certain values of δ_{CP}, the confidence level intervals measured by T2K and the reactor experiments do not overlap. This disagreement points to the fact that when combining the measurement of electron neutrino appearance by T2K and electron anti-neutrino disappearance by the reactor experiments, some of

the values of the parameter, δ_{CP} are disfavored at the 2 σ level or higher (T2K Collaboration (2014)). This result is an important first step in the measurement of δ_{CP}. Improving upon such measurements at T2K and with NOvA will require that both experiments improve the precision of both electron neutrino appearance and improve the measurement of the muon disappearance parameters.

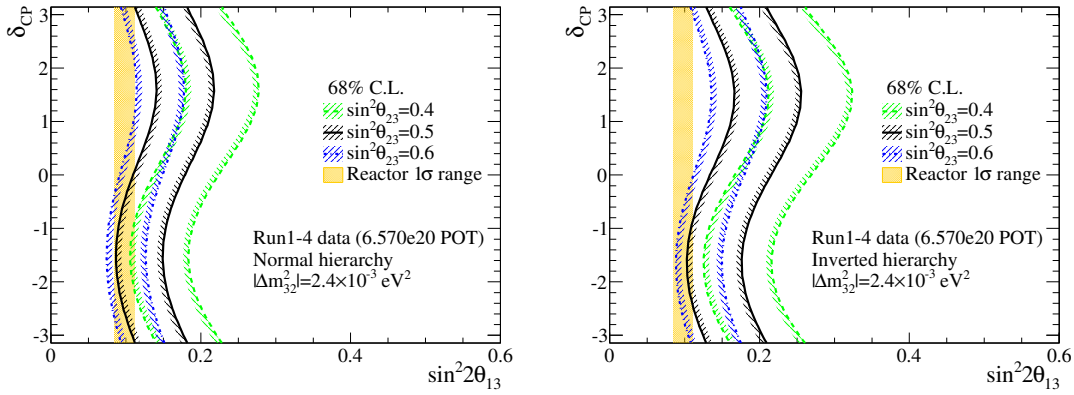

FIGURE 9.1: The 1D 68% confidence level intervals for $\sin^2\theta_{13}$ as a function of δ_{CP} for several assumed values of $\sin^2(\theta_{23})$. There are three intervals plotted, one for different values of $\sin^2(\theta_{23})$ (black, blue and green lines). These constraints come from the measurement of electron neutrino appearance at T2K using the same data as the analysis presented in this dissertation. The intervals are shown for the normal (left) and inverted (right) hierarchy assumptions. Also, overlaid are the constraints on $\sin^2\theta_{13}$ from the reactor neutrino oscillation experiments. The value of the mixing angle, $\sin^2(\theta_{23})$, is important in constraining the value of $\sin^2\theta_{13}$. Figure from (Ieki et al. (2013)).

In this dissertation, we have presented the measurement of muon neutrino disappearance at the T2K experiment, which has placed the world's best contraint on the mixing angle, $\sin^2\theta_{23}$, while putting constraints on the mass splitting Δm^2_{32} (Δm^2_{13}) for the normal (inverted) hierarchy. With the current 120 observed events, the effect of the statistical uncertainties on the measurement are larger than the effect of systematic uncertainties. Furthermore, toy data studies showed that there are physical boundary effects near $\sin^2\theta_{23} = 0.5$ that required our use of the Feldman-Cousins method to build the confidence regions in order to ensure that the regions provide

the proper coverage.

Appendix A

Frequentist Confidence Intervals

In this appendix we briefly describe the typical methods used to build frequentist confidence intervals. We emphasize the assumptions and weaknesses of these methods, because it turns out that these common methods are inadequate for the analysis decribed in this dissertation. However, we describe the common methods here in order to provide the context for the method that is used, the Feldman-Cousins procedure, which is briefly described in Chapter 8 and in more detail in Appendix B.

A confidence interval is a statistical quantity that is meant to convey the uncertainty of a given estimate. For example, suppose that one has a given data sample and a model of the data that contains some number of parameters. In such a situation, one is usually interested in the values of the parameters that give the best agreement between the model and data. One would also be interested in the range of parameter values that are consistent with the data set. For the latter, the confidence interval provides a means to quantify this range. The frequentist confidence interval is defined such that if one were to take repeated measurements of the parameter, then at least α percent of the time the parameter would be measured in the interval.

The value, α, is known as the confidence level.

Two things to note about the confidence interval. For one, it is related to observed quantities, which means that it is expected to vary depending on the data sample that was used to calculate it. The other thing to note is that the interpretation of the confidence interval might be different from a more natural interpretation of what an uncertainty interval means for some estimate. The confidence interval does not give the probability that the true value of an estimate, in our example the value of the parameters, lies within the interval. Such an interval is known as a credible interval and is associated with Bayesian statistical techniques in contrast to the frequentist methods used here. The Bayesian credible interval requires one to include estimates of prior knowledge into the construction of the interval, which can at times be difficult and/or ambiguous. In contrast, the frequentist approach to building the confidence interval does not require the definition of this prior information. However, the interpretation of the interval can be less intuitive as it makes a statement about the probability of observing a quantity again for future repeated measurements instead of giving a more direct statement about what we know about the quantity after making a measurement. If one is unlucky, the true value of the parameter may not be in the frequentist interval 1-α percent of the time.

A.1 Confidence Intervals from the χ^2 Method

As stated previously, often one wants to fit a model to some data sample. Typically, the goal is to have the model match the distribution of measurements of some observable quantity. Often, the values of the observable are divided into a series of intervals, and the number of measurements that fall within the intervals are recorded. In what is known as the χ^2 method, one then fits the model to the data by finding the parameter values that minimize the squared errors between the number of events observed and predicted in each ith of N intervals, or bins. The sum of the normalized

squared errors is known as the Pearson χ^2 test statistic and is defined as

$$\chi^2 = \sum_{i=1}^{N} \frac{(O_i - E_i)^2}{\sigma_i}, \tag{A.1}$$

where O_i is the observed number of events in the ith bin, E_i is the expected or predicted number of events by the model in the ith bin, and σ_i is the uncertainty in the prediction of the ith bin. This test statistic provides a way to quantify the agreement between the model and data.

Importantly, this quantity also provides a way to test if the model is a good fit to the data. This method centers around the ability to assign a probability to observing a value of χ^2 given a data sample. One starts by assuming that the data observed derives from the model in question and that the N errors from the N bins follow the normal distribution. In this case, the χ^2 statistic follows the probability density function (PDF) given by

$$\chi^2(x;k)_{PDF} = \frac{1}{2^{k/2}\Gamma(\frac{k}{2})} x^{\frac{k}{2}-1} e^{-\frac{x}{2}}, \tag{A.2}$$

where x is the sum of normalized squared errors (or the χ^2 test statistic above) and k is the number of degrees of freedom. In the case of the binned data example above, k would be the number of bins less the number of parameters in the fit.

The reason that this definition is so useful is that the cumulative distribution function (CDF) for the $\chi^2(x;k)$ distribution can be derived analytically from the PDF. With the CDF known, one can determine the probability that a value of the χ^2 test statistic is equal to or greater than the value observed for the data. This probability provides a quantity to reject the goodness of the fit.

Finally, the CDF of the $\chi^2(x;k)$ distribution also provides a way to build a frequentist confidence interval. One starts by expanding to second order the χ^2

statistic around the best-fit value, $\chi^2_0(\hat{\theta})$, as a function of the fit parameter, θ, where

$$\chi^2 = \chi^2_0(\hat{\theta}) - \frac{1}{2}|\frac{\partial\chi^2}{\partial^2\theta}|_{\theta=\hat{\theta}}(\theta-\hat{\theta})^2 + O((\theta-\hat{\theta})^3), \tag{A.3}$$

where the first order term is zero and the second term is negative as we are expanding around the minimum value of χ^2. Note that at second order,

$$\Delta\chi^2 = \chi^2 - \chi^2_0 \tag{A.4}$$

is proportional to the the squared difference from the best-fit value, $\hat{\theta}$, much like the original χ^2 statistic. If we take

$$\sigma^{-2} = |\frac{\partial\chi^2}{\partial^2\theta}|_{\theta=\hat{\theta}} \tag{A.5}$$

then $\Delta\chi^2$ ought to follow the χ^2 distribution as well. Therefore, we can use the CDF of the χ^2 to define confidence intervals. For a confidence level, α, defined between 0% and 100% , we define an interval for the parameter θ such that the

$$\mathrm{CDF}(\Delta\chi^2_\alpha(\theta)) \leqslant \alpha. \tag{A.6}$$

It is customary to calculate the intervals for 68% confidence level (CL) where $\Delta\chi^2 \approx 1.0$ and 90% CL where $\Delta\chi^2 \approx 2.7$ for one degree of freedom, i.e. one model parameter. In our analysis, we also want to know what the 2D confidence interval is for 68% and 90% CL where $\Delta\chi^2 \approx 2.3$ and $\Delta\chi^2 \approx 4.6$, respectively.

Note that this method assumes the χ^2 statistic as a function of θ is nearly parabolic. This is exactly true if the number of expected events in every bin is a linear function of the parameter θ. In other cases, it is necessary to check if this is a good approximation for whatever $\theta - \hat{\theta}$ value is required by the chosen confidence interval. However, the more important assumption is the normally distributed difference between the observed and predicted number of events. For the analysis

described in the thesis, the number of events is often relatively low as we are working with the weakly interacting neutrino. The next section describes methods for dealing with lower statistics.

A.2 Confidence Intervals from an Unbinned Likelihood

For the χ^2 method, the primary assumption was that the differences in the number of observed and expected events in each bin was normally distributed. This assumption is good when the number of events in each bin is large (typically tens of events in each bin is considered sufficient). However, for our analysis, we are trying to extract information using 120 events. Furthermore, the shape of the distribution is very important, so binning these 120 events such that there are enough events per bin would obscure too much of the shape information.

For low statistics, one can fit the model parameters to the data using an unbinned likelihood which was described in Chapter 6 and is the likelihood used in the oscillation analysis found in this dissertation. This likelihood is used in order to avoid losing any information in the shape of the observed distribution in the process of binning.

Besides using the χ^2 test statistic to fit the parameters of a model to data, one can also used the maximum likelihood estimator which is described in Chapter 6. Similar to what was done for the χ^2 method, one chooses the best fit parameters, $\hat{\theta}$, to be those that maximize the value of a function, $L(\theta|x)$, dependent on some parameters, θ, and a given set of observations $\mathbf{x}$.

To define a set of confidence intervals, we first expand $\ln L$ around the maximum of the likelihood, $L_o(\hat{\theta}|x)$, with respect to the best fit parameters. We then get

$$\ln L = \ln L_0(\hat{\theta}|x) - \frac{1}{2}\left|\frac{\partial^2 \ln L}{\partial \theta^2}\right|_{\theta=\hat{\theta}} (\theta - \hat{\theta})^2 + ... \tag{A.7}$$

where we know that the first derivative is zero and the second derivative term should be negative, since we are at the maximum of the function. We then note that

$$-2\Delta \ln L = \left| \frac{\partial^2 \ln L}{\partial \theta^2} \right|_{\theta=\hat{\theta}} (\theta - \hat{\theta})^2 + ..., \tag{A.8}$$

where $\Delta \ln L = \ln L(\theta|x) - \ln L_0(\hat{\theta}|x)$, i.e. the difference of the log-likelihood from its maximum. This is equivalent to $\Delta\chi^2$ above if the region near the maximum of the likelihood is sufficiently quadratic. Therefore, in this case we can use the CDF of the χ^2 distribution to define the confidence intervals for the parameters estimated using the unbinned log-likelihood.

However, the assumption that $-2\Delta \ln L \approx \chi^2$ is not often valid, especially in low statistic cases which is when we use the unbinned log-likelihood method. In these cases the measured confidence intervals can be inaccurate. Often at low statistics, the intervals will be too small and underestimate the uncertainty of the measurement of the model parameters.

However, the confidence interval is often cited using this method because it is very quick and convenient to calculate. This, of course, is due to the reliance on the χ^2 distribution which relies on the assumption that the distribution of measured parameter values is distributed normally around the true value. But when more accuracy is required or desired for low statistics analysis, then another method not based on the χ^2 distribution is needed.

In the following section, we present the Neyman construction for building confidence intervals whose strategy is to use pseudo-experiments instead of relying on the normal distribution. The calculation of intervals in this manner can be more difficult, but the result is that in most cases, the confidence intervals will be accurate by construction.

A.3 Neyman Construction of Confidence Intervals

Neyman proposed a frequentist construction of confidence intervals using the following prescription:

1. Find the measured values as a function of the true values, $\hat{\theta}_1(\theta)$ and $\hat{\theta}_2(\theta)$ such that

$$\int_{-\infty}^{\hat{\theta}_1(\theta)} P(\hat{\theta}|\theta)d\theta = \frac{1-\alpha}{2} \tag{A.9}$$

and

$$\int_{\hat{\theta}_2(\theta)}^{+\infty} P(\hat{\theta}|\theta)d\theta = \frac{1-\alpha}{2} \tag{A.10}$$

2. Use the inverse of the above functions, $\theta_1(\hat{\theta}) = \hat{\theta}_1^{-1}(\theta)$ and $\theta_2(\hat{\theta}) = \hat{\theta}_2^{-1}(\theta)$, to define the confidence interval $[\theta_1(\hat{\theta}), \theta_2(\hat{\theta})]$ for a given confidence level, α.

By construction, the confidence interval built following these steps tells us that $\alpha\%$ of the time, the true value of the parameter lies inside the interval. The Neyman confidence interval is a more generic definiton that the previous methods dicussed above as it makes no assumption about the form of $P(\hat{\theta}|\theta)$. In the special case where the probability density follows a Gaussian distribution, then the χ^2-based methods above apply.

Quite often the functions required to build the Neyman confidence interval are not analytic and must be calculated using Monte Carlo techniques. Here one scans over a range of true parameter values and for each one performs many pseudoexperiments to build the $P(\hat{\theta}|\theta)$ distribution that is needed.

Despite the generic nature of the probability distribution, the Neyman prescription is still problematic or ambiguous in certain experimental situations. Such situations are discussed in depth in (Feldman and Cousins (1998)). In the reference, the problems have to due with step 1 in the method listed above. It is not always

the case that the interval can be approached from infinity from both sides, in other words be "two-sided." Instead, one side of the interval will be up against a boundary in the allowed parameter values. In these cases one will want to define an upper or lower bound on the parameter values, or "one-sided" interval. For example, if a model involves a parameter that defines the expected number of events observed by a measurement, then the expectation cannot be a negative number. Furthermore, if such an experiment involves looking for the presence of a small signal and the measurement turns out to be consistent with zero, one will want to define an upper bound on the expected amount of signal events. The situation can be futher complicated by the fact that sometimes the choice of whether to calculate an interval or an upper/lower bound is not clear.

A method to implement step 1 generically is proposed by the Feldman-Cousins method in (Feldman and Cousins (1998)) and is described in Appendix B. Appendix B also provides some details of the implementation used in this analysis.

Appendix B

Feldman-Cousins Implementation

\$40,000
–approximate cost of calculation at
2013 market price of electricity

For the estimation of the $\sin^2\theta_{23}$-Δm^2 confidence intervals in our analysis, we use the Feldman-Cousins (F&C) method (Feldman and Cousins (1998)) instead of the using the more common $\Delta\chi^2$ method discussed in Appendix A.

As mentioned in Appendix A, the Feldman-Cousins procedure is necessary when it is ambiguous if the analysis should report an interval or an upper/lower bound. Such cases occur in the situation where the number of data events is small. The procedure is also needed when a parameter one is trying to fit is up against a physical boundary. For the analysis discussed in this dissertation both conditions apply.

The way the procedure improves upon the Neyman prescription given in Equations (A.9) and (A.10) is to provide a method for determining what parameter falls into the interval without assuming the form of the interval, i.e. two-sided or an upper/lower bound. It does this by defining an ordering parameter, $R(\hat{\theta}, \theta)$, that is a

function of the fitted parameter, $\hat{\theta}$, and true parameter value, θ. The parameter R is then used to build the interval by

1. using pseudo-experiments to build a PDF distribution of $R(\hat{\theta}, \theta)$ at each value of the true parameter value, θ, by running many fits of toy MC data,

2. using the generated distribution to determine at each value of θ a value $R^{\alpha}_{critical}(\theta)$ for some confidence level, α, such that

$$\int_0^{R_{critical}(\theta)} \mathrm{PDF}(R) dR = \alpha, \tag{B.1}$$

3. calculating the value of the parameter, $R_{data}(\hat{\theta}, \theta)$, from the data, and then

4. building the confidence interval at a given level, α, to include all values of θ where $R_{data}(\hat{\theta}, \theta) < R^{\alpha}_{critical}(\theta)$.

The ordering parameter, R, suggested by the authors of the Feldman-Cousins method is a ratio defined at each value of a parameter, θ, and for some data, $\mathbf{x}$, as

$$R(\hat{\theta}, \theta; \mathbf{x}) = \frac{P(\mathbf{x}|\theta)}{P(\mathbf{x}|\hat{\theta})}, \tag{B.2}$$

where $\hat{\theta}$ is the measured or fitted parameter value, and θ is the true value of the parameter value. Note that the data, x, refers to both toy MC pseudo-data and real data. For the case of real data, the true value is not known, but rather, various values of the parameter value are scanned over in order to determine if that value of the parameter should be in the interval.

For our analysis, we do not use the exact definition of R in Equation (B.2) but instead use an alternate form also found in (Feldman and Cousins (1998))

$$R(\hat{\theta}, \theta) = -2(\ln \mathcal{L}(\theta|\mathbf{x}) - \ln \mathcal{L}(\hat{\theta}_{\mathrm{best}}(\theta)|\mathbf{x})) \tag{B.3}$$

which is just the difference between the likelihood at a value of θ and the maximum likelihood at $\theta_{\rm best}$. We refer to this difference as $-2\Delta \ln \mathcal{L}$ and refer to its critical value as $-2\Delta \ln \mathcal{L}_{\rm crit}$.

B.1 FC Implementation for 2D Confidence Region

In our implementation of the F&C method, we perform 10,000 toy experiment fits at each of several values of $\sin^2\theta_{23}$-Δm^2_{32} for the normal hierarchy and $\sin^2\theta_{23}$-Δm^2_{13} for the inverted hierarchy. When generating the toy MC data sets, we first choose a random set of systematic uncertainty parameter values following their defined prior distributions which, for the most part, are multi-dimensional Gaussian distributions. We then calculate the expected neutrino energy spectrum and then use this spectrum to generate a set of fake measurements of neutrino energy. The number of measurements we generated follows a Poisson distribution where the expected number of events comes from the integral of the generated neutrino spectrum.

For each fit of the toy data sets, we calculate the value of R in Equation (B.3). Therefore, for each pair of oscillation parameter values, we build up a distribution of R values. We then use the R distribution to find the $-2\Delta \ln \mathcal{L}_{\rm crit}$ for α% C.L. such that α percent of toy experiments have $-2\Delta \ln \mathcal{L} < -2\Delta \ln \mathcal{L}_{\rm crit}$. The calculated values of $-2\Delta \ln \mathcal{L}_{\rm crit}$ as a function of of the oscillation parameters are shown in Figure 8.14.

Finally, $-2\Delta \ln \mathcal{L}_{data}$ is calculated for the same set of points in the $\sin^2\theta_{23}$-Δm^2_{32} plane using a fit to the data. The confidence region for the data is then built, in principle, by including all points where $-2\Delta \ln \mathcal{L}_{data} < -2\Delta \ln \mathcal{L}_{\rm crit}$. In practice, what we do is subtract from $-2\Delta \ln \mathcal{L}_{data}$ the difference between the $-2\Delta \ln \mathcal{L}_{\rm crit}$ value found by our toy MC fits and $-2\Delta \ln \mathcal{L}_{\rm crit}$ for the Gaussian case. This is equivalent

to the $-2\Delta \ln \mathcal{L}_{data} < -2\Delta \ln \mathcal{L}_{\rm crit}$ condition as can be seen by

$$\begin{aligned} -2\Delta \ln L_{data} &< -2\Delta \ln L_{critical} \\ -2\Delta \ln L_{data} &< -2\Delta \ln L_{gaus} + -2\Delta \ln L_{correction} \\ -2\Delta \ln L_{data} - -2\Delta \ln L_{correction} &< -2\Delta \ln L_{gaus} \end{aligned} \tag{B.4}$$

where $-2\Delta \ln L_{correction} = -2\Delta \ln L_{critical} - -2\Delta \ln L_{gaus}$. This trick allows us to numerically interpolate when drawing the 2D contour in the oscillation parameter plane. (In practice, we let ROOT then draw the 2D contour based on the values of $-2\Delta \ln L_{data} - -2\Delta \ln L_{correction}$.) For 68% CL, we use $-2\Delta \ln L_{gaus} = 2.3$. For 90% CL, we use $-2\Delta \ln L_{gaus} = 4.6$.

B.2 FC Implementation for 1D Confidence Intervals

In addition to 2D Feldman-Cousins allowed regions on the oscillation parameters, we calculate the individual bounds on $\sin^2\theta_{23}$ and Δm^2 using the Feldman-Cousins procedure. Just like in the 2D case, we must calculate the $-2\Delta \ln \mathcal{L}_{\rm crit}$ values using pseudo-experiments for several values of $\sin^2\theta_{23}$ and Δm^2 in order to build the confidence interval. However, for 1D bounds, we must generate the pseudo-experiments separately for each parameter and this presents a problem. When we generate toy MC data for a given oscillation parameter, we not only need to vary the systematic error values but also need to vary the "other" oscillation parameter. For example, to generate toy MC at $\sin^2\theta_{23} = 0.5$ we must choose for each pseudo-experiment a value of Δm^2_{32} along with values for the systematic parameters when generating events for each toy MC data set. While the prior distributions for the systematic errors are well defined, it is not obvious what prior distribution to use for the "other" oscillation parameter, in this example, Δm^2_{32}.

For this analysis, we decided to take a data-driven approach and use the RUN1-4 data to set the prior on the "other" oscillation parameter. Specifically, we use the

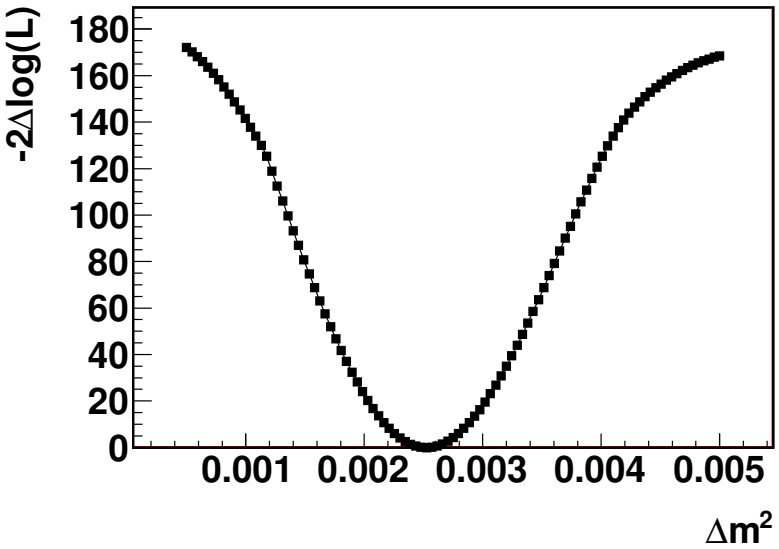

FIGURE B.1: Example $-2\Delta \ln \mathcal{L}(\Delta m^2_{32}; \sin^2\theta_{23})$ curve calculated from a profiled fit of the data. The curve is calculated for a fit with a fixed value of $\sin^2\theta_{23} = 0.375$ and assumed normal hierarchy. This curve is used to generate the likelihood distribution that will form the prior for Δm^2_{32} when $\sin^2\theta_{23} = 0.375$. The curve and the resulting prior is used when calculating the 1D Feldman-Cousins (FC) bounds on $\sin^2\theta_{23}$. Analogous curves are generated for $-2\Delta \ln \mathcal{L}(\sin^2\theta_{23}; \Delta m^2_{32})$ when calculating the 1D FC bounds on Δm^2_{32}.

profiled $-2\Delta \ln \mathcal{L}$ curve coming from a fit to the data to define the prior.

As a concrete example of this method, we describe the procedure for calculating the $-2\Delta \ln \mathcal{L}_{\text{crit}}$ value at a single value of $\sin^2\theta_{23} = 0.375$ for the normal hierarchy.

First, we must generate toy MC data at this oscillation parameter value that includes variations in the value of Δm^2_{32}. Therefore, we build a prior distribution for Δm^2_{32} by computing $-2\Delta \ln \mathcal{L}\ (\Delta m^2_{32}; \sin^2\theta_{23} = 0.375)$ using the data.

We calculate $-2\Delta \ln \mathcal{L}(\Delta m^2_{32}; \sin^2\theta_{23})$ by performing a fit to the data with $\sin^2\theta_{23}$ set to 0.375 for several values of Δm^2_{32}. The result of these fits is used to define the $-2\Delta \ln \mathcal{L}_{data}$ curve shown in Figure B.1.

Next, the $-2\Delta \ln \mathcal{L}(\Delta m^2_{32}; \sin^2\theta_{23} = 0.375)$ is used to form a prior distribution for Δm^2_{32} when $\sin^2\theta_{23} = 0.375$. It is derived from the curve using $L(\Delta m^2_{32}; \sin^2\theta_{23} =$

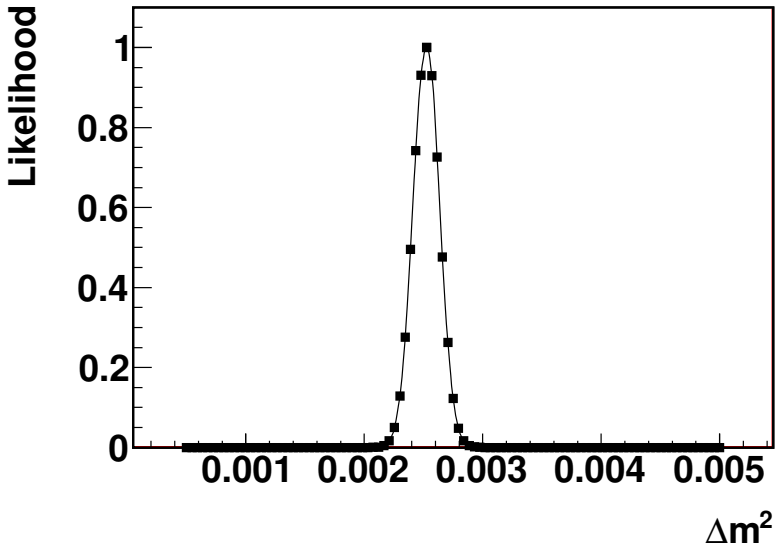

FIGURE B.2: Example likelihood distribution for Δm^2_{32} calculated from the $-2\Delta \ln \mathcal{L}$ example curve in Figure B.1. The distribution is calculated for a fit with a fixed value of $\sin^2\theta_{23} = 0.375$ and assumed normal hierarchy. This distribution defines the prior on the value of Δm^2_{32} when $\sin^2\theta_{23} = 0.375$. The distribution is used as a prior to generate toy MC data sets which vary Δm^2_{32} according to this distribution. The resulting set of toy MC events is then used to calculate the $-2\Delta \ln \mathcal{L}_{\text{crit}}$ value at $\sin^2\theta_{23} = 0.375$. Analogous likelihood distributions are generated for $\sin^2\theta_{23}$ for a given value of Δm^2_{32} when calculating the 1D FC bounds on Δm^2_{32}.

$0.375) = e^{-\frac{1}{2}(-2\Delta \ln \mathcal{L}(\Delta m^2_{32};\sin^2\theta_{23}))}$. The resulting likelihood distribution for our example is shown in Figure B.2.

Then, the likelihood distribution is used as an input to generate toy MC data sets at $\sin^2\theta_{23} = 0.375$. The data sets include variations in the systematic parameters and Δm^2_{32}. The values of Δm^2_{32} used to generate each toy MC data set are sampled from the likelihood distribution. (Note, the toy MC data sets also include variations in the remaining oscillation parameters. The parameters $\sin^2\theta_{12}$, $\sin^2\theta_{13}$, and Δm^2_{12} are given Gaussian priors whose mean and sigma are taken from PDG2012 (Beringer and Particle Data Group (2012)). The values of δ_{CP} are varied uniformly between $-\pi$ and π.)

The toy MC data sets are then used to calculate the $-2\Delta \ln \mathcal{L}_{\text{crit}}$ as defined by Feldman-Cousins procedure. This is the same procedure used in the 2D allowed region calculation. Finally, the $-2\Delta \ln \mathcal{L}_{\text{crit}}$ at $\sin^2\theta_{23} = 0.375$ is then compared to the $-2\Delta \ln \mathcal{L}_{data}$ calculated from a fit to the data with $\sin^2\theta_{23}$ set to 0.375 and the value of Δm^2_{32} profiled out. If $-2\Delta \ln \mathcal{L}_{data} < -2\Delta \ln \mathcal{L}_{\text{crit}}$ then the value of $\sin^2\theta_{23} = 0.375$ is included in the confidence interval. If it is greater than $-2\Delta \ln \mathcal{L}_{\text{crit}}$, it is not included. This same procedure is performed for several values of $\sin^2\theta_{23}$. The results of the procedure is shown in Figure 8.4.

Appendix C

OD Background Check

In the T2K analysis that saw an indication of non-zero θ_{13} (Abe et al. (2011a)), many of the vertices of the ν_e candidate events were observed to be clustered on the upstream side of the detector. This observation raised the possibility that particles produced by neutrinos outside the inner detector were making their way inside and passing the ν_e selection cuts. Such a source of background was not yet fully explored because the existing standard MC, used to build the expectations for the oscillation analysis, consisted of simulated events with interaction vertices that only extended 55 cm from the inner detector wall into the dead space. This left out the possibility that events originating from the outer detector or rock, might also be "leaking" into the detector. In order to estimate the size of such a "leakage" background, we prepared a complementary set of MC events with a wider generation volume and evaluated its effect on the background. In this section, we begin with a description of the MC samples used. We then present the our study's results, which include an estimate of the number of events that come from outside the ID and the type of events that make up this background.

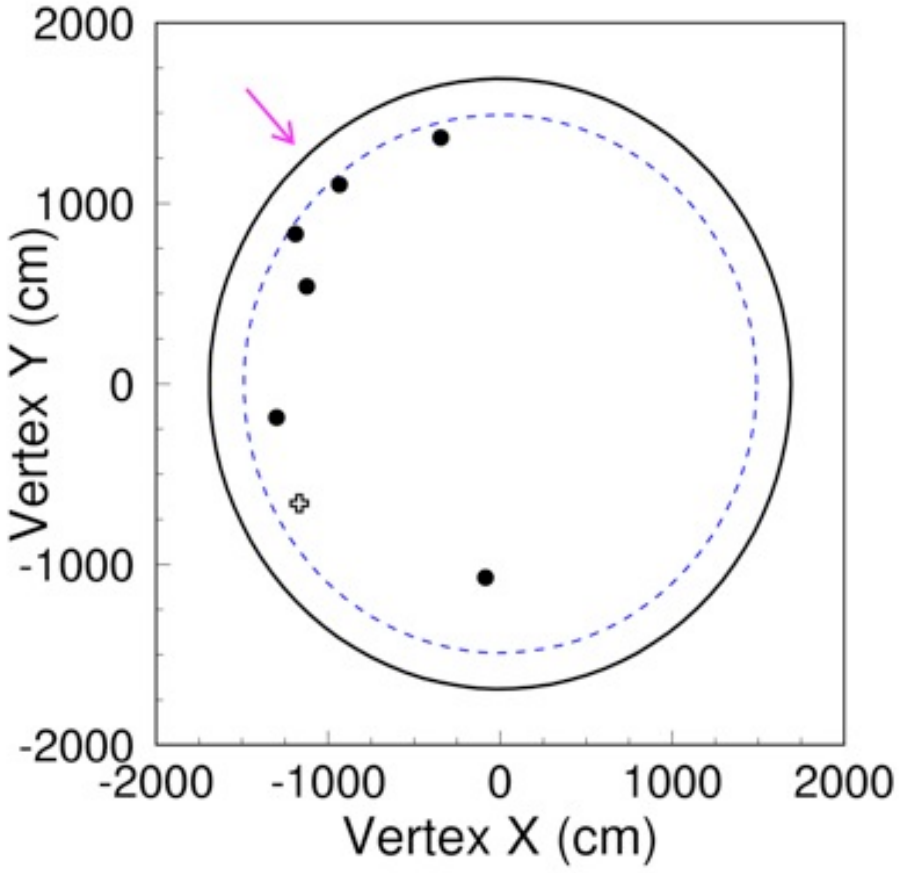

FIGURE C.1: Distribution of ν_e candidate events used in the T2K analysis that saw an indication of non-zero θ_{13}. Figure made by S. Nakayama.

C.1 Description of MC events

Instead of the standard MC for the usual FC event study, we used an additional set of the MC because the standard MC only simulates events up to 55 cm outside the ID boundary. The MC sample used in the study combined two separately generated MC samples of events involving the OD: one known as the OD MC and another referred to the "leakage" MC sample. The difference between the two has to do with the volume overwhich the events were generated. The OD MC was generated in a large volume that encapulated the Super-K detector. The leakage MC had events

generated in the volume of rock near the edge of the Super-K detector in order to quickly increase number of MCs events that would pass the T2K selection cuts. Further details about the OD MC can be found in Appendix D.

C.1.1 Outer Detector MC

The OD MC, used to study the OD events, consists of interactions generated within a large 60 m $\times$ 60 m $\times$ 60 m box in order to simulate beam events originating from the outer detector and rock. This set of MC events provides the ability to study beam events from the rock or OD which might enter the inner detector and accounts for possibility that events originating from the Super-K detector wall will make it into the final data samples. It should be noted that the OD MC includes events inside the inner detector too, which makes the OD MC a superset of the standard ID MC. (The ID MC covers a cylindrical volume with a diameter of 1,745 cm and height of 3,730 cm.)

Because the OD MC generates events both inside and outside the detector, neutrino interactions must be generated assuming different targets. Targets currently included in the OD MC are water, oxygen and silicon. In total, MC events are generated in sets with each set defined by a choice of the flavor of neutrino flux, the flavor of neutrino interacting, and the target with which the neutrino interactions. One such set we refer to as a "MC component". Once all of the components are generated, they are combined through weights given to each OD MC event. An example of one such component is a set of events generated using the ν_μ beam flux with ν_μ cross sections on oxygen. Table C.1 lists the different combinations of flux, cross section and target. Because the OD MC components are generated separately, each will have its own normalization in units of POT based on the number of events expected to have been generated in a given volume of target.

The OD MC is put together by assigning a weight to each event that includes

the following factors:

- the oscillation probability of the event
- the elemental fraction in the rock
- MC livetime calculated for each combination of beam flux flavor.

The weight applied to each events is given by

$$\text{weight} \quad = \quad P_{\text{oscilation}} \times \text{ elemental fraction } \times \frac{\text{Experiment Livetime (POT)}}{\text{Component Livetime (POT)}}. \tag{C.1}$$

These weights will be different for each MC component. Table C.1 lists the values of these weights for the different combinations of flux, cross section and target in the total OD MC sample. Note that the POT used to weight the events takes into account the density of the rock outside of the Super-K, which is taken to be 2.7 g/cm^3. The rock included elements of oxygen and silicon in the MC. The neutrino flavors of ν_μ, ν_e, $\bar{\nu}_\mu$ were simulated along with the ν_e appearance combination of ν_μ flux with ν_e cross section.

MC leakage sample

The "leakage" MC sample outside the ID was generated inside a cylindrical shell volume. Its inner surface was defined by the ID/deadspace boundary, and its outer surface defined by a cylinder that extended 550 cm outward from the ID and into the rock. This "leakage" volume is illustrated in Figure C.2.

The distribution of events is shown in Figure C.3. Over 1.5 million events were generated inside the 41,921.34 m^3 leakage volume. Due to time constraints, the leakage sample was generated only for the ν_μ component of the beam flux with ν_μ cross sections on water instead of all the rock elements. To account for the water target, events whose vertices were in the rock were given an additional reweighting factor of 2.7 to account for the larger rock density.

Table C.1: Livetimes and assigned element percentages for the different sample components of the MC for this study. LV stands for "Leakage Volume". The last three columns give the value of weights applied to each event that belongs to the set of events specified by the first three columns. The elemental percentage applied depends if the interaction occurs in the rock or the water. Note that for ν_μ interactions in the rock, we combine the events from the leakage sample with the OD MC events in the rock. Note that events with water targets are normalized using the density of water. Therefore, when water events are in the rock, the elemental percentage is multiplied by the density of the rock to get $2.7 \times 1.0\% = 2.7\%$. This is slightly different for the Leakage MC water events. Here we treat this sample as its own contained MC model with events in the rock modeled by water with density of 2.7 g/cm^3. This leads to an elemental percentage weight of $2.7 \times 100\% = 270\%$.

OD MC Component				in water	in rock
Target	Flux	σ	POT	element %	element %
List of Weights for separate MC samples					
H_2O (OD MC)	ν_μ	ν_μ	1.55×10^{22}	100.0	2.7
H_2O (OD MC)	$\bar{\nu}_\mu$	$\bar{\nu}_\mu$	1.84×10^{22}	100.0	2.7
H_2O (OD MC)	ν_e	ν_e	8.93×10^{22}	100.0	2.7
H_2O (OD MC)	ν_μ	ν_e	5.78×10^{21}	100.0	2.7
O (OD MC)	ν_μ	ν_μ	3.16×10^{21}	0.0	78.2
O (OD MC)	$\bar{\nu}_\mu$	$\bar{\nu}_\mu$	5.64×10^{21}	0.0	78.2
Si (OD MC)	ν_μ	ν_μ	4.26×10^{21}	0.0	20.8
Si (OD MC)	$\bar{\nu}_\mu$	$\bar{\nu}_\mu$	7.30×10^{21}	0.0	20.8
H_2O (Leakage MC)	ν_μ	ν_μ	5.57×10^{23}	100.0	270.0
List of Weights used when OD MC and Leakage MC are combined					
H_2O (if event not in LV)	ν_μ	ν_μ	1.55×10^{22}	100.0	2.7
H_2O (if event in LV, water)	ν_μ	ν_μ	5.73×10^{23}	100.0	N/A
H_2O (if event in LV, rock)	ν_μ	ν_μ	5.57×10^{23}	N/A	270.0
H_2O	$\bar{\nu}_\mu$	$\bar{\nu}_\mu$	1.84×10^{22}	2.7	100.0
H_2O	ν_e	ν_e	8.93×10^{22}	2.7	100.0
H_2O	ν_μ	ν_e	5.78×10^{21}	2.7	100.0
O (not in LV)	ν_μ	ν_μ	3.16×10^{21}	0.0	78.2
O (in LV, water)	ν_μ	ν_μ	5.61×10^{23}	0.0	N/A
O (in LV, rock)	ν_μ	ν_μ	5.61×10^{23}	N/A	0.0
O	$\bar{\nu}_\mu$	$\bar{\nu}_\mu$	5.64×10^{21}	0.0	78.2
Si (not in LV)	ν_μ	ν_μ	4.26×10^{21}	0.0	20.8
Si (in LV, water)	ν_μ	ν_μ	5.61×10^{23}	0.0	N/A
Si (in LV, rock)	ν_μ	ν_μ	5.61×10^{23}	N/A	0.0
Si	$\bar{\nu}_\mu$	$\bar{\nu}_\mu$	7.30×10^{21}	0.0	20.8

Table C.2: Livetimes and assigned element percentages for the combined sample components of the MC for this study. These are the factors used to weight the events of this study via equation (C.2). Note that for ν_μ interactions on water in the leakage volume, the combined POT weight factor applied is the sum of the OD MC and leakage MC samples' POT. The factors for ν_μ events in the rock portion of the leakage volume are a little more complicated. In effect, the events from the leakage MC in the rock are combined with events from the OD MC by weighted by the relative number of events. In this case, of all the events in the rock portion of the leakage volume, about 93% of events are from the leakage MC sample, while a little more than 7% are from the OD MC. These fractions are applied to their relative elemental percentage.

List of Weights for MC events in the water. Combined OD and Leakage MC.				
OD MC Component				in water
Target	Flux	σ	POT	element %
H_2O inside inner detector	ν_μ	ν_μ	1.71×10^{22}	100.0
H_2O inside leakage volume	ν_μ	ν_μ	5.74×10^{23}	100.0
H_2O inside SK tank	$\bar{\nu}_\mu$	$\bar{\nu}_\mu$	1.87×10^{23}	100.0
H_2O inside SK tank	ν_e	ν_e	1.14×10^{23}	100.0
H_2O inside SK tank	ν_μ	ν_e	8.46×10^{21}	100.0

List of Weights for MC events in the rock. Combined OD and Leakage MC.				
OD MC Component				in rock
Target	Flux	σ	POT	element %
H_2O inside leakage volume	ν_μ	ν_μ	6.34×10^{21}	100×0.929
H_2O outside SK tank	$\bar{\nu}_\mu$	$\bar{\nu}_\mu$	6.93×10^{22}	1.0×0.071
H_2O outside SK tank	ν_e	ν_e	4.22×10^{22}	1.0×0.071
H_2O outside SK tank	ν_μ	ν_e	3.13×10^{21}	1.0×0.071
O outside SK tank	ν_μ	ν_μ	3.13×10^{21}	78.2×0.071
O outside SK tank	$\bar{\nu}_\mu$	$\bar{\nu}_\mu$	1.79×10^{22}	78.2×0.071
O outside SK tank	ν_e	ν_e	4.02×10^{22}	78.2×0.071
O outside SK tank	ν_μ	ν_e	7.50×10^{20}	78.2×0.071
Si outside SK tank	ν_μ	ν_μ	3.23×10^{21}	20.8×0.071
Si outside SK tank	$\bar{\nu}_\mu$	$\bar{\nu}_\mu$	1.85×10^{22}	20.8×0.071
Si outside SK tank	ν_e	ν_e	3.85×10^{22}	20.8×0.071
Si outside SK tank	ν_μ	ν_e	7.82×10^{20}	20.8×0.071

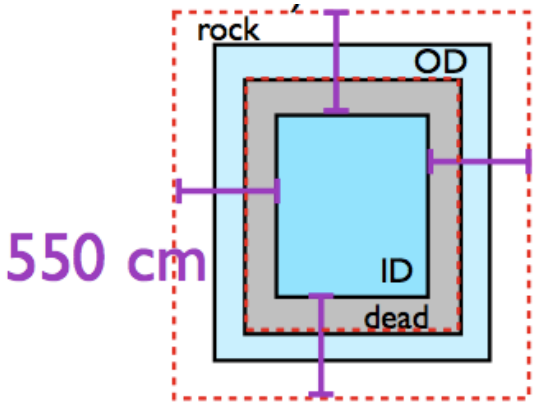

FIGURE C.2: Schematic showing the definition of the "leakage" volume in which additional T2K neutrino interactions were generated witht he purpose of studing possible beam-induced backgrounds from outside the inner detector.

The livetime for the leakage MC samples was calculated using the expected number of interactions per volume per POT for the ν_μ component of the beam at SK, i.e. 1445.4 events per 22.5 ktonne of water per 1×10^{21} POT. The total POT livetime for this MC sample is 5.570×10^{23} POT.

Combining the two MC samples by weighting through POT

In order to combine the OD MC and the leakage MC together, we treat the leakage MC events as an additional set of events for the OD MC component defined by the ν_μ flux, ν_μ cross sections, and a water target. Because this component has more events, its POT normalization must be corrected.

In order to combine the leakage sample with its matching OD MC component in the water portion of the leakage volume (+255 cm from the ID wall), interactions with a vertex in the leakage volume that were made with a ν_μ flux, ν_μ cross sections and water target must be weighted by a combined POT from the OD sample and leakage sample as opposed to their individual livetimes. The combined POT is calculated via

$$\mathrm{POT}_{\mathrm{combined}} = \mathrm{POT}_{\mathrm{Leakage\ MC}} + \mathrm{POT}_{\mathrm{OD\ MC}}, \tag{C.2}$$

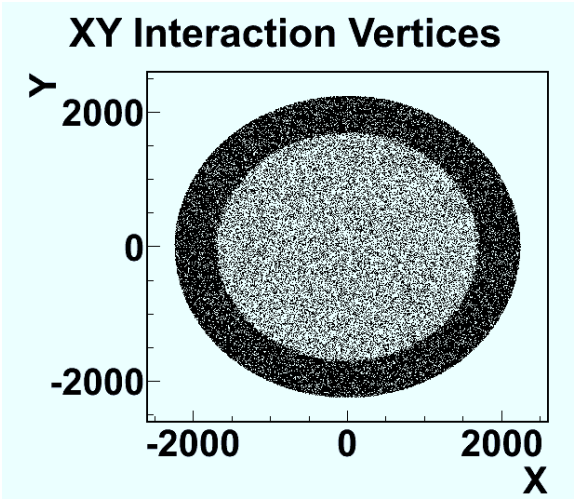

(a) XY Positions

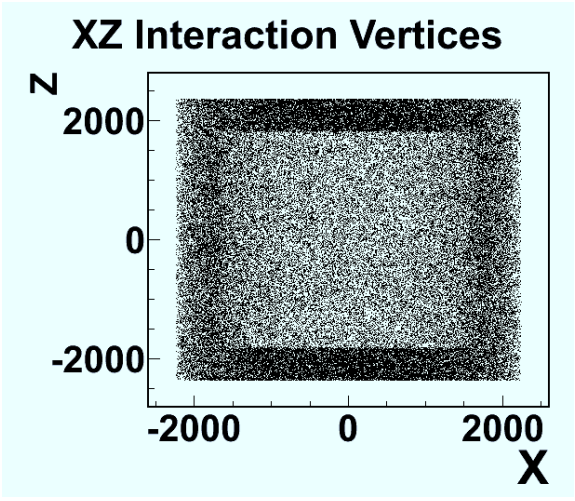

(b) XZ Positions

FIGURE C.3: Interaction positions in the MC leakage sample.

where POT is the livetime of the MC sample in a unit of protons on target. Note that this only applies to events in the leakage volume that are in the detector. This combined POT just reflects the fact that we have added additional events into this OD MC component. As was mentioned earlier, the events in the leakage volume that are also in the rock replace the events in the OD MC in the same volume. The OD MC rock events in the leakage volume are given a weight of zero.

Because the leakage MC sample is only made up of one component that has a water target, its element fraction weight, according to the OD MC rock model should be set at 1%. However, this is not an optimal use of these events, because the leakage MC has almost 10 times more events in the rock around the detector, and we would like these events to have a larger weight in the final result. Therefore, when we combine the leakage MC component with its counterpart in the OD MC for events in the detector, we treat the OD MC and leakage MC as two different models of the rock. The events of the OD MC are treated as coming from rock consisting of oxygen, silicon, and water per usual. However, the leakage MC events come from rock that is modeled as water with a scaled up density. The events from the two models are weighted by the relative number of events found in the rock inside the leakage volume. In effect, we are adding the number of events from the OD MC and the leakage MC via

$$N_{\text{total}} = aN_{\text{OD MC}} + bN_{\text{leakage MC}} \tag{C.3}$$

where

$$\begin{aligned} a &= \frac{\text{events in volume from OD MC}}{\text{Total events in volume}} \\ b &= \frac{\text{events in volume from leakage MC}}{\text{Total events in volume}}. \end{aligned} \tag{C.4}$$

In this way, we are not merely adding more events into one component as we did with the events in the water, but instead, we are combining two models of rock. Again, this is to fully utilize the statistical power in the leakage MC sample.

Results

Using the combined OD and leakage MC sample, the number of estimated number of beam-induced events originate in the dead space, OD, and rock but still enter ν_e appearance data sample was calculated to be 8.1×10^{-3} when normalized to an experimental livetime of 1.43×10^{20} POT. This is much smaller than the total background expected for the ν_e candidate sample: 1.5 events coming from ν_μ and ν_e

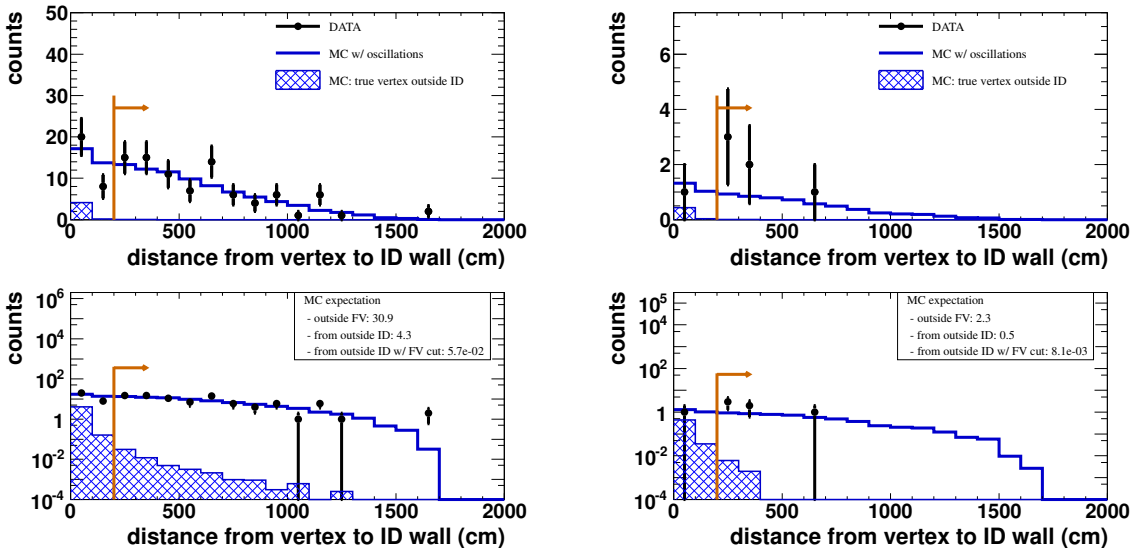

(a) FC sample. (b) ν_e candidate except for the FV cut.

FIGURE C.4: Distribution of *dwall* in the ID shows the distance between a vertex and the nearest wall by the black dots for data events and by blue line for the MC. The hatch-filled blue histogram shows the expected distribution for beam events whose true vertex is outside the inner detector (ID). The FV selection is indicated by the orange arrow at 200 cm. The bottom figures are shown in log scale from the top figures. The expectation was calculated assuming $\sin^2 2\theta_{23} = 1$, $\Delta m^2 = 2.4 \times 10^{-3}$, and $\sin^2 2\theta_{13} = 0.1$. The MC normalization also includes a rescaling of 1.036.

CC and NC interactions.

By means of the MC, Figure C.4 indicates that the reconstructed vertices of these background events rises exponentially while approaching the ID wall. Consequently, if the excess of ν_e candidate events were coming in from the dead space, outer detector or rock, one might expect there to be an excess of events outside the FV. Such an excess is not seen after the ν_e selection cuts in figure (a) nor after the early set of FC cuts in (b).

Table C.3 shows the number of events outside the FV and there is a good agreement between data and MC. The number of events expected outside the FV after the ν_e cuts is 2.2, which is consistent with the 1 event observed in the data.

Table C.3: Comparison between data and MC in the number of events whose reconstructed vertices are outside the fiducial volume.

Sample	recon. vertex outside of FV	
	Observed	MC Expectation
ν_e cand. (no FV cut)	1	2.3
FC	28	30.9

Appendix D

Outer Detector Event Reduction

In this appendix, we describe the data reduction method for the T2K Outer Detector (OD) neutrino events observed at the Super-Kamiokande far detector (Super-K). The defining characteristic of the OD events is that they all involve a neutrino from the T2K beam producing an event at Super-K where Cherenkov light is observed in the OD. The reduction consists of four stages of cuts which are designed to remove background OD events due to cosmic ray muons from the OD events due to neutrino interactions. The OD events are divided into three different classes based the segments of the Super-K detector that observe light and whether the charged particle tracks seem to be entering or exiting the Inner Detector. Because of these different OD event classes, the reduction method varies slightly for each. This appendix first discusses the three OD event types and the algorithm used to classify them. Next, it discusses the Monte Carlo model put together to estimate the efficiency of the OD reduction. Finally, the cuts used to remove the backgrounds are described along with the Monte Carlo results that helped develop them.

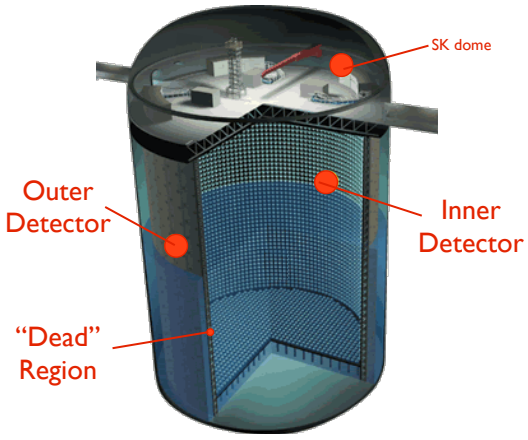

FIGURE D.1: Diagram of the Super-Kamiokande Detector. The diagram points out the locations of the Inner Detector, Outer Detector, and the "dead" region that lies between them.

D.1 Introduction

As described in Chapter 4, the Super-K detector is divided into two active detector segments: the inner detector (ID) and outer detector (OD) (see Figure D.1). Between them is an inactive dead space 55 cm thick known as the "dead space" because of its lack of PMTs.

The OD in Super-K typically acts as a cosmic ray veto for the ID. The veto is important because the data collected at Super-K are used in searches for proton decay, atmospheric neutrino oscillation, and supernova neutrino relics. All these analyses require a high purity data sample and therefore require that as many cosmic ray muon events as possible be removed from the sample.

The time at which events are tagged as cosmic ray muons is when the number hits in the Outer Detector rises above a certain threshold. When the threshold is met, the event is typically excluded from the data samples used for various physics analyses. However, there are exceptions for which events with hits in the OD are kept for analysis. Such exceptions include events termed partially-contained (PC), where

a neutrino interaction occurs inside the ID and one or more particles are deemed to have left the ID and produced light in the OD. PC events are selected by ensuring that the reconstructed interaction vertex was well within the ID. Another set of events not removed includes those tagged as upward-muon events (UPMU), where a high energy muon is seen coming up from the bottom of the tank. Such events are much more likely to be due to a neutrino instead of a cosmic ray muon, which travels downward from the atmosphere.

In the T2K experiment, many of the events with hits in the OD can also be kept for analysis. Neutrino events from the T2K beam are expected to occur within narrow, well-known time windows. By accepting events that occur within these windows, an event sample can be produced that is mostly free from cosmic ray background events. The background rate in the OD within this timing window should be suppressed to the point where a set of simple cuts can select neutrino OD events with sufficient purity. It turns out that the number of additional T2K neutrino events gained by using the OD events is comparable to the number of T2K events with vertices in the ID. In the future, these additional OD events could provide constraints on quantities such as the beam flux at Super-K or even provide additional bins to use in fits to neutrino oscillation parameters. The purpose of this appendix is to describe the the cuts used to select the OD event sample. Because events in the OD sample can be quite different, e.g. there can hits in the OD and/or ID or the presence or not of a reconstructed track in the ID, the OD event sample is divided into three different types. Consequently, this appendix starts with a discussion about the OD event classification. Next, the MC model used to develop and evaluate the OD reduction cuts is described. Finally, the OD cuts are described which take the neutrino event sample from a starting expected non-neutrino induced background contamination of 50% to a final contamination of less than 1%.

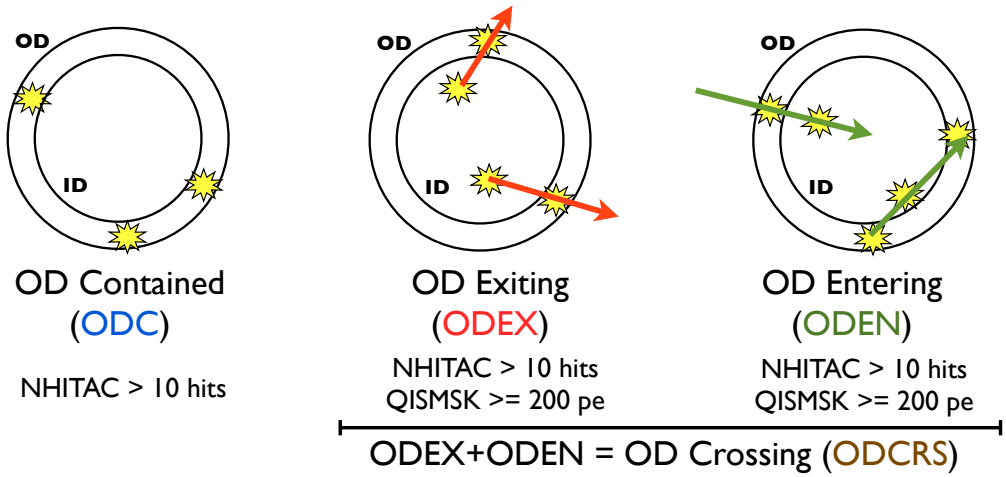

FIGURE D.2: The OD event classes. Events with light in the OD are classified based on the presence of light in the ID and track direction. OD Contained Events (left) only have light in the OD above threshold. OD Exiting Events (center) have light in the ID, and the track with most associated charge is exiting the ID. OD Entering Events (right) also have light in the ID, but the track with the most charge is entering the ID.

D.2 Event Classification

The OD events are divided into three different category types based on the detector segments that observe PMT hits. Events with enough hits to trigger only the OD but not the ID are labeled Outer Detector Contained Events, or ODC (Fig. D.2). Events with a sufficient number of hits in the ID and OD are labeled Outer Detector Crossing Events, or ODCRS. The ODCRS events are further divided into OD Exiting and OD Entering, labeled ODEX and ODEN, respectively. Events where the reconstructed track with the most charge is exiting the ID are labeled ODEX, while events with the track entering the ID are labeled ODEN.

All of the above OD event types are required to have a minimum of 10 hits in the OD cluster with the most charge. Events that pass this threshold but have a total charge in the ID below 200 pe are classified as ODC, which stands for OD Contained events. Events that pass the 10 hit OD threshold but also have a total ID charge above 200 pe are considered OD Crossing Events, or ODCRS. The purpose of this

division is to separate OD events with activity in the ID. These events are passed to the reconstruction software which looks for Cherenkov rings produced by charged particle tracks. Depending on whether the tracks found seem to be from events entering or exiting the tank allows us to divide the ODCRS events into two: ODEX, for OD exiting, and ODEN, for OD entering events. These events are divided into Entering and Exiting events using an algorithm described in the next section.

D.2.1 OD Crossing Classification: Exiting or Entering

ODCRS events are classified into exiting and entering events using a log-likelihood ratio built from two inputs. The first input is a quantity named 'CADOTAP' and is defined as the cosine between the vector starting from the largest OD cluster and ending at the reconstructed interaction vertex in the ID and the direction of the reconstructed track with the most associated charge D.3. The intention is to quantify if the particles are traveling into the tank, which corresponds to a value close to 1, or out of the tank, which corresponds to a value close to -1. The interaction vertex and tracks in the Super-K detector are reconstructed using a routine library called 'APFIT', while OD clusters and their position are calculated by a routine called 'grad_cluster'. The definition of CADOTAP assumes that the brightest track is the most energetic and, consequently, the most likely to be able to cross the ID/OD boundary to produce the observed OD cluster. The CADOTAP distribution from the T2K OD beam MC is shown in Figure D.4 for events whose true vertex is in the ID (left) and the OD or rock around the detector (right).

In addition to the cosine, the second input into the classification likelihood, labeled 'TIMEDIFF', measures the relative timing between the hits in the OD and ID. The timing information provides complementary information to the CADOTAP measure as the latter becomes less accurate when events have low charge or have tracks that take a glancing trajectory through the ID. The time of the OD is taken

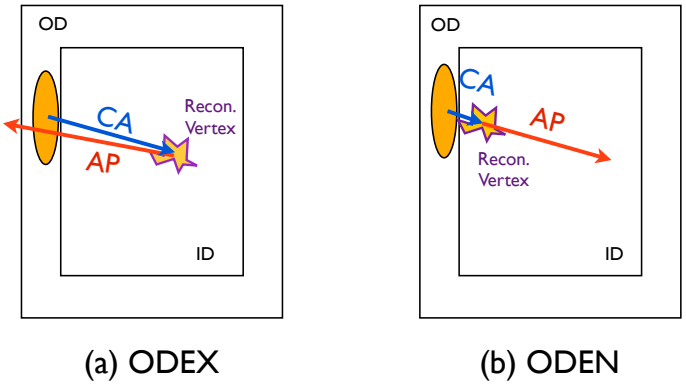

FIGURE D.3: Diagram of the CADOTAP variable. The variable is the cosine between the vector starting from the largest OD cluster and ending at the reconstructed interaction vertex in the ID, labeled CA in the figure, and the direction of the reconstructed track with the most associated charge, labeled AP. ODEX events (a) mostly have a CADOTAP value between [-1,0); ODEN events (b) mostly have values between (0, 1].

from the earliest PMT hit in the largest OD cluster. The ID time is calculated differently, depending on the amount of charge in the ID. For events with a large amount of charge (greater than 2000 p.e.), the time average of the earliest hits is used. The fraction of hits used to calculate the time varies with the total charge in the ID. A larger fraction is used when a smaller total charge is seen. This is done to average out the influence of noise in the ID. However, for events with a sufficiently low amount of ID charge (less than or equal to 2000 p.e.), the effects of background PMT activity are suppressed by taking the time average of hits that lie within 300 cm of the OD cluster. Figure D.5 shows the TIMEDIFF distributions for events with true vertices in the ID (left) and in the OD and rock (right).

Together, the two inputs, CADOTAP and TIMEDIFF, are combined with equal weights into a log-likelihood ratio, called 'ODXLLR'. The MC ODXLLR distribution for events with vertices in the ID (left) and OD/rock (right) are shown in Figure D.6.

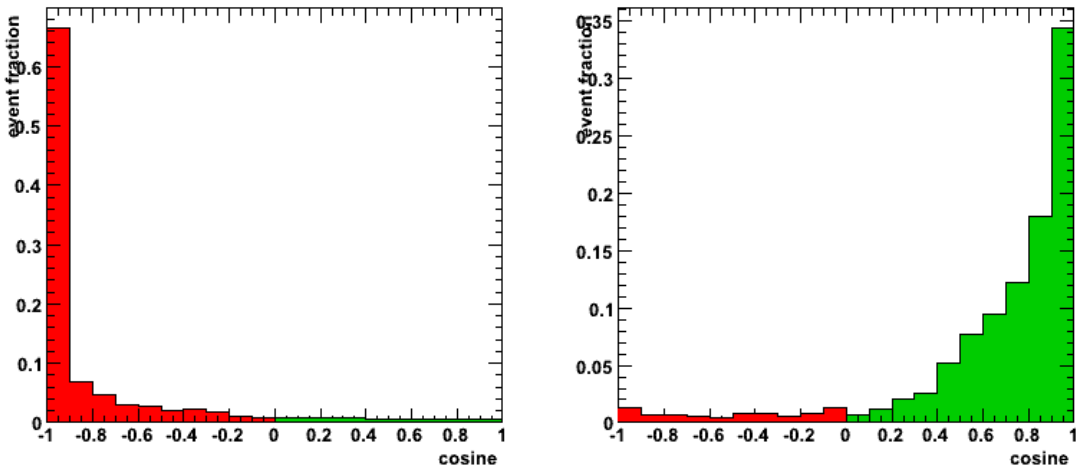

FIGURE D.4: CADOTAP Event Classification Input Variable. These plots are made from the T2K beam MC (no oscillations). CADOTAP is constructed from the dot product between the direction of the brightest particle track and the vector from the largest OD cluster to the interaction vertex. The plot on the left shows a histogram for MC events with true vertices in the ID; the right for true vertices in the OD and rock. The red portion would be classified as ODEX using only this variable, while the green portion would be classified as ODEN.

Events with a positive likelihood ratio are considered ODEX while event with a negative ratio are considered ODEN. The event classification accuracy using ODXLLR is about 96% and is an improvement from classifying events with either CADOTAP and TIMEDIFF alone. The classification accuracy of the different variables for ODEX and ODEN events are shown in Figure D.7. It should be noted that events originating in the dead space are a classification ambiguity. Most dead space tracks that pass the OD event thresholds will feature a particle first entering the ID and then exiting out to the OD. However, there are some events that have one track entering the OD and another entering the ID which, together, lead to the event being classified as Entering. Consequently, events with true interaction vertices in the dead space are not used in calculating the accuracy above.

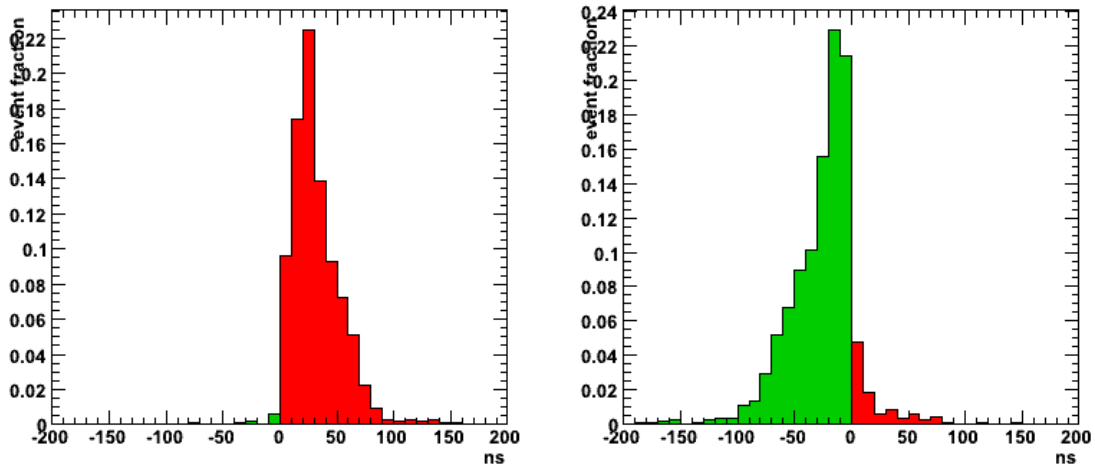

FIGURE D.5: TIMEDIFF Event Classification Input Variable. These plots are made from the T2K beam MC (no oscillations). TIMEDIFF is the relative OD-ID timing. The calculation of this quantity is adjusted slightly depending on the amount of light in the ID in order to better handle the dark noise hits in the ID. The plot on the left shows a histogram for MC events with true vertices in the ID; the right is for true vertices in the OD and rock. The red portion would be classified as ODEX using only this variable, while the green portion would be classified as ODEN.

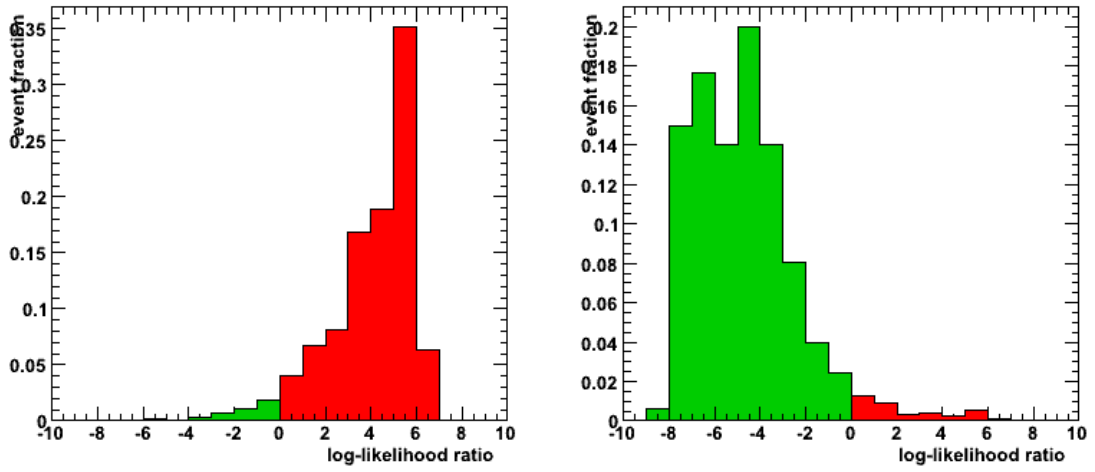

FIGURE D.6: ODXLLR Event Classification Variable. These plots are made from the T2K beam MC (no oscillations). ODXLLR is the log-likelihood ratio made from the TIMEDIFF and CADOTAP distributions. The plot on the left shows a histogram for MC events with true vertices in the ID; the right for true vertices in the OD and rock. The red portion is classified as ODEX using this variable, while the green portion is classified as ODEN.

Variable	ODEX (w/ osc)	ODEN (w/ osc)	Total (w/ osc)
CADOTAP	92.0562 (92.5866)	93.3875 (93.9301)	92.8047 (93.3451)
TIMEDIFF	89.4704 (89.6546)	98.399 (98.6156)	94.0634 (94.2976)
ODXLLR	96.2199 (96.4456)	95.7641 (96.1615)	95.9618 (96.2842)

FIGURE D.7: Classification accuracy percentage using the different crossing variables. The classification accuracy is improved by combining the CADOTAP and TIMEDIFF variables into a log-likelihood ratio, ODXLLR.

D.3 The OD Monte Carlo Model

The T2K Outer Detector (OD) Event Monte Carlo model is an extension of the standard T2K Monte Carlo used to simulate events for the Fully Contained (FC) events. The standard MC employs NEUT to generate neutrino interactions and SKDETSIM, an implementation of GEANT3, to track particles and simulate the detector response. However, neither NEUT nor SKDETSIM in the standard MC is set up to handle events outside the Super-K tank. In order to generate the OD MC events (1) NEUT is modified to produce vertices in the rock outside of the detector on targets other than water and (2) SKDETSIM has its 'UPMU' mode activated in which a 80 km x 80 km x 80 km rock region outside of the detector is defined through which particles may travel. In addition to activating these existing features, a new modification is made to SKDETSIM so that the program stores the time between the start of the event and the time at which the software trigger is activated. This timing information is important in helping to establish one of the OD reduction timing cuts that will be explained later in this note. Ultimately, the OD MC model provides a sample for T2K interactions within a 60 m x 60 m x 60 m box of rock around the Super-K origin and is a superset of the standard, FC MC.

D.3.1 Rock Model

The model of the rock that surrounds the Super-K detector is based on an elemental composition table of Mount Ikenoyama taken from (Tang et al. (2006)). The rock model uses the elements that make up 96% of the rock and inputs them, one at the time, into NEUT as targets to generate neutrino interactions. Table D.1 lists the different elements used along with their elemental fraction in the rock. All the MC events generated are combined at the end by weighting each component with its elemental composition percentage. However, it should be noted that in order to save computation time, not all of the elements were used, and any remaining elemental percentage was assigned to oxygen, the most abundant element.

In NEUT, each choice of target specifies four parameters: the Fermi surface, the maximum Fermi momentum, the nuclear potential, and the ratio of neutrons to protons. Table D.2 lists some of these parameters for the elements used. While the effect these parameters have on the neutrino cross-section requires further study, it might be of interest to note that the following relationships exist:

1. CCQE cross-section per nucleon varies directly with a dominant parameter, the neutron fraction in the nucleus, and inversely with a subdominant parameter, the momentum of the Fermi surface.

2. Coherent pion production varies inversely with A of the target.

3. Charged-current single and multiple pion cross sections vary with the neutron fraction.

In Figures D.8 to D.12 the ν_μ cross-sections for the different targets are compared relative to water for five of the interaction modes modeled in NEUT.

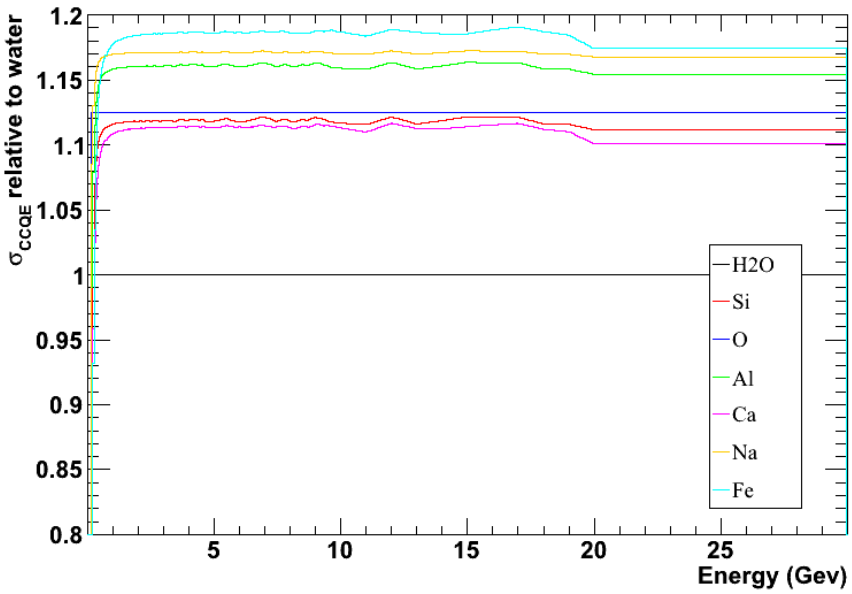

FIGURE D.8: ν_μ The CCQE cross-section per nucleon on the various targets in the rock model.

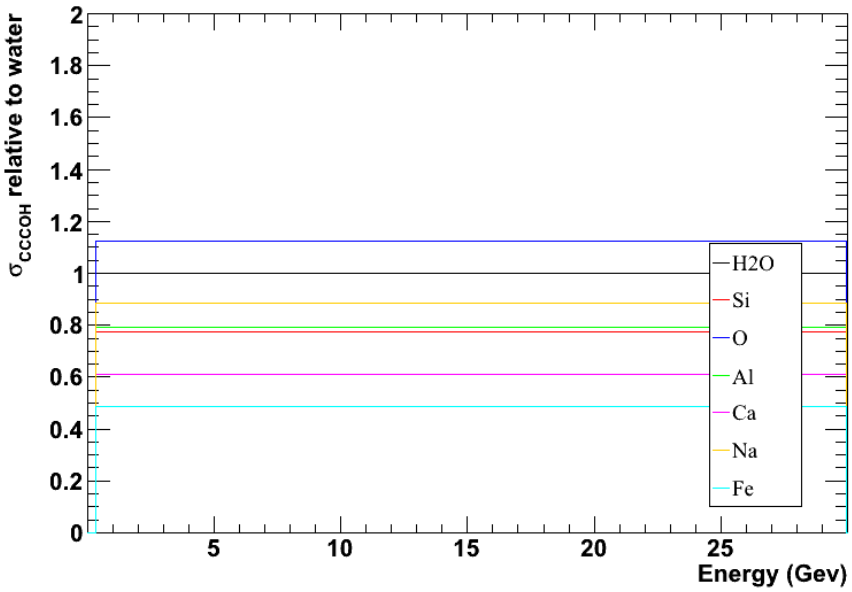

FIGURE D.9: ν_μ CC coherent pion production cross section per nucleon on the various targets in the rock model.

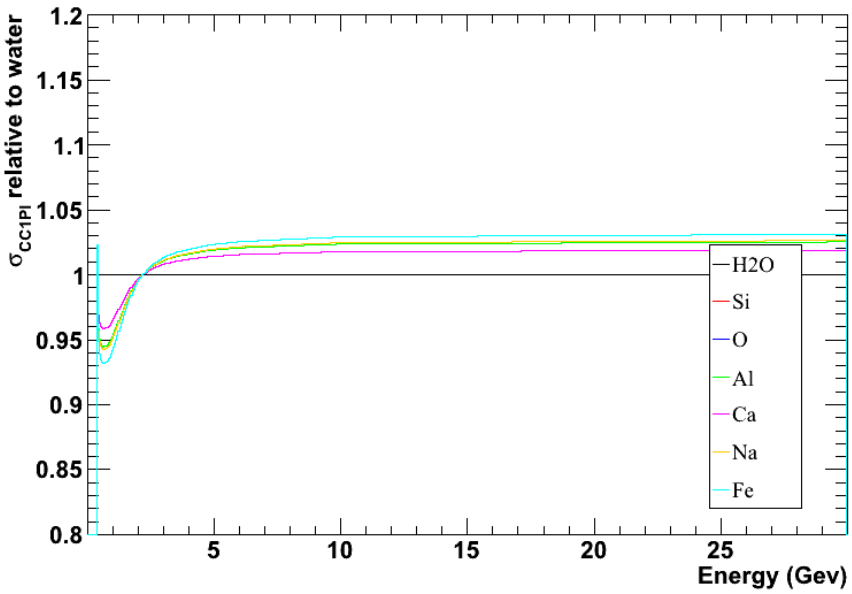

FIGURE D.10: ν_μ CC single pion cross section per nucleon on the various targets in the rock model.

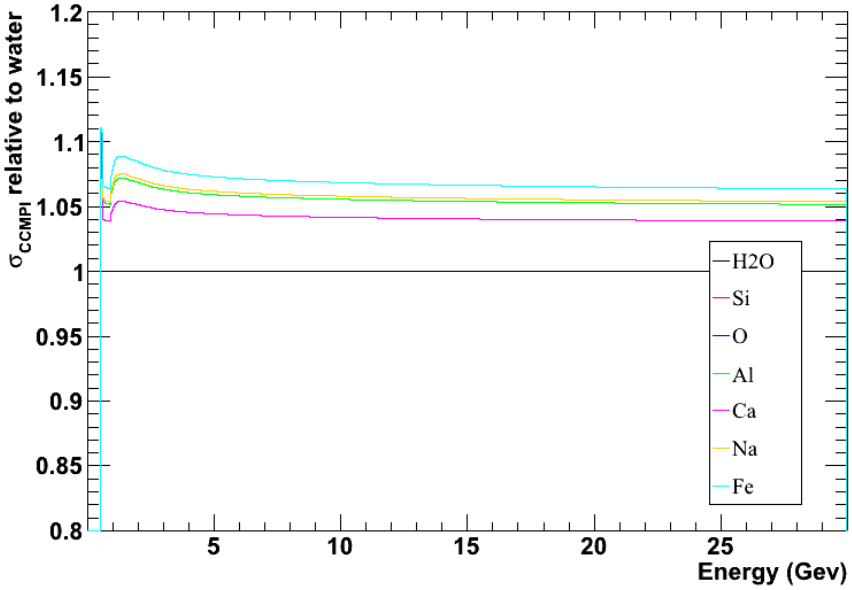

FIGURE D.11: ν_μ CC multiple pion cross-section per nucleon on the various targets in the rock model.

Element	elemental percentage
Oxygen-16	60.0% (63.5%)
Silicon-28	20.2%
Aluminium-27	7.0%
Sodium-23	4.3%
Calcium-40	3.0%
Iron-56	1.0%
H_2O	1.0%
Total	96.5% (remaining 3.5% added to O)

Table D.1: Percentage composition for each element in the OD rock model

Element	Fermi Surface (MeV)	Nuclear Potential (MeV)	Neutron Fraction
H_2O	225	-27	8/18=0.44
Oxygen-16	225	-27	8/16=0.50
Sodium-23	229	-27	12/23=0.522
Aluminium-27	233	-28	14/27=0.518
Silicon-28	234	-28	14/28=0.50
Calcium-40	241	-31	20/40=0.50
Iron-56	250	-33	30/56=0.54

Table D.2: NEUT parameters for the targets used in the OD rock model.

D.3.2 Normalization

The total set of T2K OD MC events is broken down into components with each component having a specified target, neutrino flux flavor, and neutrino cross-section flavor. (For example, one component will consist of interactions produced with the ν_μ beam flux interacting on Fe using ν_e cross-sections.) Each component is generated separately and has assigned to it a livetime given in protons on target (POT) and an elemental fraction (Table C.1). When the OD MC is combined to produce plots or for analysis, an event in each component must be weighted by its POT and rock fraction through

$$\text{weight} \quad = \quad (\text{ oscillation prob. }) \times \frac{\text{elemental rock fraction}}{\text{Component POT}} \tag{D.1}$$

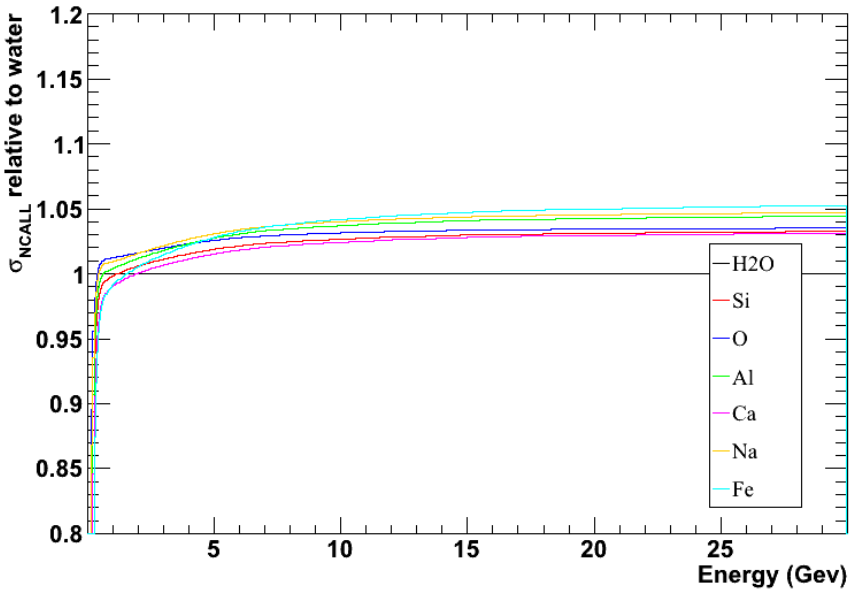

FIGURE D.12: ν_μ NC cross-sections per nucleon on the various targets in the rock model.

The MC POT in Equation (D.1) is calculated based on the total number of interactions in the Super-K fiducial volume. First, the expected number of interactions per 10^{38} protons on target (POT) is computed for a mass with the dimensions of the Super-K fiducial region and density of the rock, defined to be 2.7 g/cm^3. This expected number gives an expected rate per POT per volume. Then, for a generated MC sample component, the total number of events generated and the volume in which the events were created are calculated. Finally, the volume and number of events in each component is combined with the expected rate of events to give POT livetime of the component. Table C.1 list the different POT factors for each component in the MC.

D.3.3 SKDETSIM extensions

Two modifications to SKDETSIM were made in order that (1) particles created outside the detector volume in the rock are simulated and (2) the true time elapsed

between the time of the interaction and the time assigned by the software event trigger is recorded. Compiling SKDETSIM with the UPMU flag turns on the routines needed to simulate particles outside the rock. Extracting the true event timing required modifications to the routine `dsswtrg` (found in dsswtrg.F). Modifications to the code store into a ZBS bank the software trigger type – which includes the Low-Energy (LE), High-Energy (HE), and Outer Detector (OD) trigger – and the truth initial time of the interaction relative to the software trigger. The modifications can be activated by the turning on the flag `DSSWTRIGSTOREINFO` when compiling SKDETSIM. This timing information is used to estimate the width of the distribution between the T2K beam trigger and the Super-K event trigger called the 'bunch time'. A description of this estimate follows in the next section (Section D.3.4).

D.3.4 Bunch time Model

Within every burst, or 'spill', of neutrinos that come from the T2K beam there are a number of sub-bursts, or 'bunches'. When the beam is on, each spill occurs every 1/3 of a second, while each bunch is spaced 581 ns from the next. The number of bunches in each spill at the time this note was written is either 6, for beam runs 29 to 34, or 8, for beam runs 36 and after. This bunch structure of the beam is very important for the OD events, as much of the background in the OD sample can be removed if events are only accepted within a small time window around the beam bunches. But before a time window can be defined, the expected width of the event times around the bunch centers must be estimated. This width is expected to come from jitter in both the GPS clocks used to set the beam and detector trigger times and from the timing corrections added to the event trigger. A bunch time model has been developed to estimate how large this bunch timing distribution will be due to such timing uncertainties. Guided by such a model, timing window cuts can be set around the beam spill bunches in such a way that reduction efficiencies

and uncertainties can be calculated.

Ultimately, the MC bunch time model estimates the uncertainties due to jitter in the software trigger that sets the Super-K event time, and jitter in the corrections to the event time due to errors in the reconstructed event vertices. Jitter due to the GPS equipment or the detector components are added in at the end as an overall smearing factor apart from the MC model itself. In order to best see how errors and fluctuations might enter into the Super-K event time, this section will cover the way the elapsed time between the the T2K beam trigger and the Super-K event trigger is calculated. Letting this elapsed time be called, ΔT, it is calculated by

$$\Delta T = T_{SK} - T_{T2K} \tag{D.2}$$

where T_{T2K} is the GPS time when the T2K trigger engages the Super-K DAQ, and T_{SK} is time the neutrino reaches the center of the Super-K tank. This latter quantity is not directly measured but instead is calculated using the Super-K event trigger timing and a number of timing corrections. The calculation of T_{SK} is as follows:

$$\begin{aligned} T_{SK} \quad = \quad & t_{SK}^{SWTRG} - \Delta t_{DET} \\ & -\Delta t_{ODTRG}^{SW} - \Delta t_{ODTRG}^{TW} - \Delta t_{OD-ID} \\ & -\Delta t_{TOF}^{\nu} - \Delta t_{TOF}^{\gamma} \end{aligned} \tag{D.3}$$

The definitions for all of the event time terms are

$$
\begin{aligned}
t_{SK}^{SWTRG} &= \text{SK Event Trigger GPS time} \\
&\quad \text{(this is the time of an SK event trigger)} \\
\Delta t_{DET} &= \text{972 ns delay due to SK ID electronics} \\
\Delta t_{ODTRG}^{SW} &= \text{52.08 ns OD trigger delay} \\
&\quad \text{(if OD triggered event, i.e. ODC)} \\
\Delta t_{ODTRG}^{TW} &= \text{OD trigger time-walk correction} \\
&\quad \text{(if OD triggered event, i.e. ODC)} \\
\Delta t_{OD-ID} &= \text{-41 ns OD-ID electronics difference} \\
&\quad \text{(if OD triggered event, i.e. ODC)} \\
\Delta t_{TOF}^{\nu} &= \nu \text{ time of flight from the} \\
&\quad \text{interaction to plane crossing center of SK} \\
\Delta t_{TOF}^{\gamma} &= \text{photon time of flight} \\
&\quad \text{from interaction vertex to nearest point on the wall}
\end{aligned}
\tag{D.4}
$$

Figure D.13 provides a diagram depicting some of the event timing terms in equation (D.4). In effect, the aim of the corrections made to the event time is to calculate the time the neutrino would have passed through the center plane of the detector had it not interacted. The goal of these corrections is to remove from the event times dependence on the interaction position inside the detector. Note that for the FC, ODEN and ODEX the event trigger comes from summing hits in the Inner Detector. ODEX and ODEN events have light in the ID and will trigger the LE and/or HE ID trigger. The only event type that triggers using the number of hits in the OD is the OD Contained (ODC) events. From the resulting distribution of corrected ΔT (plot (a) in Figure D.28), the beam bunches can be seen over the background.

As can be seen from Equation (D.4) and Figure D.13, errors in the reconstruction of the event vertex reconstruction or OD cluster will cause errors in some of the correction terms above. Also, there is jitter in the time t_{SK}^{SWTRG} established by the software trigger. Typically, the size of the vertex reconstruction error is around 50 cm which is around 1.5 ns. Therefore, it turns out that most of the uncertainty in T_{SK} comes from jitter in the software trigger and drift in the GPS time stamp.

The bunch time MC model tries to capture all of these uncertainties by using the

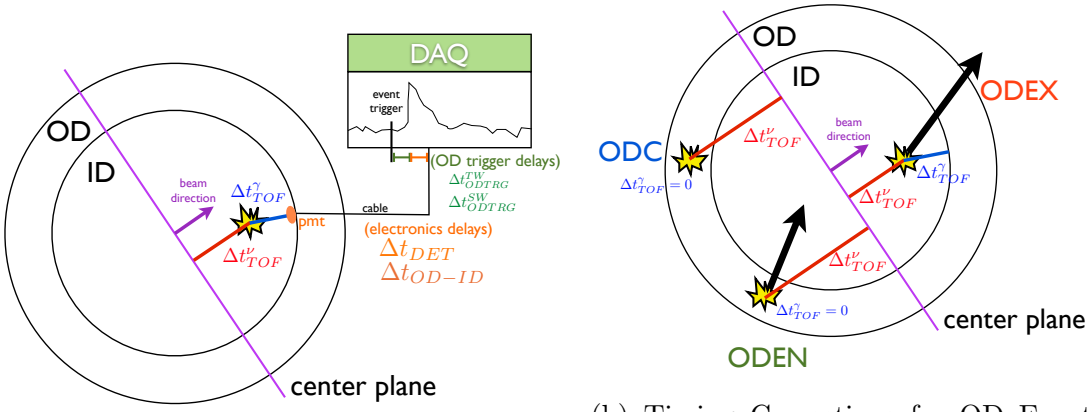

(a) General Timing Corrections

(b) Timing Corrections for OD Event Types

FIGURE D.13: Diagrams depicting different timing corrections. The plot on the left depicts the constants for a general event. The plot on the right shows the timing corrections that change for the different OD event types. Note that the only OD event type with OD trigger corrections is OD Contained (ODC).

truth timing information in SKDETSIM. The expected bunch time distribution is produced by recording for each event the differences in the timing corrections using the reconstructed and true times and positions. For the reconstructed information, a T^{Recon}_{SK} is calculating using most of the corrections in Equation (D.4) except that

$$\begin{aligned} t^{MCSWTRG}_{SK} &= \text{SK software trigger time} \\ &\quad \text{(SKDETSIM sets this to 1000 ns)} \\ t^{GPS}_{SK} &= 0 \text{ (meaningless in MC context)} \\ \Delta t_{DET} &= 0 \text{ (assuming no detector delays)} \\ \Delta t^{TW}_{ODTRG} &= 0 \text{ (comes from the MC and will be discussed later)} \\ \Delta t_{OD-ID} &= 0 \text{ (assuming no detector delays)} \end{aligned} \tag{D.5}$$

Likewise the truth information is used to calculate a T^{Truth}_{SK} by defining the time constants as

$$\begin{aligned} t^{GEANT}_{SK} &= \text{Truth interaction time (relative to SK trigger)} \\ t^{GPS}_{SK} &= 0 \text{ (meaningless in MC context)} \\ \Delta t_{DET} &= 0 \text{ (assuming no detector delays)} \\ \Delta t^{TW}_{ODTRG} &= 0 \text{ (comes from the MC and will be discussed later)} \\ \Delta t_{OD-ID} &= 0 \text{ (assuming no detector delays)} \end{aligned} \tag{D.6}$$

And just to be explicit, Δt^{ν}_{TOF} and Δt^{γ}_{TOF} are calculated using both the reconstructed and truth vertices for T^{Recon}_{SK} and T^{Truth}_{SK}, respectively. Also, note that the ODC event times contain a time-walk correction to the timing of the OD trigger that will be discussed in the following section.

After calculating T^{Recon}_{SK} and T^{Truth}_{SK}, the error in the timing due between the reconstructed MC time and the true MC time is

$$\begin{aligned} \sigma_{T_{SK}} &= T^{Recon}_{SK} - T^{Truth}_{SK} \\ &= \sigma_{\Delta t_{SWTRG}} + \sigma_{\Delta t^{\nu}_{TOF}} + \sigma_{\Delta t^{\gamma}_{TOF}} \end{aligned} \tag{D.7}$$

It is the distribution of $\sigma_{T_{SK}}$ that is used, in part, to estimate the width of the event times around the bunch centers due to jitter form the software trigger and event reconstruction. The final expected bunch time distribution is calculated after the uncertainty in the GPS times of 15 ns is smeared into the $\sigma_{T_{SK}}$. This GPS timing spread is taken from the measured difference of two GPS clocks used to record the SK and T2K triggers.

Figure D.17 shows the bunch time distributions for each event type before (plot (a)) and after the smearing (plots (b) or (c)) in the GPS timing spread. Note that the ODC distributions of the data and MC have their respective means subtracted so that both distributions center around zero. The calculated means for data and MC also are subtracted from the other OD event types. This is justified as the model above cannot predict any absolute offset between the T2K and SK GPS times. However, the model can predict any offset between different OD event types and the FC events. This offset between OD events is seen in both the MC and data (Figure D.27). For the data recorded so far, the MC and data distributions agree well. The MC distribution is then used as a guide in setting the timing window used to accept events and reject backgrounds. For any sized window, the MC distribution also is used to estimate the efficiency of the timing cut. Please refer to Section D.4.5 for a discussion of this tight timing cut.

D.3.5 ODC Time-walk correction

As mentioned above, a correction is made to the event times only for ODC events. This correction accounts for a time-walk seen in the OD trigger. Figure D.14 plots the number of hits in the largest OD cluster, NHITAC, versus the difference between the truth and reconstructed event time, i.e. $\sigma_{T_{SK}}$. A very clear relationship is seen in these two variables. An explanation for this is that for events that engage the OD software trigger with an amount of OD hits near threshold, the rise time will be longer as a larger fraction of the total hits must be summed up. In addition, the variation in the rise time will be larger since a larger portion of the hits must be counted to trigger the event thereby making the rise time more sensitive to the variations in the time between hits. Figure D.15 tries to illustrate these points. However, because there is a rather good relationship between NHITAC and the amount of time before the event is triggered, a correction is made for ODC events. This correction is parameterized by a Tanh + linear fit and is shown in Figure D.16. Figure D.17 shows the effect of the correction in data and MC. In MC, the RMS of the ODC bunch time distribution is reduced with the use of the correction. This is also seen in the data.

D.4 OD Reduction Cuts

D.4.1 OD Cuts Overview

The OD reduction routine is composed of four sets of cuts applied in succession. They are, in the order in which they are applied,

1. the BASE cut: this is a loose timing cut that selects events that occur within a -2 to +10 microsecond window of the T2K beam trigger time

2. the OD1 cuts: these are conservative cuts on the amount of hits and charge in the OD and ID. The cuts remove very energetic events which are most likely to be cosmic ray muons traversing a large segment of the detector

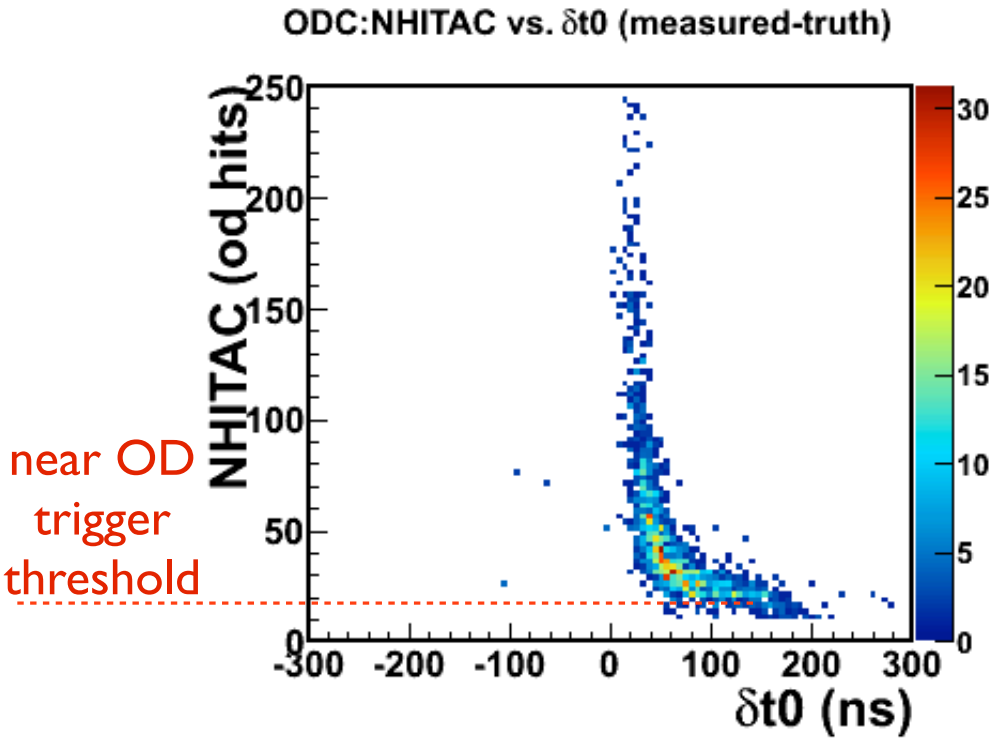

FIGURE D.14: Relationship between NHITAC and the size of the bunch time error. A clear, correctable relationship is seen for ODC events.

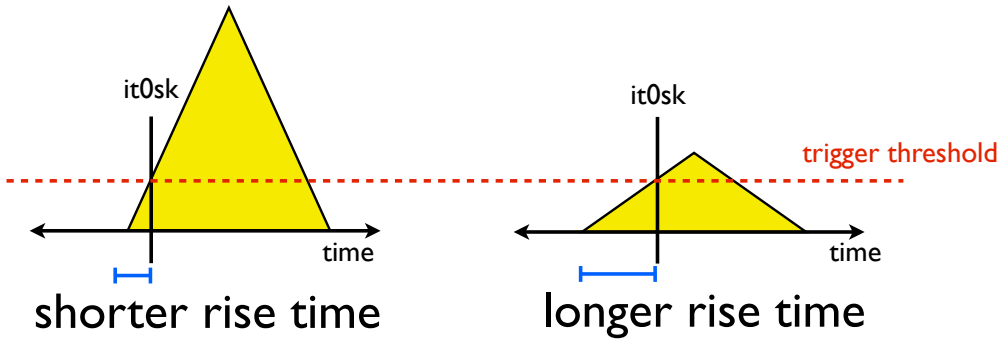

FIGURE D.15: Schematic explaining the OD time-walk seen. For events with OD hits well above threshold, the rise time is relatively quick. But for events with a low amount (right) of OD hits near the trigger threshold, a larger fraction of the hits must be counted to trigger the event and therefore the rise time delay becomes longer and more sensitive to variations in the times between hits. 'it0sk' is the name of the variable allocated for the event trigger time set by the software trigger.

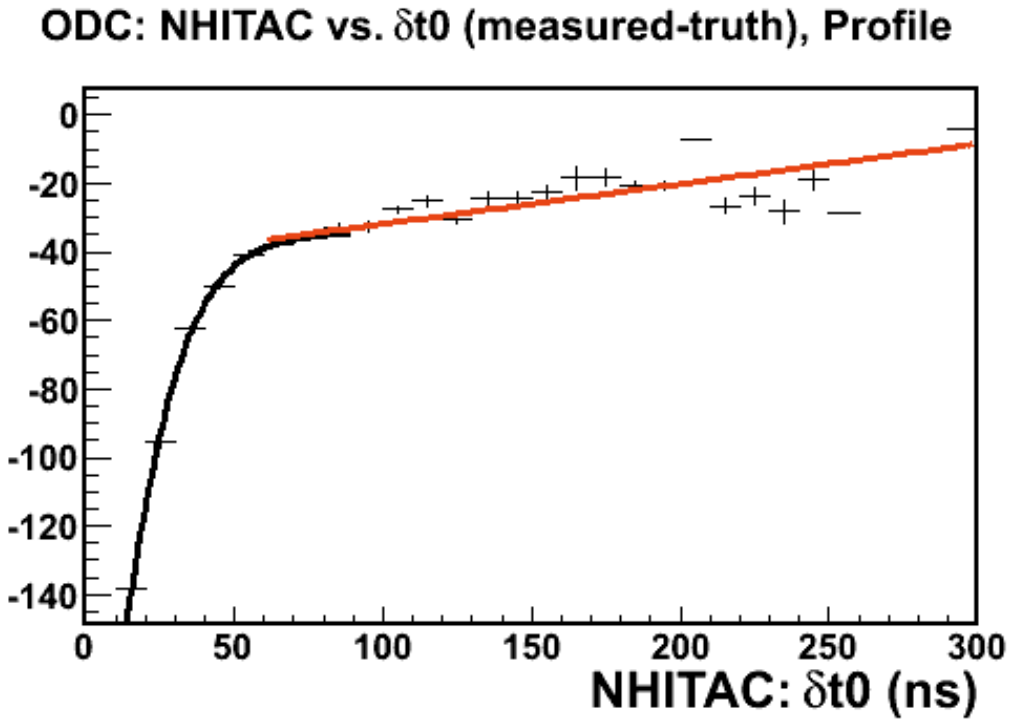

FIGURE D.16: The OD time-walk correction is parameterized using a Tanh+linear fit. The correction is applied to the trigger time for ODC events only. These events are triggered by the OD.

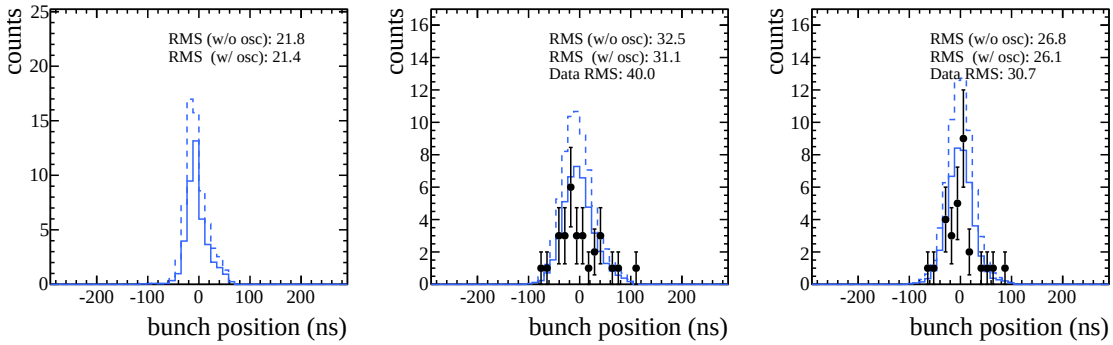

FIGURE D.17: Bunch time distribution for ODC events with or without various corrections. For all plots, the dashed line histogram is MC without oscillations, the solid line histogram is MC with oscillations, and the histogram with error bars is the data from runs 34 to 36. Also, all histograms are centered at zero. In the left plot, the MC bunch time distribution is shown without any smearing nor any time-walk correction. The center plot shows the MC distribution without the time-walk correction by after smearing by a Gaussian with a standard deviation of 15 ns. The data shown in the center plot also do not have the time-walk correction. The right plot shows the MC distribution with both smearing and the time-walk correction. The data in the right plot includes the time-walk correction.

3. OD2 cut: this cut uses the fairly strong relationship between the charge seen in the detector and the angle at which the most energetic particle is produced relative to the T2K beam direction. Cosmic ray muons, on the other hand, are seen to have an isotropic distribution in this 2D parameter space.

4. ODT cut: this cut is a much tighter timing cut around the beam spill bunch structure. The number of bunches in each spill is either 6 or 8 depending on the beam run period with each spill roughly 200 ns wide and spaced roughly 581 ns apart. The values for each of the cuts have been set after studying Monte Carlo distributions of each of the cut variable. (For more on the MC expectation please refer to Section D.3.4.)

D.4.2 BASE Cut: loose timing cut

All candidate T2K events must pass a number of quality cuts implemented in the early stages of the data reduction. For those that pass the quality cuts, events that are to be accepted into the BASE OD sample must have a value of NHITAC greater than 10 and have a time difference between the Super-K event trigger and the T2K beam trigger that falls within a -2 and +10 microsecond window. The uncorrected GPS event times are used for this cut. (This is opposed to the corrected event times described in Section D.3.4.)

D.4.3 OD1 Cut

For events in the BASE OD sample, the next step in the reduction applies a set of conservative cuts meant to remove very high energy cosmic ray events while retaining 99% signal efficiency. These sets of cuts, called the OD1 cuts, utilize the following quantities:

1. NHITAC: the number of hits in the largest OD cluster. Events must have a value less than or equal to 350 OD hits.

2. ODRMEAN: the average distance between all possible pair of hits in a 500 ns window. The window is a sliding window set by the function 'hitwin'. The value of ODRMEAN must be less than or equal to 2600 cm for ODC events and less than or equal to 2500 cm for ODEX and ODEN events.

3. ODWINHITS: the total number of OD hits in a 500 ns window. All OD events are required to have a value less than or equal to 400 hits.

4. QISMSK: the total charge in the ID within a time window. All OD events must have less than or equal to 80,000 pe in the ID.

All of these cuts remove events which might have very long path lengths through the ID and OD. Often, cosmic ray events pass through the OD twice from both exiting and entering the ID. Consequently, events that are almost certainly cosmic ray muons are expected to produce a lot of hits and charge that is spread out over a large region in the OD. The MC expectation with and without oscillations are given in Figures D.18 to Figure D.21. The plots also include the data seen after the BASE cuts for the T2K Run 1-4 data set with 6.57×10^{20} POT.

D.4.4 OD2 Cut

The OD2 cut is a kinematic cut that uses a relationship between the direction of the most energetic track and the charge deposited in the detector. Because it requires the direction of a track, the cut only applies to ODEX and ODEN events. From two body kinematics, one expects the energy of the interaction to be inversely proportional to $\cos(\theta_{beam})$. Figure D.22 plots for T2K beam MC the $\cos(\theta_{beam})$ of the most energetic track and QISMSK, which is used as a proxy for the energy of the event. Also, because cosmic rays are expected to be mostly downward going, the $\cos(\theta_{beam})$ and QISMSK space is extended by multiply QISMSK by the sign of the z-component of the most energetic track. This is done to provide more separation between the beam

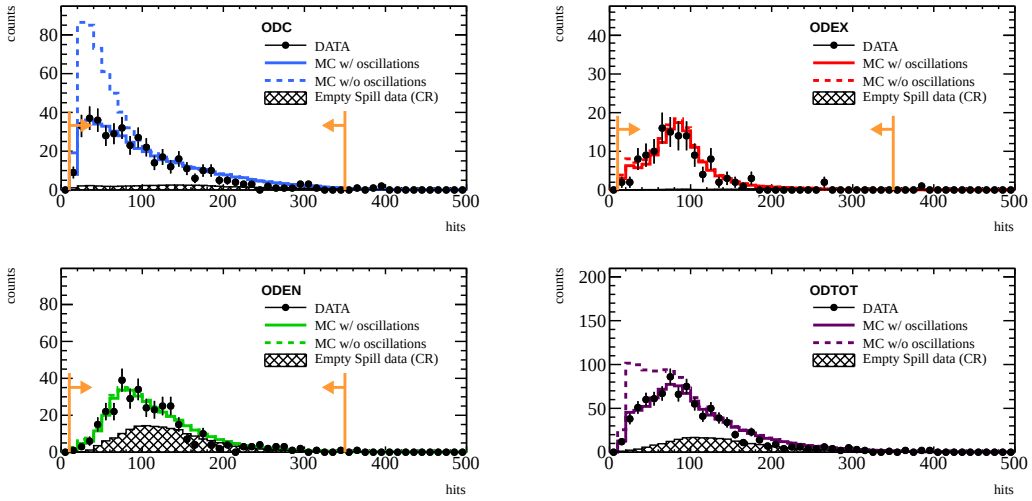

FIGURE D.18: NHITAC distribution for the different OD event types. NHITAC is the number of hits in the largest OD cluster. The dashed line is the MC distribution without oscillations. The solid line is the MC distribution with oscillations. The black points with error bars are the T2K beam events which pass the BASE cut. The dotted histogram is the expected background distribution. The MC is normalized by POT while the background is normalized by the number of spills searched. The orange line and arrow indicate the region that passes the OD1 cut.

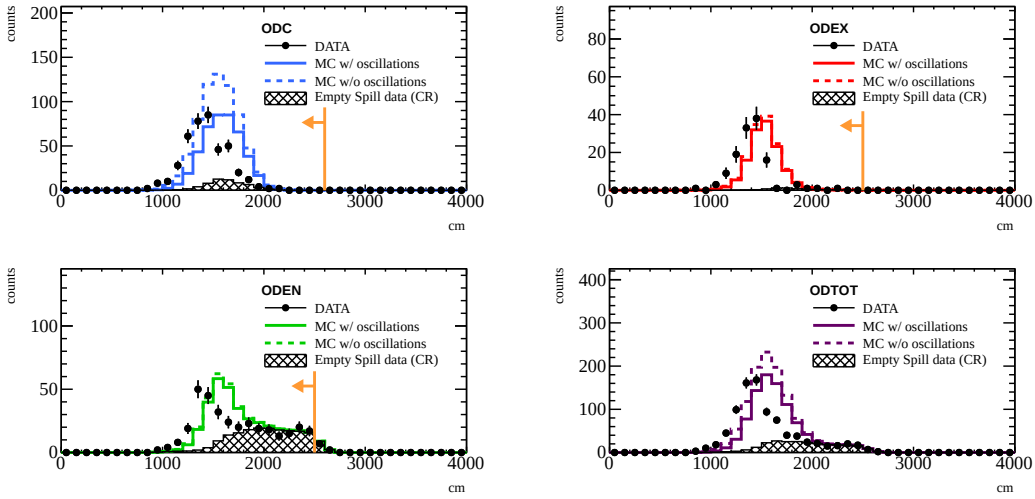

FIGURE D.19: ODRMEAN distribution for the different OD event types. ODRMEAN is the average distance between pairs of OD hits. The dashed line is the MC distribution without oscillations. The solid line is the MC distribution with oscillations. The black points with error bars are the T2K beam events which pass the BASE cut. The dotted histogram is the expected background distribution. The MC is normalized by POT while the background is normalized by the number of spills searched. The orange line and arrow indicate the region that passes the OD1 cut.

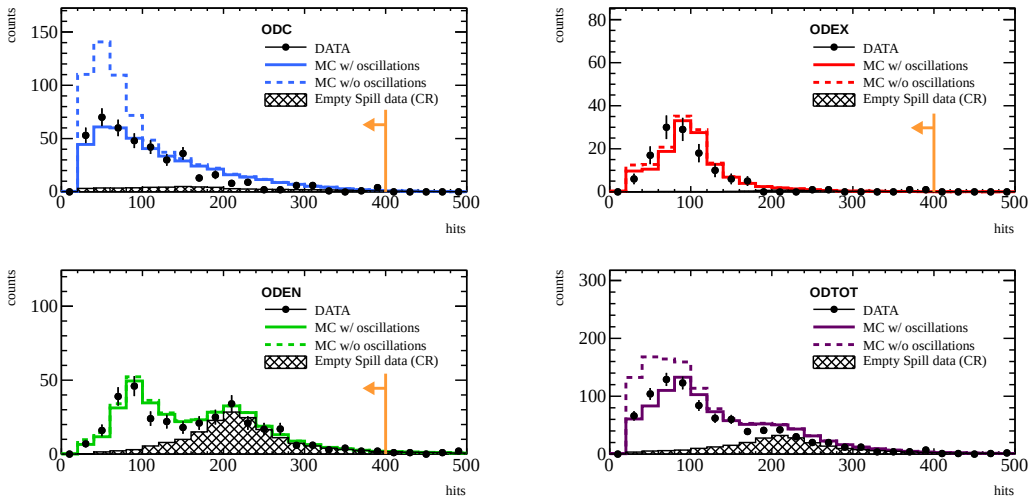

FIGURE D.20: ODWINHITS distribution for the different OD event types. ODWINHITS is the number of OD hits in a 500 ns window. The dashed line is the MC distribution without oscillations. The solid line is the MC distribution with oscillations. The black points with error bars are the T2K beam events which pass the BASE cut. The dotted histogram is the expected background distribution. The MC is normalized by POT while the background is normalized by the number of spills searched. The orange line and arrow indicate the region that passes the OD1 cut.

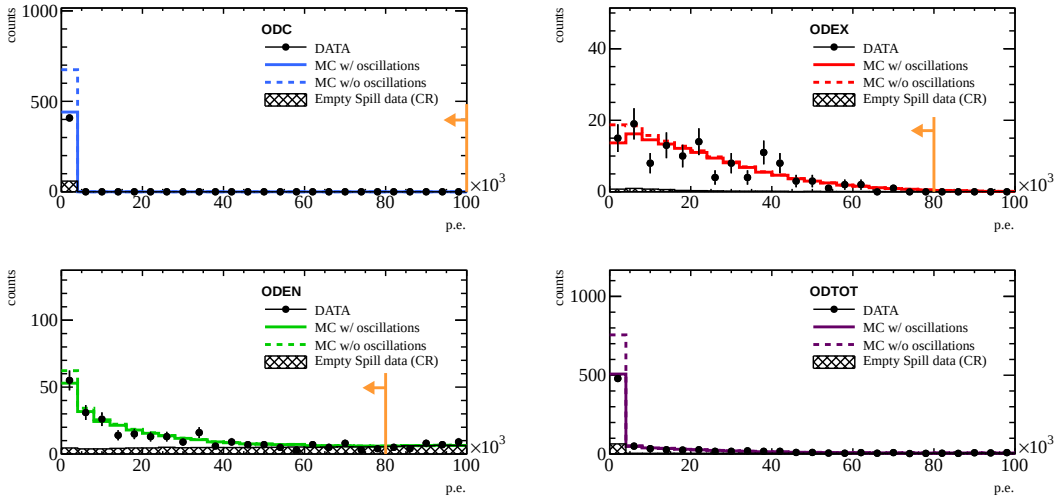

FIGURE D.21: QISMSK distribution for the different OD event types. QISMSK is the charge in the ID. The dashed line is the MC distribution without oscillations. The solid line is the MC distribution with oscillations. The black points with error bars are the T2K beam events which pass the BASE cut. The dotted histogram is the expected background distribution. The MC is normalized by POT while the background is normalized by the number of spills searched. The orange line and arrow indicate the region that passes the OD1 cut.

and background events. It turns out the the correlation is maintained for the most part despite the presence of many-bodied interactions (Figure D.22). Comparing the MC 2D distribution to the background distribution, it is clear that a significant portion of the background events can be removed by cutting out a portion of the kinematic space.

However, because the OD2 cut is employing a strong correlation between two variables, estimating the systematic uncertainty of this cut is potentially complicated. The most simplistic systematic uncertainty estimation is made by estimating a bias in each cut variable and then shifting the cut value higher and lower in order to study the effects of a potential bias on the events that pass. However, the method technically assumes that the variables are uncorrelated. Therefore, in order to use a pair of variables which can be analyzed more easily and also to help define a much simpler cut, a change of coordinates is performed on the variables QISMSK and $\mathrm{Cos}(\theta_{beam})$. Because one would expect that these variables are related hyperbolically, the variables are transformed into a hyperbolic coordinate system with variables U and V using

$$\begin{aligned} U &= -0.5\ln(\tfrac{\mathrm{QIMSK}}{1-\cos(\theta_{beam})}) \\ V &= \mathrm{sign}(\vec{v}_z) \times \sqrt{\mathrm{QIMSK} \times (1-\cos(\theta_{beam}))} \end{aligned} \tag{D.8}$$

Figure D.23 shows the expected MC, cosmic ray background, and T2K beam data distribution in the UV coordinate system. The effect of the transform is to rotate most of the background rejection power from two variables into one, which in this case is V. This can be seen by looking at both Figure D.25, which shows the distribution of MC, background, and data events in V, and Figure D.24, which shows the distributions for U. Both plots are after the OD1 cut. A simple cut can be defined such that events with V less than -200 are cut. In addition, the correlation between U and V is small, especially when compared to the correlation in the old QISMSK and cosine variables. Therefore, these variables, U and V allow for a much easier sys-

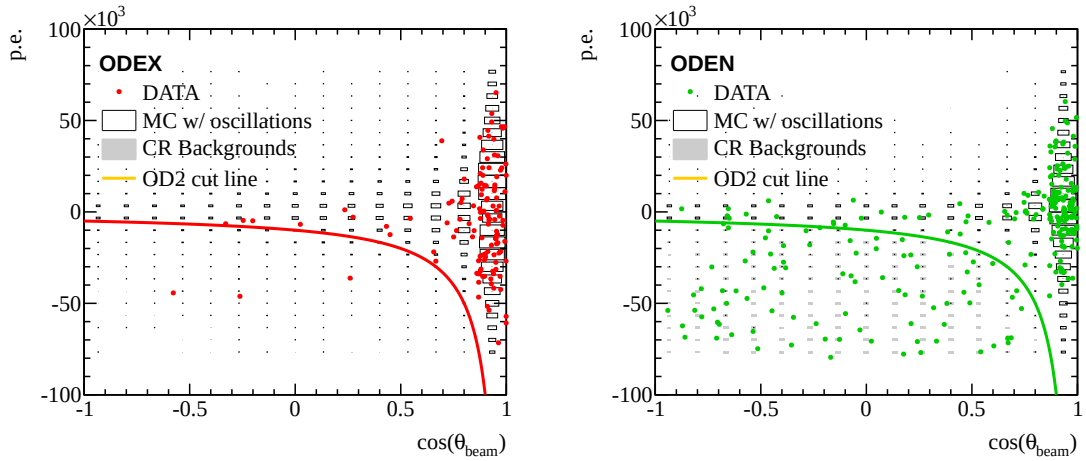

FIGURE D.22: OD2 Parameter space: QISMSK vs. Cos(θ_{beam}) for the T2K beam MC, cosmic ray background, and T2K Run 1-4 beam data distributions. The beam MC is shown in the box plot, the background is shown in the grey box plot, and the data is shown by the colored dots. All distributions are after the OD1 cut. The solid colored line running through the plot is position of the OD2 cut. Events below the line are removed. Note that the 2D space is extended by the sign of the z-component of the most energetic reconstructed track direction which is multiplied to the charge. The MC events are limited to a fraction of the total space.

tematic uncertainty estimation. Because of these advantages the OD2 cut is defined in the UV space.

D.4.5 ODT Cut

The final cut in the OD reduction is a tight timing cut around the expected arrival time of neutrinos from the beam. Neutrinos from the beam arrive in bursts, called a beam spill, with the beam spills having a further internal structure of 6 or 8 bunches. A brief description of the beam spill and bunches can be found in the beginning of Section D.3.4. A very effective cut can be defined around these bunches by rejecting all events not in and around the beam bunches. The width of the window around the bunches is optimized using a MC model also described in Section D.3.4. The MC expectation is compared to the distribution of residual event times around one of these bunches in Figure D.27 for all the OD event types plus the FC events. The events that fall within the event window pass the ODT cuts and are included in the

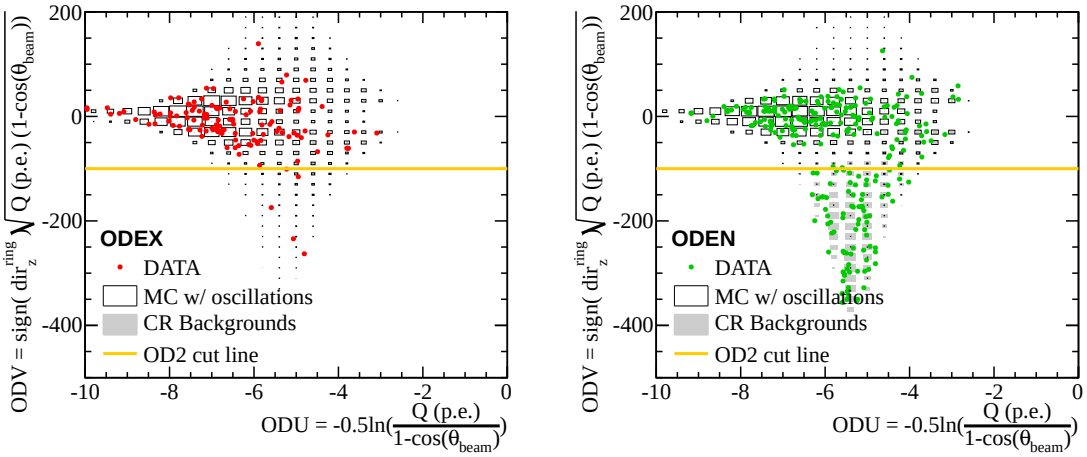

FIGURE D.23: OD2 Parameter space: OD U vs. OD V. The box plot is for the T2K MC while the overlaid colored points plot the data from the T2K Run 1 to 4 sample. The grey boxes show the T2K cosmic ray background distribution built from empty T2K beam spills. The solid orange line running through the plot is the position of the OD2 cut. Events below the line are removed. Note the 2D space is extended by the sign of the z-component of the most energetic reconstructed track direction. The MC events are limited to a fraction of the total space.

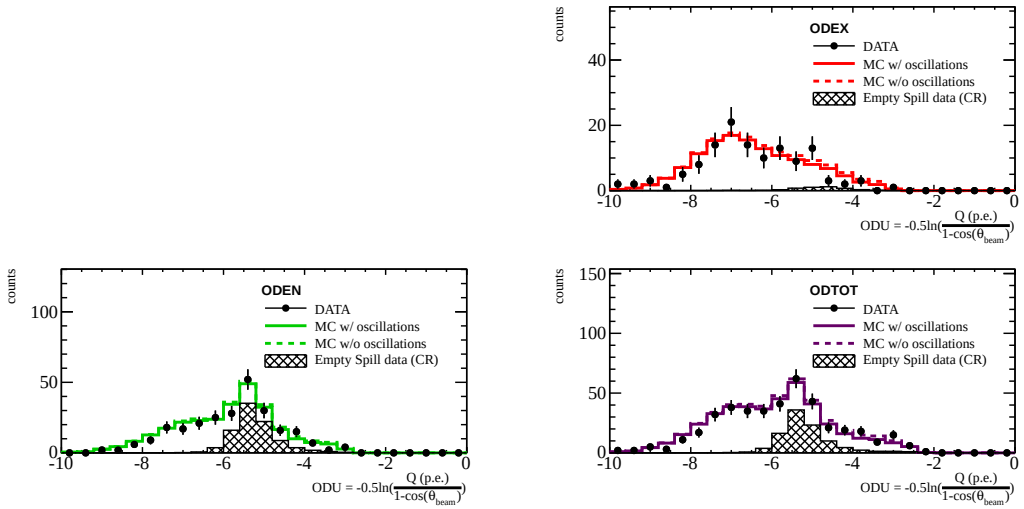

FIGURE D.24: OD2 cut variable U after the OD1 cut.

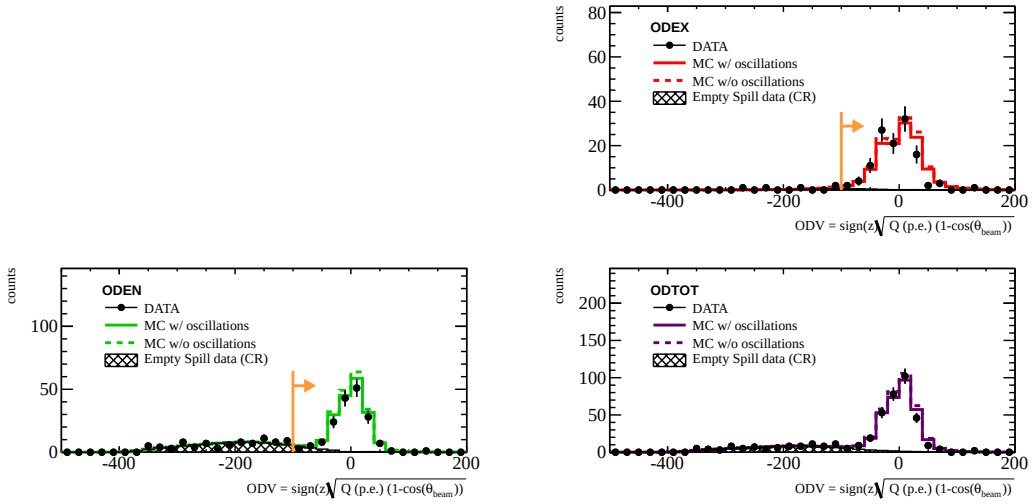

FIGURE D.25: OD2 cut variable V after the OD1 cut.

final OD sample.

However, before one can assign a bunch time position for beam events, the time of the first bunch must be determined. In theory, one should be able to calculate this first bunch time from just information about the beam and detector setup. However, it is easier for now to fit for the time of the first bunch. This is done using a log-likelihood fit to a distribution consisting of a series of Gaussians whose means are spaced 581 ns apart. The number Gaussians are determined by the number of bunches for the beam run: runs 29 to 34 have 6 bunches, while run 36 has 8. The first bunch time is found by scanning over values between 0 and 581 ns in 1 ns steps. Figure D.26 plots the negative likelihood of the fit versus the first bunch positions. The fit is done using only FC events, as this sample should be background free. Furthermore, the fit value is compared between previous runs in order to check that the fitted time is consistent and stable with past beam runs. The best fit time using this method and the data up to beam run 36 is 114.5 ns and is consistent with past runs.

With the first bunch time determined, beam events can be assigned to a bunch.

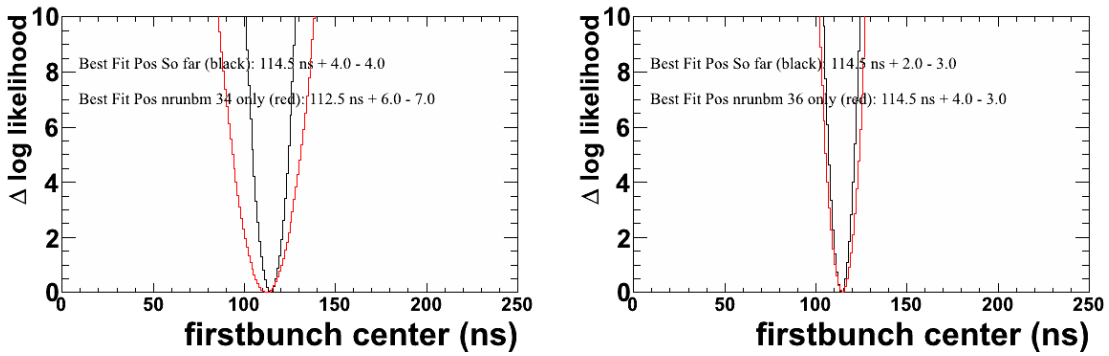

FIGURE D.26: Log-likelihood values of a fit to the data by a bunch time distribution for diffferent first bunch times.

Figure D.28 plots the relative SK to T2K trigger corrected times (i.e. ΔT in the notation of Section D.3.4) after the BASE cut. Even in the presence of background, the bunch structure of the beam is clearly visible. After the positions of the bunches are set, the bunch time distribution can be calculated for the data and the ODT cut can be performed. The time distribution of beam events can be seen in Figure D.27.

D.4.6 Reduction Performance and Summary

Figure D.29 shows the total number of OD events which remain after each cut over the course of the experiment in units of POT. The expected background is shown in those plots as the green histogram. The purpose of Figure D.29 is to demonstrate how much background has been removed by the OD reduction. At the end of Run 1-4, the signal to expected background ratio after the BASE cuts is 0.96. The expected fraction of events that are background in the events observed is 54%. After the ODT cuts, the signal to expected background ratio is 151 and the expected background fraction is 0.7%. The total signal efficiency is around 98%.

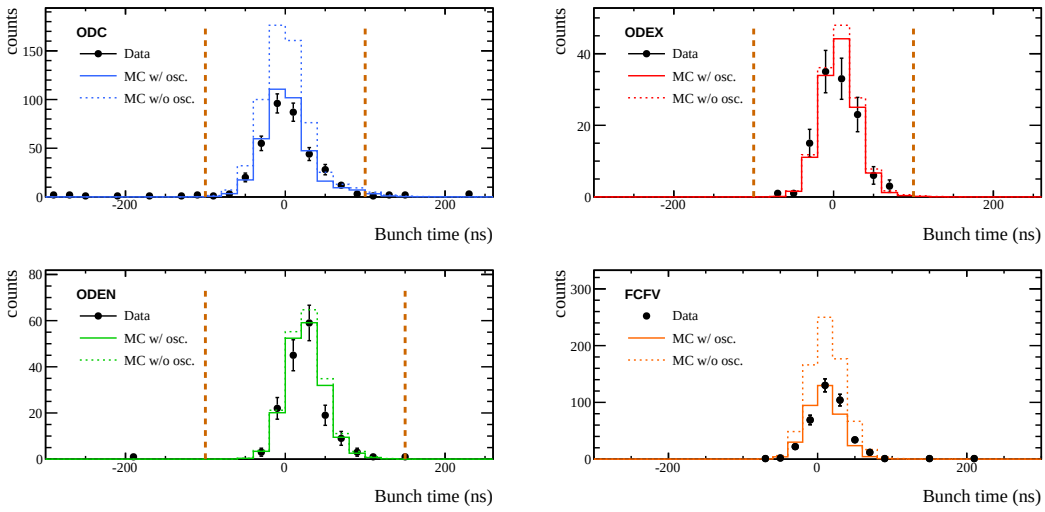

(a) Bunch time distributions after OD2 cut

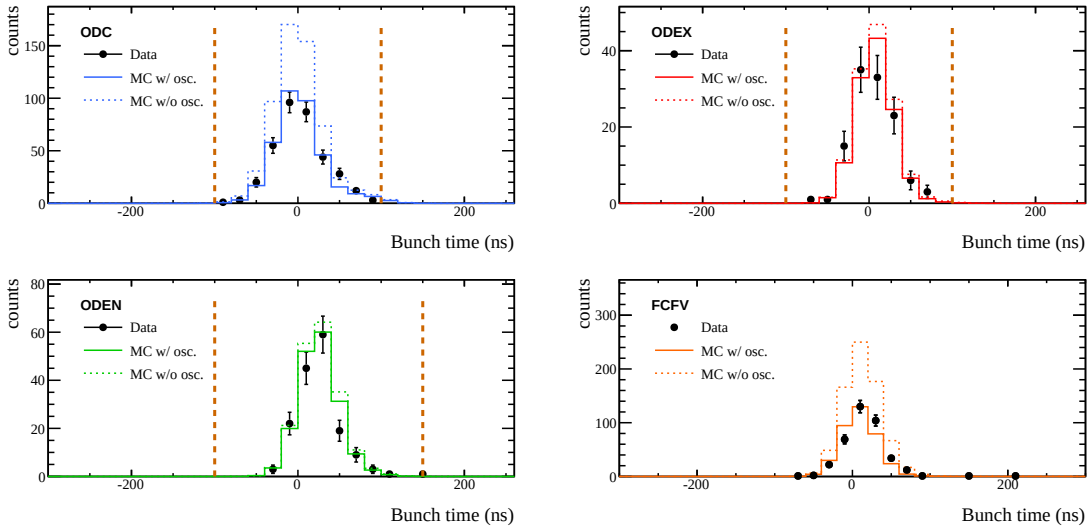

(b) Bunch time distribution after ODT cut

FIGURE D.27: Bunch Timing Distribution for events passing the OD2 and ODT cuts. The dashed line histograms are for the T2K beam MC without oscillations, and the solid line histograms are for MC with oscillations. The points with error bars are events from the T2K Run 1-4 sample with 6.57×10^{20} POT. The dashed magenta lines indicate the ODT cut window. Events passing the ODT cut (b) make up the final OD data sample. Note that the mean of the ODC bunch time distribution is removed for both MC and data so that the ODC events are centered around zero. This same mean is added as an offset to the other event types.

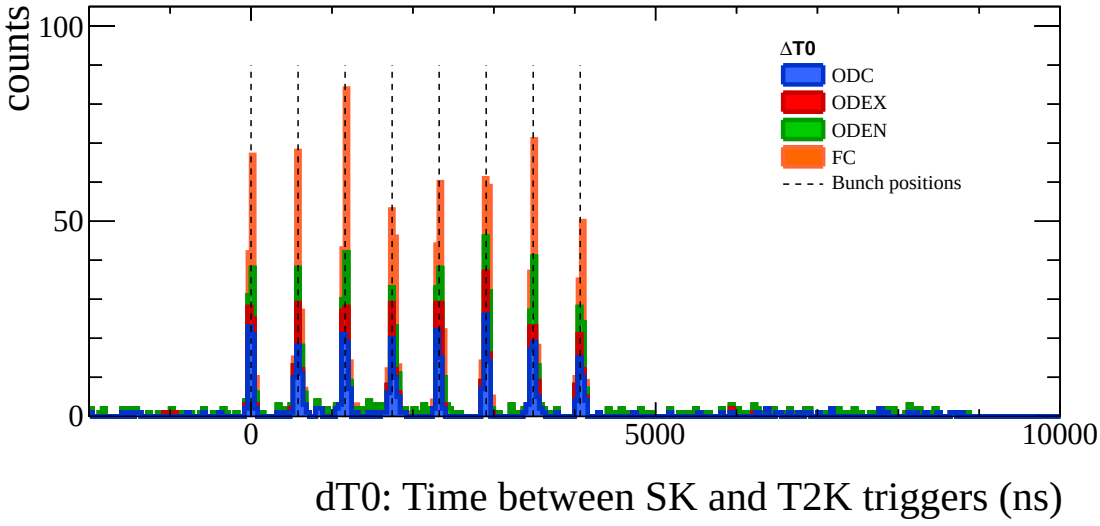

(a) dT distribution after BASE cut

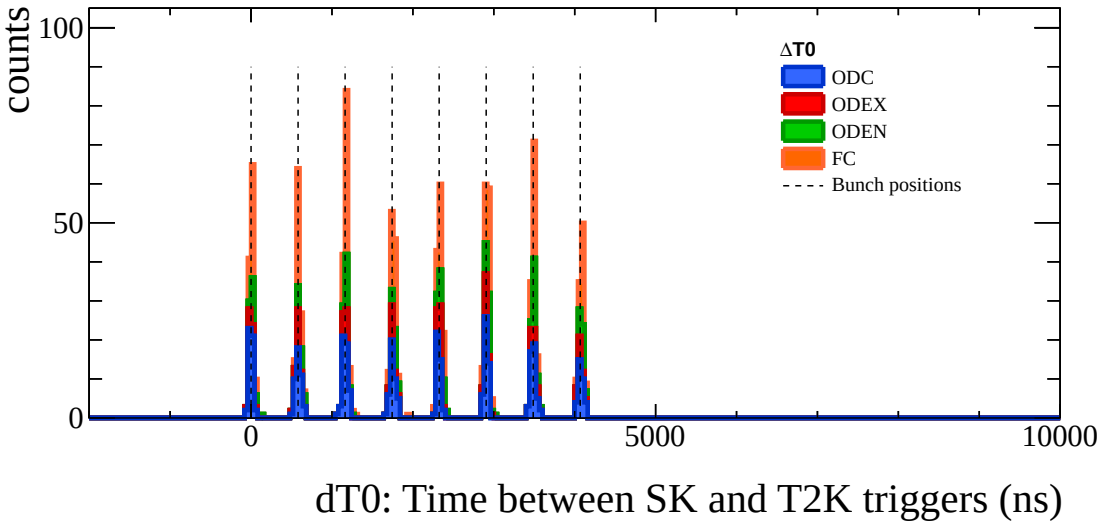

(b) dT distribution after ODT cut

FIGURE D.28: Elapsed time between correct SK and T2K event times, dT.

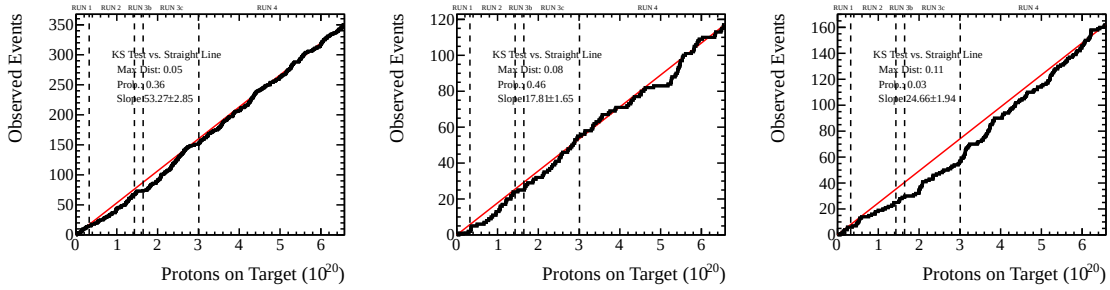

(a) The number of events of each OD type observed as a function of experiment livetime given in POT.

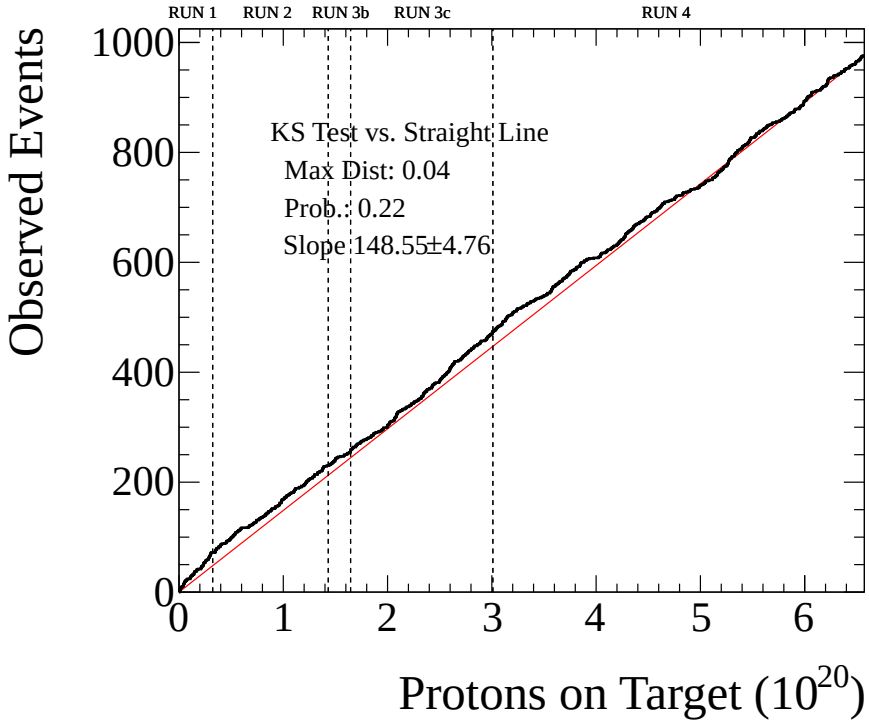

(b) The number of events of all OD events observed as a function of experiment livetime given in POT.

FIGURE D.29: Number of events observed versus livetime of the experiment in POT for each OD event type (a) and all OD events (b). All event samples are consistent with a flat, uniform rate as determined by the Kolmogorov-Smirnov test.

Bibliography

Abazov, A. I. et al. (1991), "Search for neutrinos from sun using the reaction $^{71}\mathrm{Ga}(\nu_e, e^-)^{71}\mathrm{Ge}$," *Phys. Rev. Lett.*, 67, 3332–3335.

Abe, K., Abgrall, N., Ajima, Y., Aihara, H., Albert, J. B., Andreopoulos, C., Andrieu, B., Aoki, S., Araoka, O., Argyriades, J., Ariga, A., Ariga, T., Assylbekov, S., Autiero, D., Badertscher, A., Barbi, M., Barker, G. J., Barr, G., Bass, M., Bay, F., Bentham, S., Berardi, V., Berger, B. E., Bertram, I., Besnier, M., Beucher, J., Beznosko, D., Bhadra, S., Blaszczyk, F. d. M. M., Blondel, A., Bojechko, C., Bouchez, J., Boyd, S. B., Bravar, A., Bronner, C., Brook-Roberge, D. G., Buchanan, N., Budd, H., Calvet, D., Cartwright, S. L., Carver, A., Castillo, R., Catanesi, M. G., Cazes, A., Cervera, A., Chavez, C., Choi, S., Christodoulou, G., Coleman, J., Coleman, W., Collazuol, G., Connolly, K., Curioni, A., Dabrowska, A., Danko, I., Das, R., Davies, G. S., Davis, S., Day, M., De Rosa, G., de André, J. P. A. M., de Perio, P., Delbart, A., Densham, C., Di Lodovico, F., Di Luise, S., Dinh Tran, P., Dobson, J., Dore, U., Drapier, O., Dufour, F., Dumarchez, J., Dytman, S., Dziewiecki, M., Dziomba, M., Emery, S., Ereditato, A., Escudero, L., Esposito, L. S., Fechner, M., Ferrero, A., Finch, A. J., Frank, E., Fujii, Y., Fukuda, Y., Galymov, V., Gannaway, F. C., Gaudin, A., Gendotti, A., George, M. A., Giffin, S., Giganti, C., Gilje, K., Golan, T., Goldhaber, M., Gomez-Cadenas, J. J., Gonin, M., Grant, N., Grant, A., Gumplinger, P., Guzowski, P., Haesler, A., Haigh, M. D., Hamano, K., Hansen, C., Hansen, D., Hara, T., Harrison, P. F., Hartfiel, B., Hartz, M., Haruyama, T., Hasegawa, T., Hastings, N. C., Hastings, S., Hatzikoutelis, A., Hayashi, K., Hayato, Y., Hearty, C., Helmer, R. L., Henderson, R., Higashi, N., Hignight, J., Hirose, E., Holeczek, J., Horikawa, S., Hyndman, A., Ichikawa, A. K., Ieki, K., Ieva, M., Iida, M., Ikeda, M., Ilic, J., Imber, J., Ishida, T., Ishihara, C., Ishii, T., Ives, S. J., Iwasaki, M., Iyogi, K., Izmaylov, A., Jamieson, B., Johnson, R. A., Joo, K. K., Jover-Manas, G. V., Jung, C. K., Kaji, H., Kajita, T., Kakuno, H., Kameda, J., Kaneyuki, K., Karlen, D., Kasami, K., Kato, I., Kearns, E., Khabibullin, M., Khanam, F., Khotjantsev, A., Kielczewska, D., Kikawa, T., Kim, J., Kim, J. Y., Kim, S. B., Kimura, N., Kirby, B., Kisiel, J., Kitching, P., Kobayashi, T., Kogan, G., Koike, S., Konaka, A., Kormos, L. L., Korzenev, A., Koseki, K., Koshio, Y., Kouzuma, Y., Kowalik, K., Kravtsov, V., Kreslo, I., Kropp, W., Kubo, H., Kudenko, Y., Kulkarni, N., Kurjata, R., Kutter, T., Lagoda, J., Laihem, K., Laveder, M., Lee, K. P., Le, P. T., Levy,

J. M., Licciardi, C., Lim, I. T., Lindner, T., Litchfield, R. P., Litos, M., Longhin, A., Lopez, G. D., Loverre, P. F., Ludovici, L., Lux, T., Macaire, M., Mahn, K., Makida, Y., Malek, M., Manly, S., Marchionni, A., Marino, A. D., Marteau, J., Martin, J. F., Maruyama, T., Maryon, T., Marzec, J., Masliah, P., Mathie, E. L., Matsumura, C., Matsuoka, K., Matveev, V., Mavrokoridis, K., Mazzucato, E., McCauley, N., McFarland, K. S., McGrew, C., McLachlan, T., Messina, M., Metcalf, W., Metelko, C., Mezzetto, M., Mijakowski, P., Miller, C. A., Minamino, A., Mineev, O., Mine, S., Missert, A. D., Mituka, G., Miura, M., Mizouchi, K., Monfregola, L., Moreau, F., Morgan, B., Moriyama, S., Muir, A., Murakami, A., Murdoch, M., Murphy, S., Myslik, J., Nakadaira, T., Nakahata, M., Nakai, T., Nakajima, K., Nakamoto, T., Nakamura, K., Nakayama, S., Nakaya, T., Naples, D., Navin, M. L., Nelson, B., Nicholls, T. C., Nishikawa, K., Nishino, H., Nowak, J. A., Noy, M., Obayashi, Y., Ogitsu, T., Ohhata, H., Okamura, T., Okumura, K., Okusawa, T., Oser, S. M., Otani, M., Owen, R. A., Oyama, Y., Ozaki, T., Pac, M. Y., Palladino, V., Paolone, V., Paul, P., Payne, D., Pearce, G. F., Perkin, J. D., Pettinacci, V., Pierre, F., Poplawska, E., Popov, B., Posiadala, M., Poutissou, J. M., Poutissou, R., Przewlocki, P., Qian, W., Raaf, J. L., Radicioni, E., Ratoff, P. N., Raufer, T. M., Ravonel, M., Raymond, M., Retiere, F., Robert, A., Rodrigues, P. A., Rondio, E., Roney, J. M., Rossi, B., Roth, S., Rubbia, A., Ruterbories, D., Sabouri, S., Sacco, R., Sakashita, K., Sanchez, F., Sarrat, A., Sasaki, K., Scholberg, K., Schwehr, J., Scott, M., Scully, D. I., Seiya, Y., Sekiguchi, T., and Sekiya... (2011a), "Indication of Electron Neutrino Appearance from an Accelerator-Produced Off-Axis Muon Neutrino Beam," *Physical Review Letters*, 107, 041801.

Abe, K., Abgrall, N., Aihara, H., Ajima, Y., Albert, J. B., Allan, D., Amaudruz, P. A., Andreopoulos, C., Andrieu, B., Anerella, M. D., Angelsen, C., Aoki, S., Araoka, O., Argyriades, J., Ariga, A., Ariga, T., Assylbekov, S., de André, J. P. A. M., Autiero, D., Badertscher, A., Ballester, O., Barbi, M., Barker, G. J., Baron, P., Barr, G., Bartoszek, L., Batkiewicz, M., Bay, F., Bentham, S., Berardi, V., Berger, B. E., Berns, H., Bertram, I., Besnier, M., Beucher, J., Beznosko, D., Bhadra, S., Birney, P., Bishop, D., Blackmore, E., Blaszczyk, F. d. M., Blocki, J., Blondel, A., Bodek, A., Bojechko, C., Bouchez, J., Boussuge, T., Boyd, S. B., Boyer, M., Braam, N., Bradford, R., Bravar, A., Briggs, K., Brinson, J. D., Bronner, C., Brook-Roberge, D. G., Bryant, M., Buchanan, N., Budd, H., Cadabeschi, M., Calland, R. G., Calvet, D., Rodríguez, J. C., Carroll, J., Cartwright, S. L., Carver, A., Castillo, R., Catanesi, M. G., Cavata, C., Cazes, A., Cervera, A., Charrier, J. P., Chavez, C., Choi, S., Chollet, S., Christodoulou, G., Colas, P., Coleman, J., Coleman, W., Collazuol, G., Connolly, K., Cooke, P., Curioni, A., Dabrowska, A., Danko, I., Das, R., Davies, G. S., Davis, S., Day, M., De La Broise, X., de Perio, P., De Rosa, G., Dealtry, T., Debraine, A., Delagnes, E., Delbart, A., Densham, C., Di Lodovico, F., Di Luise, S., Tran, P. D., Dobson, J., Doornbos, J., Dore, U., Drapier, O., Druillole, F., Dufour, F., Dumarchez, J., Durkin,

T., Dytman, S., Dziewiecki, M., Dziomba, M., Ellison, B., Emery, S., Ereditato, A., Escallier, J. E., Escudero, L., Esposito, L. S., Faszer, W., Fechner, M., Ferrero, A., Finch, A., Fisher, C., Fitton, M., Flight, R., Forbush, D., Frank, E., Fransham, K., Fujii, Y., Fukuda, Y., Gallop, M., Galymov, V., Ganetis, G. L., Gannaway, F. C., Gaudin, A., Gaweda, J., Gendotti, A., George, M., Giffin, S., Giganti, C., Gilje, K., Giomataris, I., Giraud, J., Ghosh, A. K., Golan, T., Goldhaber, M., Gomez-Cadenas, J. J., Gomi, S., Gonin, M., Goyette, M., Grant, A., Grant, N., Grañena, F., Greenwood, S., Gumplinger, P., Guzowski, P., Haigh, M. D., Hamano, K., Hansen, C., Hara, T., Harrison, P. F., Hartfiel, B., Hartz, M., Haruyama, T., Hasanen, R., Hasegawa, T., Hastings, N. C., Hastings, S., Hatzikoutelis, A., Hayashi, K., Hayato, Y., Haycock, T. D. J., Hearty, C., Helmer, R. L., Henderson, R., Herlant, S., Higashi, N., Hignight, J., Hiraide, K., Hirose, E., Holeczek, J., Honkanen, N., Horikawa, S., Hyndman, A., Ichikawa, A. K., Ieki, K., Ieva, M., Iida, M., Ikeda, M., Ilic, J., Imber, J., Ishida, T., Ishihara, C., Ishii, T., Ives, S. J., Iwasaki, M., Iyogi, K., Izmaylov, A., Jamieson, B., Johnson, R. A., Joo, K. K., Jover-Manas, G., Jung, C. K., Kaji, H., Kajita, T., Kakuno, H., Kameda, J., Kaneyuki, K., Karlen, D., Kasami, K., Kasey, V., Kato, I., Kawamuko, H., Kearns, E., Kellet, L., Khabibullin, M., Khaleeq, M., Khan, N., Khotjantsev, A., Kielczewska, D., Kikawa, T., Kim, J. Y., Kim, S. B., Kimura, N., Kirby, B., Kisiel, J., Kitching, P., Kobayashi, T., Kogan, G., Koike, S., Komorowski, T., Konaka, A., Kormos, L. L., Korzenev, A., Koseki, K., Koshio, Y., Kouzuma, Y., Kowalik, K., Kravtsov, V., Kreslo, I., Kropp, W., Kubo, H., Kubota, J., Kudenko, Y., Kulkarni, N., Kurchaninov, L., Kurimoto, Y., Kurjata, R., Kurosawa, Y., Kutter, T., Lagoda, J., Laihem, K., Langstaff, R., Laveder, M., Lawson, T. B., Le, P. T., Le Coguie, A., Le Ross, M., Lee, K. P., Lenckowski, M., Licciardi, C., Lim, I. T., Lindner, T., Litchfield, R. P., Longhin, A., Lopez, G. D., Lu, P., Ludovici, L., Lux, T., Macaire, M., Magaletti, L., Mahn, K., Makida, Y., Malafis, C. J., Malek, M., Manly, S., Marchionni, A., Mark, C., Marino, A. D., Marone, A. J., Marteau, J., Martin, J. F., Maruyama, T., Maryon, T., Marzec, J., Masliah, P., Mathie, E. L., Matsumura, C., Matsuoka, K., Matveev, V., Mavrokoridis, K., Mazzucato, E., McCauley, N., McFarland, K. S., McGrew, C., McLachlan, T., Mercer, I., Messina, M., Metcalf, W., Metelko, C., Mezzetto, M., Mijakowski, P., Miller, C. A., Minamino, A., Mineev, O., Mine, S., Minvielle, R. E., Mituka, G., Miura, M., Mizouchi, K., Mols, J. P., Monfregola, L., and Monmarthe, E. (2011b), "The T2K Experiment," *Nuclear Inst. and Methods in Physics Research, A*, 659, 106–135.

Abe, K., Hayato, Y., Iida, T., Iyogi, K., Kameda, J., Koshio, Y., Kozuma, Y., Marti, L., Miura, M., Moriyama, S., Nakahata, M., Nakayama, S., Obayashi, Y., Sekiya, H., Shiozawa, M., Suzuki, Y., Takeda, A., Takenaga, Y., Ueno, K., Ueshima, K., Yamada, S., Yokozawa, T., Ishihara, C., Kaji, H., Kajita, T., Kaneyuki, K., Lee, K. P., McLachlan, T., Okumura, K., Shimizu, Y., Tanimoto, N., Labarga, L., Kearns, E., Litos, M., Raaf, J. L., Stone, J. L., Sulak, L. R., Goldhaber,

M., Bays, K., Kropp, W. R., Mine, S., Regis, C., Renshaw, A., Smy, M. B., Sobel, H. W., Ganezer, K. S., Hill, J., Keig, W. E., Jang, J. S., Kim, J. Y., Lim, I. T., Albert, J. B., Scholberg, K., Walter, C. W., Wendell, R., Wongjirad, T. M., Ishizuka, T., Tasaka, S., Learned, J. G., Matsuno, S., Smith, S. N., Hasegawa, T., Ishida, T., Ishii, T., Kobayashi, T., Nakadaira, T., Nakamura, K., Nishikawa, K., Oyama, Y., Sakashita, K., Sekiguchi, T., Tsukamoto, T., Suzuki, A. T., Takeuchi, Y., Ikeda, M., Minamino, A., Nakaya, T., Fukuda, Y., Itow, Y., Mitsuka, G., Tanaka, T., Jung, C. K., Lopez, G. D., Taylor, I., Yanagisawa, C., Ishino, H., Kibayashi, A., Mino, S., Mori, T., Sakuda, M., Toyota, H., Kuno, Y., Yoshida, M., Kim, S. B., Yang, B. S., Okazawa, H., Choi, Y., Nishijima, K., Koshiba, M., Yokoyama, M., Totsuka, Y., Martens, K., Schuemann, J., Vagins, M. R., Chen, S., Heng, Y., Yang, Z., Zhang, H., Kielczewska, D., Mijakowski, P., Connolly, K., Dziomba, M., Thrane, E., Wilkes, R. J., and Super-Kamiokande Collaboration (2013a), "Evidence for the Appearance of Atmospheric Tau Neutrinos in Super-Kamiokande," *Physical Review Letters*, 110, 181802.

Abe, K., Adam, J., Aihara, H., Akiri, T., Andreopoulos, C., Aoki, S., Ariga, A., Ariga, T., Assylbekov, S., and Autiero, D. (2013b), "Measurement of neutrino oscillation parameters from muon neutrino disappearance with an off-axis beam," *Physical Review Letters*, 111, 211803.

Abe, K., Abgrall, N., Aihara, H., Akiri, T., Albert, J. B., Andreopoulos, C., Aoki, S., Ariga, A., Ariga, T., and Assylbekov, S. (2013c), "T2K neutrino flux prediction," *Physical Review D*, 87, 012001.

Abe, K., Hayato, Y., Iida, T., Iyogi, K., Kameda, J., Kishimoto, Y., Koshio, Y., Marti, L., Miura, M., Moriyama, S., Nakahata, M., Nakano, Y., Nakayama, S., Obayashi, Y., Sekiya, H., Shiozawa, M., Suzuki, Y., Takeda, A., Takenaga, Y., Tanaka, H., Tomura, T., Ueno, K., Wendell, R. A., Yokozawa, T., Irvine, T. J., Kaji, H., Kajita, T., Kaneyuki, K., Lee, K. P., Nishimura, Y., Okumura, K., McLachlan, T., Labarga, L., Kearns, E., Raaf, J. L., Stone, J. L., Sulak, L. R., Berkman, S., Tanaka, H. A., Tobayama, S., Goldhaber, M., Bays, K., Carminati, G., Kropp, W. R., Mine, S., Renshaw, A., Smy, M. B., Sobel, H. W., Ganezer, K. S., Hill, J., Keig, W. E., Jang, J. S., Kim, J. Y., Lim, I. T., Hong, N., Akiri, T., Albert, J. B., Himmel, A., Scholberg, K., Walter, C. W., Wongjirad, T., Ishizuka, T., Tasaka, S., Learned, J. G., Matsuno, S., Smith, S. N., Hasegawa, T., Ishida, T., Ishii, T., Kobayashi, T., Nakadaira, T., Nakamura, K., Nishikawa, K., Oyama, Y., Sakashita, K., Sekiguchi, T., Tsukamoto, T., Suzuki, A. T., Takeuchi, Y., Huang, K., Ieki, K., Ikeda, M., Kikawa, T., Kubo, H., Minamino, A., Murakami, A., Nakaya, T., Otani, M., Suzuki, K., Takahashi, S., Fukuda, Y., Choi, K., Itow, Y., Mitsuka, G., Miyake, M., Mijakowski, P., Tacik, R., Hignight, J., Imber, J., Jung, C. K., Taylor, I., Yanagisawa, C., Idehara, Y., Ishino, H., Kibayashi, A., Mori, T., Sakuda, M., Yamaguchi, R., Yano, T., Kuno, Y., Kim, S. B., Yang, B. S., Okazawa, H., Choi, Y., Nishijima, K., Koshiba, M., Totsuka, Y., Yokoyama,

M., Martens, K., Vagins, M. R., Martin, J. F., de Perio, P., Konaka, A., Wilking, M. J., Chen, S., Heng, Y., Sui, H., Yang, Z., Zhang, H., Zhenwei, Y., Connolly, K., Dziomba, M., and Wilkes, R. J. (2014), "Nuclear Instruments and Methods in Physics Research A," *Nuclear Inst. and Methods in Physics Research, A*, 737, 253–272.

Abe, S., Ebihara, T., Enomoto, S., Furuno, K., Gando, Y., Ichimura, K., Ikeda, H., Inoue, K., Kibe, Y., Kishimoto, Y., Koga, M., Kozlov, A., Minekawa, Y., Mitsui, T., Nakajima, K., Nakajima, K., Nakamura, K., Nakamura, M., Owada, K., Shimizu, I., Shimizu, Y., Shirai, J., Suekane, F., Suzuki, A., Takemoto, Y., Tamae, K., Terashima, A., Watanabe, H., Yonezawa, E., Yoshida, S., Busenitz, J., Classen, T., Grant, C., Keefer, G., Leonard, D., Mckee, D., Piepke, A., Decowski, M., Detwiler, J., Freedman, S., Fujikawa, B., Gray, F., Guardincerri, E., Hsu, L., Kadel, R., Lendvai, C., Luk, K. B., Murayama, H., O'Donnell, T., Steiner, H., Winslow, L., Dwyer, D., Jillings, C., Mauger, C., McKeown, R., Vogel, P., Zhang, C., Berger, B., Lane, C., Maricic, J., Miletic, T., Batygov, M., Learned, J., Matsuno, S., Pakvasa, S., Foster, J., Horton-Smith, G., Tang, A., Dazeley, S., Downum, K., Gratta, G., Tolich, K., Bugg, W., Efremenko, Y., Kamyshkov, Y., Perevozchikov, O., Karwowski, H., Markoff, D., Tornow, W., Heeger, K., Piquemal, F., Ricol, J. S., and The KamLAND Collaboration (2008), "Precision Measurement of Neutrino Oscillation Parameters with KamLAND," *Physical Review Letters*, 100, 221803.

Adamson, P., Andreopoulos, C., Arms, K. E., Armstrong, R., Auty, D. J., Ayres, D. S., Backhouse, C., Barnes, P. D., Barr, G., Barrett, W. L., Becker, B. R., Belias, A., Bernstein, R. H., Betancourt, M., Bhattacharya, D., Bishai, M., Blake, A., Bock, G. J., Boehm, J., Boehnlein, D. J., Bogert, D., Bower, C., Cavanaugh, S., Chapman, J. D., Cherdack, D., Childress, S., Choudhary, B. C., Cobb, J. H., Coelho, J. A. B., Coleman, S. J., Cronin-Hennessy, D., Culling, A. J., Danko, I. Z., de Jong, J. K., Devenish, N. E., Diwan, M. V., Dorman, M., Erwin, A. R., Escobar, C. O., Evans, J. J., Falk, E., Feldman, G. J., Frohne, M. V., Gallagher, H. R., Godley, A., Goodman, M. C., Gouffon, P., Gran, R., Grashorn, E. W., Grzelak, K., Habig, A., Harris, D., Harris, P. G., Hartnell, J., Hatcher, R., Heller, K., Himmel, A., Holin, A., Howcroft, C., Huang, X., Hylen, J., Irwin, G. M., Isvan, Z., Jaffe, D. E., James, C., Jensen, D., Kafka, T., Kasahara, S. M. S., Koizumi, G., Kopp, S., Kordosky, M., Koskinen, D. J., Krahn, Z., Kreymer, A., Lang, K., Ling, J., Litchfield, P. J., Litchfield, R. P., Loiacono, L., Lucas, P., Ma, J., Mann, W. A., Marshak, M. L., Marshall, J. S., Mayer, N., McGowan, A. M., Mehdiyev, R., Meier, J. R., Messier, M. D., Metelko, C. J., Michael, D. G., Miller, W. H., Mishra, S. R., Mitchell, J., Moore, C. D., Morfín, J., Mualem, L., Mufson, S., Musser, J., Naples, D., Nelson, J. K., Newman, H. B., Nichol, R. J., Nicholls, T. C., Ochoa-Ricoux, J. P., Oliver, W. P., Ospanov, R., Paley, J., Para, A., Patterson, R. B., Patzak, T., Pavlovic, Z., Pawloski, G., Pearce, G. F., Petyt, D. A., Pittam, R., Plunkett, R. K., Rahaman, A., Rameika, R. A., Raufer, T. M., Rebel, B., Reichenbacher,

J., Rodrigues, P. A., Rosenfeld, C., Rubin, H. A., Ryabov, V. A., Sanchez, M. C., Saoulidou, N., Schneps, J., Schreiner, P., Shanahan, P., Smart, W., Smith, C., Sousa, A., Speakman, B., Stamoulis, P., Strait, M., Tagg, N., Talaga, R. L., Thomas, J., Thomson, M. A., Thron, J. L., Tinti, G., Toner, R., Tsarev, V. A., Tzanakos, G., Urheim, J., Vahle, P., Viren, B., Ward, D. R., Watabe, M., Weber, A., Webb, R. C., West, N., White, C., Whitehead, L., Wojcicki, S. G., Wright, D. M., Yang, T., Zhang, K., Zheng, H., Zois, M., and Zwaska, R. (2009), "Search for Muon-Neutrino to Electron-Neutrino Transitions in MINOS," *Physical Review Letters*, 103, 261802.

Adamson, P., Andreopoulos, C., Arms, K. E., Armstrong, R., Auty, D. J., Ayres, D. S., Backhouse, C., Barnes, P. D., Barr, G., Barrett, W. L., Bhattacharya, D., Bishai, M., Blake, A., Bock, G. J., Boehnlein, D. J., Bogert, D., Bower, C., Cavanaugh, S., Chapman, J. D., Cherdack, D., Childress, S., Choudhary, B. C., Coelho, J. A. B., Coleman, S. J., Cronin-Hennessy, D., Culling, A. J., Danko, I. Z., de Jong, J. K., Devenish, N. E., Diwan, M. V., Dorman, M., Erwin, A. R., Escobar, C. O., Evans, J. J., Falk, E., Feldman, G. J., Frohne, M. V., Gallagher, H. R., Godley, A., Goodman, M. C., Gouffon, P., Gran, R., Grashorn, E. W., Grzelak, K., Habig, A., Harris, D., Harris, P. G., Hartnell, J., Hatcher, R., Heller, K., Himmel, A., Holin, A., Hylen, J., Irwin, G. M., Isvan, Z., Jaffe, D. E., James, C., Jensen, D., Kafka, T., Kasahara, S. M. S., Kim, J. J., Koizumi, G., Kopp, S., Kordosky, M., Koskinen, D. J., Krahn, Z., Kreymer, A., Lang, K., Ling, J., Litchfield, P. J., Litchfield, R. P., Loiacono, L., Lucas, P., Ma, J., Mann, W. A., Marshak, M. L., Marshall, J. S., Mayer, N., McGowan, A. M., Mehdiyev, R., Meier, J. R., Messier, M. D., Metelko, C. J., Michael, D. G., Miller, W. H., Mishra, S. R., Mitchell, J., Moore, C. D., Morfín, J., Mualem, L., Mufson, S., Musser, J., Naples, D., Nelson, J. K., Newman, H. B., Nichol, R. J., Nicholls, T. C., Ochoa-Ricoux, J. P., Oliver, W. P., Osiecki, T., Ospanov, R., Paley, J., Paolone, V., Patterson, R. B., Pavlovic, Z., Pawloski, G., Pearce, G. F., Petyt, D. A., Pittam, R., Plunkett, R. K., Rahaman, A., Rameika, R. A., Raufer, T. M., Rebel, B., Rodrigues, P. A., Rosenfeld, C., Rubin, H. A., Ryabov, V. A., Sanchez, M. C., Saoulidou, N., Schneps, J., Schreiner, P., Semenov, V. K., Shanahan, P., Smart, W., Smith, C., Sousa, A., Stamoulis, P., Strait, M., Tagg, N., Talaga, R. L., Thomas, J., Thomson, M. A., Tinti, G., Toner, R., Tsarev, V. A., Tzanakos, G., Urheim, J., Vahle, P., Viren, B., Watabe, M., Weber, A., Webb, R. C., West, N., White, C., Whitehead, L., Wojcicki, S. G., Wright, D. M., Yang, T., Zois, M., Zhang, K., Zwaska, R., and MINOS Collaboration (2010), "Neutrino and antineutrino inclusive charged-current cross section measurements with the MINOS near detector," *Physical Review D*, 81, 072002.

Adamson, P., Anghel, I., Backhouse, C., Barr, G., Bishai, M., Blake, A., Bock, G. J., Bogert, D., Cao, S. V., Castromonte, C. M., Childress, S., Coelho, J. A. B., Corwin, L., Cronin-Hennessy, D., de Jong, J. K., Devan, A. V., Devenish, N. E., Diwan, M. V., Escobar, C. O., Evans, J. J., Falk, E., Feldman, G. J., Frohne, M. V.,

Gallagher, H. R., Gomes, R. A., Goodman, M. C., Gouffon, P., Graf, N., Gran, R., Grzelak, K., Habig, A., Hahn, S. R., Hartnell, J., Hatcher, R., Himmel, A., Holin, A., Hylen, J., Irwin, G. M., Isvan, Z., James, C., Jensen, D., Kafka, T., Kasahara, S. M. S., Koizumi, G., Kordosky, M., Kreymer, A., Lang, K., Ling, J., Litchfield, P. J., Lucas, P., Mann, W. A., Marshak, M. L., Mathis, M., Mayer, N., McGowan, A. M., Medeiros, M. M., Mehdiyev, R., Meier, J. R., Messier, M. D., Michael, D. G., Miller, W. H., Mishra, S. R., Moed Sher, S., Moore, C. D., Mualem, L., Musser, J., Naples, D., Nelson, J. K., Newman, H. B., Nichol, R. J., Nowak, J. A., O'Connor, J., Oliver, W. P., Orchanian, M., Pahlka, R. B., Paley, J., Patterson, R. B., Pawloski, G., Phan-Budd, S., Plunkett, R. K., Qiu, X., Radovic, A., Rebel, B., Rosenfeld, C., Rubin, H. A., Sanchez, M. C., Schneps, J., Schreckenberger, A., Schreiner, P., Sharma, R., Sousa, A., Tagg, N., Talaga, R. L., Thomas, J., Thomson, M. A., Tinti, G., Tognini, S. C., Toner, R., Torretta, D., Tzanakos, G., Urheim, J., Vahle, P., Viren, B., Weber, A., Webb, R. C., White, C., Whitehead, L., Whitehead, L. H., Wojcicki, S. G., Zwaska, R., and MINOS Collaboration (2013), "Measurement of Neutrino and Antineutrino Oscillations Using Beam and Atmospheric Data in MINOS," *Physical Review Letters*, 110, 251801.

Aglietta, M., Battistoni, G., Bellotti, E., Bloise, C., Bologna, G., Broggini, C., Campana, P., Castagnoli, C., Castellina, A., and Chiarella, V. (1989), "Experimental study of atmospheric neutrino flux in the NUSEX experiment," *EPL (Europhysics Letters)*, 8, 611.

Aguilar-Arevalo, A. A., Anderson, C. E., Bazarko, A. O., Brice, S. J., Brown, B. C., Bugel, L., Cao, J., Coney, L., Conrad, J. M., Cox, D. C., Curioni, A., Djurcic, Z., Finley, D. A., Fleming, B. T., Ford, R., Garcia, F. G., Garvey, G. T., Green, C., Green, J. A., Hart, T. L., Hawker, E., Imlay, R., Johnson, R. A., Karagiori, G., Kasper, P., Katori, T., Kobilarcik, T., Kourbanis, I., Koutsoliotas, S., Laird, E. M., Linden, S. K., Link, J. M., Liu, Y., Liu, Y., Louis, W. C., Mahn, K. B. M., Marsh, W., Martin, P. S., McGregor, G., Metcalf, W., Meyers, P. D., Mills, F., Mills, G. B., Monroe, J., Moore, C. D., Nelson, R. H., Nguyen, V. T., Nienaber, P., Nowak, J. A., Ouedraogo, S., Patterson, R. B., Perevalov, D., Polly, C. C., Prebys, E., Raaf, J. L., Ray, H., Roe, B. P., Russell, A. D., Sandberg, V., Schirato, R., Schmitz, D., Shaevitz, M. H., Shoemaker, F. C., Smith, D., Soderberg, M., Sorel, M., Spentzouris, P., Stancu, I., Stefanski, R. J., Sung, M., Tanaka, H. A., Tayloe, R., Tzanov, M., Van de Water, R., Wascko, M. O., White, D. H., Wilking, M. J., Yang, H. J., Zeller, G. P., and Zimmerman, E. D. (2008), "First observation of coherent production in neutrino–nucleus interactions with," *Physics Letters B*, 664, 41–46.

Aguilar-Arevalo, A. A., Anderson, C. E., Bazarko, A. O., Brice, S. J., Brown, B. C., Bugel, L., Cao, J., Coney, L., Conrad, J. M., Cox, D. C., Curioni, A., Djurcic, Z., Finley, D. A., Fleming, B. T., Ford, R., Garcia, F. G., Garvey, G. T., Grange, J., Green, C., Green, J. A., Hart, T. L., Hawker, E., Imlay, R., Johnson, R. A.,

Karagiorgi, G., Kasper, P., Katori, T., Kobilarcik, T., Kourbanis, I., Koutsoliotas, S., Laird, E. M., Linden, S. K., Link, J. M., Liu, Y., Liu, Y., Louis, W. C., Mahn, K. B. M., Marsh, W., Mauger, C., McGary, V. T., McGregor, G., Metcalf, W., Meyers, P. D., Mills, F., Mills, G. B., Monroe, J., Moore, C. D., Mousseau, J., Nelson, R. H., Nienaber, P., Nowak, J. A., Osmanov, B., Ouedraogo, S., Patterson, R. B., Pavlovic, Z., Perevalov, D., Polly, C. C., Prebys, E., Raaf, J. L., Ray, H., Roe, B. P., Russell, A. D., Sandberg, V., Schirato, R., Schmitz, D., Shaevitz, M. H., Shoemaker, F. C., Smith, D., Soderberg, M., Sorel, M., Spentzouris, P., Spitz, J., Stancu, I., Stefanski, R. J., Sung, M., Tanaka, H. A., Tayloe, R., Tzanov, M., Van de Water, R. G., Wascko, M. O., White, D. H., Wilking, M. J., Yang, H. J., Zeller, G. P., Zimmerman, E. D., and MiniBooNE Collaboration (2010), "First measurement of the muon neutrino charged current quasielastic double differential cross section," *Physical Review D*, 81, 092005.

Aguilar-Arevalo, A. A., Anderson, C. E., Bazarko, A. O., Brice, S. J., Brown, B. C., Bugel, L., Cao, J., Coney, L., Conrad, J. M., and Cox, D. C. (2011), "Measurement of neutrino-induced charged-current charged pion production cross sections on mineral oil at E ν 1 GeV," *Physical Review D*, 83, 052007.

Ahmad, Q. R., Allen, R. C., Andersen, T. C., Anglin, J. D., Barton, J. C., Beier, E. W., Bercovitch, M., Bigu, J., Biller, S. D., Black, R. A., Blevis, I., Boardman, R. J., Boger, J., Bonvin, E., Boulay, M. G., Bowler, M. G., Bowles, T. J., Brice, S. J., Browne, M. C., Bullard, T. V., Buhler, G., Cameron, J., Chan, Y. D., Chen, H. H., Chen, M., Chen, X., Cleveland, B. T., Clifford, E. T. H., Cowan, J. H. M., Cowen, D. F., Cox, G. A., Dai, X., Dalnoki-Veress, F., Davidson, W. F., Doe, P. J., Doucas, G., Dragowsky, M. R., Duba, C. A., Duncan, F. A., Dunford, M., Dunmore, J. A., Earle, E. D., Elliott, S. R., Evans, H. C., Ewan, G. T., Farine, J., Fergani, H., Ferraris, A. P., Ford, R. J., Formaggio, J. A., Fowler, M. M., Frame, K., Frank, E. D., Frati, W., Gagnon, N., Germani, J. V., Gil, S., Graham, K., Grant, D. R., Hahn, R. L., Hallin, A. L., Hallman, E. D., Hamer, A. S., Hamian, A. A., Handler, W. B., Haq, R. U., Hargrove, C. K., Harvey, P. J., Hazama, R., Heeger, K. M., Heintzelman, W. J., Heise, J., Helmer, R. L., Hepburn, J. D., Heron, H., Hewett, J. L., Hime, A., Howe, M., Hykawy, J. G., Isaac, M. C. P., Jagam, P., Jelley, N. A., Jillings, C., Jonkmans, G., Kazkaz, K., Keener, P. T., Klein, J. R., Knox, A. B., Komar, R. J., Kouzes, R., Kutter, T., Kyba, C. C. M., Law, J., Lawson, I. T., Lay, M., Lee, H. W., Lesko, K. T., Leslie, J. R., Levine, I., Locke, W., Luoma, S., Lyon, J., Majerus, S., Mak, H. B., Maneira, J., Manor, J., Marino, A. D., McCauley, N., McDonald, A. B., McDonald, D. S., McFarlane, K., McGregor, G., Meijer-Drees, R., Miin, C., Miller, G. G., Milton, G., Moffat, B. A., Moorhead, M. E., Nally, C. W., Neubauer, M. S., Newcomer, F. M., Ng, H. S., Noble, A. J., Norman, E. B., Novikov, V. M., O'Neill, M., Okada, C. E., Ollerhead, R. W., Omori, M., Orrell, J. L., Oser, S. M., Poon, A. W. P., Radcliffe, T. J., Roberge, A., Robertson, B. C., Robertson, R. G. H., Rosendahl, S. S. E., Rowley, J. K., Rusu, V. L., Saettler, E., Schaffer, K. K., Schwendener,

M. H., Schülke, A., Seifert, H., Shatkay, M., Simpson, J. J., Sims, C. J., Sinclair, D., Skensved, P., Smith, A. R., Smith, M. W. E., Spreitzer, T., Starinsky, N., Steiger, T. D., Stokstad, R. G., Stonehill, L. C., Storey, R. S., Sur, B., Tafirout, R., Tagg, N., Tanner, N. W., Taplin, R. K., Thorman, M., Thornewell, P. M., Trent, P. T., Tserkovnyak, Y., Van Berg, R., Van de Water, R. G., Virtue, C. J., Waltham, C. E., Wang, J. X., Wark, D. L., West, N., Wilhelmy, J. B., Wilkerson, J. F., Wilson, J. R., Wittich, P., Wouters, J. M., and Yeh, M. (2002), "Direct Evidence for Neutrino Flavor Transformation from Neutral-Current Interactions in the Sudbury Neutrino Observatory," *Physical Review Letters*, 89, 011301. 6 p.

Ahn, M., Aoki, S., Bhang, H., Boyd, S., Casper, D., Choi, J., Fukuda, S., Fukuda, Y., Gajewski, W., Hara, T., Hasegawa, M., Hasegawa, T., Hayato, Y., Hill, J., Ichikawa, A., Ikeda, A., Inagaki, T., Ishida, T., Ishii, T., Ishitsuka, M., Itow, Y., Iwashita, T., Jang, H., Jang, J., Jeon, E., Jung, C., Kajita, T., Kameda, J., Kaneyuki, K., Kato, I., Kearns, E., Kibayashi, A., Kielczewska, D., Kobayashi, K., Kim, B., Kim, C., Kim, J., Kim, S., Kobayashi, T., Kohama, M., Koshio, Y., Kropp, W., Learned, J., Lim, S., Lim, I., Maesaka, H., Martens, K., Maruyama, T., Matsuno, S., Mauger, C., McGrew, C., Mine, S., Miura, M., Miyano, K., Moriyama, S., Nakahata, M., Nakamura, K., Nakano, I., Nakata, F., Nakaya, T., Nakayama, S., Namba, T., Nishikawa, K., Nishiyama, S., Noda, S., Obayashi, A., Okada, A., Ooyabu, T., Oyama, Y., Pac, M., Park, H., Sakuda, M., Sakurai, N., Sasao, N., Scholberg, K., Sharkey, E., Shiozawa, M., So, H., Sobel, H., Stachyra, A., Stone, J., Suga, Y., Sulak, L., Suzuki, A., Suzuki, Y., Takeuchi, Y., Tamura, N., Toshito, T., Totsuka, Y., Vagins, M., Walter, C., Wilkes, R., Yamada, S., Yamamoto, S., Yanagisawa, C., Yokoyama, H., Yoo, J., Yoshida, M., and Zalipska, J. (2003), "Indications of Neutrino Oscillation in a 250 km Long-Baseline Experiment," *Physical Review Letters*, 90, 041801.

Albright, C., Dueck, A., and Rodejohann, W. (2010), "Possible Alternatives to Tribimaximal Mixing," *Eur.Phys.J.C*, 70, 1099.

An, F. P., Bai, J. Z., Balantekin, A. B., Band, H. R., Beavis, D., Beriguete, W., Bishai, M., Blyth, S., Boddy, K., Brown, R. L., Cai, B., Cao, G. F., Cao, J., Carr, R., Chan, W. T., Chang, J. F., Chang, Y., Chasman, C., Chen, H. S., Chen, H. Y., Chen, S. J., Chen, S. M., Chen, X. C., Chen, X. H., Chen, X. S., Chen, Y., Chen, Y. X., Cherwinka, J. J., Chu, M. C., Cummings, J. P., Deng, Z. Y., Ding, Y. Y., Diwan, M. V., Dong, L., Draeger, E., Du, X. F., Dwyer, D. A., Edwards, W. R., Ely, S. R., Fang, S. D., Fu, J. Y., Fu, Z. W., Ge, L. Q., Ghazikhanian, V., Gill, R. L., Goett, J., Gonchar, M., Gong, G. H., Gong, H., Gornushkin, Y. A., Greenler, L. S., Gu, W. Q., Guan, M. Y., Guo, X. H., Hackenburg, R. W., Hahn, R. L., Hans, S., He, M., He, Q., He, W. S., Heeger, K. M., Heng, Y. K., Hinrichs, P., Ho, T. H., Hor, Y. K., Hsiung, Y. B., Hu, B. Z., Hu, T., Hu, T., Huang, H. X., Huang, H. Z., Huang, P. W., Huang, X., Huang, X. T., Huber, P., Isvan, Z., Jaffe, D. E., Jetter, S., Ji, X. L., Ji, X. P., Jiang, H. J., Jiang, W. Q., Jiao,

J. B., Johnson, R. A., Kang, L., Kettell, S. H., Kramer, M., Kwan, K. K., Kwok, M. W., Kwok, T., Lai, C. Y., Lai, W. C., Lai, W. H., Lau, K., Lebanowski, L., Lee, J., Lee, M. K. P., Leitner, R., Leung, J. K. C., Leung, K. Y., Lewis, C. A., Li, B., Li, F., Li, G. S., Li, J., Li, Q. J., Li, S. F., Li, W. D., Li, X. B., Li, X. N., Li, X. Q., Li, Y., Li, Z. B., Liang, H., Liang, J., Lin, C. J., Lin, G. L., Lin, S. K., Lin, S. X., Lin, Y. C., Ling, J. J., Link, J. M., Littenberg, L., Littlejohn, B. R., Liu, B. J., Liu, C., Liu, D. W., Liu, H., Liu, J. C., Liu, J. L., Liu, S., Liu, X., Liu, Y. B., Lu, C., Lu, H. Q., Luk, A., Luk, K. B., Luo, T., Luo, X. L., Ma, L. H., Ma, Q. M., Ma, X. B., Ma, X. Y., Ma, Y. Q., Mayes, B., McDonald, K. T., McFarlane, M. C., Mckeown, R. D., Meng, Y., Mohapatra, D., Morgan, J. E., Nakajima, Y., Napolitano, J., Naumov, D., Nemchenok, I., Newsom, C., Ngai, H. Y., Ngai, W. K., Nie, Y. B., Ning, Z., Ochoa-Ricoux, J. P., Oh, D., Olshevski, A., Pagac, A., Patton, S., Pearson, C., Pec, V., Peng, J. C., Piilonen, L. E., Pinsky, L., Pun, C. S. J., Qi, F. Z., Qi, M., Qian, X., Raper, N., Rosero, R., Roskovec, B., Ruan, X. C., Seilhan, B., Shao, B. B., Shih, K., Steiner, H., Stoler, P., Sun, G. X., Sun, J. L., Tam, Y. H., Tanaka, H. K., Tang, X., Themann, H., Torun, Y., Trentalange, S., Tsai, O., Tsang, K. V., Tsang, R. H. M., Tull, C., Viren, B., Virostek, S., Vorobel, V., Wang, C. H., Wang, L. S., Wang, L. Y., Wang, L. Z., Wang, M., Wang, N. Y., Wang, R. G., Wang, T., Wang, W., Wang, X., Wang, X., Wang, Y. F., Wang, Z., Wang, Z., Wang, Z. M., Webber, D. M., Wei, Y. D., Wen, L. J., Wenman, D. L., Whisnant, K., White, C. G., Whitehead, L., Whitten, C. A., Wilhelmi, J., Wise, T., Wong, H. C., Wong, H. L. H., Wong, J., Worcester, E. T., Wu, F. F., Wu, Q., Xia, D. M., Xiang, S. T., Xiao, Q., Xing, Z. Z., Xu, G., Xu, J., Xu, J., Xu, J. L., Xu, W., Xu, Y., Xue, T., Yang, C. G., Yang, L., Ye, M., Yeh, M., Yeh, Y. S., Yip, K., Young, B. L., Yu, Z. Y., Zhan, L., Zhang, C., Zhang, F. H., Zhang, J. W., Zhang, Q. M., Zhang, K., Zhang, Q. X., Zhang, S. H., Zhang, Y. C., Zhang, Y. H., Zhang, Y. X., Zhang, Z. J., Zhang, Z. P., Zhang, Z. Y., Zhao, J., Zhao, Q. W., Zhao, Y. B., Zheng, L., Zhong, W. L., Zhou, L., Zhou, Z. Y., Zhuang, H. L., and Zou, J. H. (2012), "Observation of Electron-Antineutrino Disappearance at Daya Bay," *Physical Review Letters*, 108, 171803.

Anselmann, P. et al. (1992), "Solar neutrinos observed by GALLEX at Gran Sasso." *Phys. Lett.*, B285, 376–389.

Apollonio, M., Baldini, A., Bemporad, C., Caffau, E., Cei, F., Declais, Y., De Kerret, H., Dieterle, B., Etenko, A., and George, J. (1999), "Limits on neutrino oscillations from the CHOOZ experiment," *Physics Letters B*, 466, 415–430.

Arai, Y. (2005), *AMT-3 (ATLAS Muon TDC Version 3) Users Manual[Online]*, ATLAS Collaboration, http://atlas.kek.jp/tdc/amt3/index.html, rev. 0.32 18-05-2005 edn.

Araki, T., Eguchi, K., Enomoto, S., Furuno, K., Ichimura, K., Ikeda, H., Inoue, K., Ishihara, K., Iwamoto, T., Kawashima, T., Kishimoto, Y., Koga, M., Koseki,

Y., Maeda, T., Mitsui, T., Motoki, M., Nakajima, K., Ogawa, H., Owada, K., Ricol, J. S., Shimizu, I., Shirai, J., Suekane, F., Suzuki, A., Tada, K., Tajima, O., Tamae, K., Tsuda, Y., Watanabe, H., Busenitz, J., Classen, T., Djurcic, Z., Keefer, G., McKinny, K., Mei, D. M., Piepke, A., Yakushev, E., Berger, B., Chan, Y., Decowski, M., Dwyer, D., Freedman, S., Fu, Y., Fujikawa, B., Goldman, J., Gray, F., Heeger, K., Lesko, K., Luk, K. B., Murayama, H., Poon, A., Steiner, H., Winslow, L., Horton-Smith, G., Mauger, C., McKeown, R., Vogel, P., Lane, C., Miletic, T., Gorham, P., Guillian, G., Learned, J., Maricic, J., Matsuno, S., Pakvasa, S., Dazeley, S., Hatakeyama, S., Rojas, A., Svoboda, R., Dieterle, B., Detwiler, J., Gratta, G., Ishii, K., Tolich, N., Uchida, Y., Batygov, M., Bugg, W., Efremenko, Y., Kamyshkov, Y., Kozlov, A., Nakamura, Y., Gould, C., Karwowski, H., Markoff, D., Messimore, J., Nakamura, K., Rohm, R., Tornow, W., Wendell, R., Young, A., Chen, M. J., Wang, Y. F., Piquemal, F., and KamLAND Collaboration (2005), "Measurement of Neutrino Oscillation with KamLAND: Evidence of Spectral Distortion," *Physical Review Letters*, 94, 081801.

Ashie, Y., Hosaka, J., Ishihara, K., Itow, Y., Kameda, J., Koshio, Y., Minamino, A., Mitsuda, C., Miura, M., and Moriyama, S. (2004), "Evidence for an oscillatory signature in atmospheric neutrino oscillations," *Physical Review Letters*, 93, 101801.

Barger, V., Whisnant, K., Pakvasa, S., and Phillips, R. (1980), "Matter effects on three-neutrino oscillations," *Physical Review D*, 22, 2718–2726.

Becker-Szendy, R., Bionta, R. M., Bratton, C. B., Casper, D., Claus, R., Cortez, B., Dye, S. T., Errede, S., Foster, G. W., and Gajewski, W. (1993), "IMB-3: A Large water Cherenkov detector for nucleon decay and neutrino interactions," *Nuclear Inst. and Methods in Physics Research, A*, 324, 363–382.

Benhar, O., Farina, N., Nakamura, H., Sakuda, M., and Seki, R. (2005), "Electron- and neutrino-nucleus scattering in the impulse approximation regime," *Physical Review D*, 72, –.

Benvenuti, A. C. and al, e. (1974), "Observation of Muonless Neutrino Induced Inelastic Interactions," *Physical Review Letters*, 32, 800–803.

Berger, C., Fröhlich, M., Mönch, H., Nisius, R., Raupach, F., Schleper, P., Benadjal, Y., Blum, D., Bourdarios, C., and Dudelzak, B. (1989), "Study of atmospheric neutrino interactions with the Fréjus detector," *Physics Letters B*, 227, 489–494.

Berger, C., Fröhlich, M., Mönch, H., Nisius, R., Raupach, F., Blum, D., Bourdarios, C., Dudelzak, B., Eschstruth, P., and Jullian, S. (1990), "A Study of atmospheric neutrino oscillations in the FREJUS experiment," *Physics Letters B*, 245, 305–310.

Beringer, J. and Particle Data Group (2012), "2012 Review of Particle Physics and 2013 partial update for the 2014 edition," *Physical Review D*, 86, 010001.

Bojechko, C., Caravaca, J., Castillo, R., Cervera, A., Connolly, K., Cremonesi, L., Di Lodovico, F., Dufour, F., Giganti, C., Hillairet, A., Ieva, M., Izmaylov, A., Kim, J., Lagoda, J., Lindner, T., Magaletti, L., Monfregola, L., Myslik, J., Nielsen, C., Oryszczak, W., Ravonel, M., Sanchez, F., Smith, B., Wilking, M. J., and Wilson, J. R. (2013), "CC-multiple-pion ν_μ event selections in the ND280 tracker using Run 1+2+3+4 data," *T2K Technical Notes*, 152, 1–180.

Bond, J. R., Efstathiou, G., and Silk, J. (1980), "Massive neutrinos and the large-scale structure of the universe," *Physical Review Letters*, 45.

Branco, G. C., Morozumi, T., Nobre, B. M., and Rebelo, M. N. (2001), "A Bridge between CP violation at Low Energies and Leptogenesis," *Nucl. Phys. B*, 617, 475–492. 18 p.

Brun, R., McPherson, A., Zanarini, P., Maire, M., and Bruyant, F. (1987), "GEANT 3," Tech. rep., CERN.

Casper, D., Becker-Szendy, R., Bratton, C. B., Cady, D. R., Claus, R., Dye, S. T., Gajewski, W., Goldhaber, M., Haines, T. J., and Halverson, P. G. (1991), "Measurement of atmospheric neutrino composition with the IMB-3 detector," *Physical Review Letters*, 66, 2561.

Chadwick, J. (1914), "Distribution in intensity in the magnetic spectrum of the -rays of radium," *Ver. Dtsch. Physik. Ges.*, 16, 383391.

Chadwick, J. (1932), "Possible Existance of a Neutron," *Nature*, 192, 312.

Cohen, A. G., Glashow, S. L., and Ligeti, Z. (2008), "Disentangling Neutrino Oscillations," *arXiv.org*.

Conrad, J. M., Louis, W. C., and Shaevitz, M. H. (2013), "The LSND and MiniBooNE Oscillation Searches at High Δ m2," *Annual Review of Nuclear and Particle Science*, 63, 45–67.

Covi, L., Roulet, E., and Vissani, F. (1996), "CP violating decays in leptogenesis scenarios," *Physics Letters B*, 384, 169–174.

Cox, D. (1970), *Analysis of Binary Data*, Methuen, London.

Danby, G., Gaillard, J. M., Goulianos, K., Lederman, L. M., Mistry, N., Schwartz, M., and Steinberger, J. (1962), "Observation of high-energy neutrino reactions and the existence of two kinds of neutrinos," *Physical Review Letters*, 9, 36–44.

Davis, R. (1994), "A review of the Homestake solar neutrino experiment," *Progress in Particle and Nuclear Physics*, 32, 13–32.

Day, M. and McFarland, K. S. (2012), "Differences in quasielastic cross sections of muon and electron neutrinos," *Physical Review D*, 86, 053003.

de Perio, P. (2011), "NEUT Nuclear Effects (FSI)," *T2K Technical Notes*, 33, 1–65.

de Perio, P., Mahn, K., Rodrigues, P., Sinclair, P., and Terri, R. (2012), "Implementation of the NIWG Cross Section Parametrization," *T2K Technical Notes*, 113, 1–90.

de Perio, P., Hartz, M., Hayato, Y., Mahn, K., McFarland, K., Rodrigues, P., Sinclair, P., Terri, R., and Wascko, M. (2013), "Cross section parameters for the 2012a oscillation analysis," *T2K Technical Notes*, 108, 1–117.

DONUT Collaboration (2001), "Observation of tau neutrino interactions," *Physics Letters B*, 504, 218.

Dufour, F. (2009), "Precise Study of Atmospheric Neutrino Oscillation Pattern Using Super-Kamiokande I and II," Ph.D. thesis, SuperK, Boston University.

Elliott, S. R. and Vogel, P. (2002), "Double beta decay," *arXiv preprint hep-ph/0202264*.

Feldman, G. J. and Cousins, R. D. (1998), "A Unified Approach to the Classical Statistical Analysis of Small Signals," *Phys. Rev. D*, 57, 3873–3889. 40 p.

Fermi, E. (1934a), "Sopra lo spostamento per pressione delle righe elevate delle serie spettrali," *Il Nuovo Cimento*, 11, 1–19.

Fermi, E. (1934b), "Versuch einer Theorie der -Strahlen. I," *Zeitschrift fr Physik*, 88, 161177.

Fisher, R. (1922), "On the Mathematical Foundations of Theoretical Statistics," *Philosophical Transactions of the Royal Society of London. Series A, Containing Papers of a Mathematical or Physical Character*, 222, 309–368.

FLUKA Collaboration (2005), "FLUKA: A Multi-Particle Transport Code," .

Fogli, G., Lisi, E., Marrone, A., Montanino, D., Palazzo, A., and Rotunno, A. (2003), "Solar neutrino oscillation parameters after first KamLAND results," *Physical Review D*, 67, 073002.

Forero, D. V., Tortola, M., and Valle, J. W. F. (2012), "Global status of neutrino oscillation parameters after Neutrino-2012," *arXiv*, D86, 073012.

Fukuda, S., Fukuda, Y., Hayakawa, T., Ichihara, E., Ishitsuka, M., Itow, Y., Kajita, T., Kameda, J., Kaneyuki, K., and Kasuga, S. (2003), "The Super-kamiokande Detector," *Nuclear Instruments and Methods in Physics Research Section A: Accelerators, Spectrometers, Detectors and Associated Equipment*, 501, 418–462.

Fukuda, Y., Hayakawa, T., Ichihara, E., Inoue, K., Ishihara, K., Ishino, H., Itow, Y., Kajita, T., Kameda, J., Kasuga, S., Kobayashi, K., Kobayashi, Y., Koshio, Y., Miura, M., Nakahata, M., Nakayama, S., Okada, A., Okumura, K., Sakurai, N., Shiozawa, M., Suzuki, Y., Takeuchi, Y., Totsuka, Y., Yamada, S., Earl, M. A., Habig, A., Kearns, E. T., Messier, M. D., Scholberg, K., Stone, J. L., Sulak, L. R., Walter, C. W., Goldhaber, M., Barszczak, T., Casper, D. W., Gajewski, W., Halverson, P. G., Hsu, J., Kropp, W. R., Price, L. R., Reines, F., Smy, M. B., Sobel, H. W., Vagins, M. R., Ganezer, K. S., Keig, W. E., Ellsworth, R. W., Tasaka, S., Flanagan, J. W., Kibayashi, A., Learned, J. G., Matsuno, S., Stenger, V. J., Takemori, D., Ishii, T., Kanzaki, J. I., Kobayashi, T., Mine, S., Nakamura, K., Nishikawa, K., Oyama, Y., Sakai, A., Sakuda, M., Sasaki, O., Echigo, S., Kohama, M., Suzuki, A. T., Haines, T. J., Blaufuss, E., Kim, B. K., Sanford, R., Svoboda, R., Chen, M. L., Conner, Z., Goodman, J. A., Sullivan, G. W., Hill, J., Jung, C. K., Martens, K., Mauger, C., McGrew, C., Sharkey, E., Viren, B. M., Yanagisawa, C., Doki, W., Miyano, K., Okazawa, H., Saji, C., Takahata, M., Nagashima, Y., Takita, M., Yamaguchi, T., Yoshida, M., Kim, S. B., Etoh, M., Fujita, K., Hasegawa, A., Hasegawa, T., Hatakeyama, S., Iwamoto, T., Koga, M., Maruyama, T., Ogawa, H., Shirai, J., Suzuki, A., Tsushima, F., Koshiba, M., Nemoto, M., Nishijima, K., Futagami, T., Hayato, Y., Kanaya, Y., Kaneyuki, K., Watanabe, Y., Kielczewska, D., Doyle, R. A., George, J. S., Stachyra, A. L., Wai, L. L., Wilkes, R. J., and Young, K. K. (1998), "Evidence For Oscillation Of Atmospheric Neutrinos," *Physical Review Letters*, 81, 1562.

Gamow, G. and Teller, E. (1936), "Selection Rules for the β-Disintegration," *Phys. Rev.*, 49, 895–899.

GCALOR Collaboration (????), "GCALOR: Low Energy Neutron Simulation," .

Goldhaber, M., Grodzins, L., and Sunyar, A. W. (1958), "Helicity of Neutrinos," *Phys.Rev.*, 109, 1015–1017.

Haines, T. J., Bionta, R. M., Blewitt, G., Bratton, C. B., Casper, D., Claus, R., Cortez, B. G., Errede, S., Foster, G. W., and Gajewski, W. (1986), "Calculation of atmospheric neutrino-induced backgrounds in a nucleon-decay search," *Physical Review Letters*, 57.

Halzen, F. and Martin, A. (1984), *Quarks and Leptons: An Introductory Course on Modern Particle Physics*, Wiley.

Hartz, M., Kaboth, A., and Mahn, K. (2013), "Constraining the Flux and Cross Section Models with Data from the ND280 Detector for the 2013 Oscillation Analysis (BANFF)," *T2K Technical Notes*, 166, 1–47.

Hasert, F. J. and et. al. (1973), "Observation of neutrino-like interactions without muon or electron in the Gargamelle neutrino experiment," *Phys. Lett.*, B46, 138–140.

Hayato, Y. (2002), "NEUT," *Nucl.Phys.Proc.Suppl.*, 112, 171–176.

Heinrich,J (2003), "Pitfalls of goodness-of-t from likelihood," *Proceedings of PHYSTAT2003: Statistical Problems in Particle Physics, Astrophysics, and Cosmology, Menlo Park, California*.

Himmel, A. (2013), "Recent Atmospheric Neutrino Results from Super-Kamiokande," *arXiv.org*.

Hiraide, K., Alcaraz-Aunion, J. L., Brice, S. J., Bugel, L., Catala-Perez, J., Cheng, G., Conrad, J. M., Djurcic, Z., Dore, U., and Finley, D. A. (2008), "Search for charged current coherent pion production on carbon in a few-GeV neutrino beam," *Physical Review D*, 78, 112004.

Hirata, K. S. and others (1992), "Observation of a small atmospheric muon-neutrino / electron-neutrino ratio in Kamiokande," *Phys.Lett.*, B280, 146–152.

Hirata, K. S., Kajita, T., Koshiba, M., Nakahata, M., Ohara, S., Oyama, Y., Sato, N., Suzuki, A., Takita, M., and Totsuka, Y. (1988), "Experimental study of the atmospheric neutrino flux," *Physics Letters B*, 205, 416–420.

Ieki, K., Bronner, C., and Sakashita, K. (2013), "Run1-4 p-theta Electron Neutrino Appearance Analysis," *T2K Technical Notes*, 161.

Ishihara, C. (2010), "Full Three Flavor Oscillation Analysis of Atmospheric Neutrino Data Observed in Super-Kamokande," Ph.D. thesis, University of Tokyo.

Ishimori, H., Kobayashi, T., Ohki, H., Shimizu, Y., and Okada, H. (2010), "Non-Abelian Discrete Symmetries in Particle Physics," *Prog.Theor.Phys.Suppl.*, 183, arXiv:1003.3552.

Itow, Y., Kajita, T., Kaneyuki, K., Shiozawa, M., Totsuka, Y., Hayato, Y., Ishida, T., Ishii, T., Kobayashi, T., Maruyama, T., Nakamura, K., Obayashi, Y., Oyama, Y., Sakuda, M., Yoshida, M., Aoki, S., Hara, T., Suzuki, A., Ichikawa, A., Nakaya, T., Nishikawa, K., Hasegawa, T., Ishihara, K., Suzuki, A., and Konaka, A. (2001), "The JHF-Kamioka neutrino project," *arXiv*, hep-ex.

Iyogi, K. (2011), "Chokisen nyutorino jikken no tame no kochi kenshutsu-ki supakamiokande no kosei [in Japanese]," Master's thesis, Univ. of Tokyo.

James, F. and Roos, M. (1975), "Minuit - a system for function minimization and analysis of the parameter errors and correlations," *Computer Physics Communications*, 10, 343–367.

Juszczak, C., Nowak, J. A., and Sobczyk, J. T. (2005), "Spectrum of recoil nucleons in quasi-elastic neutrino-nucleus interactions," *The European Physical Journal C*, 39, 195–200.

Kameda, J. (2013), "Updated study of the systematic error in ν_μ-disappearance analysis from Super-Kamiokande," *T2K Technical Notes*, 159, 1–45.

Kayser, B. (2011), "The Connection Between Neutrino CP Violation and Leptogenesis," .

King, S. and Luhn, C. (2013), "Neutrino Mass and Mixing with Discrete Symmetry," *Rept.Prog.Phys*, 76, arXiv:1301.1340.

Konopinski, E. J. and Mahmoud, H. M. (1953), "The universal Fermi interaction," *Physical Review*, 92, 1045.

Lavin, P. (2012), "The optics of a water drop: Mie scattering and the Debye series," .

Lee, T. D. and Yang, C. (1956), "Question of parity conservation in weak interactions," *Phys. Rev.*, 104, 254258.

LEP Collaborations and the LEP Electroweak Working Group (2001)*XX International Symposium on Lepton and Photon Interatcitons at High Energy Rome Italy*.

Lyubushkin, V., Popov, B., Kim, J. J., Camilleri, L., Levy, J. M., Mezzetto, M., Naumov, D., Alekhin, S., Astier, P., Autiero, D., Baldisseri, A., Baldo-Ceolin, M., Banner, M., Bassompierre, G., Benslama, K., Besson, N., Bird, I., Blumenfeld, B., Bobisut, F., Bouchez, J., Boyd, S., Bueno, A., Bunyatov, S., Cardini, A., Cattaneo, P. W., Cavasinni, V., Cervera-Villanueva, A., Challis, R., Chukanov, A., Collazuol, G., Conforto, G., Conta, C., Contalbrigo, M., Cousins, R., Daniels, D., Degaudenzi, H., Del Prete, T., De Santo, A., Dignan, T., Di Lella, L., do Couto e Silva, E., Dumarchez, J., Ellis, M., Feldman, G. J., Ferrari, R., Ferrère, D., Flaminio, V., Fraternali, M., Gaillard, J. M., Gangler, E., Geiser, A., Geppert, D., Gibin, D., Gninenko, S., Godley, A., Gomez-Cadenas, J. J., Gosset, J., Gößling, C., Gouanère, M., Grant, A., Graziani, G., Guglielmi, A., Hagner, C., Hernando, J., Hubbard, D., Hurst, P., Hyett, N., Iacopini, E., Joseph, C., Juget, F., Kent, N., Kirsanov, M., Klimov, O., Kokkonen, J., Kovzelev, A., Krasnoperov, A., Kulagin, S., Kustov, D., Lacaprara, S., Lachaud, C., Lakić, B., Lanza, A., La Rotonda, L., Laveder, M., Letessier-Selvon, A., Ling, J., Linssen, L., Ljubicic, A., Long, J., Lupi, A., Marchionni, A., Martelli, F., Méchain, X., Mendiburu, J. P., Meyer, J. P., Mishra, S. R., Moorhead, G. F., Nédélec, P., Nefedov, Y., Nguyen-Mau, C., Orestano, D., Pastore, F., Peak, L. S., Pennacchio, E., Pessard, H., Petti, R., Placci, A., Polesello, G., Pollmann, D., Polyarush, A., Poulsen, C., Rebuffi, L., Rico, J., Riemann, P., Roda, C., Rubbia, A., Salvatore, F., Samoylov, O., Schahmaneche, K., Schmidt, B., Schmidt, T., Sconza, A., Seaton, M., Sevior, M., Sillou, D., Soler, F. J. P., Sozzi, G., Steele, D., Stiegler, U., Stipcevic, M., Stolarczyk, T., Tareb-Reyes, M., Taylor, G. N., Tereshchenko, V., Toropin, A., Touchard, A. M., Tovey, S. N., Tran, M. T., Tsesmelis, E., Ulrichs, J., Vacavant, L., Valdata-Nappi,

M., Valuev, V., Vannucci, F., Varvell, K. E., Veltri, M., Vercesi, V., Vidal-Sitjes, G., Vieira, J. M., Vinogradova, T., Weber, F. V., Weisse, T., Wilson, F. F., Winton, L. J., Wu, Q., Yabsley, B. D., Zaccone, H., Zuber, K., and Zuccon, P. (2009), "A study of quasi-elastic muon neutrino and antineutrino scattering in the NOMAD experiment," *The European Physical Journal C*, 63, 355–381.

MACRO Collaboration (2001), "Matter effects in upward-going muons and sterile neutrino oscillations," *Physics Letters B*, 517, 59–66.

Mann, W. A. (2001), "New results on atmospheric neutrinos from Soudan 2," *Nuclear Physics B-Proceedings Supplements*, 91, 134–140.

Mikheev, S. and Smirnov, A. (1985)*Sov. J. Nucl. Phys.*, 42, 913–917.

MINOS Collaboration, Adamson, P., Anghel, I., Aurisano, A., Barr, G., Bishai, M., Blake, A., Bock, G. J., Bogert, D., Cao, S. V., Castromonte, C. M., Cherdack, D., Childress, S., Coelho, J. A. B., Corwin, L., Cronin-Hennessy, D., de Jong, J. K., Devan, A. V., Devenish, N. E., Diwan, M. V., Escobar, C. O., Evans, J. J., Falk, E., Feldman, G. J., Frohne, M. V., Gallagher, H. R., Gomes, R. A., Goodman, M. C., Gouffon, P., Graf, N., Gran, R., Grzelak, K., Habig, A., Hahn, S. R., Hartnell, J., Hatcher, R., Himmel, A., Holin, A., Huang, J., Hylen, J., Irwin, G. M., Isvan, Z., James, C., Jensen, D., Kafka, T., Kasahara, S. M. S., Koizumi, G., Kordosky, M., Kreymer, A., Lang, K., Ling, J., Litchfield, P. J., Lucas, P., Mann, W. A., Marshak, M. L., Mayer, N., McGivern, C., Medeiros, M. M., Mehdiyev, R., Meier, J. R., Messier, M. D., Michael, D. G., Miller, W. H., Mishra, S. R., Sher, S. M., Moore, C. D., Mualem, L., Musser, J., Naples, D., Nelson, J. K., Newman, H. B., Nichol, R. J., Nowak, J. A., O'Connor, J., Orchanian, M., Pahlka, R. B., Paley, J., Patterson, R. B., Pawloski, G., Perch, A., Phan-Budd, S., Plunkett, R. K., Poonthottathil, N., Qiu, X., Radovic, A., Rebel, B., Rosenfeld, C., Rubin, H. A., Sanchez, M. C., Schneps, J., Schreckenberger, A., Schreiner, P., Sharma, R., Sousa, A., Tagg, N., Talaga, R. L., Thomas, J., Thomson, M. A., Tian, X., Timmons, A., Tognini, S. C., Toner, R., Torretta, D., Tzanakos, G., Urheim, J., Vahle, P., Viren, B., Weber, A., Webb, R. C., White, C., Whitehead, L., Whitehead, L. H., Wojcicki, S. G., and Zwaska, R. (2014), "Combined analysis of ν_μ disappearance and $\nu_\mu \to \nu_e$ appearance in MINOS using accelerator and atmospheric neutrinos," *arXiv.org*.

Mituska, G. (2009), "Study of non-standard neutrinos interactions with atmospheric neu- trino data in Super-Kamiokande," Ph.D. thesis, University of Tokyo.

Mohapatra, R. N. and Smirnov, A. Y. (2005), "Neutrino Mass and New Physics," *arXiv*, hep-ph.

Moniz, E., Sick, I., Whitney, R., Ficenec, J., Kephart, R., and Trower, W. P. (1971), "Nuclear Fermi Momenta from Quasielastic Electron Scattering," *Physical Review Letters*, 26, 445.

Murnaghan, F. (1962), *The Unitary and Rotation Groups*, Sparan Books.

Neddermeyer, S. and Anderson, C. (1937), "Note on the nature of cosmic-ray particles," *Phys. Rev.*, 51, 884886.

Neyman, J. (1937), "Outline of a Theory of Statistical Estimation Based on the Classical Theory of Probability," *Philosophical Transactions of the Royal Society A: Mathematical, Physical and Engineering Sciences*, 236, 333–380.

Nishino, H., Awai, K., Hayato, Y., Nakayama, S., Okumura, K., Shiozawa, M., Takeda, A., Ishikawa, K., Minegishi, A., and Arai, Y. (2009), "High-speed charge-to-time converter ASIC for the Super-Kamiokande detector," *Nuclear Inst. and Methods in Physics Research, A*, 610, 710–717.

Parke, S. J. (1986a), "Nonadiabatic level crossing in resonant neutrino oscillations," *Physical Review Letters*, 57, 1275.

Parke, S. J. (1986b), "Resonant Neutrino Oscillations," in *Topical Mtg. of 14th SLAC Summer Inst. on Particle Physics, Stanford, CA, Aug 5-8*, FERMILAB-CONF-86/131-T.

Parke, S. J. and Walker, T. P. (1986), "Resonant-solar-neutrino-oscillation experiments," *Physical Review Letters*, 57, 2322.

Particle Physics Project Prioritization Panel (2008), "US Particle Physics: Scientific Opportunities. A Strategic Plan for the Next Ten Years." .

Patterson, R. B. (2013), "The NOvA experiment: status and outlook," *Nuclear Physics B-Proceedings Supplements*, 235-236, 151–157.

Pauli, W. (1930), "Letter to the physical society of tubingen," reproduced in physics today 31,(9):23, 1978.

Perl, M., Abrams, G., Boyarski, A., Breidenbach, M., Briggs, D., Bulos, F., Chinowsky, W., Dakin, J., and et al. (1975), "Evidence for Anomalous Lepton Production in e+e Annihilation," *Physical Review Letters*, 35, 1489.

Plank Collaboration, Ade, P. A. R., Aghanim, N., Armitage-Caplan, C., Arnaud, M., Ashdown, M., Atrio-Barandela, F., Aumont, J., Baccigalupi, C., Banday, A. J., Barreiro, R. B., Bartlett, J. G., Battaner, E., Benabed, K., Benoît, A., Benoit-Lévy, A., Bernard, J. P., Bersanelli, M., Bielewicz, P., Bobin, J., Bock, J. J., Bonaldi, A., Bond, J. R., Borrill, J., Bouchet, F. R., Bridges, M., Bucher, M., Burigana, C., Butler, R. C., Calabrese, E., Cappellini, B., Cardoso, J. F., Catalano, A., Challinor, A., Chamballu, A., Chary, R. R., Chen, X., Chiang, H. C., Chiang, L. Y., Christensen, P. R., Church, S., Clements, D. L., Colombi, S., Colombo, L. P. L., Couchot, F., Coulais, A., Crill, B. P., Curto, A., Cuttaia,

F., Danese, L., Davies, R. D., Davis, R. J., de Bernardis, P., de Rosa, A., de Zotti, G., Delabrouille, J., Delouis, J. M., Désert, F. X., Dickinson, C., Diego, J. M., Dolag, K., Dole, H., Donzelli, S., Doré, O., Douspis, M., Dunkley, J., Dupac, X., Efstathiou, G., Elsner, F., Enßlin, T. A., Eriksen, H. K., Finelli, F., Forni, O., Frailis, M., Fraisse, A. A., Franceschi, E., Gaier, T. C., Galeotta, S., Galli, S., Ganga, K., Giard, M., Giardino, G., Giraud-Héraud, Y., Gjerløw, E., González-Nuevo, J., Górski, K. M., Gratton, S., Gregorio, A., Gruppuso, A., Gudmundsson, J. E., Haissinski, J., Hamann, J., Hansen, F. K., Hanson, D., Harrison, D., Henrot-Versille, S., Hernández-Monteagudo, C., Herranz, D., Hildebrandt, S. R., Hivon, E., Hobson, M., Holmes, W. A., Hornstrup, A., Hou, Z., Hovest, W., Huffenberger, K. M., Jaffe, A. H., Jaffe, T. R., Jewell, J., Jones, W. C., Juvela, M., Keihänen, E., Keskitalo, R., Kisner, T. S., Kneissl, R., Knoche, J., Knox, L., Kunz, M., Kurki-Suonio, H., Lagache, G., Lähteenmäki, A., Lamarre, J. M., Lasenby, A., Lattanzi, M., Laureijs, R. J., Lawrence, C. R., Leach, S., Leahy, J. P., Leonardi, R., León-Tavares, J., Lesgourgues, J., Lewis, A., Liguori, M., Lilje, P. B., Linden-Vørnle, M., López-Caniego, M., Lubin, P. M., Macías-Pérez, J. F., Maffei, B., Maino, D., Mandolesi, N., Maris, M., Marshall, D. J., Martin, P. G., Martínez-González, E., Masi, S., Massardi, M., Matarrese, S., Matthai, F., Mazzotta, P., Meinhold, P. R., Melchiorri, A., Melin, J. B., Mendes, L., Menegoni, E., Mennella, A., Migliaccio, M., Millea, M., Mitra, S., Miville-Deschênes, M. A., Moneti, A., Montier, L., Morgante, G., Mortlock, D., Moss, A., Munshi, D., Murphy, J. A., Naselsky, P., Nati, F., Natoli, P., Netterfield, C. B., Nørgaard-Nielsen, H. U., Noviello, F., Novikov, D., Novikov, I., O'Dwyer, I. J., Osborne, S., Oxborrow, C. A., Paci, F., Pagano, L., Pajot, F., Paoletti, D., Partridge, B., Pasian, F., Patanchon, G., Pearson, D., Pearson, T. J., Peiris, H. V., Perdereau, O., Perotto, L., Perrotta, F., Pettorino, V., Piacentini, F., Piat, M., Pierpaoli, E., Pietrobon, D., Plaszczynski, S., Platania, P., Pointecouteau, E., Polenta, G., Ponthieu, N., Popa, L., Poutanen, T., Pratt, G. W., Prézeau, G., Prunet, S., Puget, J. L., Rachen, J. P., Reach, W. T., Rebolo, R., Reinecke, M., Remazeilles, M., Renault, C., Ricciardi, S., Riller, T., Ristorcelli, I., Rocha, G., Rosset, C., Roudier, G., Rowan-Robinson, M., Rubiño-Martín, J. A., Rusholme, B., Sandri, M., Santos, D., Savelainen, M., Savini, G., Scott, D., Seiffert, M. D., Shellard, E. P. S., Spencer, L. D., Starck, J. L., Stolyarov, V., Stompor, R., Sudiwala, R., Sunyaev, R., Sureau, F., Sutton, D., Suur-Uski, A. S., Sygnet, J. F., Tauber, J. A., Tavagnacco, D., Terenzi, L., Toffolatti, L., Tomasi, M., Tristram, M., Tucci, M., Tuovinen, J., Türler, M., Umana, G., Valenziano, L., Valiviita, J., Van Tent, B., Vielva, P., Villa, F., Vittorio, N., Wade, L. A., Wandelt, B. D., Wehus, I. K., White, M., White, S. D. M., Wilkinson, A., Yvon, D., Zacchei, A., and Zonca, A. (2013), "Planck 2013 results. XVI. Cosmological parameters," *arXiv.org*.

Pontecorvo, B. (1947), "Nuclear Capture of Mesons and the Meson Decay," *Phys. Rev.*, 72, 246.

Rein, D. and Sehgal, L. M. (1983), "Coherent π 0 production in neutrino reactions,"

Nuclear Physics B, 223, 29–44.

Reines, F. and Cowan, C. (1953), "Detection of the free neutrino," *Phys. Rev.*, 92, 830.

Sanchez, M. C. (2001), "New results on atmospheric neutrinos from Soudan 2," *Int.J.Mod.Phys.*, A16S1B, 727–729.

Segelstein, D. (1981), ""The Complex Refractive Index of Water"," Master's thesis, "University of Missouri–Kansas City".

Smy, M. and Collaboration, S.-K. (2013), "Super-Kamiokande's Solar ν Results," *Nuclear Physics B-Proceedings Supplements*, 235-236, 49–54.

Street, J. and Stevenson, E. (1937), "New evidence for the existence of a particle of mass intermediate between the proton and electron," *Phys. Rev.*, 52, 10031004.

Suzuki, T., Measday, D., and Roalsvig, J. (1987)*Phys. Rev. C*, 35, 2212.

T2K Collaboration (2014), "Observation of ν_e Appearance in a $\nu\mu$ Beam," *Physical Review Letters*, 112.

Tang, A., Horton-Smith, G., Kudryavtsev, V., and Tonazzo, A. (2006), "Muon simulations for Super-Kamiokande, KamLAND, and CHOOZ," *Physical Review D*, 74, 53007.

Weinheimer, C., Degenddag, B., Bleile, A., Bonn, J., Bornschein, L., Kazachenko, O., Kovalik, A., and Otten, E. W. (1999), "High precision measurement of the tritium β spectrum near its endpoint and upper limit on the neutrino mass," *Physics Letters B*, 460, 219–226.

Wendell, R. (2008), "Three Flavor Oscillation Analysis of Atmospheric Neutrinos in Super-Kamiokande," Ph.D. thesis, University of North Carolina – Chapel Hill.

Wendell, R. (2014), "Prob3++: software for computing three flavor neutrino oscillation probabilities," .

Wolfenstein, L. (1978), "Neutrino oscillations in matter," *Physical Review D.*

Woods, R. D. and Saxon, D. S. (1954), "Diffuse surface optical model for nucleon-nuclei scattering," *Physical Review*, 95, 577.

Wu, C. S., Ambler, E., Hayward, R. W., Hoppes, D. D., and Hudson, R. P. (1957), "Experimental Test of Parity Conservation in Beta Decay," *Phys.Rev.*, 105, 1413–1414.

Yamada, M., Miyano, K., Miyata, H., Takei, H., Mori, M., Oyama, Y., Suzuki, A., Takahashi, K., Hirata, K. S., and Kajita, T. (1991), "Measurements of the charge ratio and polarization of 1.2-TeV/c cosmic-ray muons with the Kamiokande II detector," *Physical Review D*, 44, 617.

Yamada, S., Arai, Y., Awai, K., Hayato, Y., Ishikawa, K., Kaneyuki, K., Kouzuma, Y., Minegishi, A., Nakayama, S., Nishino, H., Okumura, K., Obayashi, Y., Shimizu, Y., Shiozawa, M., Takeda, A., Uchida, and Tomohisa (2009), "Commissioning of the New Electronics and Online System for the Super-Kamiokande Experiment," *2009 16th IEEE-NPSS Real Time Conference Poceedings*, pp. 1–5.

Yates, B. (1934), "Contingency tables involving small numbers and the χ^2 test," *Supplement to the J. Roy. Statistical Society*, 1, 217–235.

Biography

Taritree Michael Wongjirad was born in Buffalo, NY USA on September 24th, 1983 to Dr. Chatree and Thanida Wongjirad. Though he retains a tortuous relationship with Buffalo through his loyalty to the Buffalo Bills football team, he moved to Bismarck, North Dakota at an early age and considers the small midwestern city his hometown. He then left Bismarck to go to Yale University where he received a Bachelors of Science degree in Physics and a Bachelor of Arts degree in Philosophy. At Yale, he worked with Professor Dan McKinsey and Professor Moshe Gai on developing new techniques related to operating a two-phase liquid xenon time-projection chamber. The intended use of such a detector was to directly detect the existence of dark matter. After graduation he worked for 5 months for U.S. Senator Byron Dorgan of North Dakota but then returned to the McKinsey lab to continue in physics. He then joined Professor Bonnie Fleming's group, also of Yale, to work on the ArgoNeuT experiment, which was a prototype liquid argon time-projection chamber that measured neutrino interactions in the NuMI neutrino beamine at Fermi Nation Laboratory in Batavio, Illinois. In 2008, he started graduate school at Duke University to work with Professors Kate Scholberg and Chris Walter on the T2K and Super-Kamiokande experiments. Upon receiving his Ph.D. he will join the Massachusettes Istitute of Technology as a Pappalardo fellow.